ENGINEERING CHARACTERIZATION OF EARTHQUAKE GROUND MOTIONS

by

Jongwon Lee

A dissertation submitted in partial fulfillment
of the requirements for the degree of
Doctor of Philosophy
(Civil Engineering)
in The University of Michigan
2009

Doctoral Committee:

Associate Professor Russell A. Green, Chair
Professor Roman D. Hryciw
Professor Radoslaw L. Michalowski
Associate Professor Michael P. Flynn
Assistant Professor Jerome P. Lynch

To My Parents

Acknowledgements

The author would like to express his sincere gratitude to his Ph.D. committee members: Professors Russell A. Green, Roman D. Hryciw, Radoslaw L. Michalowski, Jerome P. Lynch, and Michael P. Flynn for their advice and guidance. Especially, the author feels enormous indebtedness to his advisor, Professor Russell A. Green for his advice, guidance, support, and encouragement throughout the course of all his graduate studies.

Further appreciation is extended to Professors Richard D. Woods and Jerome P. Lynch who provided valuable engineering consultation opportunities and guidance during the author's graduate studies. Also, the author wishes to acknowledge his gratitude to Dr. Hyeongwon Choi for his advice on statistics.

Finally, the author is deeply grateful to his parents and girlfriend for their patience, support, and love.

This material is based upon work supported in part by the National Science Foundation under Grant Numbers: CMMI 0530378 and CMMI 0644580. Any opinions, findings, and conclusions or recommendations expressed in this material are those of the author and do not necessarily reflect the views of the National Science Foundation.

Table of Contents

List of Tables

List of Figures

Abstract

In recent years, geologic and paleoseismic evidence has raised the awareness about the seismic hazard of the stable continental region of central-eastern U.S. (CEUS). The relevance of this topic increased due to the Nation's renewed interest in the construction of new nuclear power plants in the CEUS and due to the occurrence of the M5.2 earthquake in southern Illinois in 2008. However, few ground motion predictive relations suitable for use in engineering design are available for stable continental regions, due to the paucity of strong ground motion recordings in the region. In this regard, McGuire et al. (2001) generated a database of scaled ground motions for stable continental regions for use in detailed engineering analyses. McGuire et al. developed the motions using a state-of-the-art scaling technique.

Using McGuire et al.'s strong ground motion database, this study has developed empirical ground motion predictive relations for stable continental regions. To develop these relations, an advanced regression technique (i.e., non-linear mixed effects modeling) was used to correlate various ground motion characteristics used in engineering design to earthquake magnitude, site-to-source distance, and local site conditions (i.e., rock vs. soil). Similar predictive relations were developed in this study for active shallow crustal regions (e.g., western U.S.: WUS) using recorded motions, which allowed the ground motion characteristics of the two different tectonic regions to be compared.

The comparison showed that the CEUS motions have distinct characteristics from WUS motions. Firstly, the characteristic period of CEUS motions are systematically shorter than those of WUS motions. However, the strong ground motion duration in CEUS tends to be longer than in WUS. Also, CEUS motions had consistently larger intensities than WUS motions. Finally, the number of equivalent stress cycles (Green, 2001) for CEUS motions is larger and varies more as a function of depth than WUS motions; this trend is consistent with the identified trends in the number of equivalent strain cycles (Green and Lee, 2006).

Inherently, the predictive relations for CEUS earthquake ground motions presented herein have a larger epistemic uncertainty than the relations for WUS motions. This is attributed to the sparsity of strong ground motion recordings in stable continental regions and hence the use of scaled motions to develop the CEUS relations. However, this uncertainty will only be reduced as the database of actual recorded stable continental motions increases.

References

Green, R. A. (2001). "Energy-based evaluation and remediation of liquefiable soils," Ph.D. dissertation, Virginia Polytechnic Institute and State University, Blacksburg, Virginia.

Green, R. A., and Lee, J. (2006). "Computation of number of equivalent strain cycles: a theoretical framework". *Geomechanics II: Testing, Modeling, and Simulation*, ASCE Geotechnical Special Publication 156, 471-487.

McGuire, R. K., Silva, W. J., and Costantino, C. J. (2001). "Technical basis for revision of regulatory guidance on design ground motions: Hazard-and risk-consistent ground motion spectra guidelines.", US Nuclear Regulatory Commission, Washington, DC.

Chapter 1

Introduction

1.1 Objective of Study

The objectives of this study are:

1. To develop empirical correlations (i.e., predictive equations or relationships) for stable continental regions (e.g., central/eastern US: CEUS) relating various engineering characteristic parameters of the horizontal components of earthquake ground motions to design earthquake parameters, such as earthquake magnitude, site-to-source distance, and local site conditions (i.e., rock vs. soil).
2. To identify the differences in engineering characteristics of earthquake ground motions from stable continental regions and active seismic regions (e.g., western US: WUS).

1.2 Motivation, Approach, and Scope

In recent years, geologic and paleoseismic studies have increased the awareness of the seismic hazard of the CEUS. The relevance of this topic increased due to the Nation's renewed interest in nuclear power and the occurrence of a M5.2 earthquake in southern Illinois in 2008. However, few predictive relations for earthquake ground motion characteristics have been developed for stable continental regions because of the paucity

of earthquake ground motion recordings. In this regard, McGuire et al. (2001) generated scaled ground motion data for stable continental regions for use in engineering analyses by implementing a state-of-the-art scaling technique.

The strong ground motion data set includes 28 recorded motions and 592 scaled motions for stable continental regions. The latter were scaled from the actual earthquake ground motions recorded at active shallow crustal regions worldwide by implementing a stochastic single-corner-frequency point source model (e.g., Boore, 1983; Brune, 1970; 1971; McGuire et al., 2001; Silva and Lee, 1987).

Using the strong ground motion data set, this study develops empirical correlations (or predictive relationships) for stable continental regions relating various engineering characteristic parameters of earthquake horizontal ground motions to design earthquake parameters such as earthquake magnitude, site-to-source distance, and local site conditions (i.e., rock vs. soil). The correlations were developed using the advanced regression technique, non-linear mixed effects (NLME) modeling. Also, for the purpose of consistent comparisons between stable continental and active shallow crustal ground motions (e.g., WUS motions), similar empirical correlations for active shallow crustal regions were developed from recorded strong ground motion data. These recorded motions were actually the "seed" motions from which the scaled CEUS motions were developed.

Based on the empirical correlations (or predictive relationships) for stable continental and active shallow crustal regions, similarities and/or differences in ground motion characteristics from the two different tectonic regimes were identified from trends. Also, the influences of the design earthquake parameters on each engineering characteristic parameter are identified. The engineering characteristic parameters considered herein, are listed in Table 1-1.

Table 1-1. Engineering characteristic parameters considered in this study.

Category	No.	Engineering characteristic parameter
Characteristic periods	1	Predominant spectral period (T_p)
	2	Smoothed spectral predominant period (T_0)
	3	Average spectral period (T_{avg})
	4	Mean period (T_m)
	5	Spectral velocity-acceleration ratio periods ($T_{V/A50}$ and $T_{V/A84}$)
Strong ground motion durations	6	Significant durations ($D_{5\text{-}75}$ and $D_{5\text{-}95}$)
	7	Bracketed durations ($D_{bracket}$)
	8	Effective durations (D_{eff})
Intensity measure	9	Arias intensity (I_a)
Equivalent number of uniform cycles	10	Stress cycles ($n_{eq\tau}$)
	11	Strain cycles ($n_{eq\gamma}$)
Pore pressure generation calibration parameters	12	Pseudo energy capacity (PEC)
	13	α

It should be noted that near-fault effects (e.g., forward-directivity), fault mechanism (e.g., normal vs. strike slip) and geographical effects (e.g., basin effects) are not be considered in this study. This is because this study uses mostly scaled ground motion data for stable continental regions, not actual recorded data, and the scaling procedures are not refined enough to account for these effects. Also, it is important to note that the empirical predictive relationships developed herein, should be updated and modified continuously in conjunction with improvements in ground motion scaling methods. In this vein, McGuire et al. (2001) states: "They [i.e., scaled motions] should be replaced as appropriate data become available and as simulation methods improve and become better validated for CEUS conditions".

1.3 General Background

Earthquakes occur due to sudden slips on faults in lithospheric material. Released energy radiates from the fault in all directions, with a large percentage of the energy being in the form of seismic waves. At the ground surface, the seismic waves are a complex combination of primary waves (P-waves), secondary waves (S-waves), Rayleigh waves (R-waves), and Love waves that reflect the seismogenic source, travel path, and local site conditions. Triaxial seismographs record seismic waves in three orthogonal directions – one vertical and two horizontal. Figure 1-1 shows earthquake ground motions recorded during the Loma Prieta earthquake of 1989: ground acceleration versus time for three orthogonal directions. Each plot of acceleration vs. time is called an acceleration time history.

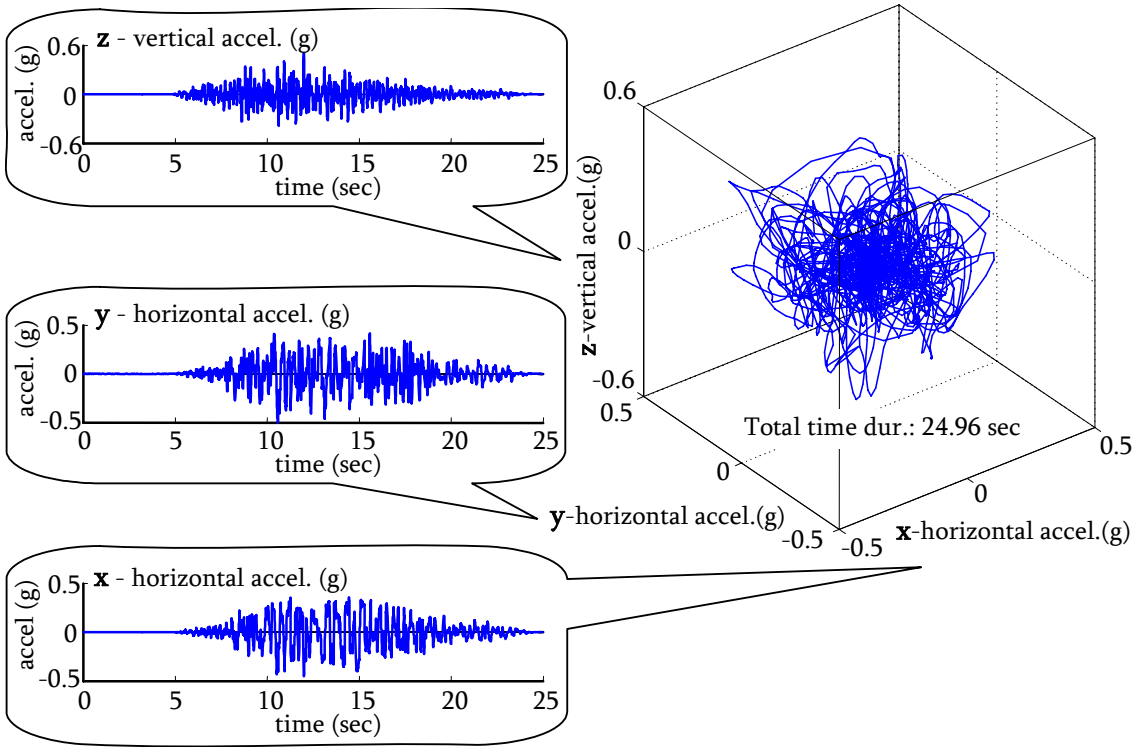

Figure 1-1. Example of earthquake ground motions from the 1989 Loma Prieta earthquake (BRN000, BRN090, and BRN-UP; magnitude = 6.9; the closest site-to-source distance = 10.3 km): acceleration time histories of three orthogonal components (acceleration in g′s: g is acceleration due to gravity); the corresponding ground acceleration in the 3-D plot.

For design purposes, the salient features of earthquake motions are quantified by "engineering characteristic parameters". For example, the duration of strong ground motion significantly influences the non-linear response of structures; hence, one important engineering parameter used in earthquake engineering is the strong ground motion duration.

A single parameter cannot account for the full complexity of earthquake motions. Multiple ground motion characteristics (e.g., amplitude, frequency, and duration) can influence the seismic response of an engineered structure. Furthermore, the complexity

of earthquake motions makes it difficult to quantify even a single ground motion characteristic by a single parameter. For example, several different ways have been proposed to quantify ground motion duration. Similarly, multiple parameters have been proposed to quantify each of the various ground motion characteristics.

Earthquake ground motion characteristics are mainly correlated to the following design earthquake parameters: earthquake magnitude, site-to-source distance (i.e., distance between an earthquake source to a particular site), local site conditions (e.g., rock vs. soil), fault mechanism (e.g. normal vs. strike slip), and tectonic environment (e.g., active shallow crustal vs. stable continental). However, due to the complexity of the earthquake faulting process, seismic wave propagation, site response, etc., it is impossible to derive rigorous theoretical equations to predict ground motion characteristics. Thus, ground motion characteristic predictive relationships (also commonly referred to as "attenuation relationships") are typically developed from statistical analysis of earthquake motions. Accordingly, empirical predictive relationships play an essential role in estimating the engineering characteristics of ground motions from future earthquakes.

Empirical predictive relationships should be periodically developed using up-to-date earthquake ground motion databases and robust regression techniques. During the past 10 years, empirical relationships for active shallow crustal regions have been regularly updated (e.g., Kempton and Stewart, 2006; Rathje et al., 2004; Travasarou et al., 2003).

The procedure used to develop the empirical predictive relationships in this study consisted of five stages, as shown in Figure 1-2. In Stage 1, the ground motion characteristic parameter is computed for each time history in the database. Stages 2-4 entail data modeling analyses. In Stage 2, pre-regression analysis, general trends in characteristic parameter data are identified as functions of the design earthquake parameters (e.g., earthquake magnitude) via visual inspection of the data, review of previous studies, and general knowledge of the earthquake processes. Also, the distribution of the scatter in the data (e.g., normal distribution or log normal distribution) is determined in this stage. Based on the observed trends, the functional form of the predictive relationship is developed, with the design earthquake parameters as independent variables. Often, several competing functional forms are developed. In Stage 3, the regression analysis of the data is performed. In Stage 4, the adequacy of the functional form of the predictive relationship is assessed by analyzing the trends in the resulting predicted ground motions characteristic parameters and the magnitude of the standard deviation of errors. Stages 2 through 4 need to be performed iteratively, with modifications being made to the functional form of the predictive relationship each iteration until trends in the predictive ground motions characteristic parameters are logical and the standard deviation of the error is minimized. Lastly, in Stage 5, the final predictive relationship is summarized and trends in the predicted ground motion characteristic parameters are identified and discussed. Additionally, it is desirable to compare the final predictive relationship to other previously developed relationships, if they exist. In this study, the "statistical computing and analysis program" R (version 2.5.0) was used to perform the non-linear mixed-effects (NLME) regression analyses.

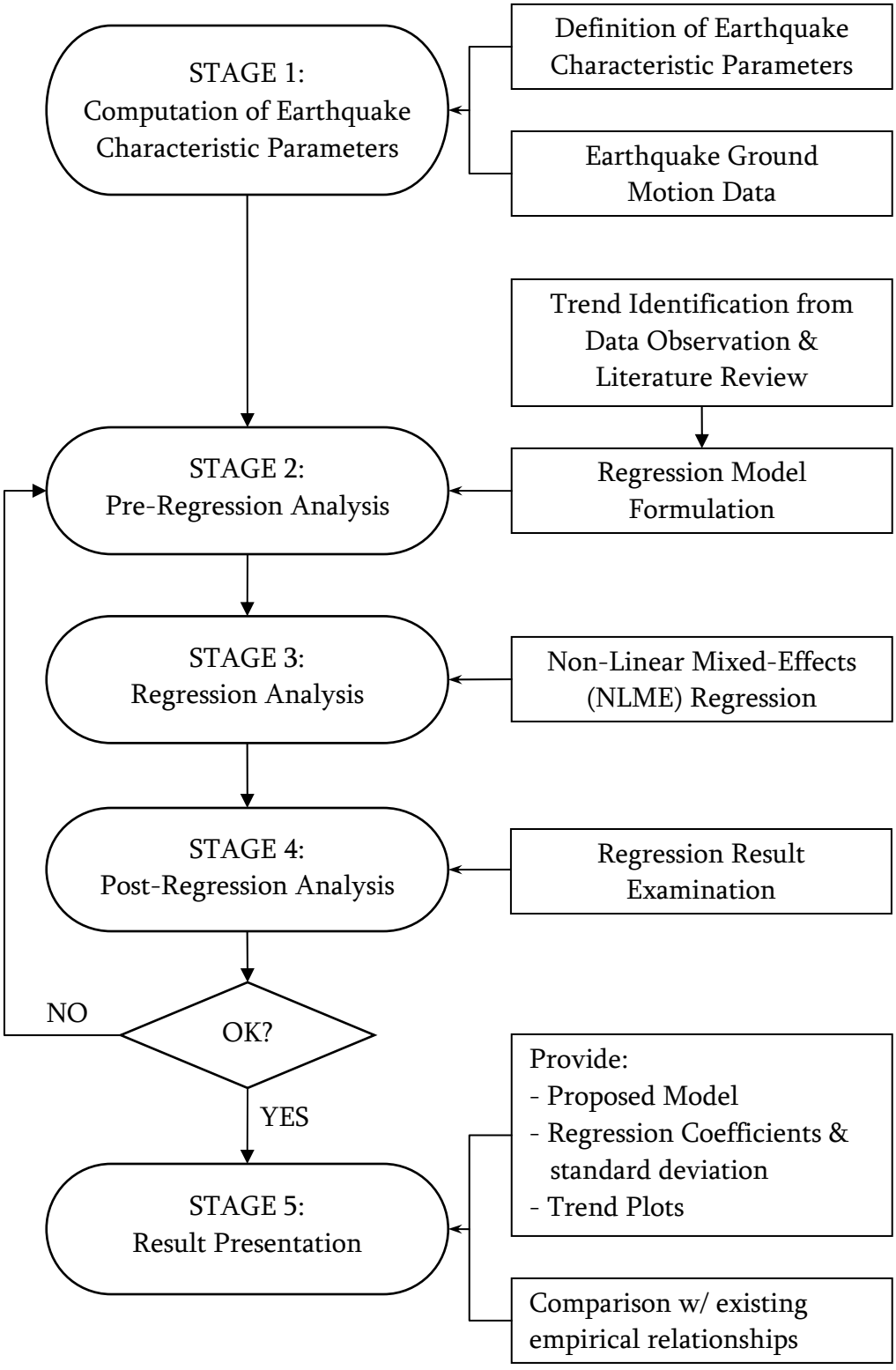

Figure 1-2. Procedure for developing an empirical relationship.

1.4 Organization of the Thesis

The remaining portion of this thesis consists of four parts: strong ground motion data set (Chapter 2), data modeling analyses: non-linear mixed-effects regression (Chapter 3), engineering characteristic parameters (Chapters 4-8), and conclusions (Chapter 9). The third part (i.e., engineering characteristic parameters) is comprised of multiple chapters that are organized based on the ground motion characteristic being quantified as summarized in Table 1-2. Since predictive relationships were developed for numerous engineering characteristic parameters in this study, background information and the resulting predictive relationships for each engineering parameter are presented together.

Table 1-2. Categories of engineering characteristic parameters.

Chapter	Category	Parameter
4	Frequency contents	Predominant spectral period
		Smoothed spectral predominant period
		Average spectral period
		Mean period
		Spectral velocity-acceleration ratio periods
5	Strong ground motion durations	Significant durations
		Bracketed duration
		Effective duration
6	Intensity measures	Arias intensity
7	Equivalent number of uniform cycles	stress cycles
		strain cycles
8	Pore pressure generation calibration	Pseudo energy capacity
		α

In Chapter 2, the strong ground motion data set used in this research is reviewed. This chapter consists of four sections: introduction; selection of ground motion time histories; statistics of strong ground motion data set; and ground motion scaling. The ground motion time history selection process used by McGuire et al. (2001) is summarized in the second section of this chapter, including all the criteria used for screening the data and organizing the data set. The next section provides the statistics of the strong ground motion data set (e.g., magnitude and site-to-source distance distributions; the number of ground motion data per data bin) both for active seismic regions and stable continental regions. Since the CEUS motion data are scaled motions, the scaling procedure used is summarized in the last section, along with a review of the stochastic point source model used in the scaling procedure. Additionally, the validity of the ground motion scaling procedure is discussed. Lastly, Appendix 2 provides the list of earthquakes and the number of recordings from each event that are in the data set.

Chapter 3 covers data modeling analyses, including: formulating regression models in the pre-regression analysis; using the non-linear mixed-effects (NLME) regression technique; and examining the resulting predictive relations as a post-regression analysis. This thesis only provides a brief overview of the theories behind the NLME modeling. A more detailed treatise is beyond the scope of this thesis; the reader is referred to Pinheiro and Bates (2000) for more detailed information of NLME modeling. Instead, this chapter aims to summarize the knowledge required to perform a regression analysis using the NLME technique and to interpret the results. Also, a detailed procedure of data modeling analyses for developing an empirical predictive relationship by the NLME method is

summarized. Lastly, an R-program (version 2.5.0) manual for performing NLME regressions and useful R-functions are provided in Appendix 3 – the author wrote the manual based on the experience gained while performing this research.

Background information on the engineering characteristic parameters and the corresponding empirical predictive relationships are presented in Chapters 4-8, organized as listed in Table 1-2. In each chapter, the first section is a review of general information about the characteristic parameters, with emphasis on their engineering use and significance. In subsequent sections, the various parameters used to quantify a ground motion characteristic are reviewed. Next, the functional form of the predictive relationship proposed in the study is introduced and justified based on knowledge of the earthquake processes, results from data observations, and/or literature reviews. Then, regression results are presented with regression coefficients and statistical parameters, and an assessment of the NLME regression results is described. Also, discussed are the trends in the predictive characteristic parameters as functions of independent variables (e.g., earthquake magnitude, distance). In the next section, the empirical predictive relationships developed in this study are compared to other previously developed relationships, if any exist. Lastly, the findings are summarized and discussed in the conclusions.

It is noted that the correlations for the calibration parameters for the pore pressure generation models in Chapter 8 were not developed using the strong ground motion data set used to develop the ground motion characteristic parameter predictive relationships.

Rather, the pore pressure model calibration parameters were developed from data from approximately 150 cyclic triaxial tests performed on soils ranging from clean sands to pure silt. However, the link between Chapter 8 and the rest of the thesis is that NLME were used for both.

Finally, the goal of this study is restated and major findings are summarized in Chapter 9. Also, a discussion is presented on the uncertainties in the empirical predictive relationships developed herein, and the inherent difficulties in reducing the uncertainties in ground motion characteristic parameter predictive relationships for stable continental regions. Lastly, recommended future studies are described.

Throughout the dissertation, the acronyms "CEUS" and "WUS" are used to refer to "stable continental" and "active shallow crustal" regions, respectively, not just to the central-eastern US and western US.

References

Boore, D. M. (1983). "Stochastic simulation of high-frequency ground motions based on seismological models of the radiated spectra". *Bulletin of the Seismological Society of America*, 73(6A), 1865-1894.

Brune, J. N. (1970). "Tectonic stress and spectra of seismic shear waves from earthquakes". *Journal of Geophysical Research*, 75(26), 611-614.

Brune, J. N. (1971). "Correction". *Journal of Geophysical Research*, 76(20), 1441-1450.

Kempton, J. J., and Stewart, J. P. (2006). "Prediction equations for significant duration of earthquake ground motions considering site and near-source effects". *Earthquake Spectra*, 22(4), 985-1013.

McGuire, R. K., Silva, W. J., and Costantino, C. J. (2001). "Technical basis for revision of regulatory guidance on design ground motions: Hazard-and risk-consistent ground motion spectra guidelines.", US Nuclear Regulatory Commission, Washington, DC.

Pinheiro, J. C., and Bates, D. M. (2000). *Mixed-effects models in S and S-PLUS*, Springer, New York.

Program-R. (version 2.5.0). "A language and environment for statistical computing and graphics: http://www.r-project.org/."

Rathje, E. M., Faraj, F., Russell, S., and Bray, J. D. (2004). "Empirical relationships for frequency content parameters of earthquake ground motions". *Earthquake Spectra*, 20(1), 119-144.

Silva, W. J., and Lee, K. (1987). "WES RASCAL Code for Synthesizing Earthquake Ground Motions: State-of-the-art for assessing earthquake hazards in the United States." *Report 24*, US Army Engineering Waterways Experiment Station Vicksburg, MS.

Travasarou, T., Bray, J. D., and Abrahamson, N. A. (2003). "Empirical attenuation relationship for Arias Intensity". *Earthquake Engineering & Structural Dynamics*, 32(7), 1133-1155.

Chapter 2

Strong Ground Motion Data Set

2.1 Introduction

In this chapter, the strong ground motion data set used in this study is described. McGuire et al. (2001) assembled the data set of strong ground motion recordings suitable for use in engineering analyses. The data set consisted of 324 three-component (i.e., one vertical and two horizontal) sets of strong ground motion time histories from active shallow crustal regions (e.g., western US: WUS) and 310 sets of stable continental regions (e.g., central/eastern US: CEUS). Thus, 648 and 620 horizontal time histories are available for WUS and CEUS, respectively. The strong motion data for active shallow crustal regions were from 49 earthquakes, with the 1999 Chi-Chi earthquake being the most recent event. Since few recorded strong ground motions are available for stable continental regions, most of the ground motion data for the CEUS were scaled from active shallow crustal region records. The stochastic, single-corner point source model was used in the scaling process to account for the differences in the seismic sources, crustal properties, and geological site effects between the two different tectonic regions. Although state-of-the-art, the scaling procedure used by McGuire et al. (2001) cannot be truly validated until additional CEUS motions are recorded, especially for large earthquake motions (i.e., magnitude greater than 6).

This chapter is organized into three parts: selection of ground motion data, statistics of strong ground motion data set, and scaling ground motions. The first part reviews the criteria and organization scheme used for assembling the strong ground motion data by McGuire et al. (2001). The second part summarizes the data statistics including the magnitude and distance distributions. The third part reviews the scaling procedure and the stochastic, single-corner point source model. Lastly, the validity of the scaling method is discussed. Appendix 2 provides a list of earthquake events included in the strong ground motion data set.

2.2 Selection of Ground Motion Data

The strong ground motion data set was assembled by McGuire et al. (2001) from the strong motion database processed by Dr. Walter Silva of Pacific Engineering & Analysis. Primarily, the data set was intended to provide a library of strong ground motion time histories suitable for engineering analyses. Hence, the data selection criteria (e.g., earthquake magnitude range) were established based on engineering interest. The criteria were categorized by: site condition, earthquake magnitude, site-to-source distance, and duration. The strong ground motion data both for stable continental regions (i.e., CEUS) and active shallow crustal regions (i.e., WUS) were organized into bins assigned to specific site conditions, and magnitude and site-to-source distance ranges, in a hierarchical order. Figure 2-1 illustrates the organization of the data bins. Also, McGuire et al. (2001) wanted at least 15 sets of motions in each distance bin to ensure that the range in motion characteristics are reasonably represented.

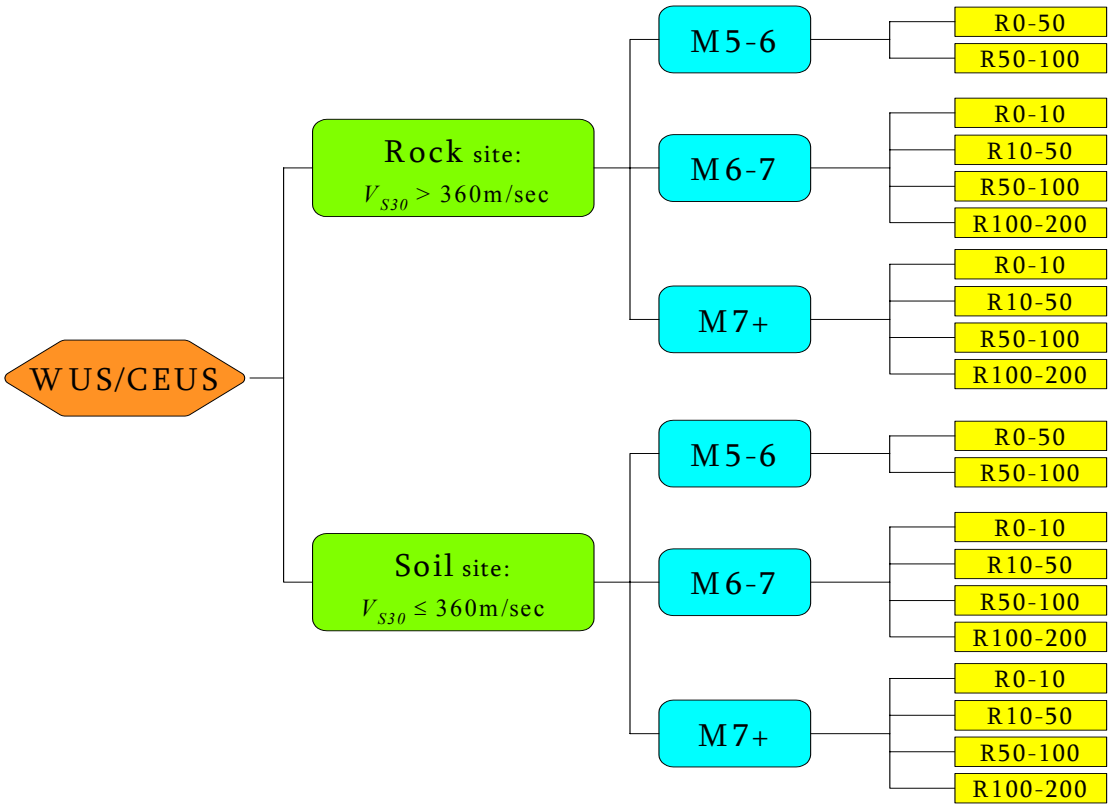

Figure 2-1. Hierarchical chart of the data bins of strong ground motion data set (M is earthquake magnitude; R is the site-to-source distance in km).

2.2.1 Ground Motion Data for WUS

Site conditions (i.e., site at which ground motions were recorded) considered in the data set consist of soft rock and firm soil sites. The site classification scheme used by McGuire et al. is based on the third letter of the Geomatrix 3-letter site classification system (Table 2-1). Site categories A and B, and C and D were considered to represent soft rock sites, and firm soil sites, respectively. The ground motion recordings were distributed into rock/soil bins based on this site classification. This categorization is similar to that of the USGS (Table 2-2), where soft rock sites encompass site class A and B, and firm soil sites encompass site classes C and D.

Table 2-1. Third letter: Geotechnical subsurface characteristics of Geomatrix 3-letter site classification.

Third letter	Site description	Comments
A	Rock	Instrument on rock (V_S > 600 mps) or < 5 m of soil over rock.
B	Shallow (stiff) soil	Instrument on/in soil profile up to 20 m thick overlying rock.
C	Deep narrow soil	Instrument on/in soil profile at least 20 m thick overlying rock, in a narrow canyon or valley no more than several km wide.
D	Deep broad soil	Instrument on/in soil profile at least 20 m thick overlying rock, in a broad valley.
E	Soft deep soil	Instrument on/in deep soil profile with average V_S < 150 mps.

Table 2-2. USGS site classification.

Site Class	Average shear wave velocity to a depth of 30 m: V_{S30}
A	$V_{S30} \geq 750$ m/s
B	$V_{S30} = 360 – 750$ m/s
C	$V_{S30} = 180 – 360$ m/s
D	$V_{S30} \leq 180$ m/s

The ground motion data was then sorted into three bins according to moment magnitude (M): 5 to 6; 6 to 7; and 7+. Further sorting into four bins was made based on site-to-source distance (R): 0 to 10 km; 10 to 50 km; 50 to 100 km; and 100 to 200 km. For the magnitude bin of M5-6, the R0-10km and R10-50km distance bins were combined together because there was insufficient data to populate the R0-10km bin, and near-fault effects (e.g., forward directivity and fling step) was not considered significant for this magnitude range. Also, it is noted that the site-to-source distance is defined as the closest

distance to the fault rupture plane (km), but for some motions, hypocentral distance was used instead, due to unavailability of the former.

McGuire et al. (2001) also used strong ground motion duration as a criterion for selecting records. The criterion was based on the 5-75% significant duration ($D_{5\text{-}75}$), which is defined as the time duration corresponding to the 5% to 75% of the normalized cumulative energy to its total energy (Dobry et al., 1978, Husid, 1969). Specifically, McGuire et al. selected motions where the average $D_{5\text{-}75}$ of the two horizontal components fell within the range of $1/1.5 \times D_{5\text{-}75\ AS}$ to $1.5 \times D_{5\text{-}75\ AS}$, where $D_{5\text{-}75\ AS}$ is the median $D_{5\text{-}75}$ predicted using the relationship developed by Abrahamson and Silva (1996). To compute $D_{5\text{-}75\ AS}$, McGuire et al. (2001) used the central M and R (on log scale) for each bin. For example, the duration criteria for rock motions for M6-7 bin are illustrated in Figure 2-2.

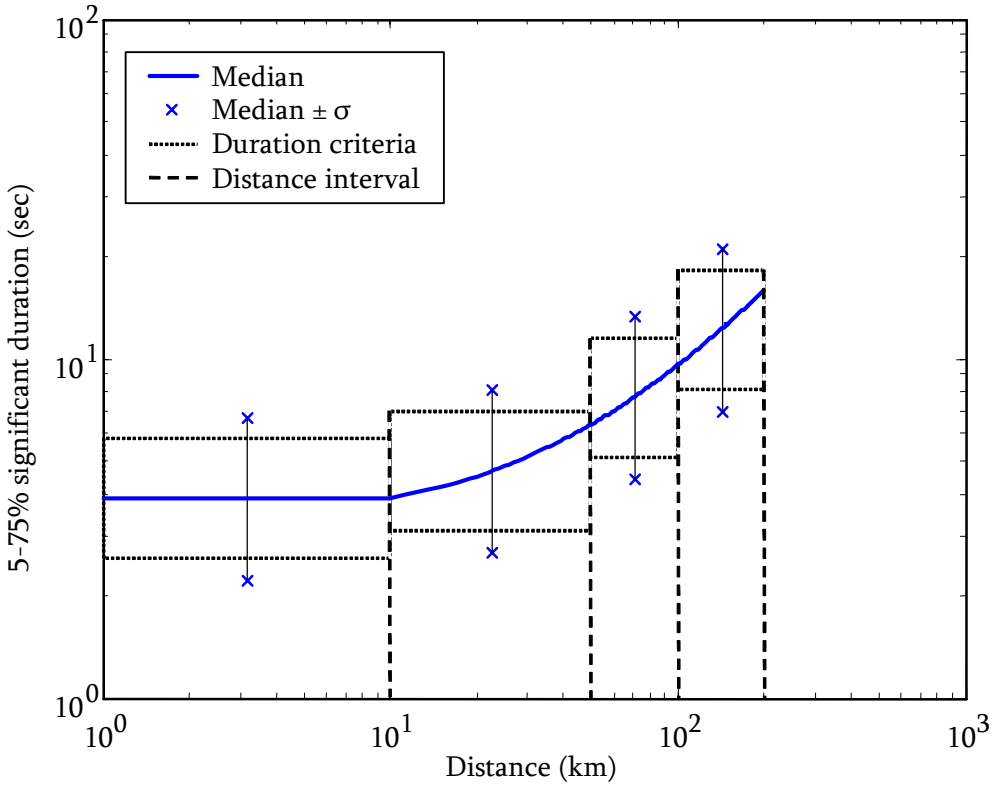

Figure 2-2. Example of duration criteria determination for rock sites: M6-7 bin (adapted from McGuire et al., 2001).

Additionally, for the R0-10km bin M7+, recorded motions are predominately from 1999 Chi-Chi earthquake. However, there is uncertainty in the site classification of many of these recordings. As a result, some of the Chi-Chi motions were replaced with several M 6.8-6.9 rock motions from the 1989 Loma Prieta (M 6.9), the 1976 Gazli (M 6.8), and the 1995 Kobe (M 6.9) earthquakes. For the soil site bins, ground motions from the soil site Takarazuka recorded during the 1995 Kobe (M 6.9) earthquake had pronounced directivity effects; the site was located at the end of the rupture (i.e., the maximum directivity). The motions from this site were added to the close distance bin (i.e., R0-10km) in both the intermediate and large magnitude bins (i.e., M6-7 and M7+).

2.2.2 Ground Motion Data for CEUS

Because of the paucity of the strong ground motion data for stable continental regions, the CEUS bin (i.e., stable continental region data bin) was supplemented to a large extent with scaled motions, using the WUS records as "seed" motions. The scaling was performed by Dr. Walter Silva and involves computing response spectral transfer functions, and matching the response spectra. The response spectral transfer functions were generated using the stochastic point source model, which allows the transfer functions to account for the differences in seismic source, wave propagation path properties, and site effects between the two regions. Details of the scaling method are described in section 2.4.

2.3 Statistics of Strong Ground Motion Data Set

The strong ground motion data set for the WUS has a total of 324 three-component sets of time histories from 49 earthquakes (648 horizontal and 324 vertical ground motions). The moment magnitudes of these events range from 5.0 to 7.6, and the site-to-source distances range from 0.1 km to 199.1 km. For the CEUS, the data set includes a total of 310 three-component sets of ground motions, consisting of 14 sets of recorded motions and 296 sets of scaled motions (620 horizontal and 310 vertical ground motions). The moment magnitudes for these motions range from 4.5 to 7.6, and the site-to-source distances range from 0.1 km to 199.1 km. The recorded motions include the 1988 Saguenay (M 4.5 and M 5.9), the 1985 Nahanni (M 6.8), and the 1989 New Madrid, MO (M 4.7) earthquakes. Figure 2-3 shows the magnitude and site-to-source distance distributions for both regions. The detailed statistics for each bin are also listed in Table

2-3 and Table 2-4 for WUS and CEUS, respectively. In addition, Appendix 2 provides the lists of all the earthquakes included in the data set; year of their occurrence, their magnitude, and the number of motion sets in each bin.

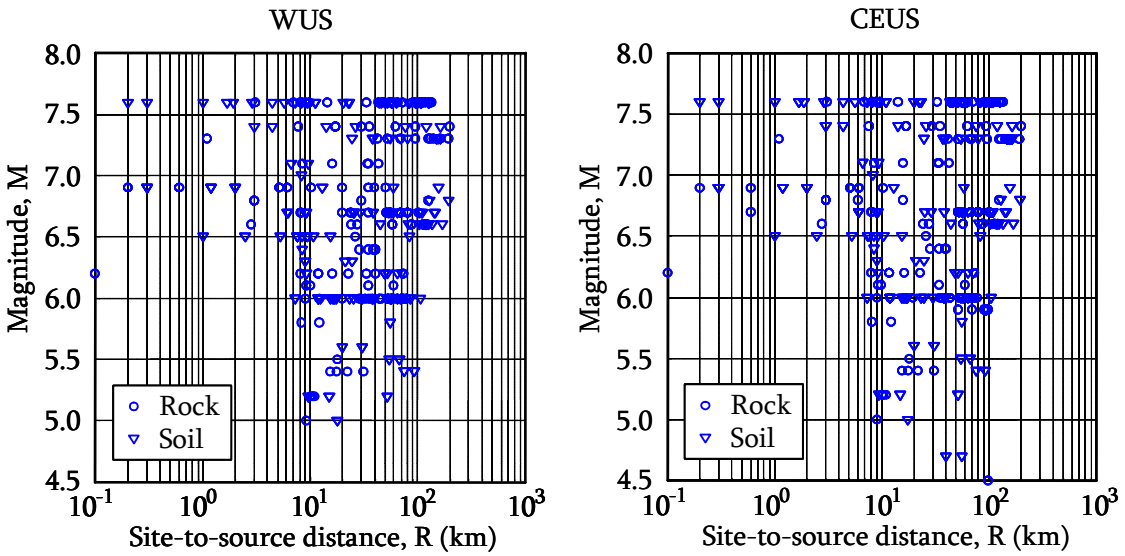

Figure 2-3. Earthquake magnitude and site-to-source distance distributions of the strong ground motion data set.

Table 2-3. Statistics of the strong ground motion data set: WUS bin.

Mag. Bin	Dist. Bin	Magnitude				Distance (km)				No. of sets
		min.	max.	median	avg.	min.	max.	median	avg.	
WUS: Rock										
M5-6	R0-50	5.0	6.0	5.40	5.50	8.2	36.6	12.20	17.29	15
	R50-100	6.0	6.0	6.00	6.00	52.4	78.3	65.30	64.88	15
M6-7	R0-10	6.0	6.9	6.70	6.53	0.1	11.8	8.00	6.00	15
	R10-50	6.0	6.9	6.40	6.39	11.8	49.9	31.35	31.29	30
	R50-100	6.0	6.7	6.60	6.38	51.6	86.6	65.30	66.12	15
	R100-200	6.6	6.8	6.70	6.66	51.6	124.7	86.60	89.03	15
M7+	R0-10	6.8	7.6	7.30	7.25	0.2	10.3	6.90	5.83	15
	R10-50	7.1	7.6	7.40	7.38	14.3	48.7	33.80	31.48	15
	R50-100	7.3	7.6	7.60	7.49	51.7	96.8	71.60	76.88	15
	R100-200	7.3	7.6	7.60	7.49	102.8	199.1	128.40	135.03	15
										Σ165
WUS: Soil										
M5-6	R0-50	5.0	6.0	6.00	5.77	7.3	30.8	16.30	16.97	15
	R50-100	5.2	6.0	6.00	5.75	38.2	93.5	64.80	64.38	15
M6-7	R0-10	6.2	6.9	6.50	6.58	0.3	9.3	6.85	5.74	18
	R10-50	6.0	6.9	6.50	6.41	10.6	49.0	25.70	27.83	15
	R50-100	6.2	6.9	6.70	6.57	52.0	83.0	64.40	67.10	15
	R100-200	6.0	6.9	6.70	6.64	103.1	195.0	125.60	131.53	15
M7+	R0-10	6.9	7.6	7.60	7.40	0.2	9.7	4.40	4.62	21
	R10-50	7.3	7.6	7.60	7.47	11.1	46.3	26.10	29.60	15
	R50-100	7.3	7.6	7.60	7.53	50.0	95.2	63.20	68.79	15
	R100-200	7.3	7.6	7.40	7.44	100.2	164.5	127.70	134.73	15
										Σ159

Table 2-4.Statistics of the strong ground motion data set: CEUS bin.

Mag. Bin	Dist. Bin	Magnitude				Distance (km)				No. of sets †
		min.	max.	median	avg.	min.	max.	median	avg.	
CEUS: Rock										
M5-6	R0-50	5.0	6.0	5.40	5.50	8.2	36.6	12.20	17.29	0 (15)
	R50-100	4.5	6.0	5.90	5.85	51.9	99.4	73.20	78.34	8 (7)
M6-7	R0-10	6.0	6.9	6.70	6.53	0.1	11.8	7.05	6.18	2 (14)
	R10-50	6.0	6.8	6.40	6.32	11.8	43.8	27.50	28.58	1 (14)
	R50-100	6.0	6.7	6.60	6.38	51.6	86.6	65.30	66.12	0 (15)
	R100-200	6.6	6.8	6.70	6.66	51.6	124.7	86.60	89.03	0 (15)
M7+	R0-10	6.8	7.6	7.30	7.25	0.2	10.3	6.90	5.83	0 (15)
	R10-50	7.1	7.6	7.40	7.38	14.3	48.7	33.80	31.48	0 (15)
	R50-100	7.3	7.6	7.60	7.49	51.7	96.8	71.60	76.88	0 (15)
	R100-200	7.3	7.6	7.60	7.49	102.8	199.1	128.40	135.03	0 (15)
										Σ151
CEUS: Soil										
M5-6	R0-50	4.7	6.0	6.00	5.69	7.3	39.9	16.90	18.81	1 (14)
	R50-100	4.7	6.0	5.80	5.66	38.2	95.6	64.80	64.99	2 (13)
M6-7	R0-10	6.2	6.9	6.50	6.58	0.3	9.3	6.85	5.74	0 (18)
	R10-50	6.0	6.9	6.50	6.41	10.6	49.0	25.70	27.83	0 (15)
	R50-100	6.2	6.9	6.70	6.57	52.0	83.0	64.40	67.10	0 (15)
	R100-200	6.0	6.9	6.70	6.64	103.1	195.0	125.60	131.53	0 (15)
M7+	R0-10	6.9	7.6	7.60	7.40	0.2	9.7	4.40	4.62	0 (21)
	R10-50	7.3	7.6	7.60	7.47	11.1	46.3	26.10	29.60	0 (15)
	R50-100	7.3	7.6	7.60	7.53	50.0	95.2	63.20	68.79	0 (15)
	R100-200	7.3	7.6	7.40	7.44	100.2	164.5	127.70	134.73	0 (15)
										Σ159

† The numbers of recorded motion sets is the number outside the parentheses and the number of scaled-motion sets is inside the parentheses.

2.4 Scaling Ground Motions

The empirical ground motion characteristic parameter predictive relationships for stable continental regions developed herein are largely based on the regression of scaled WUS motion data. Therefore, the validity of the predictive relationships is inherently tied to the validity of the procedure used to scale the motions. In this context, this section reviews the scaling procedure used to modify WUS "seed" motions to look like CEUS motions and discusses the procedure's validity.

2.4.1 Scaling Procedure

The scaling procedure used by McGuire et al. (2001) consists of the following computation processes: (1) determination of response spectral transfer function, (2) computation of response spectrum for the given ground motion, (3) determination of target response spectrum, and (4) spectral matching of the time history. A response spectral transfer function is obtained by first using the stochastic single-corner frequency point source model to compute smoothed Fourier amplitude spectra (FAS) for both the CEUS and WUS (e.g., Brune, 1970; Brune, 1971; Boore, 1983; Hanks and McGuire, 1981; McGuire et al., 2001; Silva and Lee, 1987); this model is described in the following section. Next, random vibration theory is used to generate response spectra from the FAS. The ratio of these two response spectra is the spectral transfer function. The response spectral transfer functions were generated for each site condition; horizontal/vertical component; earthquake magnitudes of 5.5, 6.5, and 7.5 (i.e., center value of magnitude bins); and distances of 1, 5, 30, 75, and 130 km. A total 60 different transfer functions were used. Example transfer functions for M6.5 cases are shown in Figure 2-4. The response spectrum (5% damping) of a WUS "seed" acceleration time

history is then computed. Next, the CEUS target response spectrum is obtained by multiplying the "seed" motion's response spectrum by the appropriate response spectral transfer function (i.e., the transfer function for the distance closest to the actual site-to-source distance of the "seed" time history was used). Lastly, the "seed" acceleration time history is scaled to match the target CEUS response spectrum (Silva and Lee, 1987). In the spectral matching process, a sample time interval Δt of 0.005 sec (the corresponding Nyquist frequency is 100 Hz) was used to avoid aliasing effects in the frequency range of interest.

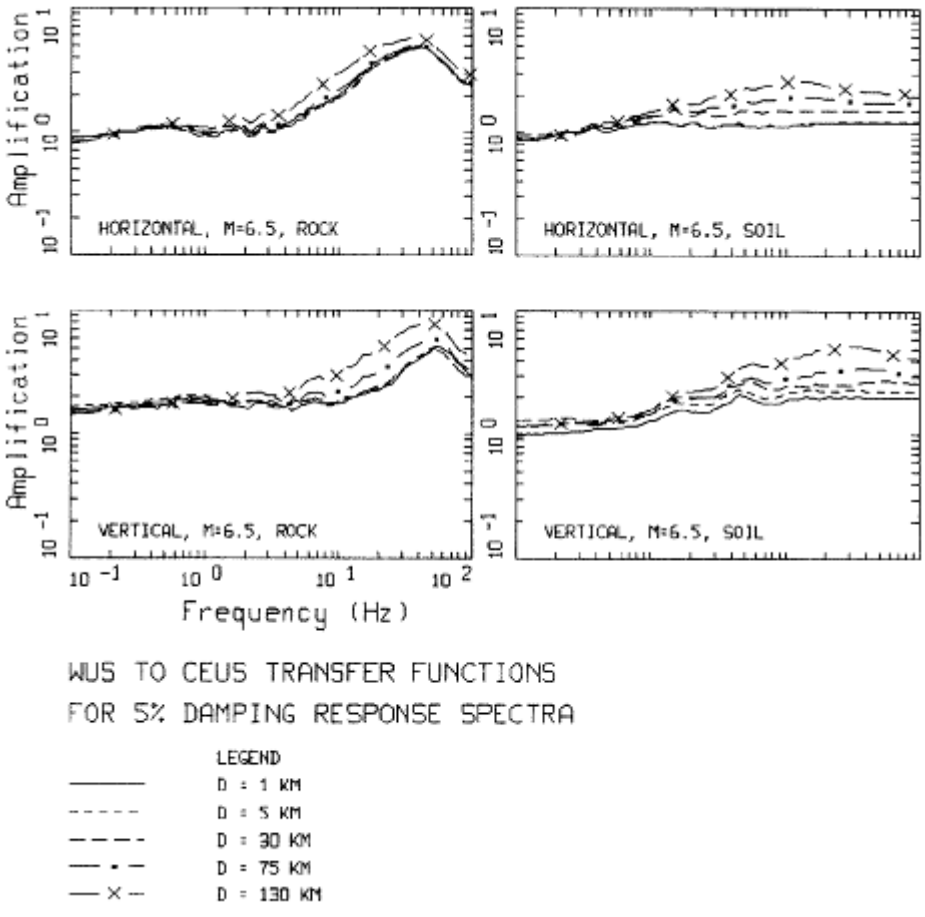

Figure 2-4. Response spectral transfer functions for M6.5, rock and soil sites, horizontal and vertical components, and each distance cases – from McGuire et al. (2001).

2.4.2 Stochastic Point Source Model

The stochastic ground motion model used in McGuire et al. (2001) is based on the Brune's point source model (Brune, 1970; 1971), which has a single-corner frequency. The single-corner frequency point source model predicts the Fourier amplitude spectrum for accelerations at the hypocentral distance *R* (e.g., Atkinson and Boore, 1995; McGuire et al., 2001; Silva and Lee, 1987) which is given by:

$$FA(f) = C \cdot \frac{(2 \cdot \pi \cdot f)^2 M_0}{1 + \left(\frac{f}{f_c}\right)^2} \cdot \frac{P(f)}{R} \cdot D(R, f) \cdot A(f) \qquad \text{(Eq. 2-1)}$$

where:

$FA(f)$ = Fourier amplitude (cm/s) as a function of frequency f (Hz);

$$C = \frac{R_p \cdot F \cdot V}{4 \cdot \pi \cdot \rho_0 \cdot \beta_0{}^3}; \qquad \text{(Eq. 2-2)}$$

where: R_p = source radiation pattern averaged over a sphere (= 0.55) (Boore, 1986);

F = free surface amplification (= 2);

V = energy partition into two horizontal components ($=1/\sqrt{2}$);

ρ_0 = crustal density in the source region (gm/cm^3);

β_0 = shear wave velocity of the crust at the source (km/sec);

$$P(f) = e^{-\pi \cdot \kappa \cdot f}; \qquad \text{(Eq. 2-3)}$$

$P(f)$ is a high-frequency cut-off filter for representing rapid-decay of amplitude at high frequency (Anderson and Hough, 1984);

where: κ = a parameter that represents damping in the shallow crust directly below the site (sec);

$$D(R,f) = e^{\frac{-\pi \cdot f \cdot R}{\beta_0 \cdot Q(f)}}; \qquad \text{(Eq. 2-4)}$$

$D(R, f)$ represents the crustal path attenuation from the source to the site;

where: $Q(f) = Q_0 \cdot f^n$; (Eq. 2-5)

$Q(f)$ is the frequency dependent quality factor, where Q_0 and n are regional dependent parameters (Herrmann, 1980);

R = hypocentral distance (km);

$$f_c = 4.9 \times 10^6 \cdot \beta_0 \cdot (\Delta\sigma / M_0)^{1/3}; \qquad \text{(Eq. 2-6)}$$

f_c, corner frequency (Hz) is the frequency that separates the relatively-flat portion of the Fourier amplitude spectrum at intermediate frequencies from the decaying portion at low frequencies.

where: $\Delta\sigma$ represents the stress drop at the source (bars);

M_0 = seismic moment (dyne-cm), which can be related to moment magnitude M by the equation:

$\log M_0 = 1.5M + 16.05$ (Hanks and Kanamori, 1979); (Eq. 2-7)

$A(f)$ = crustal amplification factor (Boore, 1986);

The point source parameters used by McGuire et al. (2001) are shown in Table 2-5. Also, the compression (P) and shear (S) wave velocity profiles for WUS (soft rock) and CEUS (hard rock) crustal conditions are shown in Figure 2-5. The crustal amplification factors $A(f)$ based on the shear wave velocity profiles is shown in Figure 2-6.

Table 2-5. Point source parameters for WUS and CEUS motions.

	WUS	CEUS
$\Delta\sigma$ (bars)	65	120
κ (sec)	0.040	0.006
Q_0	220	351
n	0.60	0.84
β_0 (km/sec)	3.50	3.52
ρ_0 (gm/cm^3)	2.70	2.60

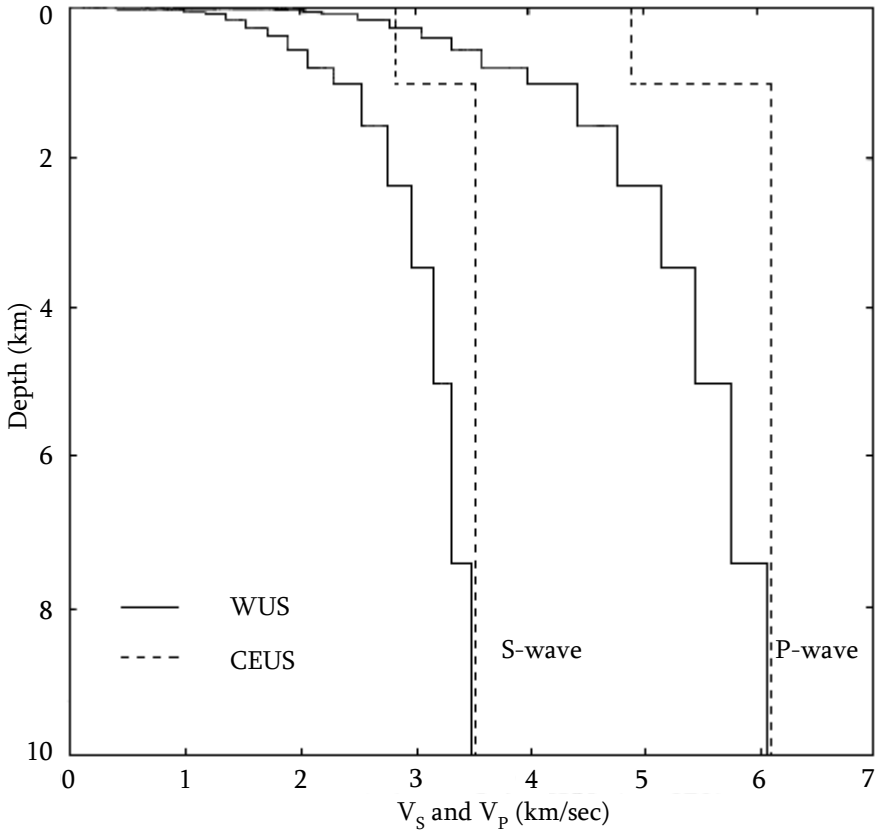

Figure 2-5. P- and S-wave velocity model profiles for WUS and CEUS – adapted from McGuire et al. (2001).

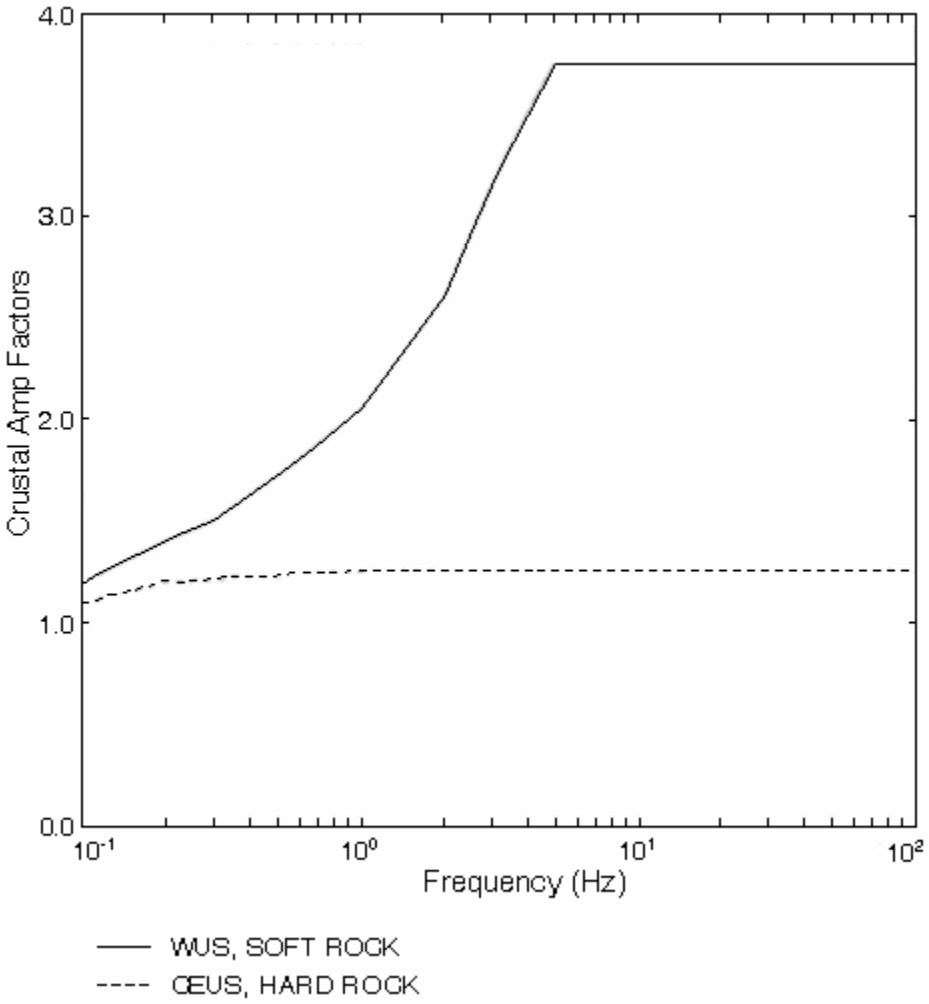

Figure 2-6. Crustal amplification factors $A(f)$ corresponding to the shear wave velocity profiles shown in Figure 2-5 – adapted from McGuire et al.(2001).

Using Parseval's theorem (Eq. 2-8), the root-mean-square (rms) acceleration (definition given in Eq. 2-9) can be computed from the smoothed Fourier amplitude spectrum computed using the point source model. Then, based on random vibration theory (RVT), the rms acceleration a_{rms} is related to the response of an oscillator having a damping ratio ξ and natural frequency f_n (Hanks and McGuire, 1981; Boore, 1983; Silva and Lee, 1987), which is to compute the response spectra corresponding to the smoothed FAS and then the response spectral transfer functions.

$$\int_{-\infty}^{\infty} a^2(t)\,dt = \int_{-\infty}^{\infty} FA^2(f)\,df \qquad \text{(Eq. 2-8)}$$

where: $a(t)$ is the acceleration time history; $FA(f)$ is the Fourier amplitude in terms of frequency f.

$$a_{rms} = \left(\frac{1}{t_d} \int_0^{\infty} a^2(t)\,dt \right)^{1/2} \qquad \text{(Eq. 2-9)}$$

where: t_d is the total duration of the acceleration time history in seconds.

2.5 Validity of the Scaling Method

The response spectral transfer functions play the primary role in the scaling process, adjusting the response spectra for the WUS motions for CEUS conditions. The transfer functions are computed based on a stochastic Brune point source model having a single-corner frequency. The model accounts for the salient features of the seismic source, the wave propagation path, and local site effects in ground motions using relatively simple parametric terms. Also, applying RVT to the Brune source model allows the model to provide statistically stable predictions of peak ground motions or response spectra without having to spend effort to generate a large number of synthetic time histories. Furthermore, based on its good agreement with numerous recorded strong ground motions (mostly WUS motions) many seismological publications have shown successful results of the RVT point source modeling for predicting strong ground motion characteristics, such as peak ground motions and response spectra both for WUS and

CEUS (Boore, 1983; 1986; Hanks and McGuire, 1981; McGuire et al., 1984; Schneider et al., 1993; Silva, 1993). In this context, the simple stochastic point source model seems to be a reliable and reasonable approach for predicting spectral characteristics of strong ground motions for engineering analyses. In addition to that, the WUS recorded motions were used as "seed" or input motions in the spectral scaling process, which results in the scaled motions having realistic characteristics.

It should be, however, recognized that the predictions based on the point source model are approximations with intrinsic uncertainties. All the point source model parameters were empirically calibrated based on the observations of ground motion characteristics from available ground motion data. As a result, the model parameters include the inherent randomness (i.e., aleatory uncertainty) of nature. Moreover, there are physical behaviors and processes of earthquakes that have not been identified, explained, or applied to the model, which results in more uncertainties (i.e., epistemic uncertainty) in ground motion predictions.

Because of the complex nature of earthquakes, resolving most of the uncertainties in the predictions relies heavily on the analysis of existing earthquake motion recordings. For example, from a statistical perspective, the confidence level of the estimated medians for the model parameters may be enhanced through observations of numerous earthquake ground motions. Also, the unknown seismological effects may be reasonably explained and parameterized from a larger ground motion database. In this regard, the stochastic point source model for estimating CEUS motions may tend to be less reliable, having

more uncertainties relative to that for WUS motions due to a lack of strong ground motion recordings and sparsity in seismic activity in CEUS.

For instance, the Fourier amplitude spectra estimated by using the current point source model for CEUS motions were significantly different from those based on actual data from the 1988 Saguenay (M5.8) earthquake (Atkinson, 1993; Boore and Atkinson, 1992). Consequently, Atkinson (1993) proposed an empirical "double" corner source model for CEUS motions, but the basis for this model is limited. Likewise, there is certainly a need to verify the stochastic point source model with a much larger ground motion database that includes strong ground motions from a large earthquake of magnitude greater than 6 to develop more reliable spectral characteristic estimations for CEUS motions.

Appendix 2: List of Earthquake Events

Tables A2-1 through A2-4 list the earthquake events included in the data set and their number of three-component (i.e., two horizontal and one vertical) sets of ground motion time histories by bin categories. The bins for active shallow crustal region and stable continental region are labeled as WUS and CEUS bins, respectively.

Table A2-1. Earthquake events and the number of three-component sets of ground motion recordings: WUS-Rock.

Mag. Bin	Dist. Bin	Year	Earthquake Event	M	No. of Sets
M5-6	R0-50	1970	Lytle Creek	5.4	2
		1976	Fruili, Italy	5.5	1
		1978	Santa Barbara	6.0	1
		1980	Livermore	5.4	2
		1980	Mammoth Lakes	5.0	1
		1983	Coalinga	5.2	4
		1983	Coalinga	5.8	2
		1986	N. Palm Springs	6.0	1
		1987	Whittier Narrows	6.0	1
	R50-100	1952	Southern California	6.0	1
		1986	N. Palm Springs	6.0	7
		1987	Whittier Narrows	6.0	7
M6-7	R0-10	1935	Helena, Montana	6.2	1
		1966	Parkfield	6.1	2
		1971	San Fernando	6.6	1
		1976	Gazli, USSR	6.8	1
		1984	Morgan Hill	6.2	2
		1987	Whittier Narrows	6.0	1
		1989	Loma Prieta	6.9	2
		1994	Northridge	6.7	3
		1995	Kobe	6.9	2
	R10-50	1971	San Fernando	6.6	2
		1979	Imperial Valley	6.5	1
		1980	Mammoth Lakes	6.0	2
		1980	Victoria, Mexico	6.1	1
		1983	Coalinga	6.4	4
		1984	Morgan Hill	6.2	3
		1986	N. Palm Springs	6.0	1
		1986	Chalfant Valley	6.2	2
		1987	Whittier Narrows	6.0	5
		1988	Spitak, Armenia	6.8	1
		1989	Loma Prieta	6.9	4
		1994	Northridge	6.7	4

	R50-100	1966	Parkfield	6.1	1
		1971	San Fernando	6.6	2
		1987	Whittier Narrows	6.0	5
		1991	Georgia, USSR	6.2	1
		1994	Northridge	6.7	6
	R100-200	1968	Borrego Mtn.	6.8	1
		1971	San Fernando	6.6	7
		1994	Northridge	6.7	7
M7+	R0-10	1976	Gazli, USSR	6.8	1
		1989	Loma Prieta	6.9	3
		1992	Cape Mendocino	7.1	1
		1992	Landers	7.3	1
		1995	Kobe	6.9	2
		1999	Kocaeli, Turkey	7.4	1
		1999	Chi-Chi, Taiwan	7.6	6
	R10-50	1978	Tabas, Iran	7.4	1
		1992	Cape Mendocino	7.1	1
		1992	Landers	7.3	1
		1999	Kocaeli, Turkey	7.4	4
		1999	Duzce, Turkey	7.1	3
		1999	Chi-Chi, Taiwan	7.6	5
	R50-100	1978	Tabas, Iran	7.4	1
		1992	Landers	7.3	4
		1999	Kocaeli, Turkey	7.4	1
		1999	Chi-Chi, Taiwan	7.6	9
	R100-200	1978	Tabas, Iran	7.4	1
		1992	Landers	7.3	5
		1999	Chi-Chi, Taiwan	7.6	9
					∑165

Table A2-2. Earthquake events and the number of three-component sets of ground motion recordings: WUS-Soil.

Mag. Bin	Dist. Bin	Year	Earthquake Event	M	No. of Sets
M5-6	R0-50	1967	Northern Calif	5.6	1
		1980	Mammoth Lakes	6.0	1
		1983	Mammoth Lakes	5.2	1
		1983	Coalinga	5.0	1
		1983	Coalinga	5.2	1
		1986	N. Palm Springs	6.0	2
		1986	Chalfant Valley	5.6	1
		1987	Whittier Narrows	6.0	7
	R50-100	1938	Northern Calif	5.5	1
		1951	Northern Calif	5.8	1
		1970	Lytle Creek	5.4	2
		1979	Imperial Valley	5.2	1
		1983	Trinidad offshore	5.5	2
		1986	N. Palm Springs	6.0	2
		1987	Whittier Narrows	6.0	6
M6-7	R0-10	1979	Imperial Valley	6.5	8
		1980	Mammoth Lakes	6.3	1
		1983	Coalinga	6.4	1
		1986	Chalfant Valley	6.2	1
		1992	Erzican, Turkey	6.9	1
		1994	Northridge	6.7	4
		1995	Kobe	6.9	2
	R10-50	1971	San Fernando	6.6	1
		1979	Imperial Valley	6.5	2
		1981	Taiwan SMART1 (5)	6.3	1
		1986	N. Palm Springs	6.0	1
		1987	Whittier Narrows	6.0	3
		1987	Superstition Hills (A)	6.3	1
		1989	Loma Prieta	6.9	1
		1991	Georgia, USSR	6.2	1
		1994	Northridge	6.7	4
	R50-100	1971	San Fernando	6.6	1
		1983	TaiwanSMART1(25)	6.5	3
		1984	Morgan Hill	6.2	2
		1989	Loma Prieta	6.9	1
		1991	Georgia, USSR	6.2	1
		1994	Northridge	6.7	7
	R100-200	1956	El Alamo	6.8	1
		1968	Borrego Mtn	6.8	1
		1971	San Fernando	6.6	6
		1987	Whittier Narrows	6.0	1
		1994	Northridge	6.7	5
		1995	Kobe	6.9	1
M7+	R0-10	1940	Imperial Valley	7.0	1
		1978	Tabas, Iran	7.4	1
		1992	Erzican, Turkey	6.9	1

		1992	Cape Mendocino	7.1	1
		1995	Kobe	6.9	2
		1999	Kocaeli, Turkey	7.4	1
		1999	Chi-Chi, Taiwan	7.6	13
		1999	Duzce, Turkey	7.1	1
	R10-50	1978	Tabas, Iran	7.4	1
		1986	TaiwanSMART1(45)	7.3	3
		1992	Landers	7.3	2
		1999	Kocaeli, Turkey	7.4	1
		1999	Chi-Chi, Taiwan	7.6	8
	R50-100	1992	Landers	7.3	3
		1999	Kocaeli, Turkey	7.4	1
		1999	Chi-Chi, Taiwan	7.6	11
	R100-200	1952	Kern County	7.4	1
		1978	Tabas, Iran	7.4	2
		1992	Landers	7.3	6
		1999	Chi-Chi, Taiwan	7.6	6
					∑159

Table A2-3. Earthquake events and the number of three-component sets of ground motion recordings: CEUS-Rock.

Mag. Bin	Dist. Bin	Year	Earthquake Event	M	No. of Sets
M5-6	R0-50	1970	Lytle Creek	5.4	2
		1976	Fruili, Italy	5.5	1
		1978	Santa Barbara	6.0	1
		1980	Livermore	5.4	2
		1980	Mammoth Lakes	5.0	1
		1983	Coalinga	5.2	4
		1983	Coalinga	5.8	2
		1986	N. Palm Springs	6.0	1
		1987	Whittier Narrows	6.0	1
	R50-100	1952	Southern California	6.0	1
		1986	N. Palm Springs	6.0	6
		1988	Saguenay, Canada	4.5	1 †
		1988	Saguenay, Canada	5.9	7 †
M6-7	R0-10	1935	Helena, Montana	6.2	1
		1966	Parkfield	6.1	2
		1971	San Fernando	6.6	1
		1976	Gazli, USSR	6.8	1
		1984	Morgan Hill	6.2	2
		1987	Whittier	6.0	1
		1989	Loma Prieta	6.9	2
		1994	Northridge	6.7	4
		1976	Gazli, USSR	6.8	1 †
		1985	Nahanni, Canada	6.8	1 †
	R10-50	1971	San Fernando	6.6	2
		1979	Imperial Valley	6.5	1
		1980	Mammoth Lakes	6.0	2
		1980	Victoria, Mexico	6.1	1
		1983	Coalinga	6.4	4
		1984	Morgan Hill	6.2	3
		1986	N. Palm Springs	6.0	1
		1985	Nahanni, Canada	6.8	1 †
	R50-100	1966	Parkfield	6.1	1
		1971	San Fernando	6.6	2
		1987	Whittier Narrows	6.0	5
		1991	Georgia, USSR	6.2	1
		1994	Northridge	6.7	6
	R100-200	1968	Borrego Mtn.	6.8	1
		1971	San Fernando	6.6	7
		1994	Northridge	6.7	7
M7+	R0-10	1976	Gazli, USSR	6.8	1
		1989	Loma Prieta	6.9	3
		1992	Cape Mendocino	7.1	1
		1992	Landers	7.3	1
		1995	Kobe	6.9	2
		1999	Kocaeli, Turkey	7.4	1

		1999	Chi-Chi, Taiwan	7.6	6
	R10-50	1978	Tabas, Iran	7.4	1
		1992	Cape Mendocino	7.1	1
		1992	Landers	7.3	1
		1999	Kocaeli, Turkey	7.4	4
		1999	Chi-Chi, Taiwan	7.6	5
		1999	Duzce, Turkey	7.1	3
	R50-100	1978	Tabas, Iran	7.4	1
		1992	Landers	7.3	4
		1999	Kocaeli, Turkey	7.4	1
		1999	Chi-Chi, Taiwan	7.6	9
	R100-200	1978	Tabas, Iran	7.4	1
		1992	Landers	7.3	5
		1999	Chi-Chi, Taiwan	7.6	9

- Most of the data are scaled motions.
- † indicates "recorded" data.

∑151

Table A2-4. Earthquake events and the number of three-component sets of ground motion recordings: CEUS-Soil.

Mag. Bin	Dist. Bin	Year	Earthquake Event	M	No. of Sets
M5-6	R0-50	1967	Northern Calif	5.6	1
		1980	Mammoth Lakes	6.0	1
		1983	Mammoth Lakes	5.2	1
		1983	Coalinga	5.0	1
		1983	Coalinga	5.2	1
		1986	N. Palm Springs	6.0	2
		1986	Chalfant Valley	5.6	1
		1987	Whittier Narrows	6.0	6
		1989	New Madrid, MO	4.7	1 †
	R50-100	1938	Northwest Calif	5.5	1
		1951	Northwest Calif	5.8	1
		1970	Lytle Creek	5.4	2
		1979	Imperial Valley	5.2	1
		1983	Trinidad offshore	5.5	2
		1986	N. Palm Springs	6.0	2
		1987	Whittier Narrows	6.0	4
		1988	Saguenay	5.9	1 †
		1989	New Madrid, MO	4.7	1 †
M6-7	R0-10	1979	Imperial Valley	6.5	8
		1980	Mammoth Lakes	6.3	1
		1983	Coalinga	6.4	1
		1986	Chalfant Valley	6.2	1
		1992	Erzican, Turkey	6.9	1
		1994	Northridge	6.7	4
		1995	Kobe	6.9	2
	R10-50	1971	San Fernando	6.6	1
		1979	Imperial Valley	6.5	2
		1981	Taiwan SMART1(5)	6.3	1
		1986	N. Palm Springs	6.0	1
		1987	Whittier Narrows	6.0	3
		1987	Superstition Hills (A)	6.3	1
		1989	Loma Prieta	6.9	1
		1991	Georgia, USSR	6.2	1
		1994	Northridge	6.7	4
	R50-100	1971	San Fernando	6.6	1
		1983	Taiwan SMART1(25)	6.5	3
		1984	Morgan Hill	6.2	2
		1989	Loma Prieta	6.9	1
		1991	Georgia, USSR	6.2	1
		1994	Northridge	6.7	7
	R100-200	1956	El Alamo	6.8	1
		1968	Borrego Mtn	6.8	1
		1971	San Fernando	6.6	6
		1987	Whittier Narrows	6.0	1
		1994	Northridge	6.7	5
		1995	Kobe	6.9	1

M7+	R0-10	1940	Imperial Valley	7.0	1
		1978	Tabas, Iran	7.4	1
		1992	Erzican, Turkey	6.9	1
		1992	Cape Mendocino	7.1	1
		1995	Kobe	6.9	2
		1999	Kocaeli, Turkey	7.4	1
		1999	Chi-Chi, Taiwan	7.6	13
		1999	Duzce, Turkey	7.1	1
	R10-50	1978	Tabas, Iran	7.4	1
		1986	Taiwan SMART1 (45)	7.3	3
		1992	Landers	7.3	2
		1999	Kocaeli, Turkey	7.4	1
		1999	Chi-Chi, Taiwan	7.6	8
	R50-100	1992	Landers	7.3	3
		1999	Kocaeli, Turkey	7.4	1
		1999	Chi-Chi, Taiwan	7.6	11
	R100-200	1952	Kern County	7.4	1
		1978	Tabas, Iran	7.4	2
		1992	Landers	7.3	6
		1999	Chi-Chi, Taiwan	7.6	6

- Most of the data are scaled motions.
- † indicates "recorded" data.

∑159

References

Abrahamson, N. A., and Silva, W. J. (1996). "Empirical ground motion models." *Report*, Brookhaven National Laboratory.

Anderson, J. G., and Hough, S. E. (1984). "A model for the shape of the fourier amplitude spectrum of acceleration at high frequencies". *Bulletin of the Seismological Society of America*, 74(5), 1969-1993.

Atkinson, G. M. (1993). "Earthquake source spectra in eastern North America". *Bulletin of the Seismological Society of America*, 83(6), 1778-1798.

Atkinson, G. M., and Boore, D. M. (1995). "Ground-motion relations for eastern North America". *Bulletin of the Seismological Society of America*, 85(1), 17-30.

Boore, D. M. (1983). "Stochastic simulation of high-frequency ground motions based on seismological models of the radiated spectra". *Bulletin of the Seismological Society of America*, 73(6A), 1865-1894.

Boore, D. M. (1986). "Short-period P- and S-wave radiation from large earthquakes: Implications for spectral scaling relations". *Bulletin of the Seismological Society of America*, 76(1), 43-64.

Boore, D. M., and Atkinson, G. M. (1992). "Source spectra for the 1988 Saguenay, Quebec, earthquakes". *Bulletin of the Seismological Society of America*, 82(2), 683-719.

Brune, J. N. (1970). "Tectonic stress and spectra of seismic shear waves from earthquakes". *Journal of Geophysical Research*, 75(26), 611-614.

Brune, J. N. (1971). "Correction". *Journal of Geophysical Research*, 76(20), 1441-1450.

Dobry, R., Idriss, I. M., and Ng, E. (1978). "Duration characteristics of horizontal components of strong-motion earthquake records". *Bulletin of the Seismological Society of America*, 68(5), 1487-1520.

Hanks, T. C., and Kanamori, H. (1979). "A moment magnitude scale". *Journal of Geophysical Research*, 84, 2348-50.

Hanks, T. C., and McGuire, R. K. (1981). "The character of high-frequency strong ground motion". *Bulletin of the Seismological Society of America*, 71(6), 2071-2095.

Herrmann, R. B. (1980). "Q estimates using the coda of local earthquake". *Bulletin of the Seismological Society of America*, 70(2), 447-468.

Husid, L. R. (1969). "Características de terremotos. Análisis general." *Revista del IDIEM 8*, Santiago de Chile, 21-42.

McGuire, R. K., Becker, A. M., and Donovan, N. C. (1984). "Spectral estimates of seismic shear waves". *Bulletin of the Seismological Society of America*, 74(4), 1427-1440.

McGuire, R. K., Silva, W. J., and Costantino, C. J. (2001). "Technical basis for revision of regulatory guidance on design ground motions: Hazard-and risk-consistent ground motion spectra guidelines.", US Nuclear Regulatory Commission, Washington, DC.

Schneider, J. F., Silva, W. J., and Stark, C. (1993). "Ground Motion Model for the 1989 M 6.9 Loma Prieta Earthquake Including Effects of Source, Path, and Site". *Earthquake Spectra*, 9(2), 251-287.

Silva, W. (1993). "Factors controlling strong ground motion and their associated uncertainties." *Dynamic Analysis and Design Considerations for High-Level Nuclear Waste Repositories*, San Francisco, CA, USA, 132-161.

Silva, W. J., and Lee, K. (1987). "WES RASCAL Code for Synthesizing Earthquake Ground Motions: State-of-the-art for assessing earthquake hazards in the United States." *Report 24*, US Army Engineering Waterways Experiment Station Vicksburg, MS.

Chapter 3

Data Modeling Analyses: Non-linear Mixed-effects Regression

3.1 Introduction

In this chapter, background information and the process for developing the predictive relationships for individual characteristic parameters are described. The overall procedure of data modeling, followed in this study, comprises three analyses: formulation of regression models as a pre-regression analysis; regression analysis; and examination of the model fit in the post-regression analysis. The non-linear mixed-effects (NLME) regression technique was employed for developing all the empirical predictive relationships in this study.

Regarding the organization of this chapter, first the approach and tips for constructing regression models are presented. Then, the NLME regression method is reviewed starting with the basic concepts including: inter- and intra-group variability; underlying assumptions; and the advantages of the regression method. Next, examining model fits as a post-regression analysis is covered. Lastly, the procedure for data modeling analysis is summarized. The definitions of all the statistical parameters used in the regression analysis are explained as they are presented. For future R-program users of NLME regression, Appendix 3 presents a R (version 2.5.0) manual that the author wrote for

performing NLME regressions. Also, additional useful R-functions are listed in this appendix.

3.2 Pre-regression Analysis: Building Regression Model

Once the engineering characteristic parameter data to be regressed have been computed from the strong ground motion records, the data is analyzed to identify the distribution of the scatter in the data and the trends in the data as functions of the independent variables (i.e., design earthquake parameters). These analyses form the bases for establishing the functional form of the predictive relationship (or regression model).

First, the distribution of the scatter in the data is identified using a histogram and/or normal quantile-quantile (Q-Q) plot. Figure 3-1 shows examples of a histogram and a normal Q-Q plot for the natural log of Arias intensity data. A histogram is a graphical display showing the frequency of the data within each interval. From the example histogram shown in Figure 3-1, the data seems to be normally distributed except for the data less than -5. Note that if the histogram plots as a normal distribution, the data is log-normally distributed because the log of the data is plotted in the histogram. The normal Q-Q plot is another graphical method for determining if the data is normally distributed. If the data points plot approximately as a straight line, it indicates that the data is normally distributed. Therefore, based on the example normal Q-Q plot in Figure 3-1, the data seem to be normally distributed although there are multiple outliers from the straight line, consistent with the observations made from the histogram. Since the earthquake characteristic parameter data is commonly known to have a log-normal distribution and

the normal Q-Q plot provides clearer presentations than the histogram for determining the normal distribution of data, the normal Q-Q plot is a preferable tool for this study.

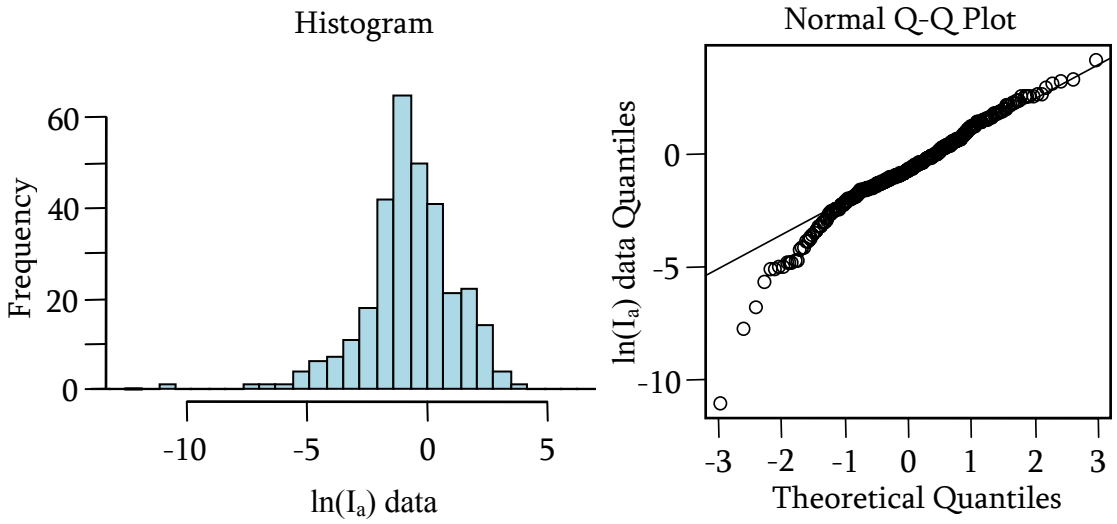

Figure 3-1. Example of histogram and normal Q-Q plot for the data of the natural log of Arias intensity – CEUS.

Next, the functional forms of the predictive relationships are formulated. As mentioned in Chapter 1, the regression model herein is formulated as a function of the following independent variables: earthquake magnitude, site-to-source distance, and local site condition. An easy way to scrutinize the data trends with respect to each independent variable is by plotting the data in terms of independent variables. Figure 3-2 shows example plots with simple linear model fits by the least squares method, which is used to identify trends.

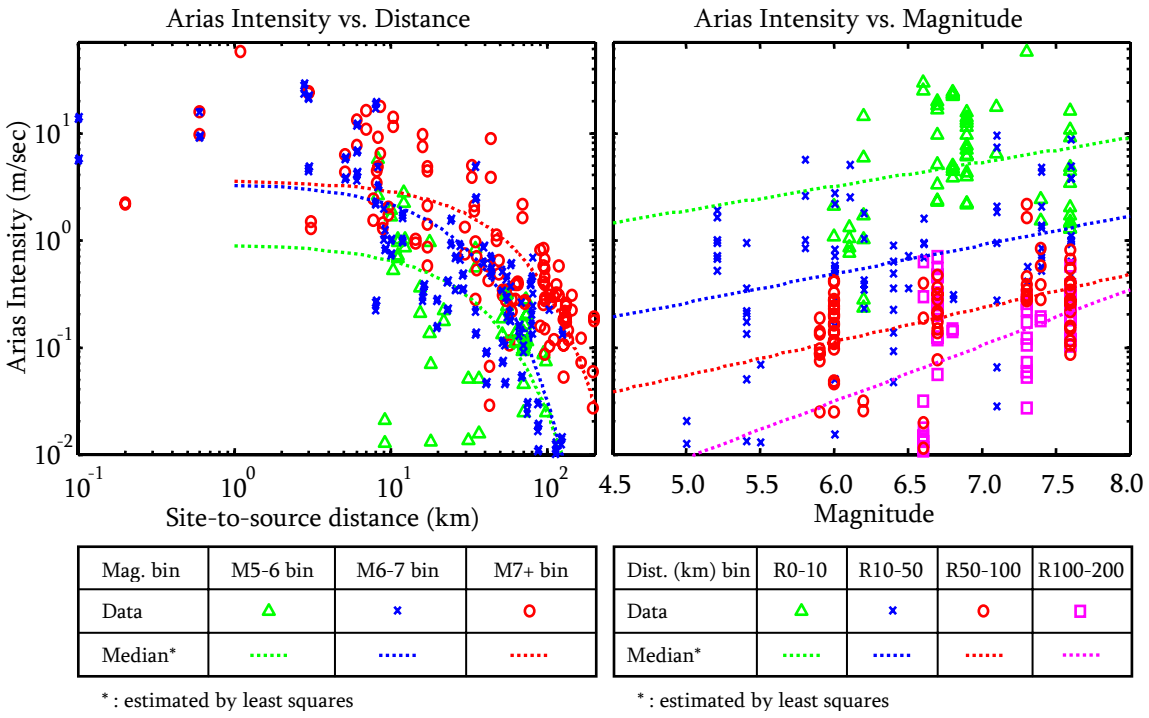

Figure 3-2. Example trend plots for Arias intensity parameter – CEUS, Rock.

A good regression model should accurately interpret scientific data, yielding the smallest standard error/deviation, as well as representing the underlying physics of the problem. Obviously, it is unfeasible to obtain the regression model solely from visual inspection of the data. Rather, the regression model is achieved through "trial and error". That is, try numerous functional forms of the predictive relationships in the NLME analyses, modify the relationships based on the comparisons of the regression results, and iterate until the best model is obtained. It is easier to start with simple regression models and add complex terms during the modification process (Gelman and Hill, 2007). Yet, it should be noted that overly complex models (e.g., ones with high degree of a polynomial) may show a good fit of the particular data being regressed but may lose flexibility. As a result, it may not work for the other data. Furthermore, overly complex models may end up being wrong from a physical standpoint. In this regard, the model should be simple

enough to avoid problems during modification. The appropriateness of the functional form of the predictive relationships is checked in the post-regression analysis by examining the model fits to the data.

3.3 NLME Regression Analysis

The mixed-effects regression technique is often used in diverse areas where data consisting of multiple groups are analyzed. In this study, a "group" of motions represents those from the same earthquake event. In comparison to applying a fixed-effects regression technique, which is equivalent to the least squares method to the entire dataset, a mixed-effects regression method allows both inter- and intra-group (i.e., between- and within-event) uncertainty to be quantified. The mixed-effects regression method produces unbiased fittings for each group (i.e., earthquake event) having different numbers of data (i.e., ground motion recordings), which is important in analyzing earthquake ground motion data. Furthermore, non-linear mixed-effects (NLME) modeling allows the functional form of the predictive relationship to be theoretically or empirically based and to be non-linear – the NLME modeling utilizes non-linear regression. Accordingly, the NLME modeling is a robust regression technique suitable for analyzing earthquake ground motion datasets. This study used the statistical analysis program R (version 2.5.0), along with a NLME package.

3.3.1 Basic Concepts

NLME modeling is a maximum likelihood method based on normal (Gaussian) distribution and is used particularly for analyzing grouped data. The NLME regression method allows the regression models to incorporate both fixed-effects that do not vary

with the entire population of data and random-effects that vary by group. The random-effects are associated with earthquake events that are considered as a group herein.

For a given data set and regression model, the NLME modeling estimates the variation in the mean values among events (i.e., inter-event variability) and the variation in the data for a single event (i.e., intra-event variability) via the variances of inter-event errors and intra-event errors, respectively. The inter-event error is designated by η_i where the subscript, *i* represents the i^{th} event (i.e., group). The inter-event error is defined as the difference between the medians for the i^{th} event and all of the events (i.e., model median) and has mean of zero and variance of τ^2. The intra-event error is designated by ε_{ij} where the subscript, *ij* indicates the j^{th} record of the i^{th} event. The intra-event error is defined as the difference between the data value of the j^{th} record and the median for the i^{th} event and has mean of zero and variance of σ^2. Figure 3-3 illustrates the inter- and intra-event errors. The total error for the j^{th} record of the i^{th} event is defined as the sum of the corresponding inter- and intra-event errors (i.e., $\eta_i + \varepsilon_{ij}$). The standard deviation of the total errors is given by:

$$\sigma_{total} = \sqrt{\tau^2 + \sigma^2} \qquad \text{(Eq. 3-1)}$$

where: σ_{total} is the standard deviation of total errors, also called the total standard deviation.

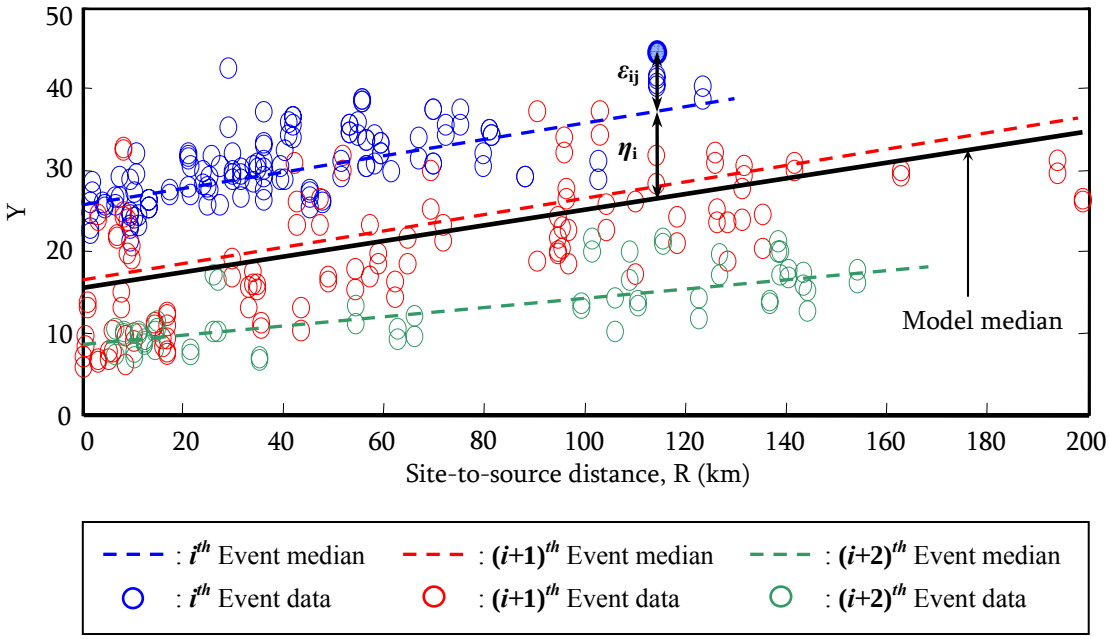

Figure 3-3. Schematic plot of inter- and intra-event errors of the NLME regression for example data, Y.

There are two assumptions inherent in the NLME modeling (Pinheiro and Bates, 2000):

1. The intra-event errors are independent and normally distributed, with a mean of zero and variance σ^2, and they are independent of the random effects.
2. The random-effects are normally distributed, with a mean of zero and covariance matrix Ψ (not depending on the group) and are independent for different groups.

The validity of these assumptions should be checked during post-regression analysis since the distributional assumptions underlie the theoretical formulation of the NLME regression analyses. The normal Q-Q plot is used to assess the distributional assumptions. This is described in more detail in section 3.4.

3.3.2 Advantage of Using NLME Regression Method

One of the key advantages of using the NLME regression method is that it produces unbiased fitting results, irrespective of the amount of data in each group. In contrast, a

model fit using the conventional least squares method will tend to be biased toward the group (i.e., earthquake event) having the largest amount of the data.The NLME regression represents the overall characteristics of the data, independent of whether the amount of data varies from group to group. This is because the NLME regression method estimates not only the median within a group but also estimates the median among groups. This is illustrated in Figure 3-4 in which the data (i.e., significant duration) were fitted by both the least squares and the NLME methods. One can easily observe the difference between the predictions resulting from the two regression methods: the regression line by the least squares method tends to follow the data trend from the Chi-Chi earthquake which has the largest number of data.

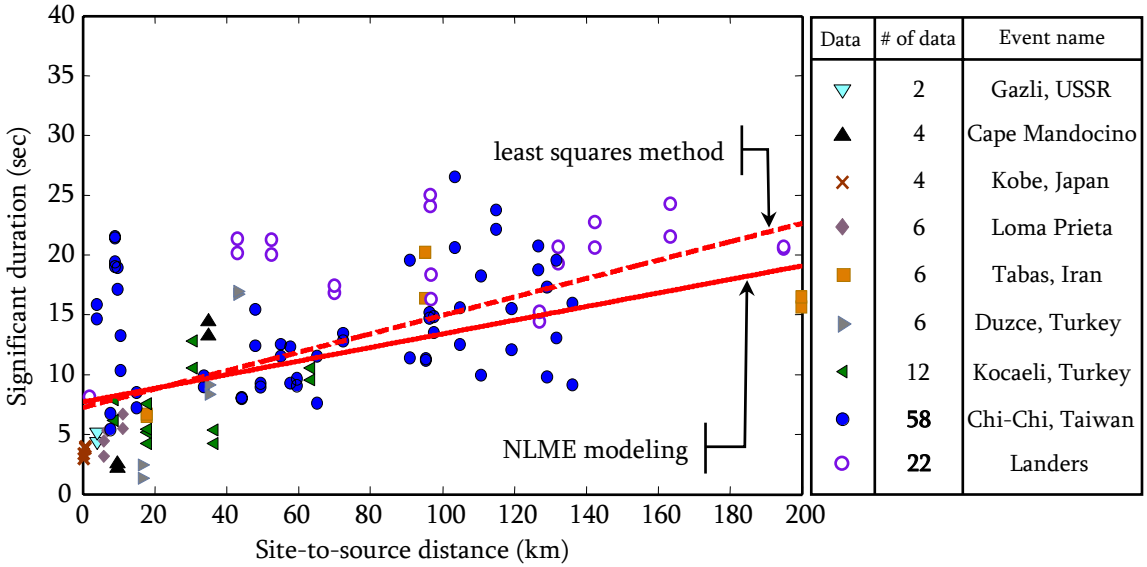

Figure 3-4. Comparison of fittings by the least squares and mixed-effects modeling: 5-75% significant duration data for WUS, Rock (M7+).

3.4 Post-regression Analysis: Examining Model Fit

In the post-regression analysis, the appropriateness of the resulting predictive relationship is evaluated, which involves checking the statistical validity of regression results and assessing the functional forms and statistical parameters of a model fit. This is a crucial part of data modeling analyses because:

- The statistical estimators (e.g., standard deviation) resulting from a regression analysis are important factors to assess the overall fit of the data and statistical significance of individual terms in the regression model.
- However, the statistical estimators violating the distributional assumptions are not valid. This is because the computational methods in the NLME regression analyses are based on the assumptions.
- An overly complex model may lose its flexibility.

The distributional assumptions regarding the intra-event errors and random-effects should be assessed. This can be done using the normal Q-Q plot, similar to identifying the distribution of the scatter in the data. Example normal Q-Q plots for intra-event errors and random-effects are shown in Figure 3-5. In this figure, the theoretical quantiles of the standard normal distribution versus the standardized intra-event errors (i.e., intra-event errors divided by their standard deviation) and random-effects are plotted. For the normal Q-Q plots in Figure 3-5, it appears that both intra-event errors and random-effects follow normal distributions, consistent with the assumptions inherent to NLME modeling.

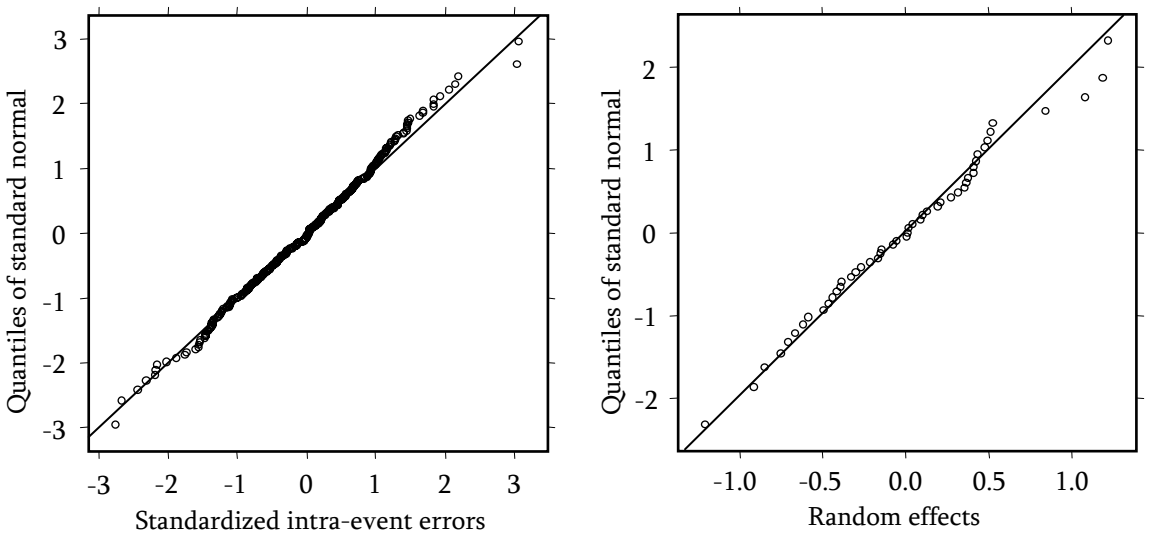

Figure 3-5. Example of normal Q-Q plots for intra-event errors and random-effects: Arias intensity – WUS.

Once the validity of the distributional assumptions has been confirmed, the model fits are assessed by their resulting statistical estimators. This is important in selecting the best functional form of the predictive relationship, as well as for modifying the functional forms. The statistical estimators used in this study to assess the model fit were the standard deviation of total errors and the p-value. The standard deviation is a measure of statistical dispersion, quantifying how widely spread the data points are around the model prediction (i.e., median) – a smaller standard deviation is indicative of a more accurate fit. Thus, the decision regarding which regression model represents the data more accurately can be made by comparing the standard deviations of the various competing models. In addition, the p-value, which is a measure of the statistical significance of a regression coefficient in the model, is checked. A p-value close to zero indicates that the corresponding regression coefficient has a significant statistical contribution. A p-value of 5% (i.e., 0.05) is typically considered as a threshold of p-value (i.e., a coefficient with a p-value smaller than 0.05 is statistically significant). Based on the p-value, the

functional form of the predictive relationship might be modified by removing a term with a regression coefficient that is not statistically significant. However, excluding a term may not necessarily improve the overall fit of the data, but it will likely result in a simpler model. Based on the author's experience and judgment, a term may be kept in the model in the following cases:

- Removal of the statistically-insignificant term causes a considerable increase in total standard deviation, which rarely happens.
- The term provides a desired physical interpretation but turns out to be statistically insignificant (Gelman and Hill, 2007).

The functional form of the predictive relationship ultimately chosen may end up being overly complicated because of the model modification process. As a result, there may be a loss in the model's flexibility and/or the model may predict a misleading overall trend as a consequence of the determination of the regression coefficients being biased by local trends in the data. To avoid these problems, the regression model should be checked graphically by plotting the predictive relationship along with the actual data and checking whether the model appropriately represents the data from a physical sense (i.e., check whether the regression curve shows any unnecessarily complicated trends).

3.5 Data Modeling Procedure

The following is a summary of the steps in the procedure for data modeling discussed above:

1. Based on the observed trends and existing theoretical or empirical models (if available), formulate multiple regression models with various combinations of simple functional terms that represent the trends.
2. Perform the NLME regression analyses using the functional form of the predictive relationship developed in Step 1. See Appendix 3 for details on performing NLME regressions using the program-R (version 2.5.0).
3. Assess the adequacy of the functional form of the predictive relationship, as described in section 3.4.
4. For the next round of regressions, modify the model/models based on the finding from Step 3.
5. Repeat Steps 2-4. Through this trial and error process, one can gain a sense of the importance of the various terms in the predictive relationship. This process will help in establishing the final form of the regression model.
6. Once the final predictive relationship is obtained, ensure that the model does not violate the distributional assumptions and that the predicted trends make physical sense.
7. Finally, present the results by providing model trend plots, the model, regression coefficients, and standard deviation.

Appendix 3: Program-R Manual for NLME Regression Analysis (version 2.5.0)

- Notes
  - ✓ For clarity, different fonts are used for all R-command codes and the results displayed by program-R. Specifically, R-functions are presented in **bold**.
  - ✓ Commentary annotations added in R-command codes are followed by '#'.
  - ✓ Arias intensity for stable continental regions (e.g., central/eastern US: CEUS) is used as an example data.

A3.1. Procedure for Non-linear Mixed-effects Regression in Program-R

Step 1) Generate the input data in a text file and save it in the same folder as the R-program uses. An example format of the input data file is shown below. Note that a set of data and each variable value are arranged by row and by column, respectively. The file name of the example data file was saved as CEUS_AI_avg.txt. [Note that SS is a binary number for the local site conditions: 0 = rock; 1 = soil.]

Event	Mag.	Dist.	ln(I_a)	SS
29	5.40	21.90	-1.612910	0
29	5.40	15.40	-1.256217	0
42	5.50	17.90	-3.184495	0
45	6.00	36.60	-3.393616	0
54	5.40	31.00	-3.445647	0
54	5.40	17.60	-0.605423	0
65	5.00	9.10	-4.092199	0
79	5.20	11.00	-0.155815	0
79	5.20	11.00	-0.179425	0
79	5.20	10.00	0.582980	0
79	5.20	10.40	-0.641218	0
80	5.80	8.20	1.426784	0
80	5.80	12.20	-0.054189	0
103	6.00	34.90	-0.359427	0
117	6.00	12.10	0.928298	0
14	6.00	70.00	-3.340516	0
103	6.00	55.40	-1.259513	0

103	6.00	73.70	-1.847611	0
103	6.00	63.30	-2.073166	0
103	6.00	71.90	-1.524528	0
.	.	.	.	.
.	.	.	.	.
.	.	.	.	.
129	7.30	148.80	-0.633413	1
129	7.30	157.70	-1.576136	1
129	7.30	164.50	-0.733587	1
129	7.30	150.40	-0.988805	1
142	7.60	100.20	-0.608266	1
142	7.60	127.20	-1.218495	1
142	7.60	127.70	-1.947958	1
142	7.60	108.10	-2.546807	1

Step 2) Perform a preliminary regression to determine initial values of the regression coefficients for use in the NLME regression. Use *nls* (non-linear least squares) of *stats* package provided by the program-R. Since the algorithm for NLME regression analysis requires computational iterations, the initial values of the regression coefficients typically reduce the number of iterations required for converge. Note that you do not need to load the *stats* package manually because it is a default package. In this example, the assumed functional form of the predictive relationship is:

$$\ln I_a = C_1 + C_2(M-6) + C_3(M-6)^2 + C_4 \ln(M/6) + C_5 \ln(\sqrt{R^2+h^2}) + [S_1 + S_2(M-6)]SS$$

where: I_a is Arias intensity; C_1-C_5, h, S_1 and S_2 are regression coefficients; M is earthquake magnitude; R is site-to-source distance; SS is a binary for local site condition (i.e., 0 for rock sites; 1 for soil sites).

- Read the input data file and save the input data with the assigned variable names.

```
Data = read.table("CEUS_AI_avg.txt", header = TRUE, sep = "\t")
Event = Data[,1]
M = Data[,2]
```

```
R = Data[,3]
logAIa = Data[,4]
SS = Data[,5]
```

- Perform nls regression named as ‘pr_model’.

```
pr_model<-nls(logAIa ~ (c1 + c2*(M-6) + c3*(M-6)^2 + c4*log(M/6)
  + c5*log(sqrt(R^2 + h^2)) + (s1+ s2*(M-6))*SS),
  start=list(c1=1, c2=1, c3=1, c4=1, c5=1, h=1, s1=1, s2=1))

# nls regression also requires the initial values of the regression
coefficients to be specified but these are less sensitive than
those for nlme regression. Herein, all are set equal to 1.
```

- Display the nls regression result.

```
summary(pr_model)

Formula: logAIa ~ (c1 + c2*(M - 6) + c3*(M - 6)^2 + c4*log(M/6)
               + c5*log(sqrt(R^2 + h^2)) + (s1 + s2*(M - 6))*SS)

Parameters:
   Estimate Std. Error t value Pr(>|t|)
c1   3.5613     0.5087   7.000 1.66e-11 ***
c2 -48.7867    15.5310  -3.141  0.00185 **
c3   3.0598     1.1840   2.584  0.01023 *
c4 302.4886    92.2811   3.278  0.00117 **
c5  -1.3579     0.1249 -10.876  < 2e-16 ***
h   -7.4164     2.3256  -3.189  0.00158 **
s1   0.5673     0.1743   3.255  0.00126 **
s2  -0.4659     0.1724  -2.703  0.00726 **
---
Signif. codes:  0 '***' 0.001 '**' 0.01 '*' 0.05 '.' 0.1 ' ' 1

Residual standard error: 1.078 on 302 degrees of freedom

Number of iterations to convergence: 6
Achieved convergence tolerance: 5.111e-06
```

- Use the regression coefficients listed in the "`Estimate`" column as the initial values for NLME regression.

Step 3) Load *nlme* package:

Go to *Package* in the main menu of the program and choose *Load package…*

Select *nlme*, then R will load the *nlme* package.

Step 4) Perform the NLME regression analysis.

```
Data = read.table("CEUS_AI_avg.txt", header = TRUE, sep = "\t")
Event = Data[,1]
M = Data[,2]
R = Data[,3]
logAIa = Data[,4]
SS = Data[,5]

# nlme regression named as 'model'
model <- nlme(logAIa ~ (c1 + c2*(M-6) + c3*(M-6)^2 + c4*log(M/6)
                 + c5*log(sqrt(R^2 + h^2)) + (s1+ s2*(M-6))*SS),
  fixed = c1+c2+c3+c4+c5+h+s1+s2~1, #'1' on the right hand side of
    the formula indicates that a single parameter is associated
    with the effect.#
  random = c1~1|Event,
  start = list(c1=1, c2=1, c3=1, c4=1, c5=1, h=1, s1=1, s2=1,
  fixed = c(3.56, -48.8, 3.06, 302.5, -1.36, -7.42, 0.57, -0.466)),
                        # the starting estimates from the
                        preliminary regression #
   verbose = TRUE)
```

- Note that the regression coefficient, c1 is set as both random-effects and fixed-effects parameter associated with Event. As a result, the resulting c1 value cannot be zero, which is one of the underlying assumptions of fixed-effects modeling.

- Adding the optional argument, `verbose = TRUE`, the iteration history of the NLME regression is shown:

```
**Iteration 1
LME step: Loglik: -430.6677 , nlm iterations: 2
reStruct  parameters:
    Event
0.2746107

PNLS step: RSS =  243.927
 fixed effects:3.22088  -107.616  7.91389  651.306  -1.2763
  -6.05644  0.556359  -0.452761
 iterations: 3

Convergence:
      fixed    reStruct
0.613337840 0.001261273

**Iteration 2
LME step: Loglik: -430.6565 , nlm iterations: 1
reStruct  parameters:
    Event
0.2742129
```

```
  PNLS step: RSS =  243.927
   fixed effects:3.22088  -107.616  7.91389  651.306  -1.2763
         -6.05644  0.556359  -0.452761
   iterations: 1

  Convergence:
         fixed     reStruct
0.000000e+00 9.568245e-10
```

Step 5) Assess the NLME regression results. Use the following R-functions.

(1) **`print(`**`model`**`)`**: this function displays a brief summary of the regression results as shown below. [The **`summary(`**`model`**`)`** function will display more detailed regression results, as described subsequently.]

```
Nonlinear mixed-effects model fit by maximum likelihood
Model: logAIa ~ (c1 + c2*(M - 6) + c3*(M - 6)^2 + c4*log(M/6)
             + c5*log(sqrt(R^2 + h^2)) + (s1 + s2*(M - 6))*SS)
Data: NULL
Log-likelihood: -430.6565
Fixed: c1 + c2 + c3 + c4 + c5 + h + s1 + s2 ~ 1
c1           c2           c3           c4           c5            h
3.2208817 -107.6162745 7.9138853 651.3064860 -1.2762981  -6.0564441
    s1           s2
   0.5563588   -0.4527610

Random effects:
 Formula: c1 ~ 1 | Event
               c1 Residual
StdDev: 0.6743106 0.887052

Number of Observations: 310
Number of Groups: 53
```

(2) **`summary(`**`model`**`)`**: displays detailed regression result.

```
Nonlinear mixed-effects model fit by maximum likelihood
Model: logAIa ~ (c1 + c2*(M - 6) + c3*(M - 6)^2 + c4*log(M/6)
             + c5*log(sqrt(R^2 + h^2)) + (s1 + s2*(M - 6))*SS)
Data: NULL
      AIC      BIC    logLik
  881.313 918.6788 -430.6565
```

```
Random effects:
 Formula: c1 ~ 1 | Event
            c1 Residual
StdDev: 0.6743106 0.887052

Fixed effects: c1 + c2 + c3 + c4 + c5 + h + s1 + s2 ~ 1
       Value Std.Error  DF    t-value p-value
c1    3.2209   0.44400  49   7.254160  0.0000
c2 -107.6163  26.27167  49  -4.096287  0.0002
c3    7.9139   2.12976  49   3.715864  0.0005
c4  651.3065 155.74929  49   4.181762  0.0001
c5   -1.2763   0.10648 254 -11.986117  0.0000
h    -6.0564   1.89336 254  -3.198789  0.0016
s1    0.5564   0.16846 254   3.302637  0.0011
s2   -0.4528   0.15981 254  -2.833038  0.0050
 Correlation:
   c1     c2     c3     c4     c5     h      s1
c2  0.009
c3 -0.026 -0.996
c4 -0.009 -1.000  0.996
c5 -0.897 -0.108  0.103  0.108
h  -0.785 -0.141  0.138  0.140  0.820
s1 -0.165  0.030 -0.029 -0.027 -0.029  0.003
s2  0.122 -0.028  0.025  0.025  0.033 -0.032 -0.754

Standardized Within-Group Residuals:
        Min          Q1         Med          Q3         Max
-2.71047087 -0.69258161  0.05276737  0.67889789  3.13668358

Number of Observations: 310
Number of Groups: 53
```

- Note: 1. Inter-event errors standard deviation (τ) = 0.674;

  Intra-event errors standard deviation (σ) = 0.887

  (i.e., " `StdDev: 0.6743106 0.887052`" in the output file)

  Therefore, the standard deviation of the total error is determined by:

$$\sigma_{total} = \sqrt{\tau^2 + \sigma^2} = \sqrt{0.674^2 + 0.887^2} = 1.114$$

2. The resulting p-values for all the regression coefficients are less than 0.05.

   Therefore, all the coefficients appear to be statistically significant.

(3) **`coef(`**`model`**`)`**: shows the resulting regression coefficients for each Event.

```
     c1      c2       c3      c4      c5       h        s1      s2
  1  2.5650  -107.62  7.9139  651.31  -1.2763  -6.0564  0.5564  -0.4528
  4  3.3310  -107.62  7.9139  651.31  -1.2763  -6.0564  0.5564  -0.4528
  5  3.5843  -107.62  7.9139  651.31  -1.2763  -6.0564  0.5564  -0.4528
  6  3.0193  -107.62  7.9139  651.31  -1.2763  -6.0564  0.5564  -0.4528
 11  3.4652  -107.62  7.9139  651.31  -1.2763  -6.0564  0.5564  -0.4528
 12  3.4214  -107.62  7.9139  651.31  -1.2763  -6.0564  0.5564  -0.4528
 14  2.8055  -107.62  7.9139  651.31  -1.2763  -6.0564  0.5564  -0.4528
 19  3.6737  -107.62  7.9139  651.31  -1.2763  -6.0564  0.5564  -0.4528
 25  2.4613  -107.62  7.9139  651.31  -1.2763  -6.0564  0.5564  -0.4528
 26  3.0677  -107.62  7.9139  651.31  -1.2763  -6.0564  0.5564  -0.4528
 28  3.0716  -107.62  7.9139  651.31  -1.2763  -6.0564  0.5564  -0.4528
 29  2.6523  -107.62  7.9139  651.31  -1.2763  -6.0564  0.5564  -0.4528
 30  2.5941  -107.62  7.9139  651.31  -1.2763  -6.0564  0.5564  -0.4528
 41  3.7259  -107.62  7.9139  651.31  -1.2763  -6.0564  0.5564  -0.4528
 42  2.5727  -107.62  7.9139  651.31  -1.2763  -6.0564  0.5564  -0.4528
 45  2.4875  -107.62  7.9139  651.31  -1.2763  -6.0564  0.5564  -0.4528
  .     .       .       .       .        .        .       .        .
  .     .       .       .       .        .        .       .        .
  .     .       .       .       .        .        .       .        .
122  4.1612  -107.62  7.9139  651.31  -1.2763  -6.0564  0.5564  -0.4528
124  2.4788  -107.62  7.9139  651.31  -1.2763  -6.0564  0.5564  -0.4528
125  2.8317  -107.62  7.9139  651.31  -1.2763  -6.0564  0.5564  -0.4528
127  3.8128  -107.62  7.9139  651.31  -1.2763  -6.0564  0.5564  -0.4528
129  3.6764  -107.62  7.9139  651.31  -1.2763  -6.0564  0.5564  -0.4528
131  4.0635  -107.62  7.9139  651.31  -1.2763  -6.0564  0.5564  -0.4528
133  3.5475  -107.62  7.9139  651.31  -1.2763  -6.0564  0.5564  -0.4528
141  2.6795  -107.62  7.9139  651.31  -1.2763  -6.0564  0.5564  -0.4528
142  2.2665  -107.62  7.9139  651.31  -1.2763  -6.0564  0.5564  -0.4528
143  3.0901  -107.62  7.9139  651.31  -1.2763  -6.0564  0.5564  -0.4528
```

- The first column is the event number. The variation of c1 value for each event shows that the c1 represents random-effects associated with Event.
- Note that the mean of the c1 values is equal to the c1 determined from the fixed-effects regression shown by the function, **`summary(`**`model`**`)`**.

(4) **`resid(`**`model, level = 0:1`**`)`**: shows the residuals (i.e., errors) in the total and intra-event (i.e., level = 0 for total errors; level = 1 for intra-event errors). Therefore, the inter-event errors can be computed from the difference between the total and intra-event residual values (i.e., inter-event error = total error – intra-event error).

```
           fixed        Event
1    0.355738407  0.924325114
2    0.307765940  0.876352646
3   -1.769877785 -1.121695822
4   -2.002523785 -1.269140191
5   -1.056609303 -1.070553760
6    1.108630425  1.094685967
7   -1.043609888 -0.661408387
8    1.897303257  0.691006824
9    1.873693257  0.667396824
10   2.544890973  1.338594541
11   1.357697352  0.151400919
12   1.409718229  0.951795599
 .        .            .
 .        .            .
 .        .            .
```

- Note that the columns labeled fixed and Event are the total errors and intra-event errors, respectively.

(5) **`predict(`**`model, level=0:1`**`)`**: shows the predictions in two levels.

```
    Event predict.fixed predict.Event
1      29   -1.96864841   -2.53723511
2      29   -1.56398294   -2.13256965
3      42   -1.41461721   -2.06279918
4      45   -1.39109221   -2.12447581
5      54   -2.38903770   -2.37509324
6      54   -1.71405342   -1.70010897
7      65   -3.04858911   -3.43079061
8      79   -2.05311826   -0.84682182
9      79   -2.05311826   -0.84682182
10     79   -1.96191097   -0.75561454
11     79   -1.99891535   -0.79261892
12     80    0.01706577    0.47498840
 .      .         .              .
 .      .         .              .
 .      .         .              .
```

- The columns labeled "predict.fixed" and "predict.Event" are the predicted values computed using the c1 for all events (i.e., c1 for fixed effects = 3.2209 in this example), and using the c1 for each event (i.e., within-group fitted), respectively.

- Note that **predict(**model**)** is a function equivalent to **predict(**model, level=0:1**)**[,3]. That is, **predict(**model**)** shows the third column (i.e., predict.Event) of the results shown by **predict(**model, level=0:1**)** function.

(6) **intervals(**model**)**: shows the 95% confidence intervals of the regression coefficients for random- and fixed-effects; standard deviations of random effects (i.e., inter-event errors standard deviation) and within-group errors (i.e., intra-event errors standard deviation).

```
Approximate 95% confidence intervals

 Fixed effects:
          lower          est.       upper
c1    2.3402090    3.2208817   4.1015544
c2 -159.7254862 -107.6162745 -55.5070627
c3    3.6895646    7.9138853  12.1382061
c4  342.3815373  651.3064860 960.2314346
c5   -1.4832734   -1.2762981  -1.0693228
h    -9.7366926   -6.0564441  -2.3761955
s1    0.2289132    0.5563588   0.8838044
s2   -0.7634040   -0.4527610  -0.1421180
attr(,"label")
[1] "Fixed effects:"

 Random Effects:
  Level: Event
           lower      est.     upper
sd(c1) 0.4853799 0.6743106 0.9367812

 Within-group standard error:
    lower      est.     upper
0.8139843 0.8870520 0.9666788
```

(7) **ranef(**model**)**: shows the random-effects variation (i.e., random-effects for each event). Please recall that c1 was set as both random-effects and fixed-effects in this example, which means the c1 is not zero due to the fixed-effects; the c1 would have

been zero according to the underlying assumptions if it had been set only for random-effects. Therefore, the random-effects should be equal to the difference between the c1 from fixed-effects and the c1 values for each event (i.e., c1 for each event minus c1 for all events). Basically, it shows the deviations of the c1 values (i.e., random-effects) varying with each event from the mean of the c1 values.

```
              c1
1   -0.655925045
4    0.110073210
5    0.363448425
6   -0.201605861
11   0.244281750
12   0.200549286
14  -0.415411345
19   0.452843298
25  -0.759568501
26  -0.153210892
28  -0.149232791
29  -0.568586706
30  -0.626765649
 .         .
 .         .
 .         .
129  0.455514456
131  0.842639901
133  0.326574996
141 -0.541333762
142 -0.954388323
143 -0.130781634
```

(8) **`plot(ranef(`**`model`**`))`**: shows a scatter plot of the random-effects, which is useful for checking marginal normality and identifying outliers. These checks can also be done using the function **`qqnorm`**, as discussed subsequently. The example plot is shown in Figure A3-1.

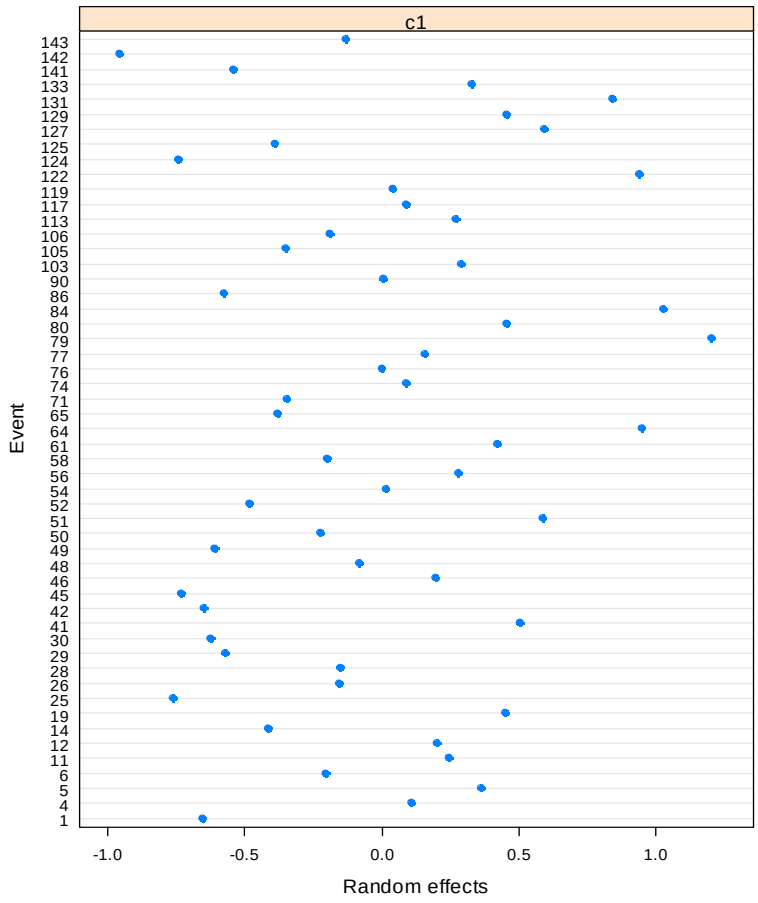

Figure A3-1. A scatter plot of random-effects.

(9) **`plot(model)`**: shows a scatter plot of standardized residuals vs. fitted values. This plot can be used to assess the assumption of constant variance of the intra-event errors. The standardized residual is defined as the intra-event error minus its mean and divided by its standard deviation, σ. Note that the mean of intra-event errors is zero, per the assumption underlying the regression method. The example plot is shown in Figure A3-2.

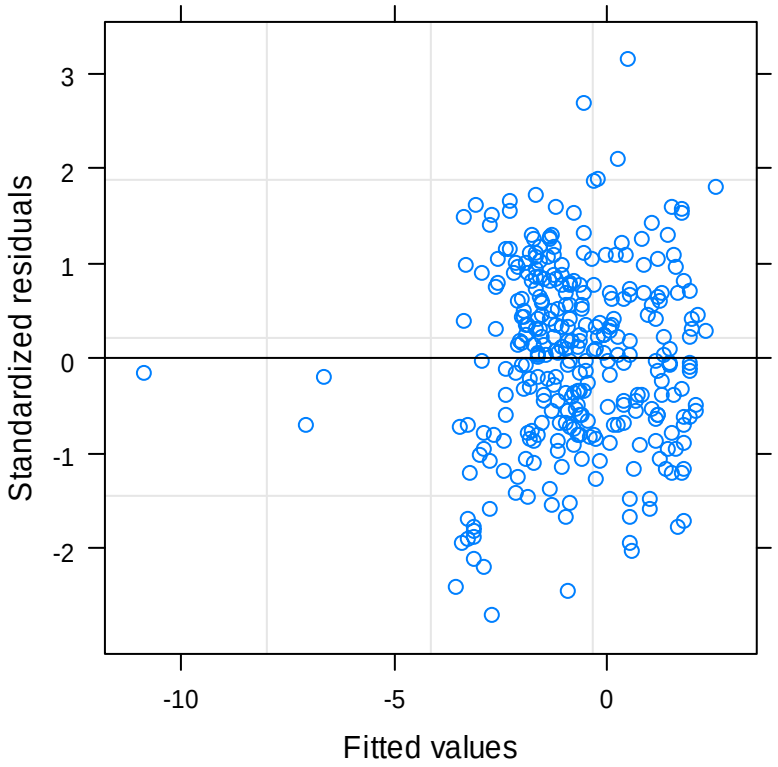

Figure A3-2. A scatter plot of intra-event errors.

- From the plot, one can check if the standardized residuals are approximately symmetrically distributed around zero, which is an indication that the intra-event errors follow the normal distribution.

(10) **`anova(model)`**: shows the statistical parameters used to assess the significance of the terms in the fixed-effects part of the model.

```
   numDF denDF   F-value p-value
c1     1    49  92.43109  <.0001
c2     1    49  75.26411  <.0001
c3     1    49  32.36087  <.0001
c4     1    49  20.42553  <.0001
c5     1   254 263.24762  <.0001
h      1   254  10.46949  0.0014
s1     1   254   3.15343  0.0770
s2     1   254   8.02611  0.0050
```

- This information can also be shown by **`summary(model)`**.

(11) **qqnorm(**`model, abline=c(0,1)`**)**: shows the normal Q-Q plot for intra-event errors used to check the distributional assumption on the intra-event errors. The example normal Q-Q plot is shown in Figure A3-3.

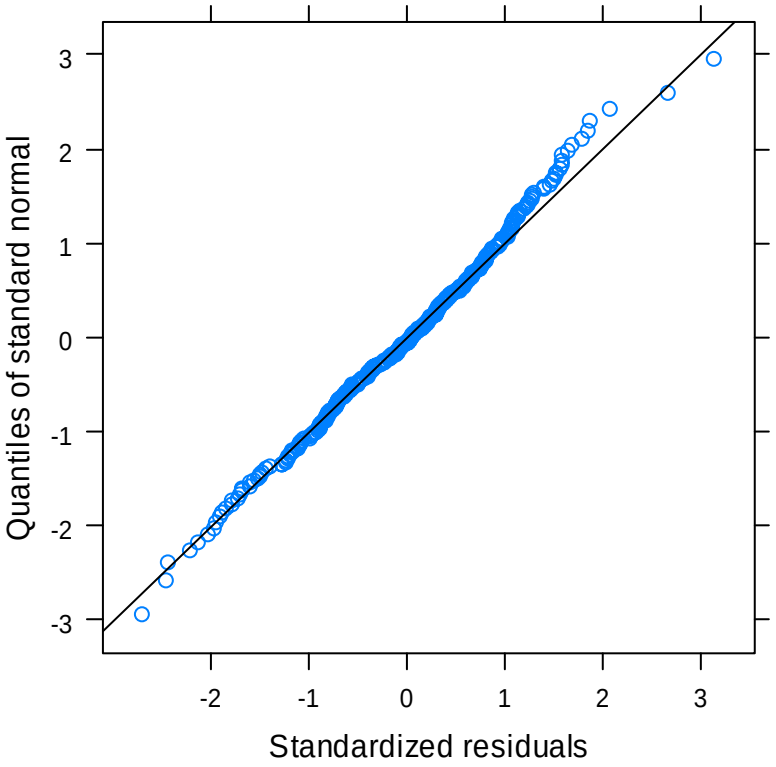

Figure A3-3. Normal Q-Q plot for intra-event errors.

- The data distribution in Figure A3-3 appears to be normally distributed.

(12) **qqnorm(**`model,~ranef(.,level=1)`**)**: shows the normal Q-Q plot for random-effects, which can be used to assess the distributional assumption on random effects. The example normal Q-Q plot is shown in Figure A3-4.

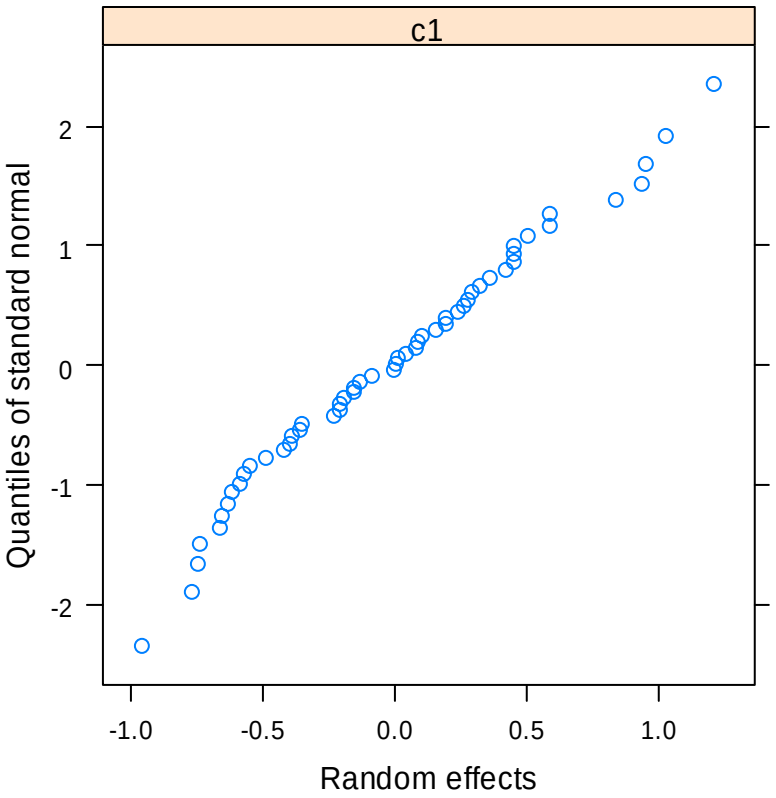

Figure A3-4. Normal Q-Q plot for random-effects.

(13) **`plot(`**`logAIa, `**`predict(`**`model, level=0:1)[,2], asp=1)`**

`abline(``0, 1)`**: shows a comparison plot of the observed data and predicted values. logAIa is the variable name for the observed values to be plotted on the x-axis in this example. **`predict(`**`model, level=0:1)[,2]` is a command code for the predicted values with the random-effects coefficient for all events [See (5) **`predict(`**`model, level=0:1)`** above]. `asp` is an argument for the aspect ratio of y/x-axes. In this example, the ratio is set as 1. Lastly, **`abline(`**`0, 1)`** is for drawing a straight line having the y-interception of 0 and the slope of 1. The example comparison plot for this example is shown in Figure A3-5.

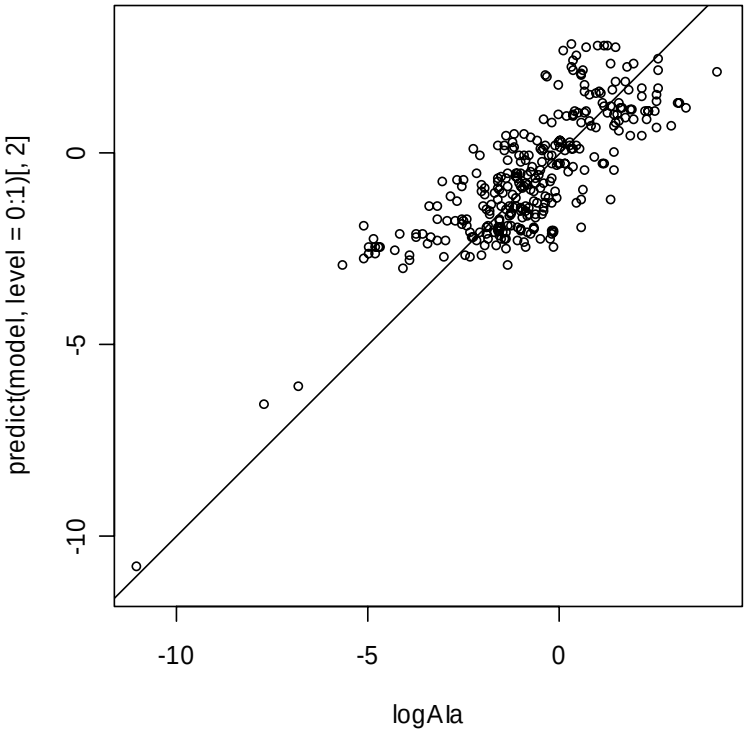

Figure A3-5. Predicted values versus observed data.

A3.2. Other Useful R-functions

(1) **hist(**logAIa**)**: plots a histogram for logAIa data as shown in Figure A3-6.

```
> hist(logAIa, br = c(-12:5), col='lightblue')
```

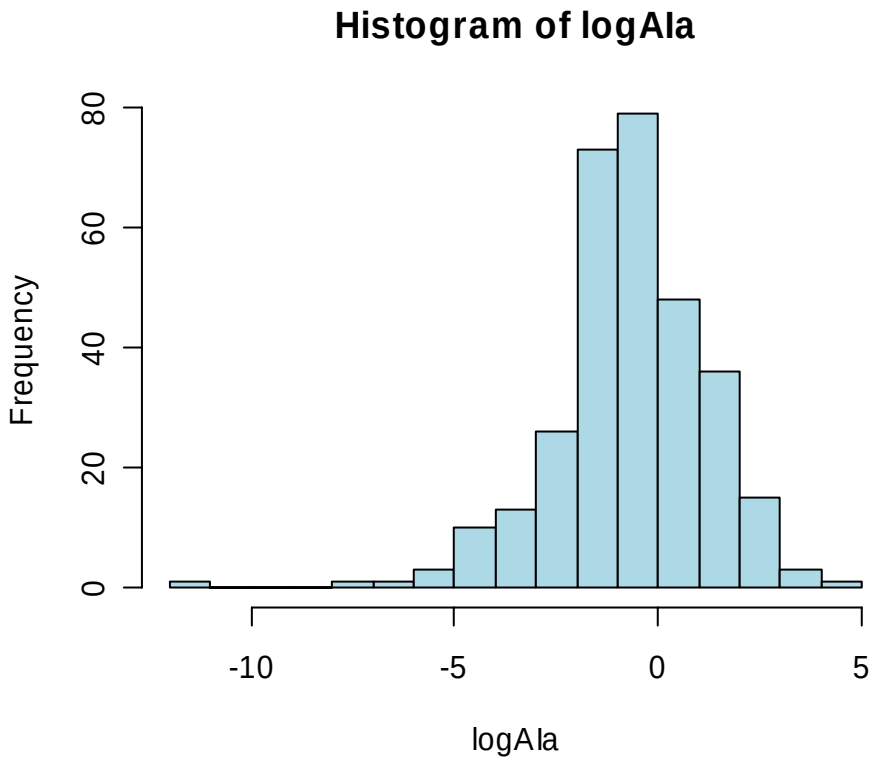

Figure A3-6. A histogram for logAIa data.

(2) **mean(**logAIa <= -5**)**: computes the probability that the logAIa data is less than or equal to -5.

```
> mean(logAIa<= -5)
[1] 0.019354847   # i.e., 1.9% probability
```

- Note that the probability value is computed by the ratio of the number of logAIa data less than or equal to -5 and the total population.

(3) `R_n5 = R[logAIa <= -5]`: using the brackets **`[ ]`**, one can sort data meeting specified criteria. In this example, site-to-source distances (R) corresponding to logAIa data that is less than or equal to -5 will be sorted into a new variable, R_n5.

- Put the brackets **`[ ]`** next to a variable which you want to sort according to the condition/conditions specified in the **`[ ]`**.

Ex. a) `R[R>=25 && R<100]  ## R values smaller than 100 and greater than or equal to 25.`

Ex. b) `R[M>6.5]  ## R whose corresponding M (magnitude) is greater than 6.5.`

(4) **`range(`**`logAIa`**`)`**: returns the minimum and maximum values.

```
> range(logAIa)
[1] -11.013876   4.153355
```

(5) **`quantile(`**`logAIa`**`)`**: returns the quantiles.

```
> quantile(logAIa)
       0%         25%         50%         75%        100%
-11.0138760  -1.5643995  -0.7297255  0.4696963  4.1533550
```

References

Gelman, A., and Hill, J. (2007). *Data analysis using regression and multilevel/hierarchical models*, Cambridge University Press, New York.

Pinheiro, J. C., and Bates, D. M. (2000). *Mixed-effects models in S and S-PLUS*, Springer, New York.

Program-R. (version 2.5.0). "A language and environment for statistical computing and graphics: http://www.r-project.org/."

Chapter 4

Frequency Content Parameters

4.1 Background

Frequency content is an important characteristic of earthquake ground motions for seismic design. This is because the dynamic response of geotechnical and structural systems are significantly dependent on the frequency content of earthquake motions (e.g., Green and Cameron, 2003; Rathje et al., 2004). For example, if the characteristic period of an earthquake ground motion coincides with the natural frequency of a structure, the structure can have severe damage due to resonant response. Earthquake motions are comprised of a range of frequencies, and a "characteristic frequency" is difficult to define. Consequently, numerous definitions have been proposed to quantify the most representative period of earthquake ground motions. Of the various definitions of the characteristic periods, considered herein are predominant spectral period (T_p), smoothed spectral predominant period (T_0), average spectral period (T_{avg}), mean period (T_m), and spectral velocity-acceleration ratio periods ($T_{V/A50}$ and $T_{V/A84}$).

The T_p, T_0, and T_{avg} are based on a pseudo acceleration spectrum of a ground acceleration time history. A pseudo acceleration spectrum is a plot of the maximum absolute acceleration responses of similarly damped, elastic single-degree-of-freedom (SDOF)

oscillators subjected to a base excitation (e.g., earthquake motion). The maximum responses are plotted as a function of the natural period T_n (or T) of the oscillator. An example pseudo acceleration spectrum is shown in Figure 4-1. The underlying idea of using the response spectra for defining characteristic periods is that the natural period T_n of the oscillator having the largest spectral acceleration (i.e., predominant spectral period, T_p) corresponds to the representative period of the ground motion.

The predominant spectral period (T_p) was commonly used by many engineers (e.g., Seed et al., 1969) but it was found to have considerable defects: inconsistency in the estimated periods between comparable ground motions and disregard of the frequency content around the peak spectral acceleration (Rathje et al., 1998; Rathje et al., 2004). As a result, Rathje et al. (1998) proposed the smoothed spectral predominant period (T_o) that utilizes a "smoothed" pseudo acceleration spectrum.

On the other hand, the mean period (T_m), also proposed by Rathje et al. (1998), utilizes the Fourier amplitude spectrum that is a more direct representation of the frequency content of ground motions. Fourier amplitudes are the absolute values of the complex numbers (i.e., square-root of the sum of the squared real and imaginary parts) obtained from computing the Fourier transform of an acceleration time history. The Fourier amplitudes are plotted versus frequency on log scales for both axes, this is called, the Fourier amplitude spectrum. This spectrum allows a direct comparison of the magnitudes of amplitudes at a range of frequencies.

The spectral velocity-acceleration ratio period ($T_{V/A50}$ and $T_{V/A84}$) is the period at the intersection of the constant spectral velocity and acceleration regions of design spectrum (see Figure 4-5 and the section 4.2.1.5 for examples of design spectra plotted on tripartite paper). This definition has been employed as the characteristic periods of ground motions for engineering design (Shimazaki and Sozen, 1984; Green and Cameron, 2003) based on its good-correlation with the parameter of interest.

Forward-directivity affects characteristic periods of near-fault motions, which may occur in motions recorded within about 20 km from a fault (Bray and Rodriguez-Marek, 2004). Generally, the forward-directivity effects occur in the near-fault regions when a fault rupture front propagates toward the site at which ground motions are recorded and involves overlapping of wave pulses. Consequently, near-fault ground motions having forward-directivity effects tend to have longer periods than motions at comparable distances that do not have directivity effects. This trend was observed both in the CEUS and WUS motion data used in this study. However, due to the limited number of data in the close distance bins (i.e., R0-10 km), forward-directivity effects cannot be independently considered in regression analyses. Furthermore, the majority of the CEUS motion data are not actually recorded motions and no studies have been made for validating the scaled CEUS motions regarding the forward-directivity effects. In this context, this study focuses on developing the empirical relations best representing all the characteristic period data without separating out the forward-directivity motions. This was achieved by using two different models for a regression analysis: a near-field model and a far-field model. Assuming that the former and latter are forward-directivity

dependent and forward-directivity independent, respectively, only the latter is considered in comparison studies.

As for the organization of the chapter, the various definitions of the characteristic periods are reviewed first. The proposed functional forms of the predictive relationships are introduced along with the backgrounds supporting the models. Then, the NLME regression results are presented and comparisons of trends in the results are described, including comparisons of CEUS rock vs. soil motions and CEUS vs. WUS motions. Also, both the CEUS and WUS relations are compared to existing relationships (Rathje et al., 1998; Rathje et al., 2004), and the findings are described and discussed. Finally, a conclusion section summarizes major findings from this study.

4.2 Characteristic Periods

4.2.1 Definitions

4.2.1.1 Predominant Spectral Period: T_p

For a given ground motion recording, the predominant spectral period (T_p) is defined as the period corresponding to the maximum pseudo spectral acceleration (PSA) of the motion. Figure 4-1 shows the predominant spectral period (T_p) determination for a 5% damped pseudo acceleration spectrum of a ground motion recording from the 1989 Loma Prieta earthquake. The predominant spectral period will vary with the damping ratio (ξ) used for construction of the response spectra. This study only considers the pseudo

acceleration spectra having $\xi = 5\%$, since this ratio is most commonly used in engineering practice.

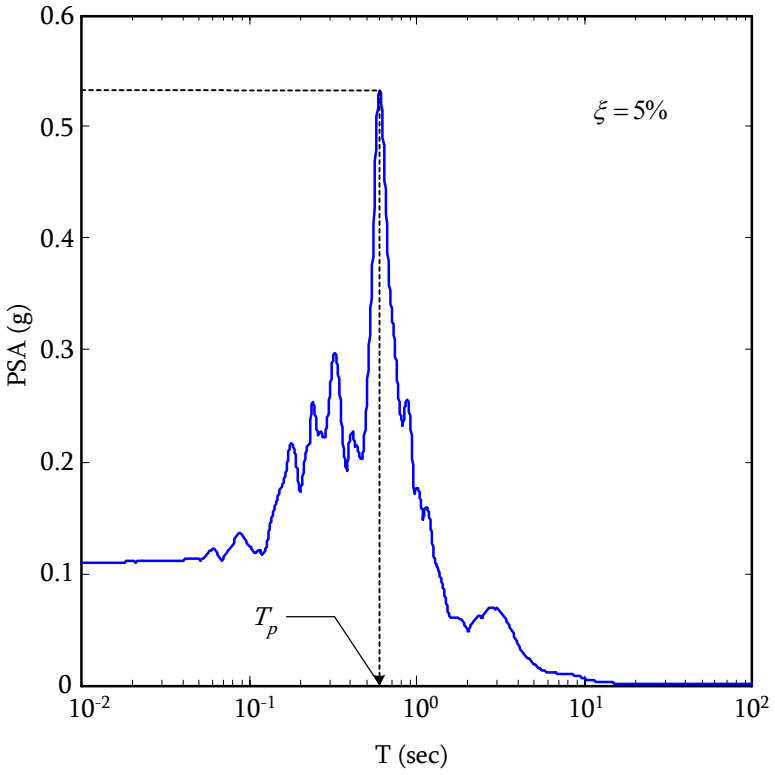

Figure 4-1. Determination of predominant spectral period from the pseudo acceleration spectrum (damping ratio $\xi = 5\%$) for the acceleration time history (BES090: M6.9; R49.9km) from the 1989 Loma Prieta earthquake.

4.2.1.2 Smoothed spectral predominant period: T_0

As described previously, the predominant spectral period (T_p) is solely based on the peak pseudo spectral acceleration without considering the frequency content around the peak. Furthermore, T_p was found to have relatively large variations even between comparable ground motions (Rathje et al., 1998). As such, Rathje et al. (1998) proposed a "smoothed

spectral predominant period" (T_o), which is determined by using the 5% damped pseudo acceleration spectra normalized by the peak ground acceleration. T_o is defined as:

$$T_0 = \frac{\sum_i T_i \cdot \ln\left(\frac{PSA(T_i)}{pga}\right)}{\sum_i \ln\left(\frac{PSA(T_i)}{pga}\right)} \quad \text{for } T_i \text{ with } \frac{PSA}{pga} \geq 1.2,\ \Delta \log T_i \leq 0.02 \qquad \text{(Eq. 4-1)}$$

where: $PSA(T_i)$ is the 5% damped pseudo spectral acceleration at T_i; and pga is the peak ground acceleration. In computing T_o, PSA are computed for oscillators having natural periods that are equally spaced on a log scale (i.e., $\Delta \log T_i$). Essentially, Eq. 4-1 results in a "smoothing" of the normalized pseudo spectral acceleration response greater than or equal to 1.2. Thus, the resulting value has a period similar to the predominant spectral period (T_p). However, Rathje et al. (1998) showed that based on their empirical relations, T_0 can be predicted with more certainty than T_p. Figure 4-2 shows an example of a normalized pseudo acceleration spectrum along with the minimum value of the normalized spectrum considered in the period determination.

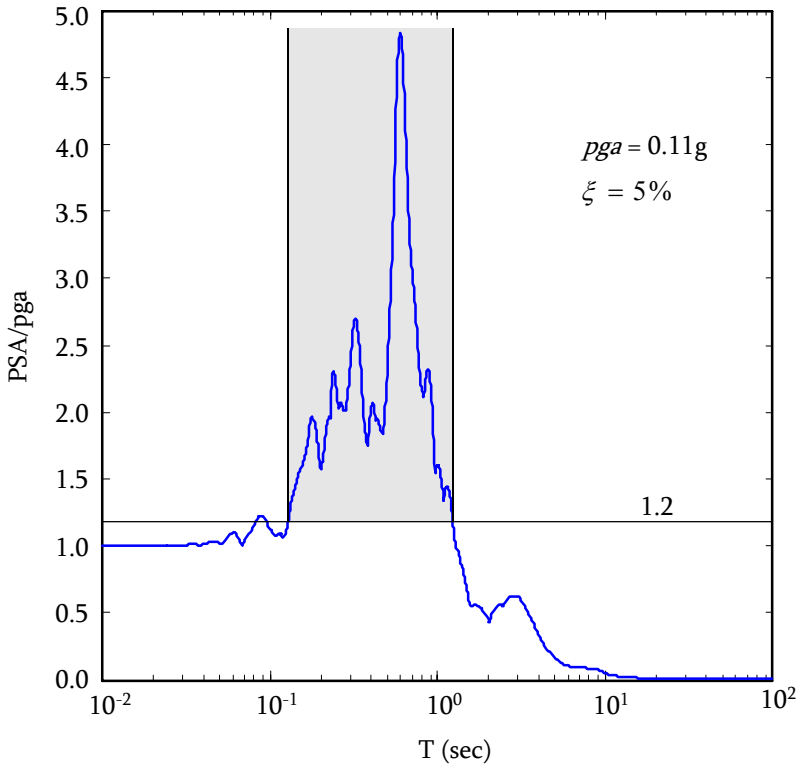

Figure 4-2. Example of normalized pseudo spectral acceleration spectrum (damping ratio $\xi = 5\%$) and the range considered in computation of T_0 (shown in gray background) for the acceleration time history (BES090: M6.9; R49.9km) from the 1989 Loma Prieta earthquake.

4.2.1.3 Average Spectral Period: T_{avg}

Similar in concept to the smoothed spectral predominant period, Rathje et al. (2004) proposed the average spectral period (T_{avg}), which is also computed from the normalized pseudo spectral acceleration response spectrum:

$$T_{avg} = \frac{\sum_i T_i \cdot \left(\frac{PSA(T_i)}{pga} \right)^2}{\sum_i \left(\frac{PSA(T_i)}{pga} \right)^2} \quad \text{for } 0.05 \text{ sec} \le T_i \le 4 \text{ sec}, \text{ with } \Delta T \le 0.05 \text{ sec} \quad \text{(Eq. 4-2)}$$

where: PSA_i is the 5% damped pseudo spectral acceleration at T_i; T_i is the discrete period; and ΔT is the period interval. As may be surmised from Eq. 4-2, T_{avg} is a weighted

average of period, with the weighting based on the squared pseudo spectral acceleration amplitude over the period range of 0.05 to 4.0 sec. Figure 4-3 shows an example of a normalized pseudo acceleration spectrum along with the period range over which T_{avg} is computed.

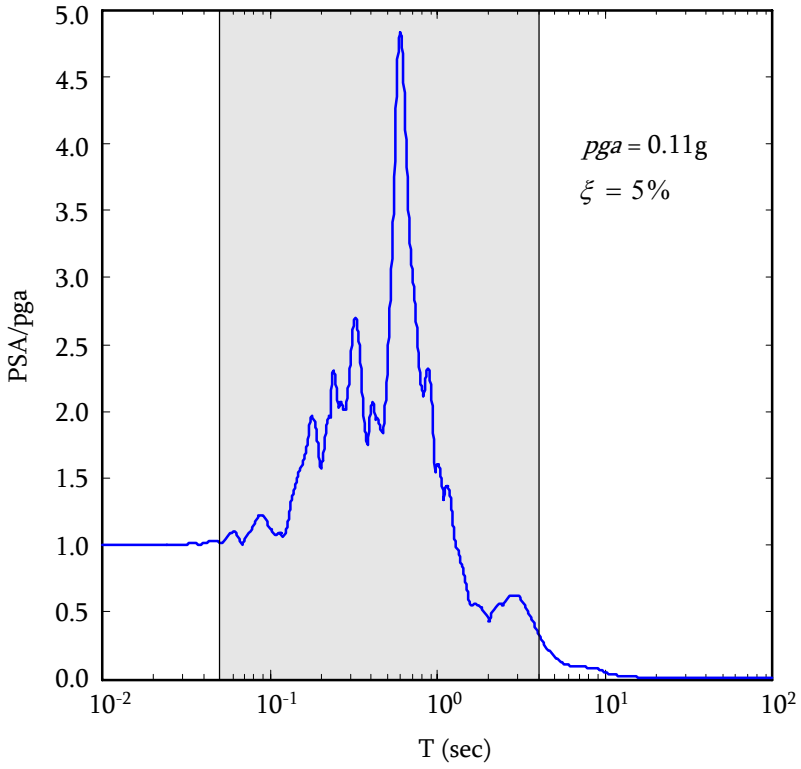

Figure 4-3. Example of normalized pseudo spectral acceleration spectrum (damping ratio $\xi = 5\%$) and the period range considered in computation of T_{avg} (shown in gray background) for the acceleration time history (BES090: M6.9; R49.9km) from the 1989 Loma Prieta earthquake.

4.2.1.4 Mean Period: T_m

The mean period (T_m) is computed from the Fourier amplitude spectrum of an acceleration time history by the following equation (Rathje et al., 1998):

$$T_m = \frac{\sum_i FA_i^2 (1/f_i)}{\sum_i FA_i^2} \quad \text{for } 0.25\ Hz \le f_i \le 20\ Hz\ , \text{ with } \Delta f \le 0.05\ Hz \qquad \text{(Eq. 4-3)}$$

where: FA_i is the Fourier amplitude; f_i is the discrete frequency corresponding to the FA_i; and Δf is the frequency interval. Figure 4-4 shows an example of the Fourier amplitude spectrum for an earthquake motion and the frequency range over which T_m is computed. Similar to Eq. 4-2 for T_{avg}, Eq. 4-3 also computes the weighted average of the period (i.e., $1 / f_i$ in Eq. 4-3), with the weighting based on the squared Fourier amplitudes over the range of frequency. The period ranges considered in computing T_m and T_{avg} are identical.

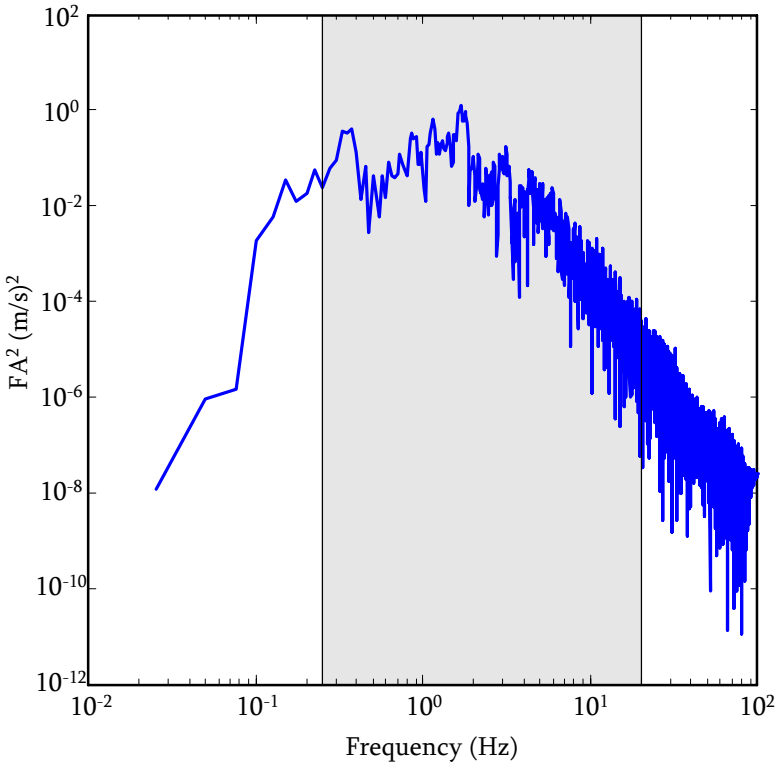

Figure 4-4. Example of squared Fourier amplitude and the frequency range considered in computation of T_m (shown in gray background) for the acceleration time history (BES090: M6.9; R49.9km) from the 1989 Loma Prieta earthquake.

4.2.1.5 Spectral Velocity-Acceleration Ratio Periods: $T_{V/A50}$ and $T_{V/A84}$

The definition of the spectral velocity-acceleration ratio period ($T_{V/A}$: $T_{V/A50}$ and $T_{V/A84}$) is given by:

$$T_{\mathrm{V/A}} = 2\pi \cdot \frac{pgv}{pga} \cdot \frac{\alpha_V(\xi = 5\%)}{\alpha_A(\xi = 5\%)} \qquad \text{(Eq. 4-4)}$$

where: *pgv* and *pga* are the peak ground velocity and acceleration, respectively; α_V and α_A are the amplification factors, which are functions of the damping ratio (ξ); $T_{V/A}$ is based on $\xi = 5\%$.

The amplification factors were developed by Newmark and Hall (1982) and are the ratio of spectral responses to peak ground motion parameters (i.e., *pga*, *pgv*, and peak ground displacement (*pgd*)). These factors are used to construct the Newmark and Hall (1982) design spectra (i.e., starting with the peak ground motion parameters, the spectral values are obtained by multiplying the peak parameters by the appropriate amplification factors). Newmark and Hall (1982) used a tripartite plot for design spectra that shows all the spectral responses in terms of period (i.e., the natural periods of the oscillators) – the pseudo spectral velocity *PSV* and the periods *T* are on the vertical axis and the horizontal axis, respectively; the pseudo spectral acceleration *PSA* and the spectral displacement *SD* are on the axes at 135 degrees and 45 degrees to the horizontal axis, respectively. Figure 4-5 shows an example of a tripartite plot for the response spectrum of an earthquake ground motion. The response spectra on tripartite plots consist of the three regions over which one of the spectral responses tends to remain constant: the constant spectral displacement region at relatively long periods; the constant spectral acceleration region at

relatively short periods; and the constant spectral velocity region at intermediate periods (Green and Cameron, 2003). For each region, Newmark and Hall (1982) developed the empirical relationships for the amplification factors as a function of the damping ratio. The amplification factors are denoted as α_A, α_V, and α_D for the constant spectral acceleration, velocity, and displacement regions, respectively. As an example, Figure 4-5 shows the two design spectra constructed by using the Newmark and Hall (1982) relations: one is based on the medians (i.e., 50% percentile) of the amplification factors; and the other is based on the median plus one standard deviation (σ) (i.e., 84.1% percentile) of the amplification factors. The peak ground motion parameters used are from a ground motion recording from the 1989 Loma Prieta earthquake: *pga* = 0.11g, *pgv* = 0.162 m/sec, and *pgd* = 0.057 m.

Herein, the $T_{V/A}$ periods based on the median and the median plus σ of amplification factor are designated by $T_{V/A50}$ and $T_{V/A84}$, respectively. As shown in Figure 4-5, the $T_{V/A}$ indicates the period at which the constant-velocity and -acceleration regions intersect.

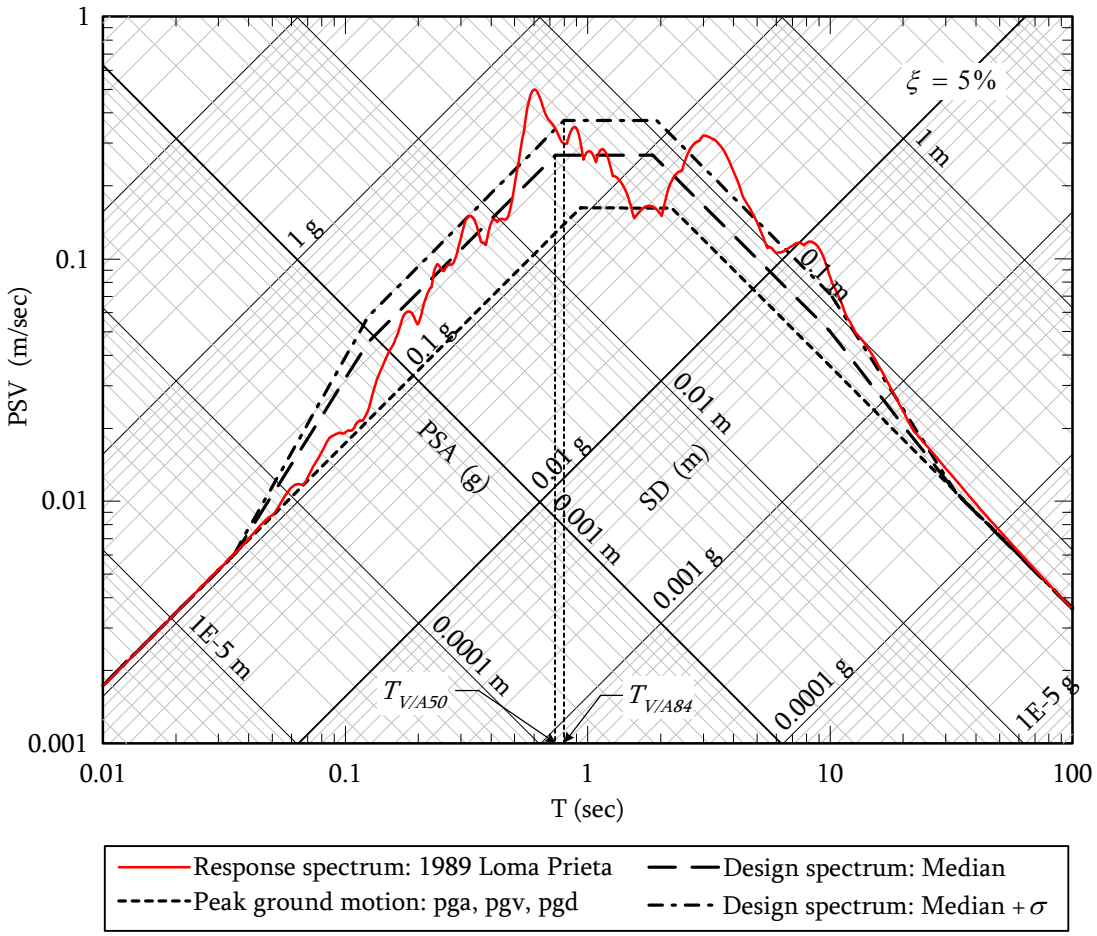

Figure 4-5. Example tripartite plot of design spectrum by Newmark and Hall (1982) relations for amplification factors and actual response spectrum of a ground acceleration time history (BES090: M6.9; R49.9km) from the 1989 Loma Prieta earthquake.

The spectral velocity-acceleration ratio periods can be physically interpreted as the natural period of simple harmonic responses (e.g., a sine wave) of elastic SDOF oscillators since the natural period of a harmonic motion can be expressed with the ratio of the maximum velocity to the maximum acceleration. For the derivation of the natural period of a harmonic motion, let's consider a simple sinusoidal motion for displacement $d(t)$ with a frequency of ω and the maximum amplitude of unity:

$$d(t) = \sin(\omega \cdot t) \qquad \text{(Eq. 4-5)}$$

where: ω is the angular frequency (i.e., $2\pi f$, where f is the frequency) of motion; t is time. The velocity $v(t)$ and acceleration $a(t)$ of the sinusoidal motion can be obtained by taking the first and second derivatives, respectively of the displacement $d(t)$ with respect to time:

$$v(t) = \omega \cos(\omega \cdot t) \quad \text{(Eq. 4-6)}$$

$$a(t) = -\omega^2 \sin(\omega \cdot t) \quad \text{(Eq. 4-7)}$$

Then, the ratio of the maximum velocity v_{max} to acceleration a_{max} is written as:

$$\frac{v_{\max}}{a_{\max}} = \frac{\omega}{\omega^2} = \frac{1}{\omega} = \frac{1}{2\pi \cdot f} \quad \text{(Eq. 4-8)}$$

Thus, the period T of harmonic motion is given by:

$$T = 2\pi \cdot \frac{v_{\max}}{a_{\max}} \quad \text{(Eq. 4-9)}$$

For earthquake ground motions, the peak ground velocity and acceleration (i.e., *pgv* and *pga*) are the maximum velocity and acceleration, respectively. Extending the concept to the spectral responses, the spectral velocity-acceleration ratio periods can be interpreted as the natural period of simple harmonic responses of elastic SDOF oscillators having peak amplitudes of $pga \times \alpha_A$ and $pgv \times \alpha_V$.

In this study, the amplification factor relations developed by Cameron (2009) were used instead of the Newmark and Hall (1982) relations. This was because the Newmark and Hall relations were based on limited ground motion data, while Cameron developed her relations using the ground motion data set discussed in Chapter 2 of this thesis. Also, Cameron's relations were developed for each magnitude and distance range, site condition (i.e., rock and soil), and tectonic regime (i.e., CEUS and WUS). Cameron's

relations for the amplitude factors are shown in Eq. 4-10 and the coefficients for CEUS and WUS are tabulated in Table 4-1 and Table 4-2, respectively.

$$\alpha_V \text{ or } \alpha_A = c_1 - c_2 \ln(\xi) \qquad \text{(Eq. 4-10)}$$

where: c_1 and c_2 are the regression coefficients; ξ is the damping ratio of the SDOF oscillator in percent. Again, in this study, a damping ratio of 5% was used for computing the amplification factors.

Table 4-1. Coefficients for amplification factors for CEUS (Cameron, 2009).

Site			Rock				Soil			
Mag. Range	Dist. Range (km)	α	Median (50th percentile)		Median + σ (84th percentile)		Median (50th percentile)		Median + σ (84th percentile)	
			c_1	c_2	c_1	c_2	c_1	c_2	c_1	c_2
5-6	0-50	V	2.131	0.397	3.738	0.789	2.380	0.443	3.781	0.799
		A	2.989	0.660	4.156	1.002	3.497	0.738	5.142	1.228
	50-100	V	2.880	0.616	5.540	1.374	3.404	0.740	5.178	1.229
		A	3.748	0.900	6.010	1.605	3.563	0.799	5.198	1.279
6-7	0-10	V	1.793	0.310	2.904	0.553	1.996	0.341	3.161	0.611
		A	2.492	0.499	3.492	0.757	2.967	0.588	4.326	0.962
	10-50	V	1.960	0.390	3.198	0.677	2.572	0.533	4.019	0.907
		A	3.140	0.725	4.651	1.181	3.694	0.832	5.542	1.372
	50-100	V	3.014	0.669	4.567	1.107	3.018	0.655	4.686	1.104
		A	3.297	0.821	4.406	1.168	3.137	0.687	4.750	1.147
	100-200	V	2.355	0.521	3.824	0.905	3.187	0.738	4.940	1.204
		A	3.281	0.797	4.355	1.110	3.518	0.837	4.999	1.268
7+	0-10	V	1.376	0.259	2.484	0.509	1.964	0.355	2.941	0.565
		A	3.175	0.716	4.656	1.195	3.024	0.619	4.523	1.065
	10-50	V	1.578	0.310	2.737	0.562	2.352	0.464	3.645	0.779
		A	3.224	0.759	4.491	1.144	3.425	0.769	4.880	1.181
	50-100	V	2.007	0.436	3.317	0.785	2.806	0.617	4.336	1.045
		A	3.367	0.841	4.773	1.273	3.531	0.821	4.895	1.227
	100-200	V	2.274	0.462	3.440	0.761	3.293	0.741	4.919	1.191
		A	2.707	0.687	3.585	0.942	3.074	0.736	4.309	1.094

Table 4-2. Coefficients for amplification factors for WUS (Cameron, 2009).

Site			Rock				Soil			
Mag. Range	Dist. Range (km)	α	Median (50^{th} percentile)		Median + σ (84^{th} percentile)		Median (50^{th} percentile)		Median + σ (84^{th} percentile)	
			c_1	c_2	c_1	c_2	c_1	c_2	c_1	c_2
5-6	0-50	V	2.528	0.473	4.004	0.838	2.383	0.426	3.812	0.791
		A	3.527	0.676	5.891	1.347	3.337	0.650	4.923	1.117
	50-100	V	2.678	0.551	4.592	1.077	3.521	0.751	5.427	1.287
		A	3.953	0.876	6.133	1.540	3.704	0.778	5.373	1.267
6-7	0-10	V	2.257	0.399	3.607	0.723	1.746	0.292	2.970	0.573
		A	2.757	0.510	4.097	0.851	3.238	0.636	4.800	1.084
	10-50	V	2.256	0.444	3.763	0.827	2.391	0.484	3.841	0.849
		A	3.248	0.664	4.848	1.106	3.764	0.812	5.521	1.341
	50-100	V	3.191	0.700	4.904	1.198	2.782	0.593	4.292	0.999
		A	4.422	1.021	6.291	1.614	3.541	0.733	5.797	1.371
	100-200	V	2.199	0.471	3.721	0.859	3.081	0.706	5.120	1.249
		A	4.548	1.061	6.558	1.701	3.740	0.837	5.481	1.355
7+	0-10	V	1.711	0.298	2.969	0.575	1.685	0.289	2.684	0.506
		A	2.962	0.600	4.680	1.086	3.101	0.617	4.596	1.067
	10-50	V	1.461	0.261	2.733	0.537	2.097	0.401	3.341	0.713
		A	3.308	0.681	5.180	1.218	3.646	0.793	5.282	1.263
	50-100	V	1.827	0.375	3.106	0.708	2.648	0.568	4.332	1.036
		A	4.101	0.978	6.168	1.624	3.672	0.836	5.547	1.380
	100-200	V	2.361	0.459	3.840	0.839	2.954	0.637	4.697	1.104
		A	3.526	0.772	5.081	1.255	3.594	0.791	5.308	1.307

4.2.2 Proposed Model

The functional form of the predictive relationship for characteristic periods used in this study were modified from those developed by Rathje et al. (2004). Rathje et al. used Brune's point source model (see Chapter 2) identifying earthquake magnitude and distance dependences of the mean period (T_m), which is computed from the Fourier amplitude spectrum. Accordingly, Rathje et al. derived a theoretical relationship by substituting the smoothed Fourier amplitude spectra computed using Brune's point source model for the Fourier amplitude of actual ground motions in the equation for mean period

(i.e., Eq. 4-3). The resulting theoretical model showed that the natural log of the mean period was linearly related with distance and non-linearly related with earthquake magnitude. Rathje et al. (2004) simplified the magnitude dependence with a linear relationship up to M7.25 and a constant relationship for larger magnitudes. Note that the theoretical model does not account for the near-fault effects such as the forward-directivity.

Based on the trends observed from the data used in this study, however, a non-linear dependence on earthquake magnitude was not clearly observed. Moreover, from the regression analyses of the data set used in this study, a linear model for the magnitude dependence produced better fits than non-linear models. Consequently, a linear relationship was used for the earthquake magnitude dependence of the natural log of mean period (T_m). Also, the proposed relationship was found to be suitable for the other characteristic periods based on the resulting total standard deviations.

The strong ground motion data set used in this study includes considerable ground motion recordings with forward-directivity effects. A total of 64 horizontal ground motions in the data set for WUS, mostly in the distance bin R0-10 km for large magnitudes (i.e., M6-7 and M7+), had forward-directivity effects per Bray and Rodriguez-Marek (2004). As a result, a single linear relationship for the distance dependence cannot be used for the entire distance range. Rather, it is desirable to perform the two separate regression analyses with two different models for distance: one regression without the forward-directivity motions and the other only with the forward-

directivity motions. However, this was not feasible because excluding the motions with forward-directivity effects caused unreliable statistical results due to insufficient data population in the R0-10 km distance bins for large magnitudes (i.e., M6-7 and M7+). Thus, all the data were fitted by two separate models for near- and far-fields that included a distance cut-off through a NLME regression analysis for both CEUS and WUS. The near-field model includes a functional term representing the forward-directivity effects.

Additionally, it was observed that for most of the characteristic period definitions, the earthquake magnitude and distance dependences vary with local site conditions. In this regard, the terms accounting for their dependences coupled with local site conditions were added into the model proposed in this study. After performing numerous regression analyses with various functional forms, the predictive relationship best representing the characteristic period data for horizontal ground motions was determined as:

$$\ln T_{char} = \begin{cases} C_1 + C_2(M-6) + C_3 R + [S_1 + S_2(M-6) + S_3 R]S_S & \text{for } R \geq R_C \\ C_1 + C_2(M-6) + C_3 R + C_4 \ln(R/R_C) + [S_1 + S_2(M-6) + S_3 R]S_S & \text{for } R < R_C \end{cases} \quad \text{(Eq. 4-11)}$$

where: T_{char} is the characteristic periods in seconds (i.e., T_p; T_0; T_{avg}; T_m; $T_{V/A50}$; and $T_{V/A84}$); C_1 through C_4 and S_1 through S_3 are regression coefficients; M is moment magnitude; R is the closest distance to the fault rupture plane (km); R_C is the distance cut-off (km); and S_S is a binary number representing local site conditions: $S_S = 0$ for rock sites, $S_S = 1$ for soil sites. The distance cut-off of 20 km was used for WUS motions but for CEUS motions, 25 km was used since it produced a better fit.

Since the forward-directivity effects are included in the near-field predictive relationship (i.e., for $R < R_C$), it overestimates the characteristic periods of near-field motions that do not have forward-directivity effects. However, based on the linear relationship for the distance dependence (Rathje et al., 2004) theoretically established for the mean periods, the far-field model (i.e., for $R \geq R_C$) can be extended to estimate the characteristic periods for the non-forward-directivity motions in the near-field region. Consequently, the far-field predictive relationship can be used to estimate the characteristic period of motions for $R \geq R_C$ where the motions do not have near-fault effects. Accordingly, the characteristic period model proposed in this study is shown below:

$$\ln T_{char} = \begin{cases} C_1 + C_2(M-6) + C_3 R + [S_1 + S_2(M-6) + S_3 R]S_S \\ \qquad \text{for non-forward-directivity} \\ C_1 + C_2(M-6) + C_3 R + C_4 \ln(R/R_C) + [S_1 + S_2(M-6) + S_3 R]S_S \\ \qquad \text{for forward-directivity with } R < R_C \end{cases} \quad \text{(Eq. 4-12)}$$

where all the definitions of the coefficients and parameters are the same as in Eq. 4-11. It should be noted that the proposed model for forward-directivity motions may underestimate the characteristic periods of these motions because the ground motion data used in regressions include non-forward-directivity motions too. Especially for the CEUS, the model for forward-directivity motions may not be valid because most of the CEUS motion data are not recorded motions (i.e., no information of fault locations and sites is available) and no studies have been made for validating the scaled CEUS motions for the forward-directivity effects.

4.2.3 Regression Results

The results of the NLME regression analyses for T_p, T_0, T_{avg}, T_m, $T_{V/A50}$, and $T_{V/A84}$ are listed in Table 4-3 both for CEUS and WUS. Included in this table are the regression coefficients, p-values, and standard deviations. Although several coefficients turned out to be statistically insignificant based on p-values greater than 5 % (i.e., 0.05), it was decided to keep them in the proposed model to achieve lower total standard deviations. Comparing the total standard deviations of CEUS and WUS, they are comparable for most of the characteristic periods, except for the predominant spectral period (T_p). Also, in comparisons of the total standard deviations among the different characteristic periods, the predominant spectral period (T_p) showed significantly larger deviations than the others, which indicates the predominant spectral period (T_p) has the largest uncertainty in its prediction, which is consistent with the findings of Rathje et al. (2004).

Table 4-3. Regression coefficients; their p-values (in parentheses); and standard deviations of inter-event, intra-event, and total errors.

CEUS										
T_{char}	C_1	C_2	C_3	C_4	S_1	S_2	S_3	τ_{ln}	σ_{ln}	$\sigma_{ln\ total}$
T_p	-2.95 (0.000)	-0.11 (0.078)	0.0012 (0.243)	-0.016 (0.636)	1.13 (0.000)	0.66 (0.000)	-0.00051 (0.660)	0.09	0.63	0.64
T_0	-2.59 (0.000)	0.043 (0.386)	0.002 (0.000)	-0.005 (0.813)	0.85 (0.000)	0.46 (0.000)	-0.0027 (0.000)	0.18	0.33	0.38
T_{avg}	-1.37 (0.000)	0.47 (0.000)	0.0034 (0.000)	-0.13 (0.000)	0.32 (0.000)	0.074 (0.117)	-0.0029 (0.000)	0.22	0.36	0.42
T_m	-1.65 (0.000)	0.33 (0.000)	0.0026 (0.000)	-0.14 (0.000)	0.42 (0.000)	0.16 (0.000)	-0.0025 (0.000)	0.25	0.36	0.44
T_{TV50}	-2.20 (0.000)	0.24 (0.000)	0.0062 (0.000)	-0.11 (0.000)	0.71 (0.000)	0.30 (0.000)	-0.0043 (0.000)	0.24	0.42	0.48
T_{TV84}	-1.99 (0.000)	0.25 (0.000)	0.0055 (0.000)	-0.10 (0.000)	0.57 (0.000)	0.29 (0.000)	-0.0037 (0.000)	0.24	0.42	0.48
WUS										
T_{char}	C_1	C_2	C_3	C_4	S_1	S_2	S_3	τ_{ln}	σ_{ln}	$\sigma_{ln\ total}$
T_p	-1.67 (0.000)	0.18 (0.019)	0.0032 (0.000)	-0.11 (0.000)	-0.022 (0.783)	0.22 (0.000)	0.00082 (0.414)	0.23	0.51	0.56
T_0	-1.67 (0.000)	0.22 (0.000)	0.0047 (0.000)	-0.097 (0.000)	0.14 (0.012)	0.17 (0.000)	-0.0012 (0.101)	0.20	0.36	0.41
T_{avg}	-1.03 (0.000)	0.40 (0.000)	0.0034 (0.000)	-0.11 (0.000)	0.23 (0.000)	0.091 (0.028)	-0.0021 (0.000)	0.19	0.32	0.37
T_m	-1.17 (0.000)	0.27 (0.000)	0.0037 (0.000)	-0.12 (0.000)	0.24 (0.000)	0.12 (0.011)	-0.0016 (0.017)	0.22	0.34	0.40
T_{TV50}	-1.50 (0.000)	0.30 (0.000)	0.0040 (0.000)	-0.15 (0.000)	0.23 (0.000)	0.13 (0.018)	-0.00038 (0.651)	0.20	0.43	0.47
T_{TV84}	-1.43 (0.000)	0.37 (0.000)	0.0042 (0.000)	-0.15 (0.000)	0.25 (0.000)	0.090 (0.099)	-0.00065 (0.434)	0.20	0.43	0.47

The distributional assumptions for intra-event errors and random-effects were assessed by the normal Q-Q plots shown in Figure 4-6 through Figure 4-10 for T_p, T_0, T_{avg}, T_m, and $T_{V/A50}$, respectively; the normal Q-Q plots for $T_{V/A84}$ was omitted since they were similar to those for $T_{V/A50}$. For all the characteristic periods, it seems plausible that the overall distributions of both intra-event errors and random-effects follow normal distributions.

Additionally, the scatter plots for intra-event errors and random-effects are shown in Figure 4-11 through Figure 4-15 for T_p, T_0, T_{avg}, T_m, and $T_{V/A50}$, respectively. Some outliers were observed, but excluding these outliers, the overall distributions appear to be symmetrical with respect to the zero lines of the standardized inter-event errors and random-effects.

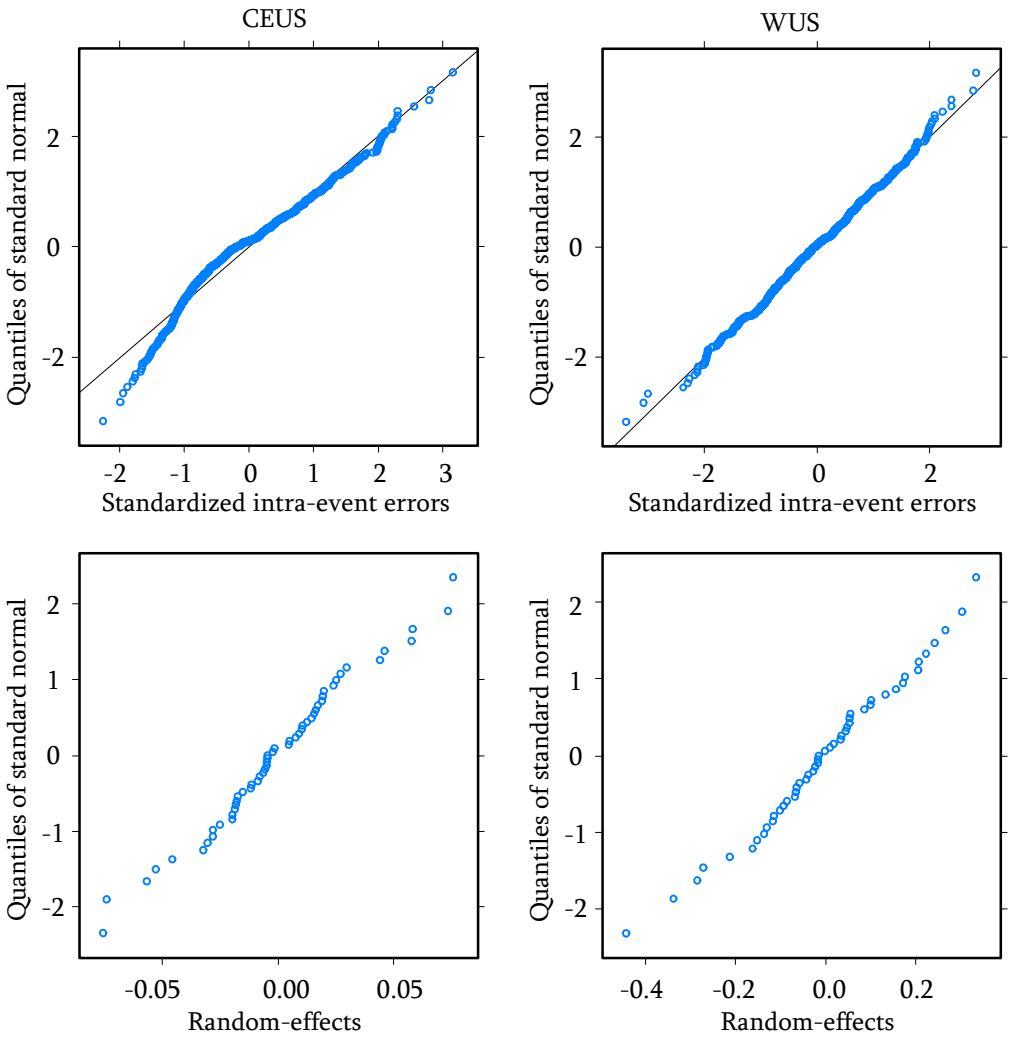

Figure 4-6. Normal Q-Q plots of intra-event errors (top) and random-effects (bottom) for CEUS (left) and WUS (right): T_p.

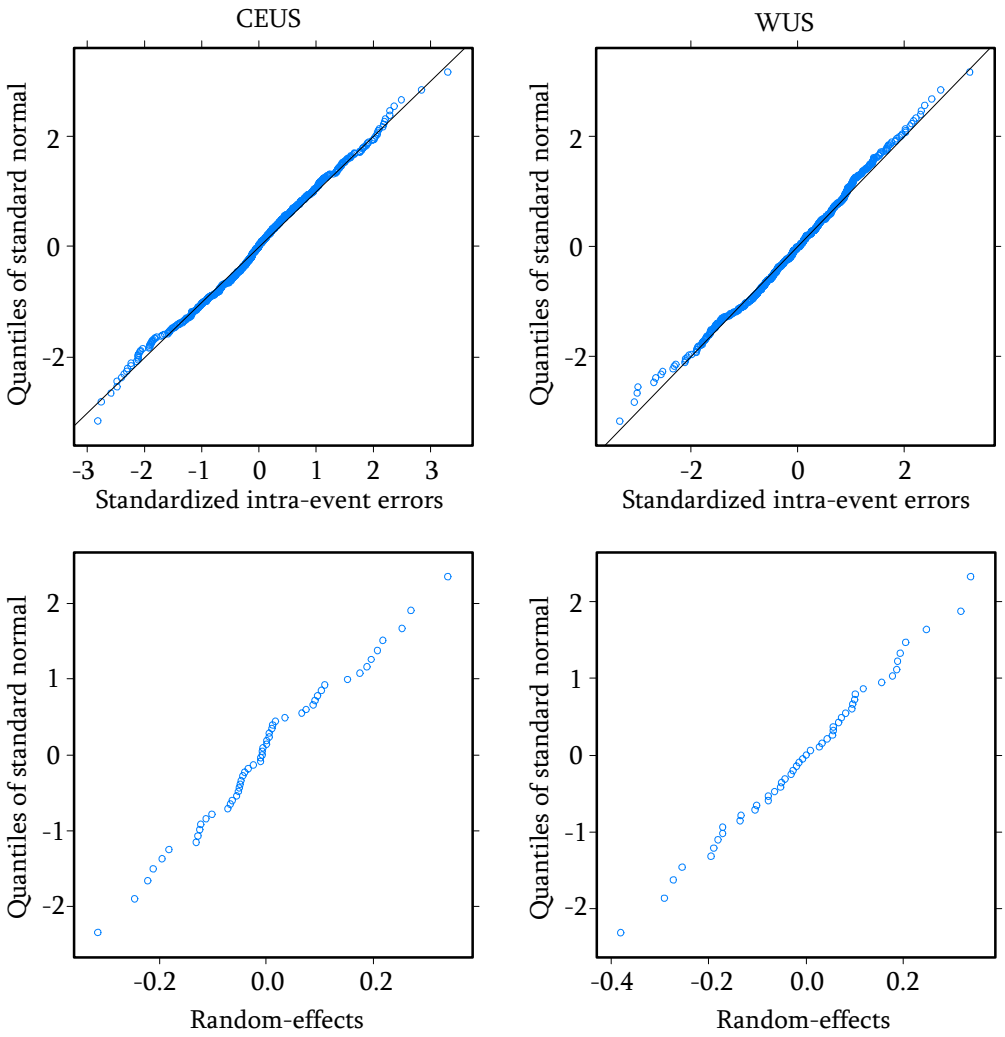

Figure 4-7. Normal Q-Q plots of intra-event errors (top) and random-effects (bottom) for CEUS (left) and WUS (right): T_0.

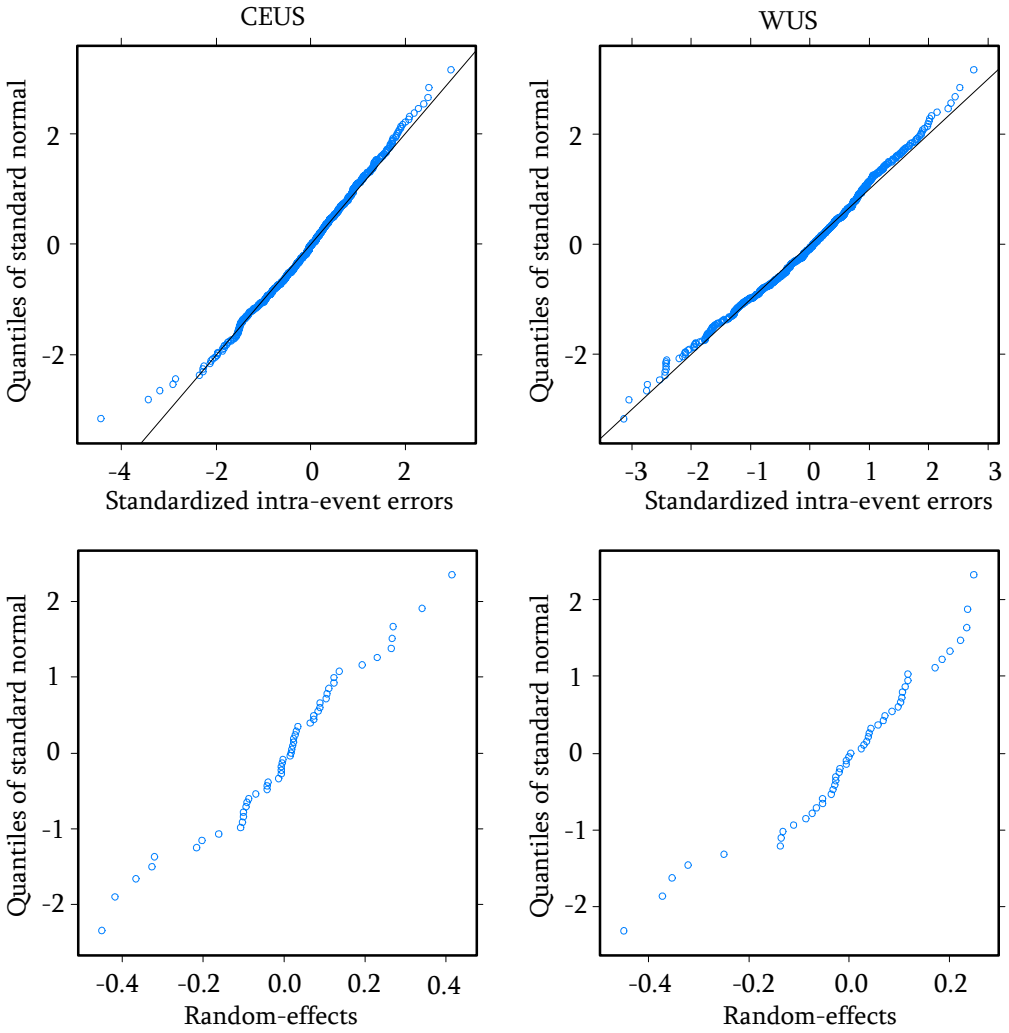

Figure 4-8. Normal Q-Q plots of intra-event errors (top) and random-effects (bottom) for CEUS (left) and WUS (right): T_{avg}.

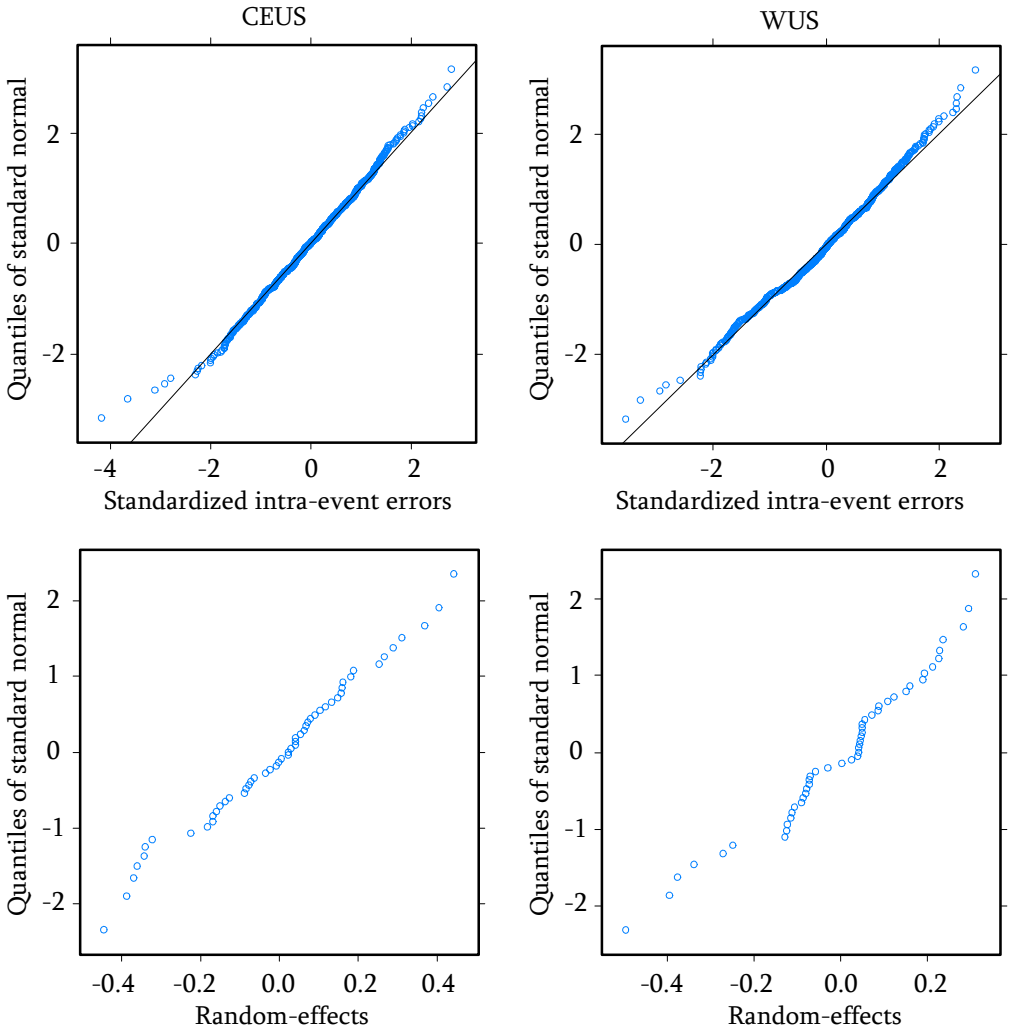

Figure 4-9. Normal Q-Q plots of intra-event errors (top) and random-effects (bottom) for CEUS (left) and WUS (right): T_m.

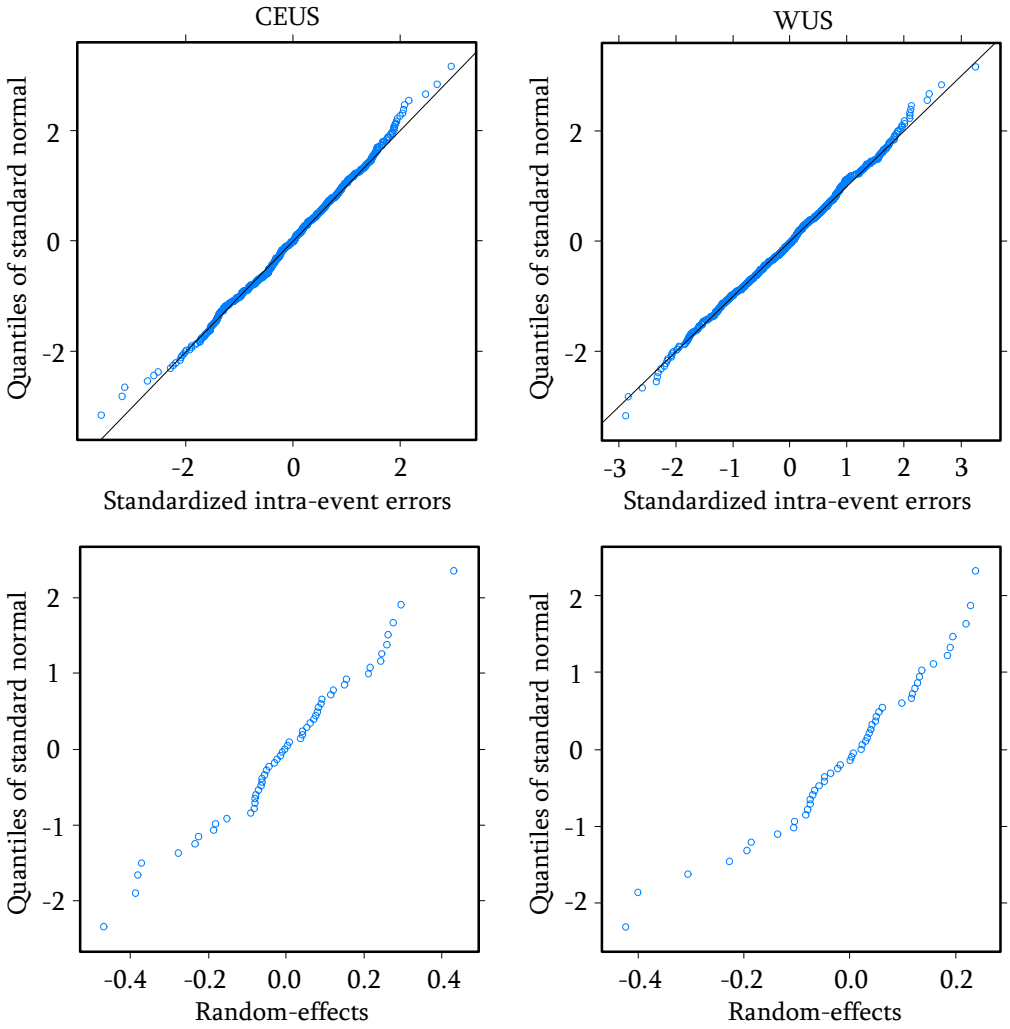

Figure 4-10. Normal Q-Q plots of intra-event errors (top) and random-effects (bottom) for CEUS (left) and WUS (right): $T_{V/A50}$.

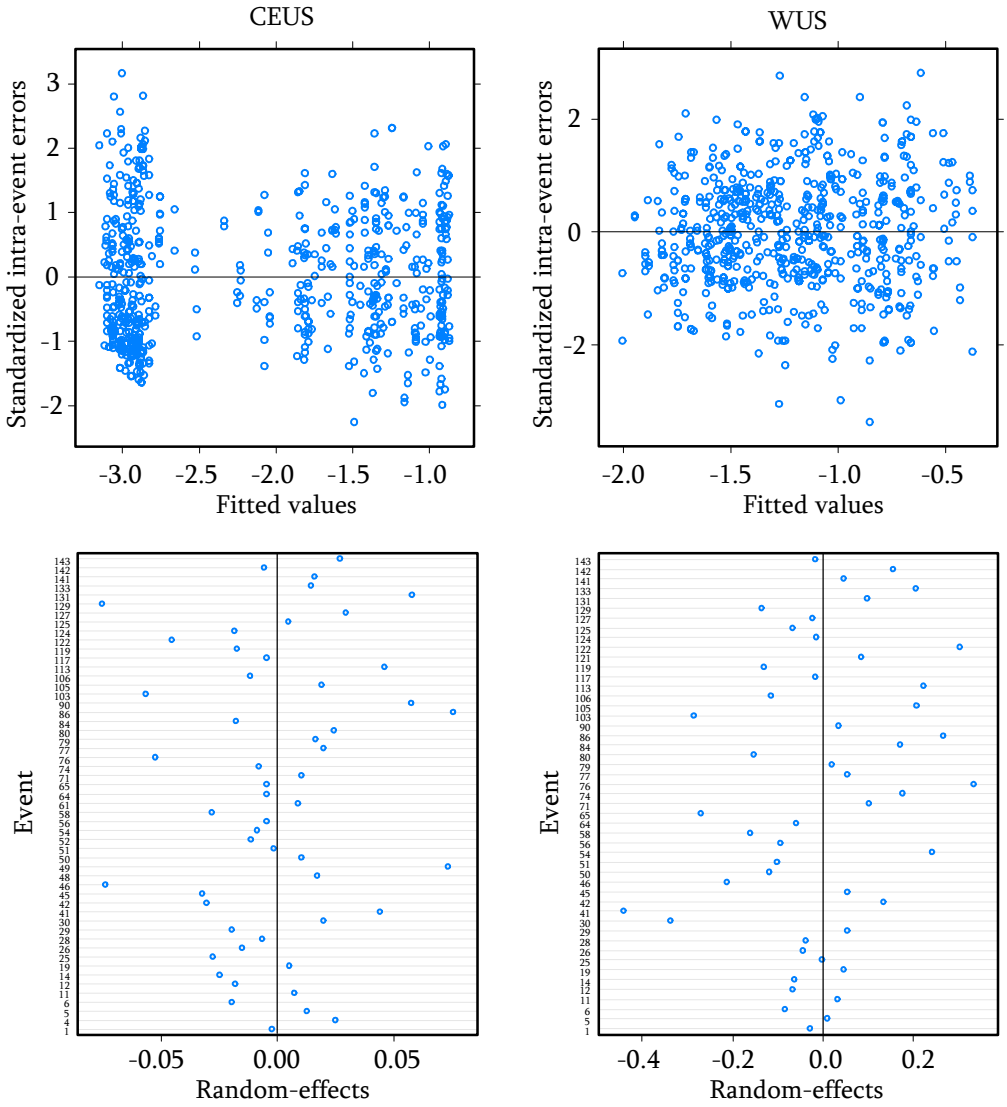

Figure 4-11. Scatter plots of intra-event errors (top) and random-effects (bottom) for CEUS (left) and WUS (right): T_p.

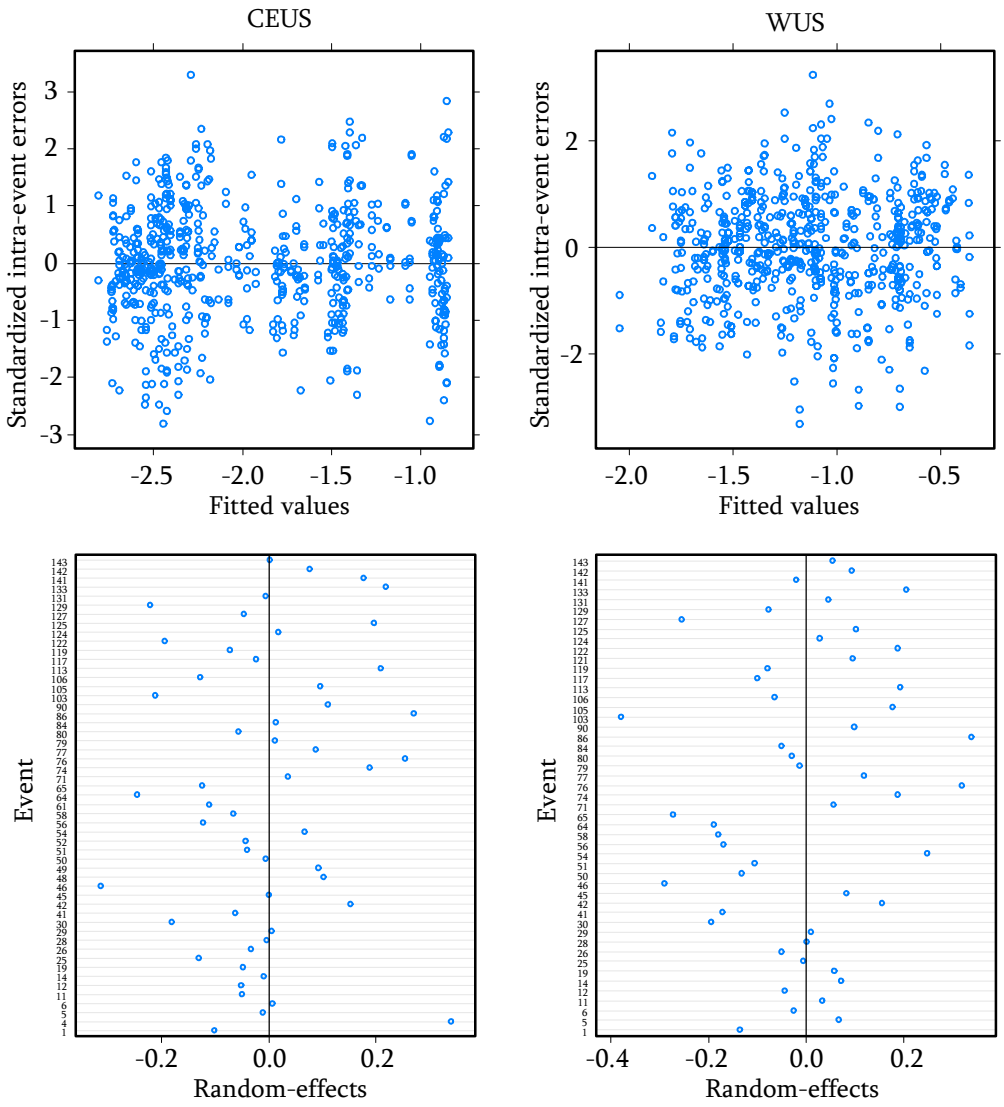

Figure 4-12. Scatter plots of intra-event errors (top) and random-effects (bottom) for CEUS (left) and WUS (right): T_0.

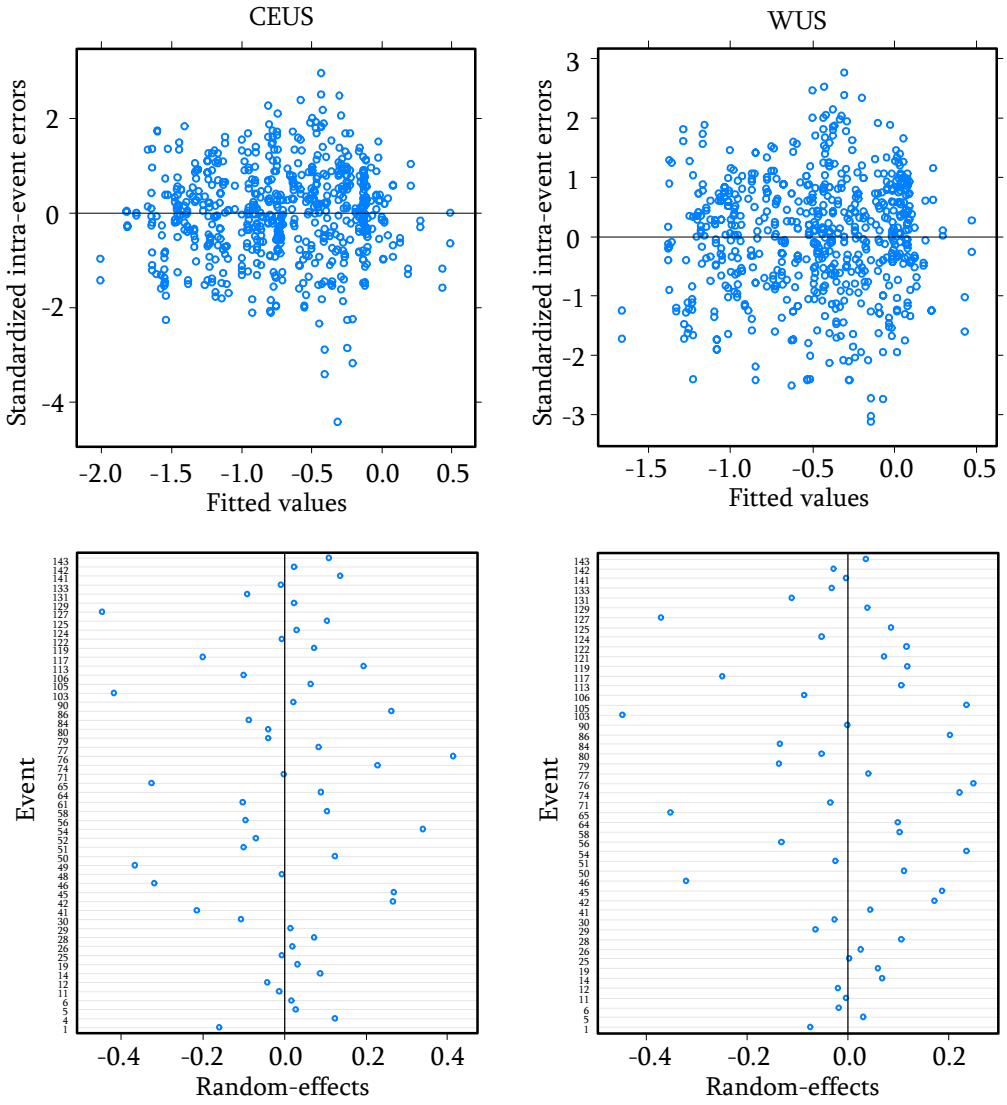

Figure 4-13. Scatter plots of intra-event errors (top) and random-effects (bottom) for CEUS (left) and WUS (right): T_{avg}.

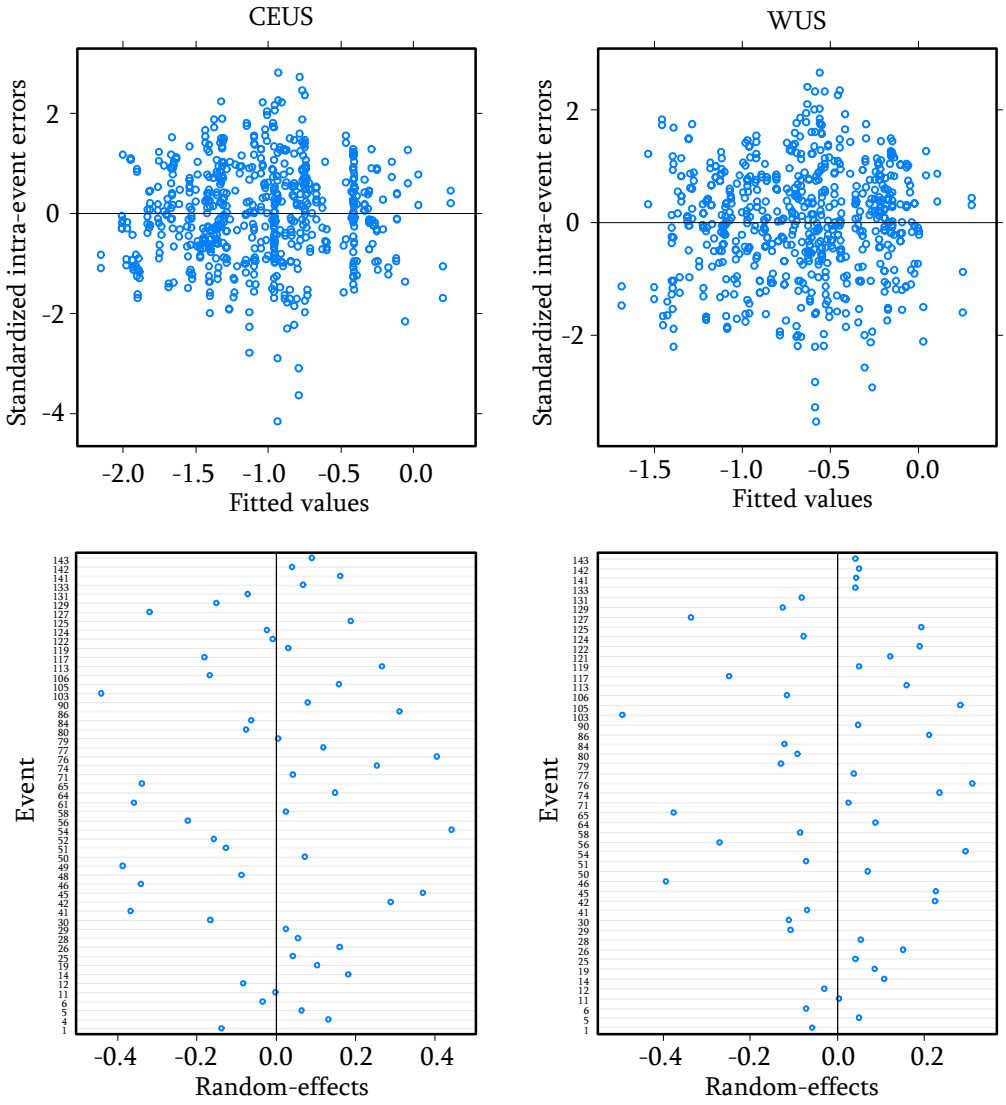

Figure 4-14. Scatter plots of intra-event errors (top) and random-effects (bottom) for CEUS (left) and WUS (right): T_m.

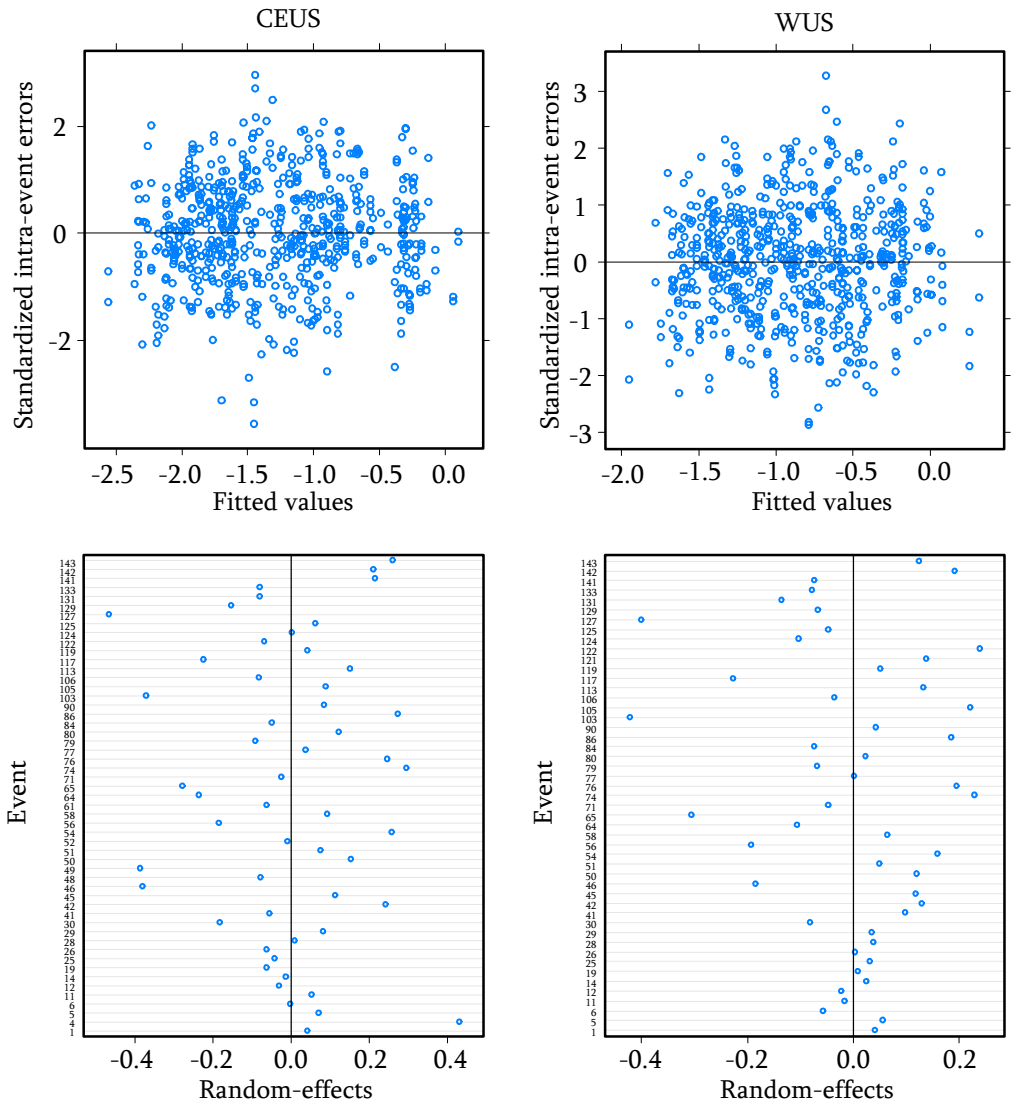

Figure 4-15. Scatter plots of intra-event errors (top) and random-effects (bottom) for CEUS (left) and WUS (right): $T_{V/A50}$.

The predicted medians of the T_p, T_0, T_{avg}, T_m, $T_{V/A50}$, and $T_{V/A84}$ for CEUS are compared with the actual data from the magnitude bins in Figure 4-16 through Figure 4-21. The central values of magnitude bins (i.e., M5.5, M6.5, and M7.5) were used for plotting the proposed predictive relationships. Also, shown in these figures are predicted values of the median plus/minus one total standard deviation ($\sigma_{ln\ total}$), which represents a range

encompassing about 68% of the observed data. In these figures, the extrapolated medians from the far-field model to short site-to-source distances are also shown in these plots, representing motions that do not have forward-directivity effects in the near-fault region. As may be observed from these plots, the proposed predictive relations represent the data well throughout the magnitude and distance ranges of the data. It should be noted that the proposed relations for small magnitudes (i.e., M 5-6) at distances below about 8 km may not be valid due to the absence of near-fault ground motion recordings for the magnitudes in the ground motion data set.

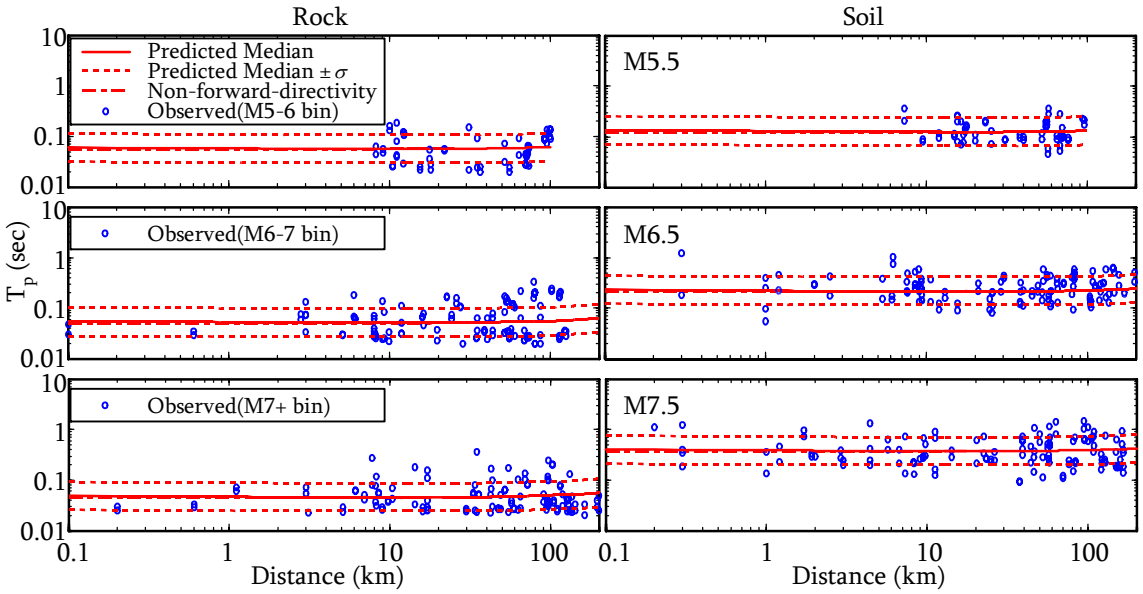

Figure 4-16. Predicted medians for T_p versus site-to-source distance for three magnitude bins for rock (left) and soil (right) sites for CEUS. The center values of magnitude bins are used to compute the predicted values. Also plotted are the actual data computed from the corresponding ground motion data sets.

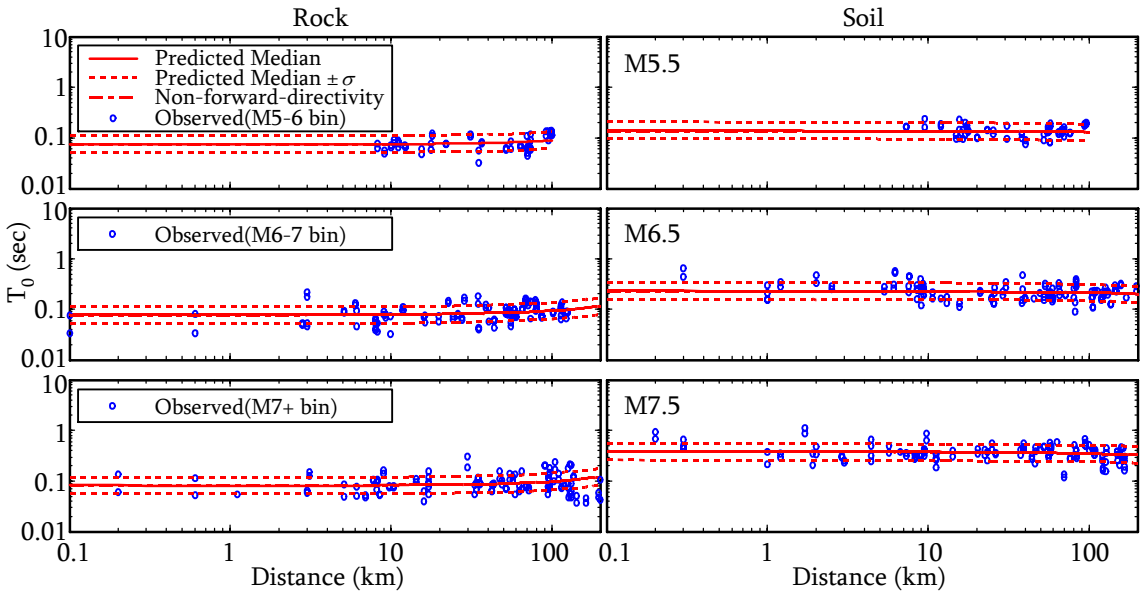

Figure 4-17. Predicted medians for T_0 versus site-to-source distance for three magnitude bins for rock (left) and soil (right) sites for CEUS. The center values of magnitude bins are used to compute the predicted values. Also plotted are the actual data computed from the corresponding ground motion data sets.

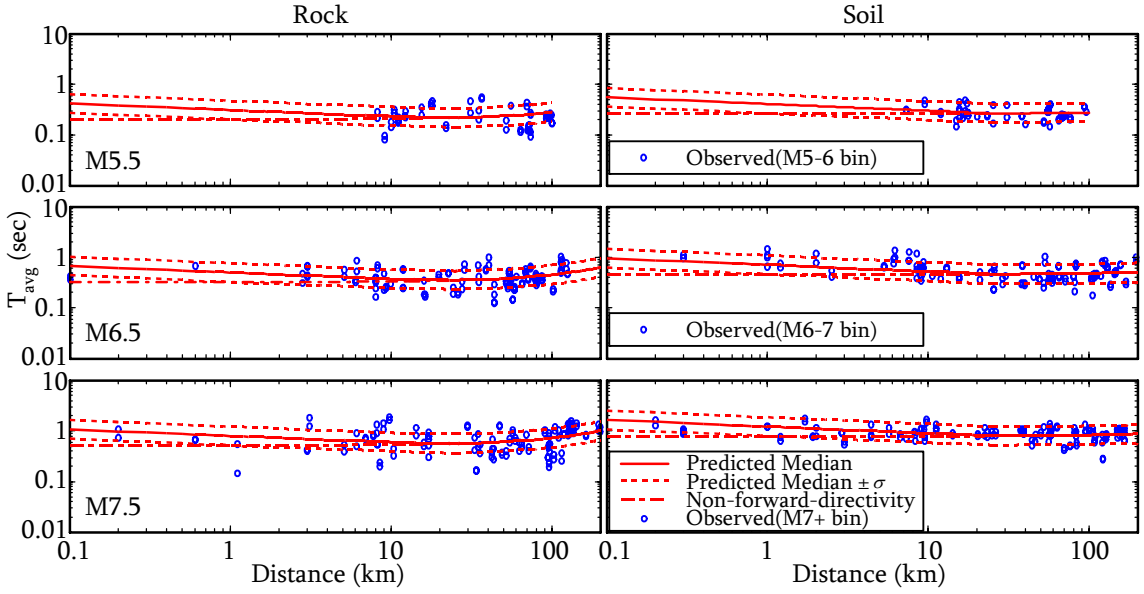

Figure 4-18. Predicted medians for T_{avg} versus site-to-source distance for three magnitude bins for rock (left) and soil (right) sites for CEUS. The center values of magnitude bins are used to compute the predicted values. Also plotted are the actual data computed from the corresponding ground motion data sets.

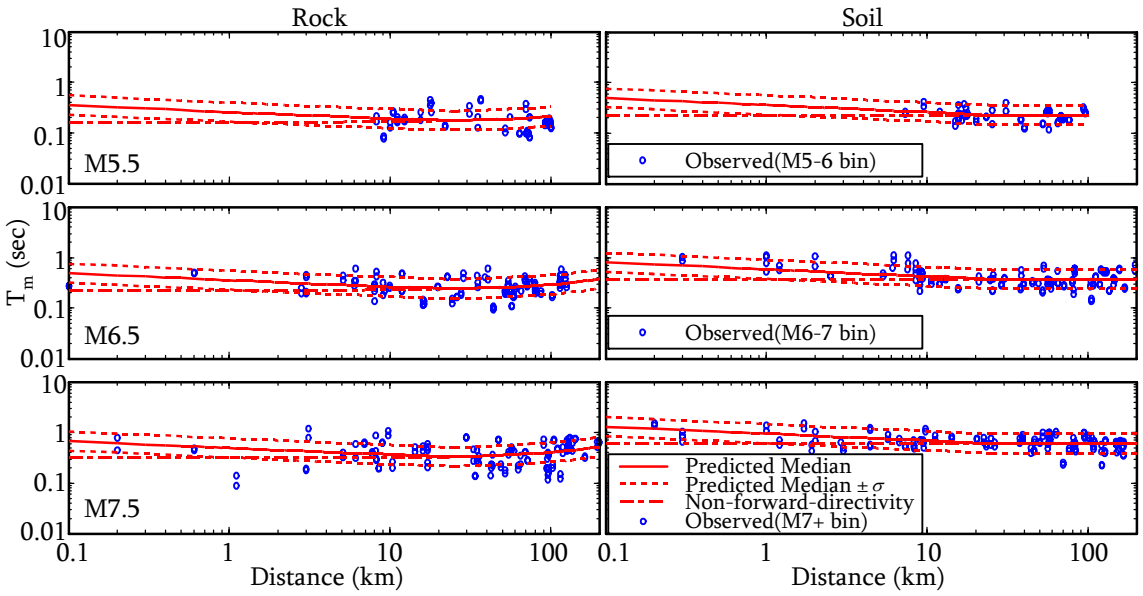

Figure 4-19. Predicted medians for T_m versus site-to-source distance for three magnitude bins for rock (left) and soil (right) sites for CEUS. The center values of magnitude bins are used to compute the predicted values. Also plotted are the actual data computed from the corresponding ground motion data sets.

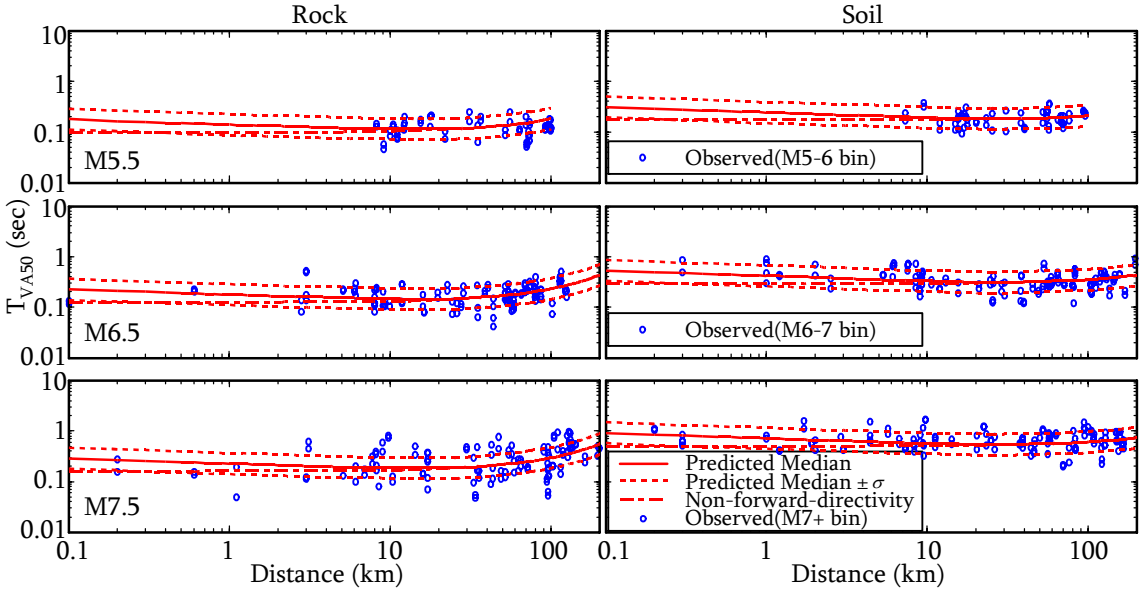

Figure 4-20. Predicted medians for $T_{V/A50}$ versus site-to-source distance for three magnitude bins for rock (left) and soil (right) sites for CEUS. The center values of magnitude bins are used to compute the predicted values. Also plotted are the actual data computed from the corresponding ground motion data sets.

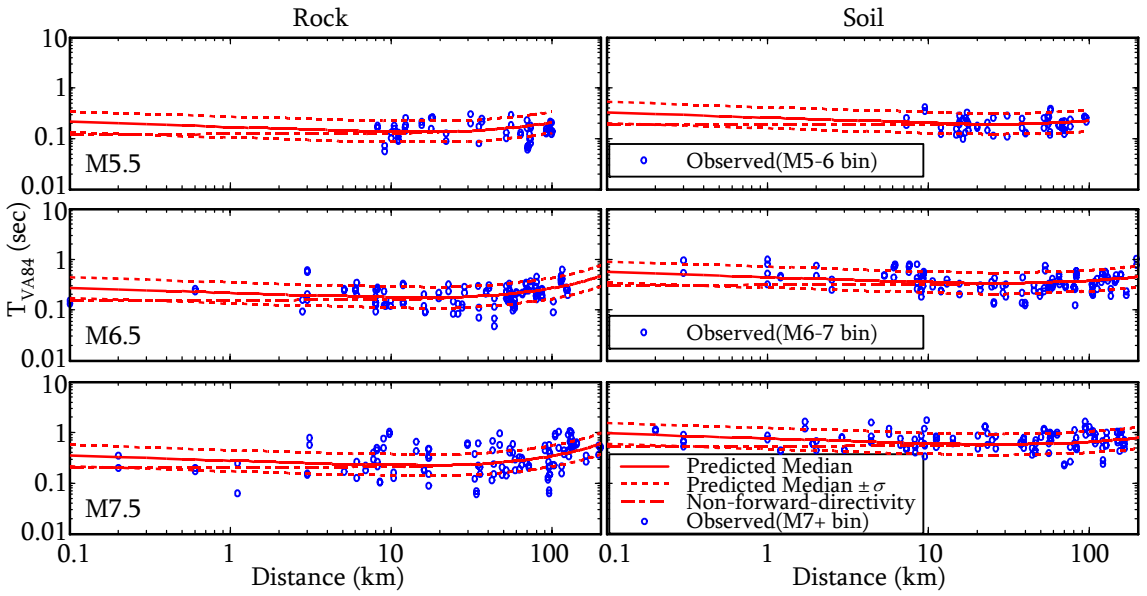

Figure 4-21. Predicted medians for $T_{V/A84}$ versus site-to-source distance for three magnitude bins for rock (left) and soil (right) sites for CEUS. The center values of magnitude bins are used to compute the predicted values. Also plotted are the actual data computed from the corresponding ground motion data sets.

Using the non-forward-directivity model of Eq. 4-12 and the regression coefficients listed in Table 4-3, the predicted medians for the characteristic periods of CEUS motions are plotted. Figure 4-22 shows the medians of the T_p and T_0 for rock and soil motions in CEUS. Both for the T_p and T_0, rock motions are consistently estimated to have shorter periods (i.e., higher frequencies) than soil motions, which is an expected trend because the high frequency seismic waves tend to get filtered out as the motions propagate up through the soil column. Also, T_p and T_o for rock motions are much less influenced by earthquake magnitude than soil motions. A strange trend is observed for the T_p of rock motions; T_p are predicted to have decreasing periods as earthquake magnitude increases. This trend conflicts with common physical understanding that larger-magnitude earthquakes tend to generate longer period motions. Considering the large total standard deviation for the T_p predictions, and the similarity in the predicted periods for rock

motions among the different earthquake magnitudes, the magnitude-dependence of the T_p for rock motions may be too small to be correctly reflected in the predictive relation. However, the predictive relation can provide reasonably narrow period ranges for rock motions at desired distances. Another unexpected trend is observed for the T_0 of soil motions that are estimated to have shorter periods for the ground motions at farther distances, which is inconsistent with the common understanding of ground motions in active shallow crustal regions (i.e., motions at farther distances from an earthquake source have longer periods because high frequency waves rapidly decay with distance from the source). Further investigation is required to explain this opposite trend. Figure 4-23 shows the T_{avg} and T_m predictions for CEUS. Rock motions appear to have shorter periods than soil motions except for the T_{avg} at the distances farther than about 130 km for intermediate and large earthquake magnitudes (i.e., M6.5 and M7.5). Both for rock and soil sites, the periods increase with increasing earthquake magnitudes and increasing distances. As observed from Figure 4-23, rock motions are consistently estimated to have much higher rates of period increase with distance than soil motions. Interestingly, for soil motions, the periods seem to be almost independent of distance. Additional studies are needed to better understand these trends. The $T_{V/A50}$ and $T_{V/A84}$ predictions for CEUS are shown in Figure 4-24. Similar trends to the T_{avg} and T_m predictions are observed but the $T_{V/A50}$ and $T_{V/A84}$ for soil motions clearly show distance dependence.

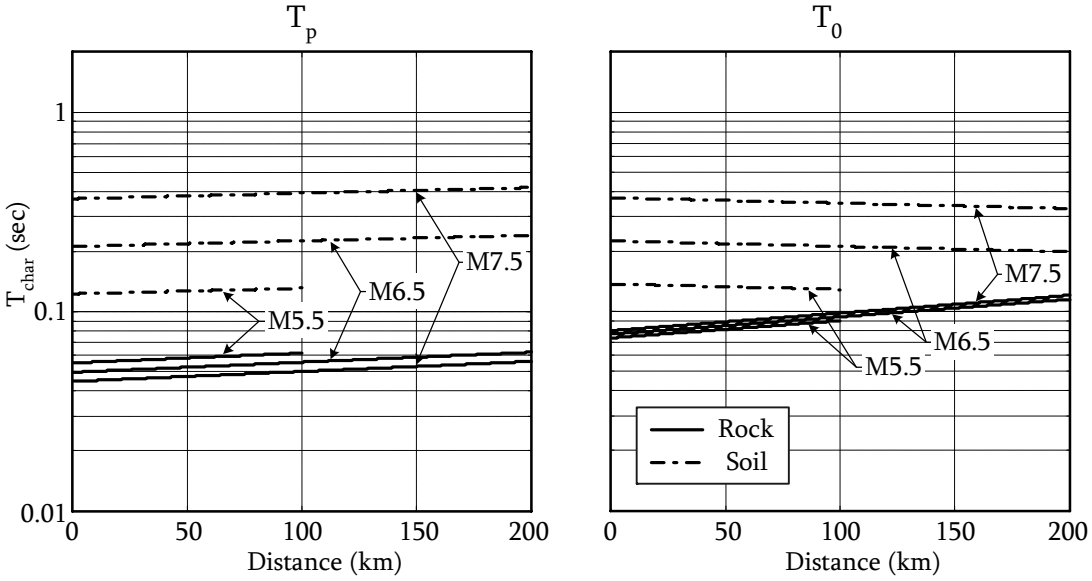

Figure 4-22. Predicted medians for T_p (left) and T_0 (right) versus distance for the magnitudes 5.5, 6.5, and 7.5 at rock and soil sites for CEUS.

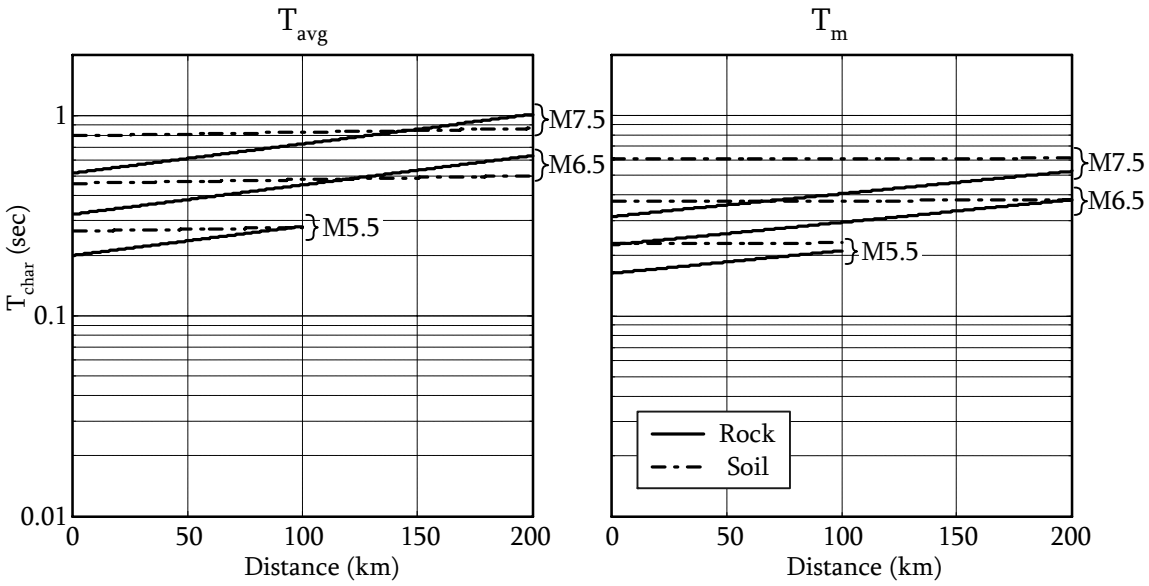

Figure 4-23. Predicted medians for T_{avg} (left) and T_m (right) versus distance for the magnitudes 5.5, 6.5, and 7.5 at rock and soil sites for CEUS.

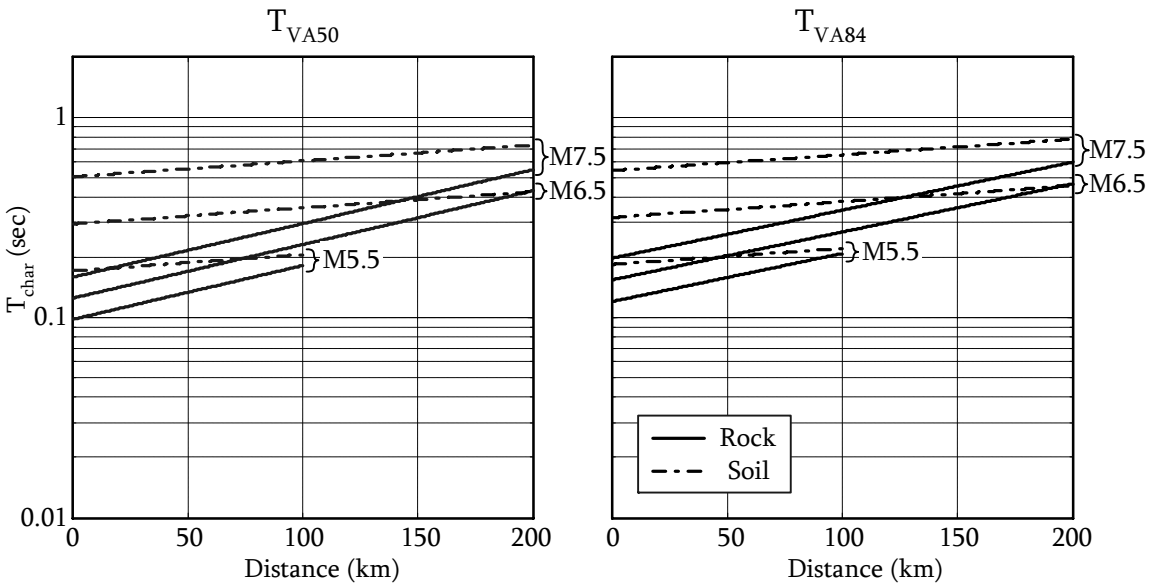

Figure 4-24. Predicted medians for $T_{V/A50}$ (left) and $T_{V/A84}$ (right) versus distance for the magnitudes 5.5, 6.5, and 7.5 at rock and soil sites for CEUS.

To identify differences in the characteristic periods between CEUS and WUS, comparison plots for the T_p, T_0, T_{avg}, T_m, $T_{V/A50}$, and $T_{V/A84}$ for CEUS and WUS motions are shown in Figure 4-25 through Figure 4-30. In all the plots, the medians were predicted using the non-forward-directivity model of Eq. 4-12 in conjunction with the regression coefficients listed in Table 4-3. For all the definitions of characteristic periods, CEUS motions are consistently observed to have shorter periods (i.e., higher frequencies) than comparable WUS motions, which agrees with the commonly-understood observation that ground motions in stable continental regions (e.g., CEUS) are richer in high frequencies than those in active shallow crustal regions (e.g., WUS). This is attributed to stiffer crustal conditions in CEUS than in WUS. Also, it is seen that for soil motions, the distance dependencies of characteristic periods are consistently less in CEUS than in WUS. Again, further study is needed to better understand this trend.

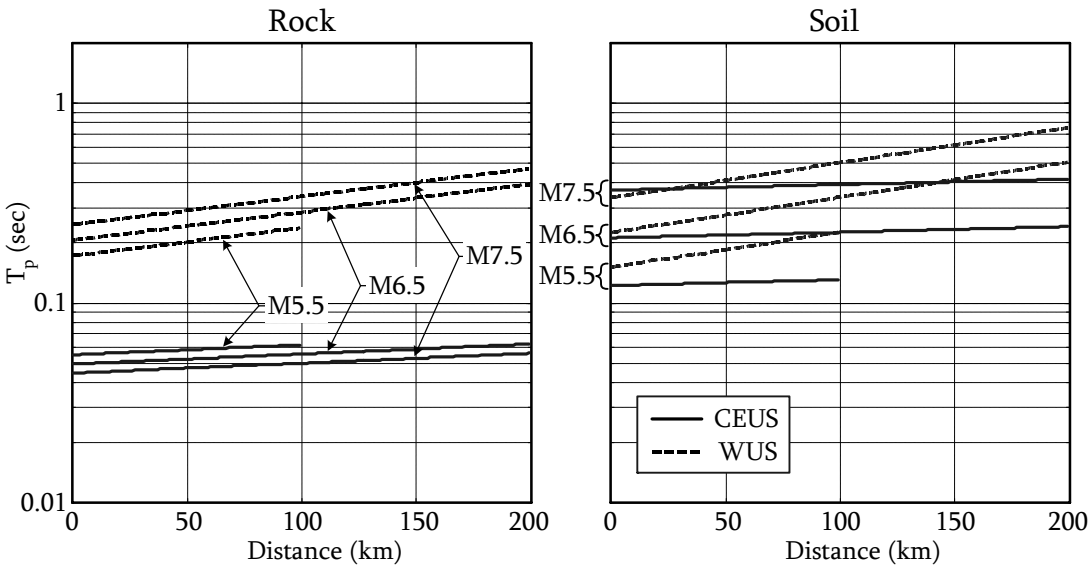

Figure 4-25. T_p comparison of CEUS and WUS for rock (left) and soil (right) sites.

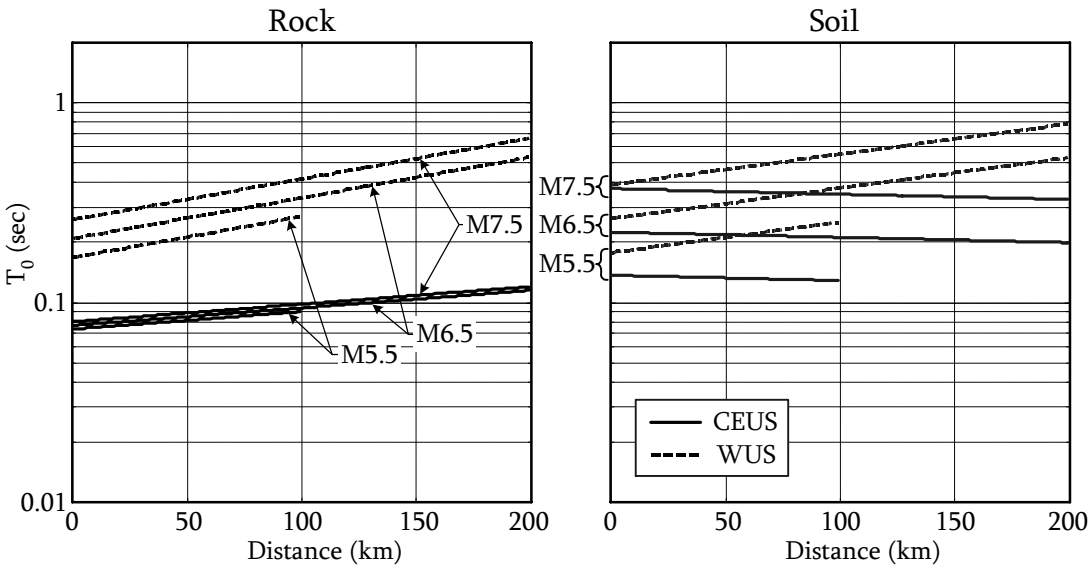

Figure 4-26. T_0 comparison of CEUS and WUS for rock (left) and soil (right) sites.

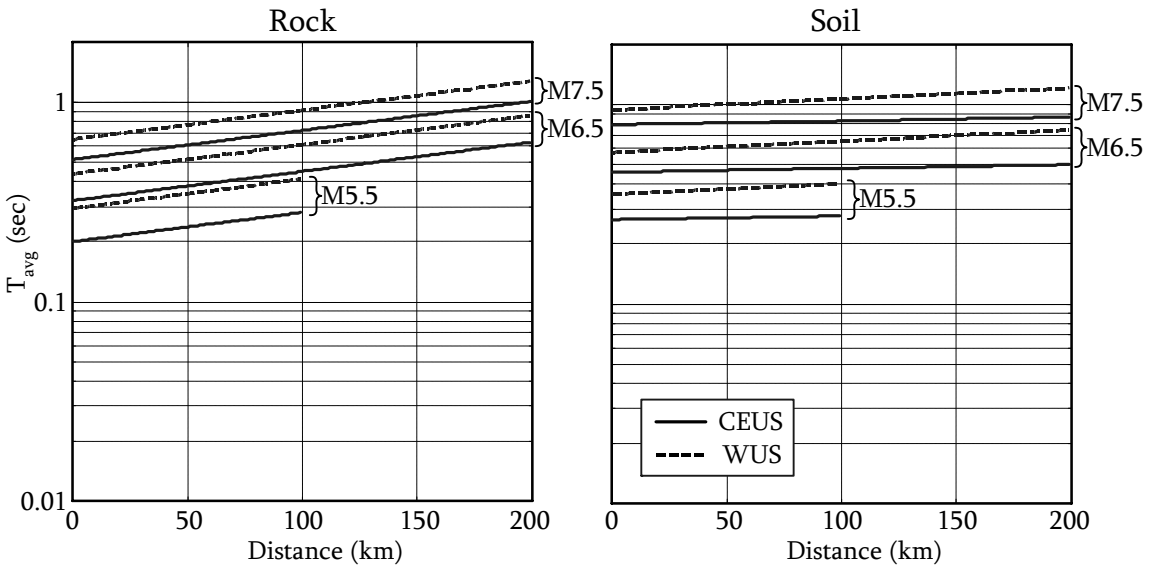

Figure 4-27. T_{avg} comparison of CEUS and WUS for rock (left) and soil (right) sites.

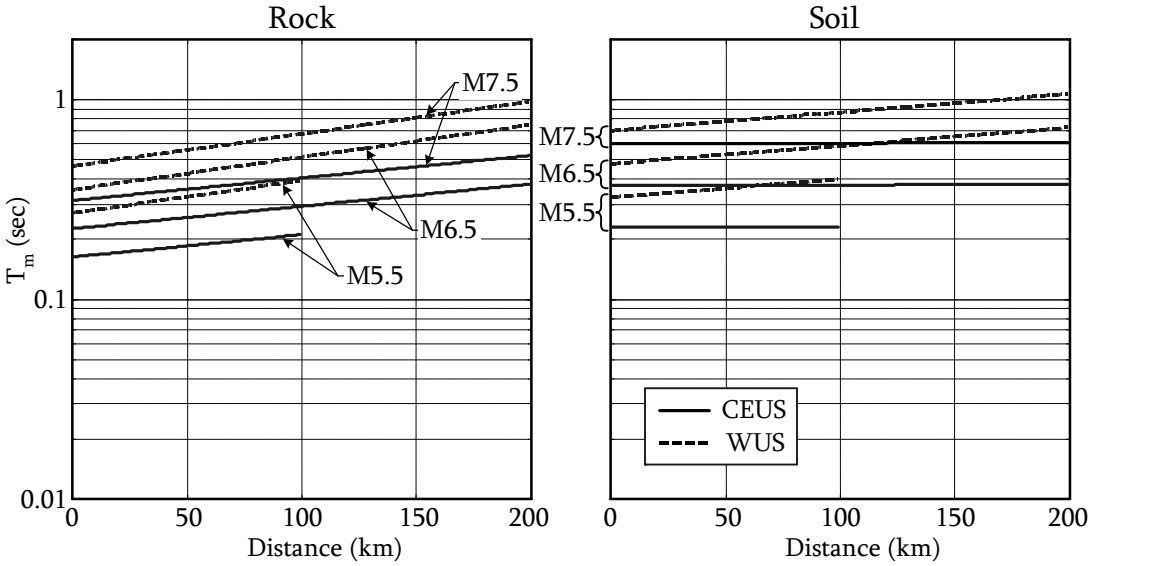

Figure 4-28. T_m comparison of CEUS and WUS for rock (left) and soil (right) sites.

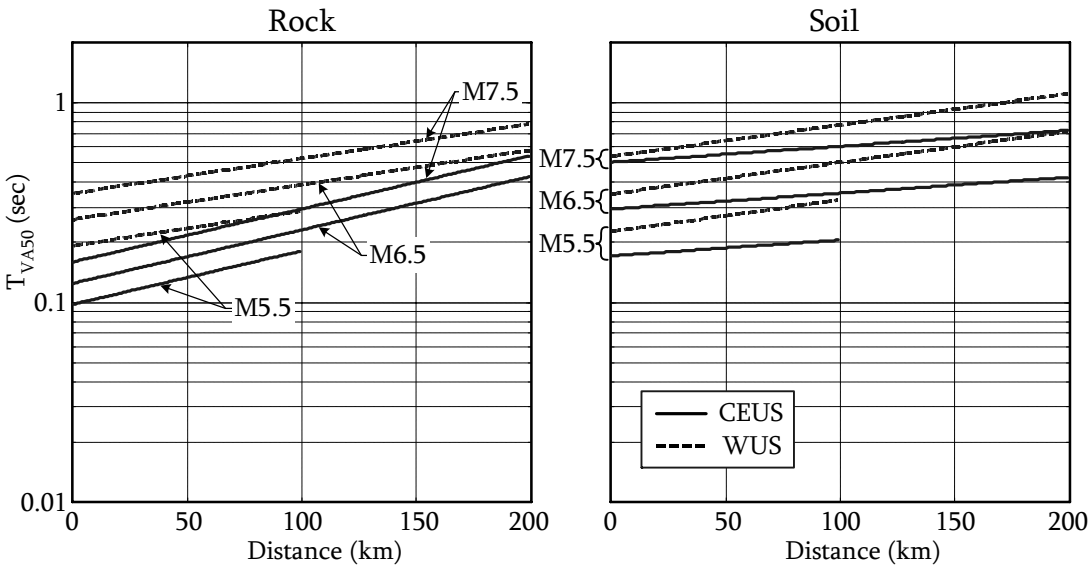

Figure 4-29. $T_{V/A50}$ comparison of CEUS and WUS for rock (left) and soil (right) sites.

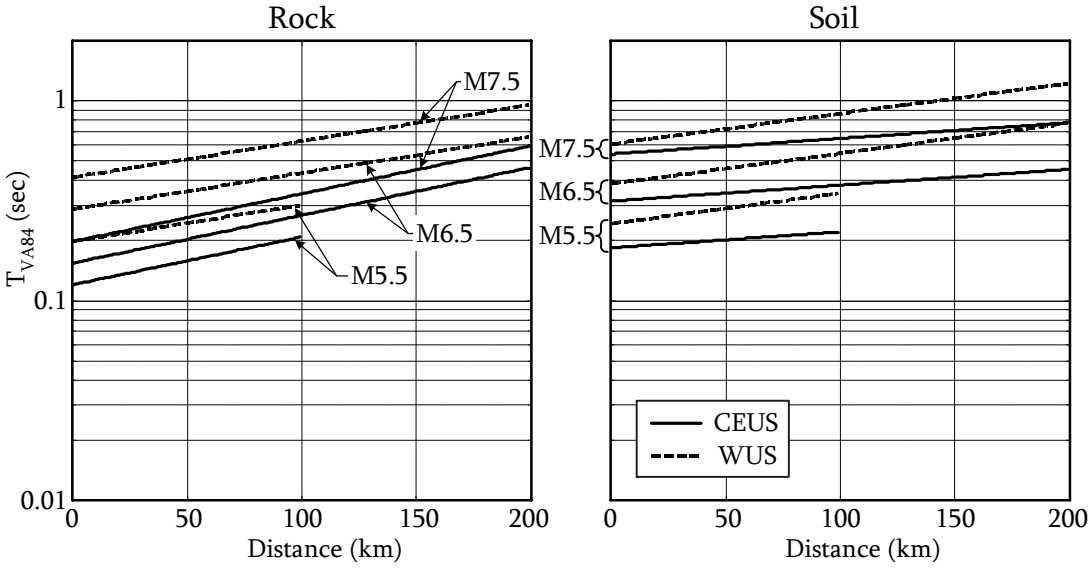

Figure 4-30. $T_{V/A84}$ comparison of CEUS and WUS for rock (left) and soil (right) sites.

4.2.4 Comparison with Existing Relationships

The proposed predictive relationships for CEUS and WUS are compared to existing empirical relationships for active shallow crustal regions. For T_m, one model derived from Brune's point source model (Brune, 1970; 1971) for stable continental regions is available for comparison with this study's CEUS model. However, no comparisons are made for the spectral velocity-acceleration ratio periods since no existing relationships are available.

For the predominant spectral period T_p, the model proposed by Rathje et al. (1998) is used for comparison. The model was developed using non-linear least-squares regressions of data from 306 strong ground motion recordings from 20 earthquakes in active shallow crustal regions. Rathje et al. expressed their relationship as a function of earthquake magnitude, site-to-source distance, and local site conditions. They used the same site classification scheme as was used as in this study (i.e., Geomatrix site codes). Different from this study, Rathje et al. used the geometric mean (i.e., square root of the product of the *PSA* for two orthogonal components) of the spectral acceleration (*PSA*) values of two orthogonal horizontal components to compute the periods. In contrast, this study treated the data from each horizontal component separately. Figure 4-31 shows the comparison of the predictions by Rathje et al. (1998) and this study. Good agreement is observed for rock motions between the WUS models by Rathje et al. (1998) and this study. Also, T_p for CEUS motions at rock sites predicted using the relations developed in this study have shorter periods than comparable WUS motions predicted using the

relations from Rathje et al. For soil motions, CEUS motions appear to have shorter periods except for the magnitude 7.5 at distances below about 50 km.

For T_0, T_{avg}, and T_m, the models proposed by Rathje et al. (2004) are used for comparison. The Rathje et al. (2004) models were developed using NLME regressions, same as in this study, of data from 835 motions from 44 earthquakes from active shallow crustal regions. The Rathje et al. (2004) relationships are expressed as a function of earthquake magnitude, distance, local site conditions, and forward-directivity. The geotechnical site classification system by Rodriguez-Marek et al. (2001) was used for local site conditions. Also, similar to Rathje et al. (1998), Rathje et al. (2004) used the geometric means of the *PSA* values for two orthogonal horizontal components to determine T_0 and T_{avg} values. For T_m, the Fourier amplitude spectra for two orthogonal horizontal components were combined by using the Euclidean norm (i.e., square-root of the sum of squared Fourier amplitudes), which were then used in the period computations. Figure 4-32 through Figure 4-34 show the comparisons of this study's predictive relationships and the Rathje et al. (2004) models for T_0, T_{avg}, and T_m, respectively. Comparing the WUS models from this study and Rathje et al. (2004), the overall predictions for T_0, T_{avg}, and T_m for rock sites by both models are in a good agreement. Especially, the T_0 and T_m predictions for M7.5 at rock sites appear to be almost identical as shown in Figure 4-32 and Figure 4-34, respectively. For WUS soil sites, there are relatively large discrepancies between the predictions of T_0, T_{avg}, and T_m by this study and Rathje et al. This is because the magnitude and distance dependencies coupled with site conditions were not incorporated in Rathje et al. model. Comparing the CEUS models from this study with the Rathje et al.

(2004) WUS models, CEUS motions still have shorter periods than comparable WUS motions.

Lastly, the CEUS predictive relationship for T_m proposed in this study is compared to the one for rock motions in stable continental regions proposed by Rathje et al. (1998). Rathje et al. model was derived using Brune's point source model (Brune, 1970; 1971) in conjunction with the point source model parameters for the seismic source and crustal path for stable continental regions listed in Table 4-4. Also listed in this table are the parameters used for scaling WUS motions to CEUS motions by McGuire et al. (2001). Rathje et al. (1998) did not explicitly state the assumed value of the crustal density of the source region (ρ_0) that they assumed. As may be observed from this table, several point source parameters differed between the Rathje et al. and McGuire et al. studies. Figure 4-35 shows the comparison of the empirical relationship proposed in this study and the theoretical relation proposed by Rathje et al.(1998) for rock motions in stable continental regions. Although Rathje et al. model predicts systematically longer periods than this study's model, their differences remain quite small (less than about 0.1 sec) for the ranges of magnitude and distance.

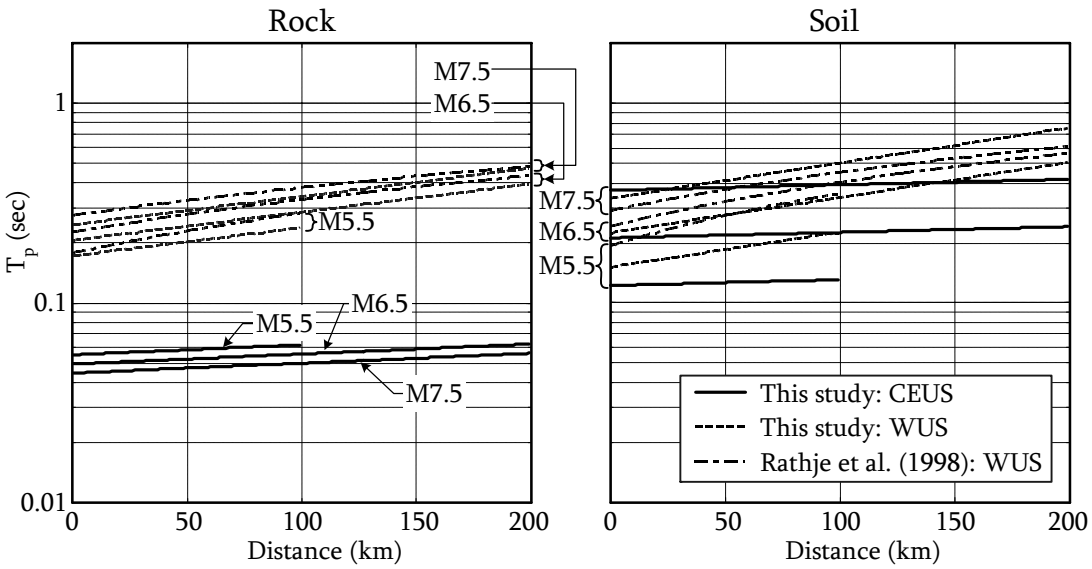

Figure 4-31. T_p comparison of models by this study and Rathje et al. (1998).

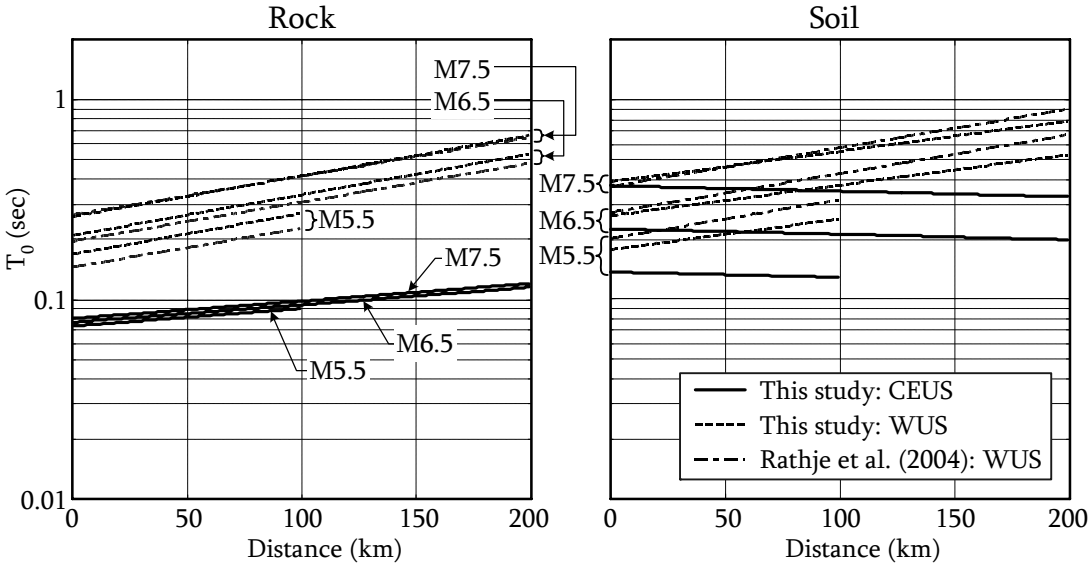

Figure 4-32. T_0 comparison of models by this study and Rathje et al. (2004).

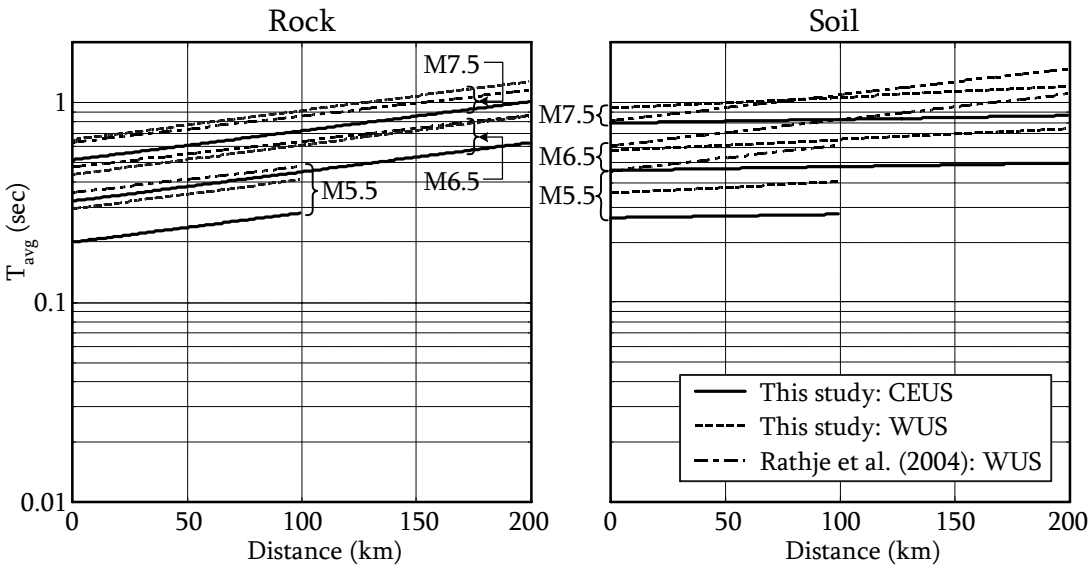

Figure 4-33. T_{avg} comparison of models by this study and Rathje et al. (2004).

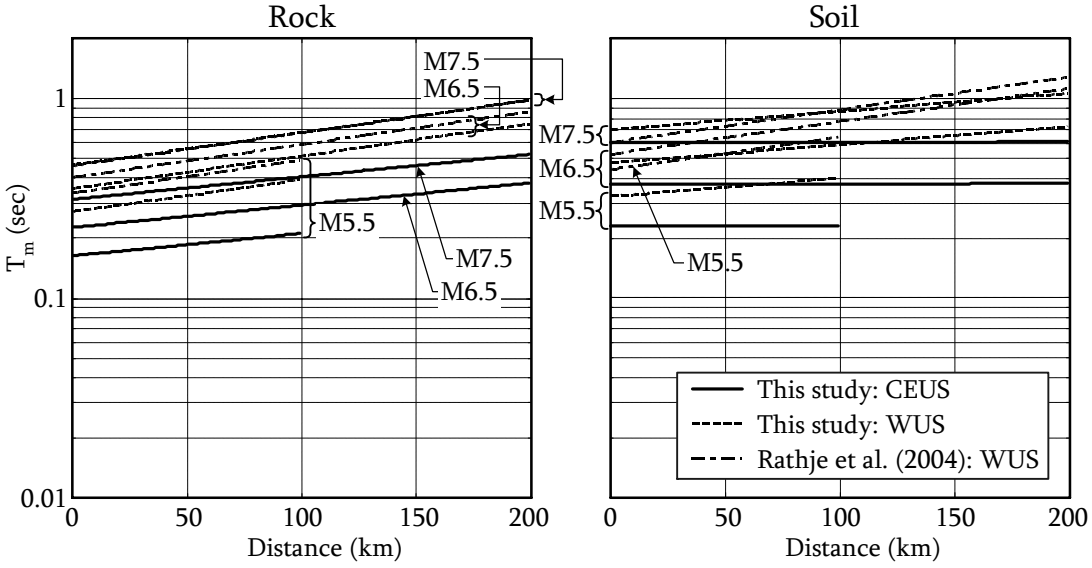

Figure 4-34. T_m comparison of models by this study and Rathje et al. (2004).

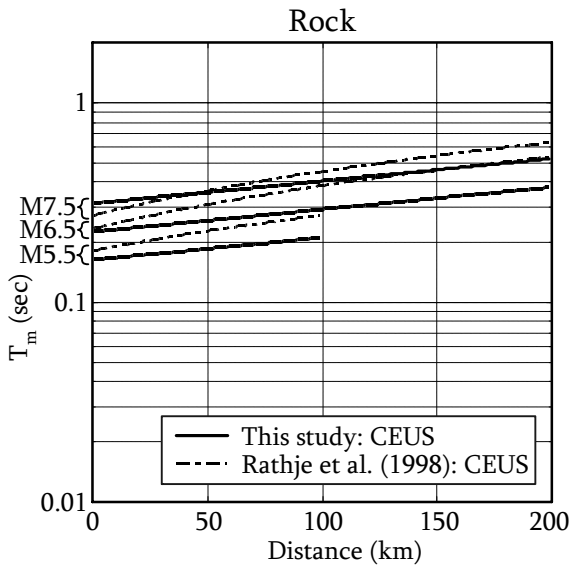

Figure 4-35. T_m comparison of models by this study and Rathje et al. (1998).

Table 4-4. Comparison of the point source parameters used for stable continental region motions.

	Rathje et al. (1998)	McGuire et al. (2001)
$\Delta\sigma$ (bars)	120	120
κ (sec)	0.006	0.006
Q_0	670	351
n	0.33	0.84
β_0 (km/sec)	3.50	3.52
ρ_0 (gm/cm^3)	-	2.60

4.3 Conclusions

The empirical relationships for characteristic periods of horizontal CEUS motions are proposed in this study. The characteristic periods considered herein were the predominant spectral period (T_p), the smoothed spectral predominant period (T_0), the average spectral

period (T_{avg}), the mean period (T_m), and the spectral velocity-acceleration ratio periods ($T_{V/A50}$ and $T_{V/A84}$). From the comparison of the characteristic periods of rock and soil motions in CEUS, it was consistently observed that rock motions exhibit shorter periods than soil motions. Also, rock motions were consistently estimated to have higher rates of period increase with increasing distance than soil motions. The CEUS motions were observed to have shorter periods than WUS motions for all characteristic periods. Additionally, for rock motions in CEUS, the mean periods predicted by this study were compared to those by the theoretical model for stable continental motions by Rathje et al. (1998). The predictions from the two studies are generally in a good agreement.

References

Bray, J. D., and Rodriguez-Marek, A. (2004). "Characterization of forward-directivity ground motions in the near-fault region". *Soil Dynamics and Earthquake Engineering*, 24(11), 815-828.

Brune, J. N. (1970). "Tectonic stress and spectra of seismic shear waves from earthquakes". *Journal of Geophysical Research*, 75(26), 611-614.

Brune, J. N. (1971). "Correction". *Journal of Geophysical Research*, 76(20), 1441-1450.

Cameron, W. I. (2009). "Spectral shapes for engineering use," Ph.D. dissertation, University of Michigan, Ann Arbor, Michigan.

Green, R. A., and Cameron, W. I. (2003). "The influence of ground motion characteristics on site response coefficients." *Proc., 7th Pacific Conference on Earthquake Engineering*, University of Canterbury, Christchurch, New Zealand, 8 pp.

McGuire, R. K., Silva, W. J., and Costantino, C. J. (2001). "Technical basis for revision of regulatory guidance on design ground motions: Hazard-and risk-consistent ground motion spectra guidelines.", US Nuclear Regulatory Commission, Washington, DC.

Newmark, N. M., and Hall, W. J. (1982). *Earthquake Spectra and Design*, EERI, Berkeley, California.

Rathje, E. M., Abrahamson, N. A., and Bray, J. D. (1998). "Simplified frequency content estimates of earthquake ground motions". *Journal of Geotechnical and Geoenvironmental Engineering*, 124(2), 150-159.

Rathje, E. M., Faraj, F., Russell, S., and Bray, J. D. (2004). "Empirical relationships for frequency content parameters of earthquake ground motions". *Earthquake Spectra*, 20(1), 119-144.

Rodriguez-Marek, A., Bray, J. D., and Abrahamson, N. A. (2001). "An Empirical Geotechnical Seismic Site Response Procedure". *Earthquake Spectra*, 17(1), 65-87.

Seed, H. B., Idriss, I. M., and Kiefer, F. W. (1969). "Characteristics of rock motions during earthquakes". *Journal of the Soil Mechanics and Foundations Division, ASCE*, 95(5), 1199-1218.

Shimazaki, K., and Sozen, M. A. (1984). "Seismic drift of reinforced concrete structures." Special Research Paper (Draft), Hazama Corp.

Chapter 5

Duration of Strong Ground Motions

5.1 Background

Strong ground motion duration is an important parameter for seismic risk assessment because it, along with the amplitude and frequency content of the ground motions, significantly influences the response of geotechnical and structural systems. For example, when the non-linear behavior (i.e., degradation of stiffness) of a system is considered, strong motion duration is a critical feature regarding the amount of potential damage (e.g., Bommer and Martinez-Pereira, 1999). In this vein, various definitions of strong motion duration have been proposed for quantifying the strong motion phase of earthquake ground shakings, which is the portion of the motion that is of engineering interest.

Of the numerous definitions of strong motion duration, significant durations ($D_{5\text{-}75}$ and $D_{5\text{-}95}$) and bracketed duration ($D_{bracket}$) are most commonly used in engineering practice. Their definitions are based on either relative or absolute criterion. In this regard, Bommer and Martinez-Pereira (1999) proposed effective duration (D_{eff}) as an attempt to combine the two criteria. Accordingly, significant durations, bracketed duration, and effective duration are considered herein for developing duration relations. Also, note that this study only considers horizontal components of ground motions.

This chapter is divided into two parts: significant durations and bracketed and effective durations. In each part, definitions are reviewed, and the proposed predictive relationships and the NLME regression results are presented. For the bracketed and effective durations, since the data contain motions having zero-duration, an approach for incorporating the effects of zero-durations in the predictive model is introduced. For the significant durations, the CEUS model is compared to the WUS model developed in this study. Additionally, the WUS model is compared to existing empirical relationships (i.e., Abrahamson and Silva, 1996; Kempton and Stewart, 2006). For the bracketed duration, the relationship proposed by Chang and Krinitzsky (1977) is compared to those from this study. However, to date no empirical relationships for the effective duration have been developed by other researchers. Thus, only the comparison between CEUS and WUS motions is made for the effective duration based on this study's predictive relationships.

5.2 Significant Durations: $D_{5\text{-}75}$ and $D_{5\text{-}95}$

5.2.1 Definitions

Significant duration is one of the most frequently used definitions by engineering seismologists and earthquake engineers. The normalized cumulative squared acceleration, $H(t)$, is used in its definition:

$$H(t) = \frac{\int_0^t a^2(t)\,dt}{\int_0^{t_d} a^2(t)\,dt} \qquad \text{(Eq. 5-1)}$$

where: $a(t)$ is the acceleration time history, and t_d is the total duration of the acceleration time history. As may be surmised from this equation, the normalized cumulative squared

acceleration varies from 0 to 1 or 0% to 100%. Significant duration is most often defined as the time interval between $H(t)$ = 5% and 75% (Somerville et al., 1997), or $H(t)$ = 5% and 95% (Trifunac and Brady, 1975), denoted as $D_{5\text{-}75}$ and $D_{5\text{-}95}$, respectively. Figure 5-1 illustrates the determination of the significant durations $D_{5\text{-}75}$ and $D_{5\text{-}95}$ for an example acceleration time history using the $H(t)$ plot, known as the Husid plot (Husid, 1969). The significant duration is useful because it reasonably represents the most significant portion of ground motions in terms of time. However, it is undesirable that ground motions with low amplitudes (i.e., motions not of engineering interest) can have non-zero durations. This is attributed to significant duration's definition being based on only a relative criterion (Bommer and Martinez-Pereira, 1999). Hence, when significant duration is used in seismic risk assessment, amplitude of acceleration must also be considered (Kempton and Stewart, 2006).

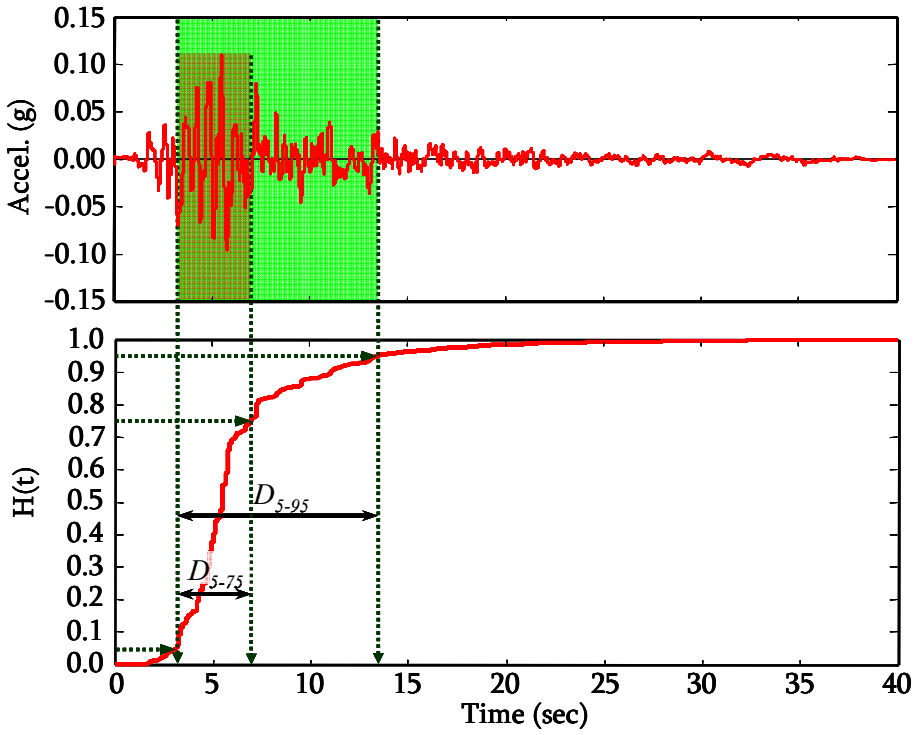

Figure 5-1. Signification duration determination using the Husid plot for a ground acceleration time history (BES090: M6.9; R49.9km) from the 1989 Loma Prieta earthquake.

5.2.2 Proposed Model

The functional form of the predictive relationship was obtained by modifying the model developed by Abrahamson and Silva (1996). They used the seismic source duration relation (Hanks, 1979; McGuire and Hanks, 1980; Boore, 1983):

$$D_0 = f_c^{-1} \qquad \text{(Eq. 5-2)}$$

where: D_0 is source duration, and f_c is corner frequency that separates the relatively-flat portion at intermediate frequencies from the decaying portion at low frequencies in Fourier amplitude spectrum. The corner frequency is related to earthquake magnitude by the following relations:

$$f_c = 4.9 \times 10^6 \cdot \beta_0 \cdot \left(\Delta\sigma / M_0\right)^{1/3} \quad \text{(Brune, 1970; 1971)} \qquad \text{(Eq. 5-3)}$$

$$\log M_0 = 1.5M + 16.05 \quad \text{(Hanks and Kanamori, 1979)} \qquad \text{(Eq. 5-4)}$$

where: β_0 is shear wave velocity at the source (km/sec); $\Delta\sigma$ is stress drop at the source (bars); M_0 is seismic moment (dyne-cm); and M is moment magnitude. Also, Abrahamson and Silva (1996) modeled the magnitude dependence of $\Delta\sigma$ expressed as:

$$\Delta\sigma(M) = \exp\left[b_1 + b_2(M - 6)\right] \qquad \text{(Eq. 5-5)}$$

where, b_1 and b_2 are regression coefficients. Assuming a log-normal distribution for the significant duration data, the functional form for both $D_{5\text{-}75}$ and $D_{5\text{-}95}$ was:

$$\ln D_{5-75} \text{ or } \ln D_{5-95} = \ln\left(\frac{\left(\frac{\Delta\sigma(M)}{10^{1.5M+16.05}}\right)^{-\frac{1}{3}}}{4.9 \times 10^6 \beta_0} + f_1(R) + f_2(M, R, S_S)\right) \qquad \text{(Eq. 5-6)}$$

where: R is site-to source distance (km); S_S is a binary parameter representing local site conditions (i.e., $S_S = 0$ for rock site; $S_S = 1$ for soil site); and $f_1(R)$ and $f_2(M, R, S_S)$ represent the site-to-source distance and local site condition dependences, respectively.

The model proposed in this study, the complex term (i.e., magnitude-β_0 term) in Eq. 5-6 was simplified to an exponential term for magnitude. This was done because the trends for the complex and simplified terms were found to be equivalent to each other as shown in Figure 5-2, where $b_1 = 5.20$; $b_2 = 0.85$; and $\beta_0 = 3.2$ km/sec were used per Abrahamson and Silva (1996). It should be noted that the predictive model with this simplified term produced lower standard deviations than the previous model by Abrahamson and Silva (1996).

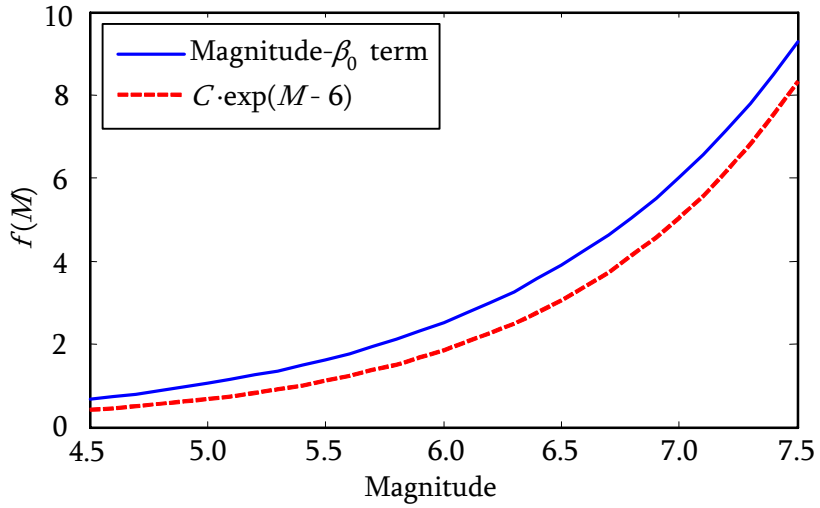

Figure 5-2. Comparison between the magnitude-β_0 term and an exponential term (C is a regression coefficient; C =1.86 was used for this comparison).

Based on the data observations and the standard deviations from numerous regressions using various functional forms for the predictive relationships, linear relationships were found to be the best functional form for site-to-source distance dependence (i.e., $f_1(R)$), local site effects, and magnitude and site-to-source dependences coupled with local site effects (i.e., $f_2(M, R, S_S)$). The resulting function form of the predictive relationship for significant durations of horizontal ground motions proposed in this study is:

$$\ln D_{5-75} \text{ or } \ln D_{5-95} = \ln\{C_1 + C_2 \exp(M-6) + C_3 R + [S_1 + S_2(M-6) + S_3 R]S_S\} \quad \text{(Eq. 5-7)}$$

where, C_1 through C_3 and S_1 through S_3 are regression coefficients; M is the moment magnitude; R is the closest distance to the fault rupture plane (km); and S_S is a binary number representing local site conditions: $S_S = 0$ for rock sites and $S_S = 1$ for soil sites. It should be noted that some terms were removed from the model for $D_{5\text{-}75}$ regressions

because such removal lowered the standard deviations. For those terms, zero-coefficients are assigned instead of using a separate model for $D_{5\text{-}75}$.

5.2.3 Regression Results

The results of NLME regressions (i.e., coefficients, p-values, and standard deviations) for $D_{5\text{-}75}$ and $D_{5\text{-}95}$ are listed in Table 5-1 for both CEUS and WUS. For $D_{5\text{-}75}$, the coefficient C_1 was removed from the model since the model without the term produced a lower total standard deviation. Additionally, the coefficients S_2 and S_3 for WUS were removed, based on the total standard deviation and p-values. As shown in Table 5-1, multiple coefficients have p-values greater than 5 % (i.e., 0.05), but it was decided to keep these coefficients in the proposed model since they were considered necessary to either lower the standard deviations or ensure valid physical interpretation of the data. Comparing the total standard deviations of the duration predictions for CEUS and WUS motions, CEUS appears to have larger standard deviations of the total errors than WUS for both $D_{5\text{-}75}$ and $D_{5\text{-}95}$. This is mainly attributed to much larger standard deviations of inter-event errors for the CEUS predictions than for the WUS ones. The total standard deviations for $D_{5\text{-}95}$ are consistently smaller than those for $D_{5\text{-}75}$.

Table 5-1. Regression coefficients; p-values (in parentheses); and standard deviations of inter-event, intra-event, and total errors.

CEUS									
	C_1	C_2	C_3	S_1	S_2	S_3	τ_{ln}	σ_{ln}	$\sigma_{ln\ total}$
$D_{5\text{-}75}$	0 (n/a)	2.23 (0.000)	0.10 (0.000)	-0.72 (0.007)	-0.19 (0.500)	-0.014 (0.078)	0.46	0.35	0.58
$D_{5\text{-}95}$	2.50 (0.014)	4.21 (0.000)	0.14 (0.000)	-0.98 (0.122)	-0.45 (0.493)	-0.0071 (0.626)	0.37	0.32	0.49
WUS									
	C_1	C_2	C_3	S_1	S_2	S_3	τ_{ln}	σ_{ln}	$\sigma_{ln\ total}$
$D_{5\text{-}75}$	0 (n/a)	1.86 (0.000)	0.06 (0.000)	0.22 (0.165)	0 (n/a)	0 (n/a)	0.28	0.37	0.46
$D_{5\text{-}95}$	1.50 (0.010)	3.22 (0.000)	0.11 (0.000)	2.01 (0.000)	0.80 (0.094)	-0.0097 (0.341)	0.26	0.28	0.38

The distributional assumptions for intra-event errors and random-effects were assessed by the normal Q-Q plots shown in Figure 5-3 and Figure 5-4 for $D_{5\text{-}75}$ and $D_{5\text{-}95}$, respectively. For standardized intra-event errors below -3, there are several data points that do not plot close to the straight lines for $D_{5\text{-}75}$ for both CEUS and WUS, and for $D_{5\text{-}95}$ in CEUS. Yet, it seems reasonable that the overall intra-event errors follow the normal distribution. Also, the random-effects are shown to be normally distributed both for $D_{5\text{-}75}$ and $D_{5\text{-}95}$ for both CEUS and WUS. Additionally, scatter plots for intra-event errors and random-effects are shown in Figure 5-5 and Figure 5-6 for $D_{5\text{-}75}$ and $D_{5\text{-}95}$, respectively. There are some outliers for $D_{5\text{-}75}$ for both CEUS and WUS, and $D_{5\text{-}95}$ in CEUS, which correspond to the outliers in the normal Q-Q plots. However, overall distributions appear to be symmetrical with respect to the zero lines of the standardized inter-event errors and random-effects.

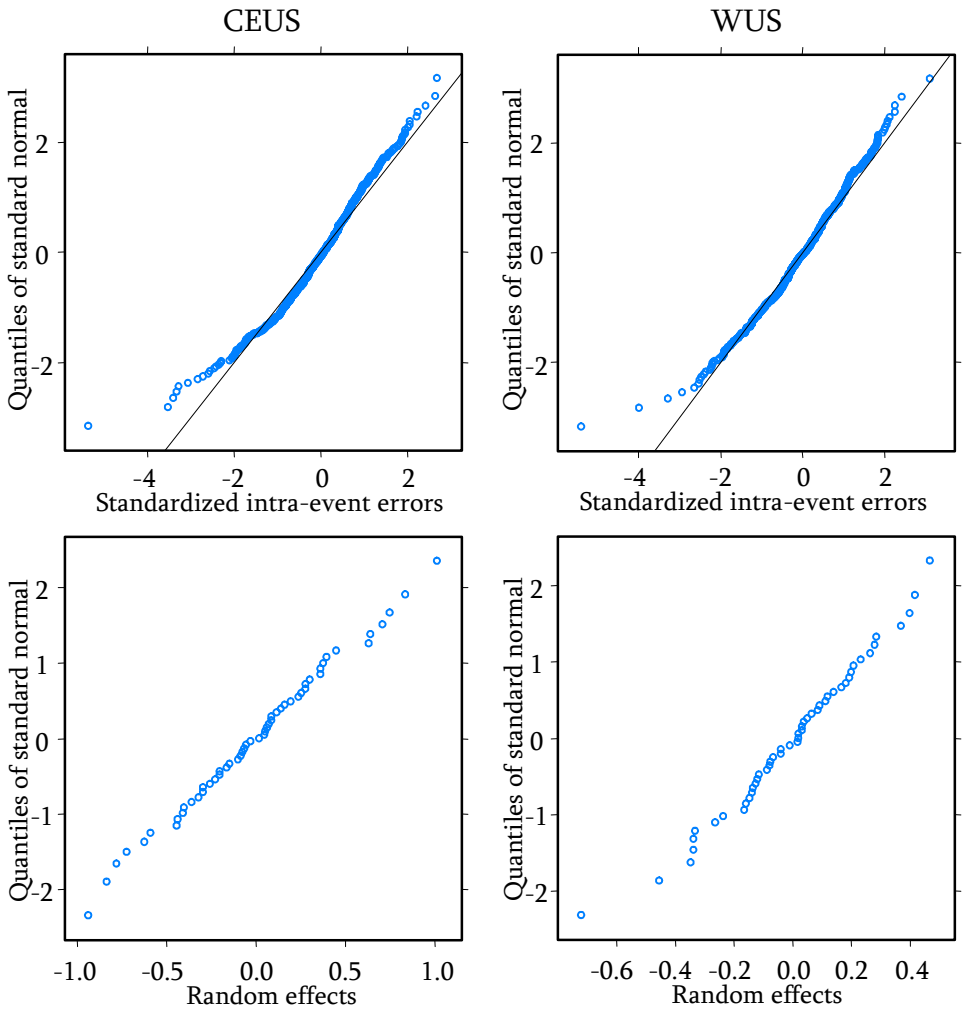

Figure 5-3. Normal Q-Q plots of intra-event errors (top) and random-effects (bottom) for CEUS (left) and WUS (right): $D_{5\text{-}75}$.

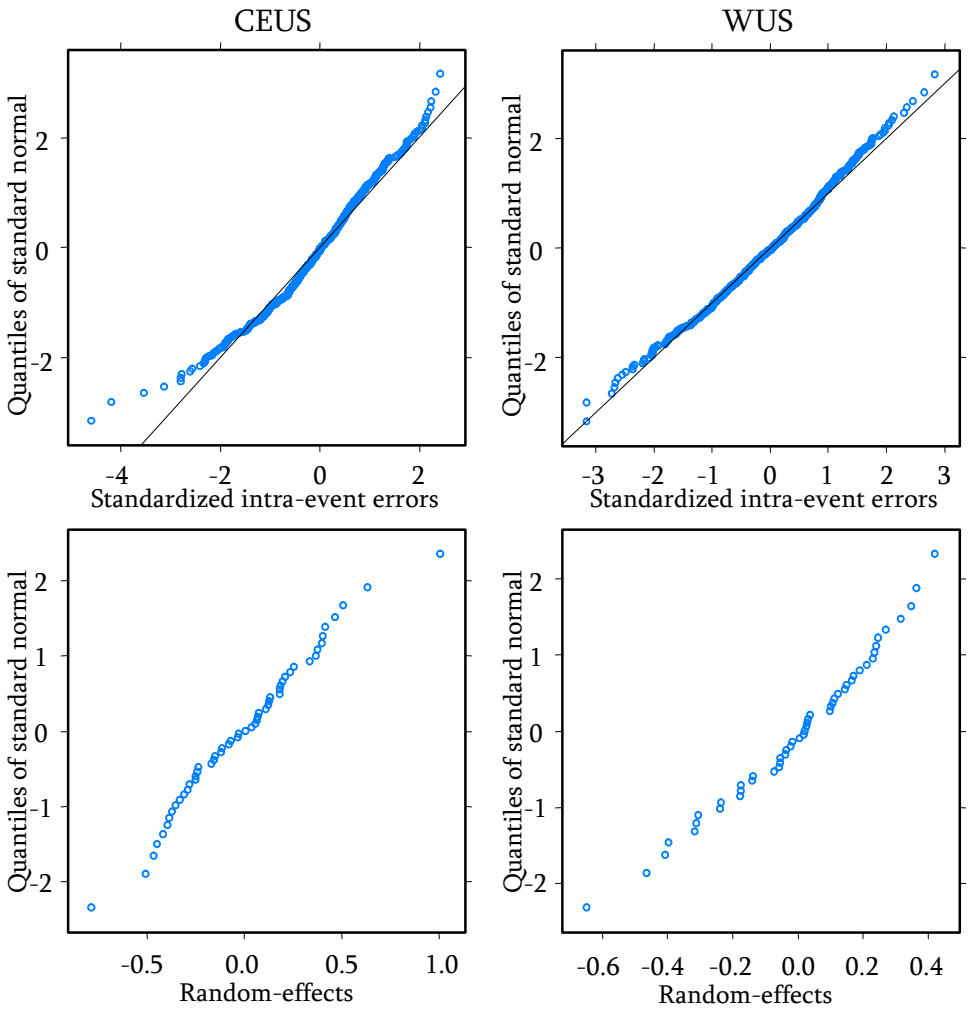

Figure 5-4. Normal Q-Q plots of intra-event errors (top) and random-effects (bottom) for CEUS (left) and WUS (right): $D_{5\text{-}95}$.

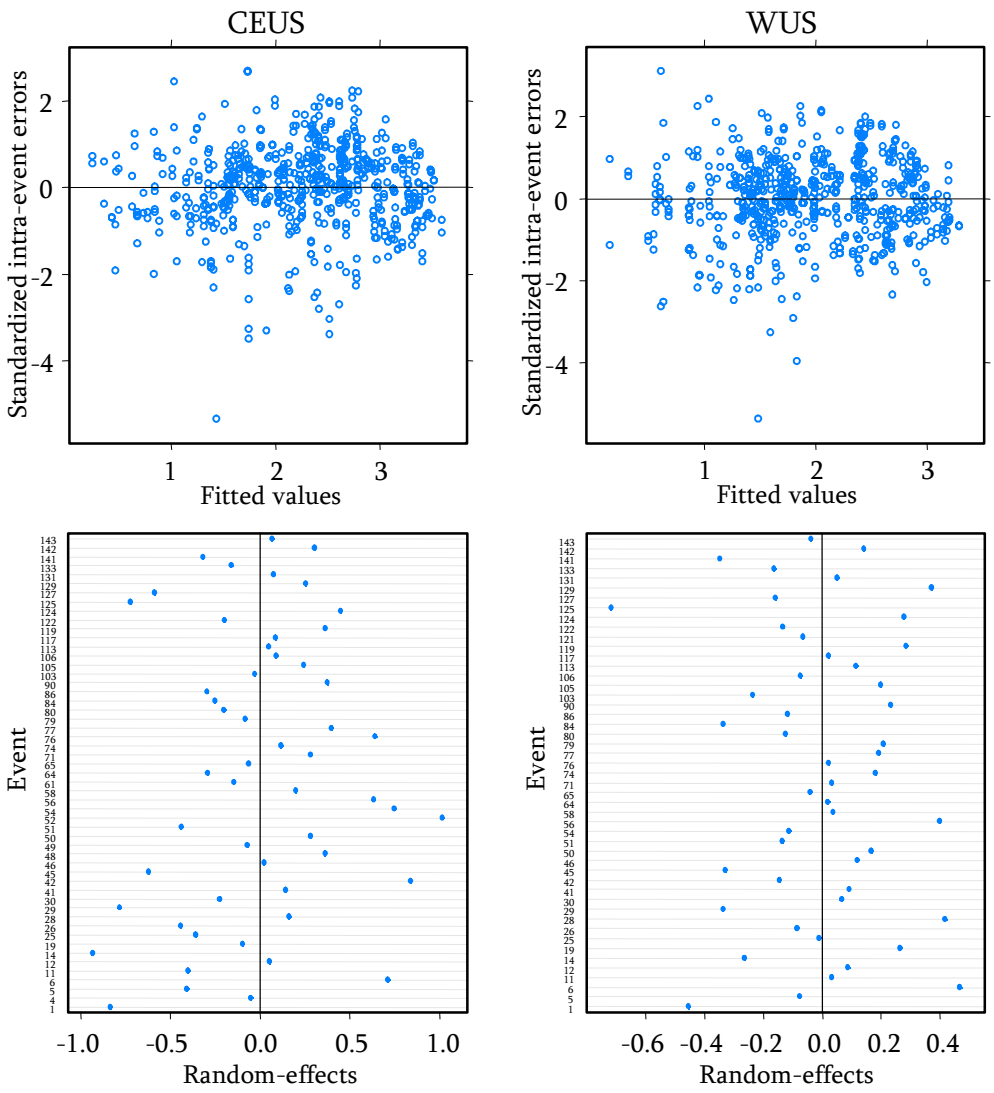

Figure 5-5. Scatter plots of intra-event errors (top) and random-effects (bottom) for CEUS (left) and WUS (right): $D_{5\text{-}75}$.

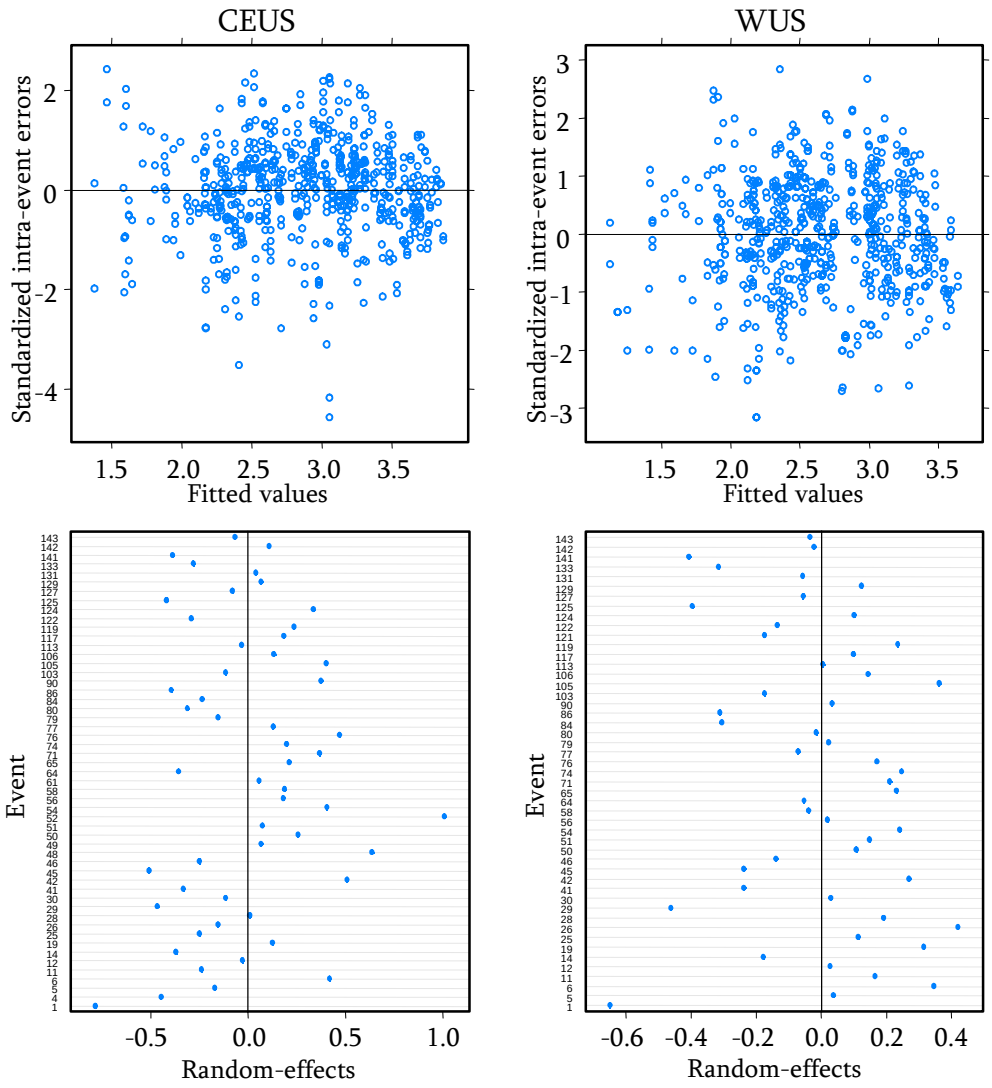

Figure 5-6. Scatter plots of intra-event errors (top) and random-effects (bottom) for CEUS (left) and WUS (right): $D_{5\text{-}95}$.

The $D_{5\text{-}75}$ and $D_{5\text{-}95}$ predictions for CEUS motions are compared with actual data values per magnitude bin in Figure 5-7 and Figure 5-8, respectively. The center values (i.e., 5.5, 6.5, and 7.5) of magnitude bins were used for plotting the proposed predictive relationships. Also plotted in these figures are curves for the median plus/minus one total standard deviation ($\sigma_{ln\ total}$). This range encompasses about 68% of the observed data. As shown in Figure 5-7 and Figure 5-8, the proposed relations represent the data well for the

magnitude and distance ranges. It should be noted that the extrapolation of the proposed relations for small magnitudes (i.e., M 5-6) at the distances below about 8 km may not be valid due to the absence of near-fault ground motion recordings for small magnitudes in the ground motion data set.

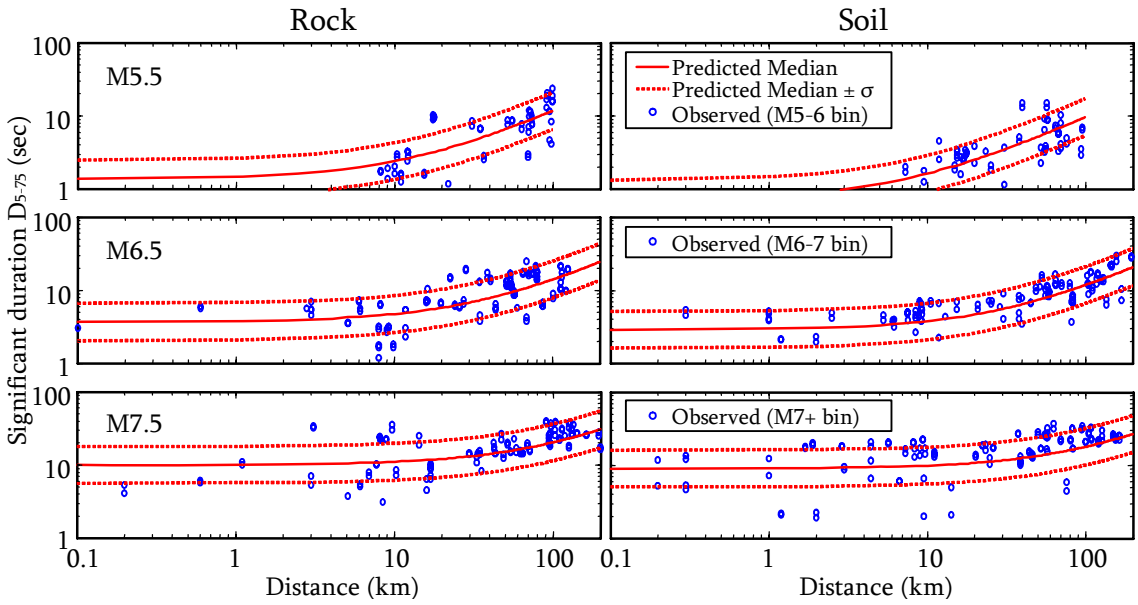

Figure 5-7. Predicted median and median +/- $\sigma_{ln\ total}$ for $D_{5\text{-}75}$ versus distance for M5.5, M6.5, and M7.5 for rock (left) and soil (right) sites for CEUS. Also plotted are the data from the respective magnitude bins.

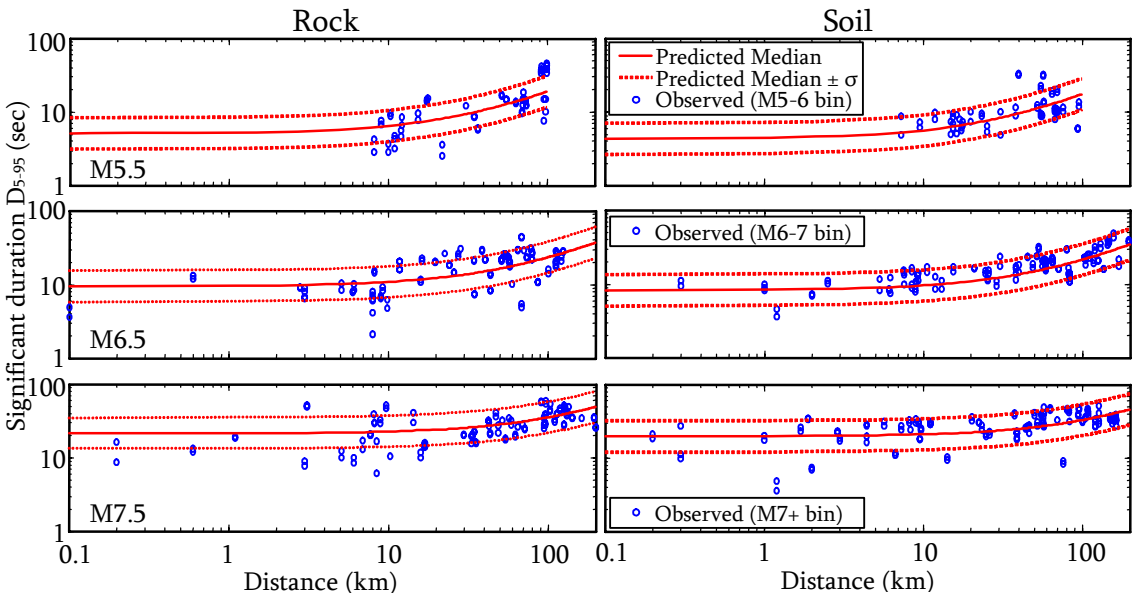

Figure 5-8. Predicted median and median +/- $\sigma_{ln\ total}$ for $D_{5\text{-}95}$ versus distance for M5.5, M6.5, and M7.5 for rock (left) and soil (right) sites for CEUS. Also plotted are the data from the respective magnitude bins.

Using Eq. 5-7 in conjunction with the coefficients listed in Table 5-1, $D_{5\text{-}75}$ and $D_{5\text{-}95}$ medians for CEUS are plotted in Figure 5-9 as functions of site-to-source distance (R) for M5.5, M6.5, and M7.5 for rock sites and soil sites. Similar to the trends observed from WUS motions by other investigators (e.g., Abrahamson and Silva, 1996; Kempton and Stewart, 2006), it is clearly seen from Figure 5-9 that significant durations for CEUS increases as site-to-source distance and magnitude increase. However, contrary to WUS motions, significant durations of rock motions in CEUS tend to be slightly longer than those of soil motions. It is not straightforward to explain this inconsistent trend between WUS and CEUS motions because significant durations are associated with both amplitude and frequency of ground motions. Additional analyses are required to better understand this unexpected trend.

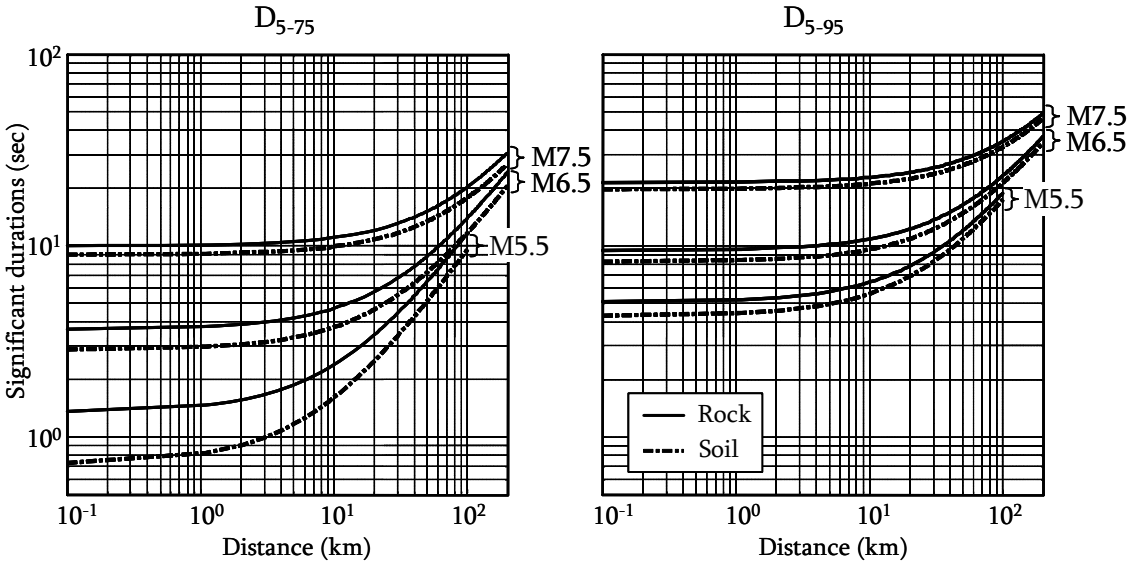

Figure 5-9. Predicted medians for $D_{5\text{-}75}$ and $D_{5\text{-}95}$ versus distance for the magnitudes 5.5, 6.5, and 7.5 for rock and soil sites for CEUS.

To identify differences in $D_{5\text{-}75}$ and $D_{5\text{-}95}$ predictions for CEUS versus WUS, comparison plots are shown in Figure 5-10 and Figure 5-11, respectively. For rock motions, the significant durations for CEUS are systematically longer than those for WUS. In contrast, for soil motions, an opposite trend is observed for small and intermediate earthquake magnitudes (i.e., M5.5 and M6.5) for R < 20 km. However, the differences are small.

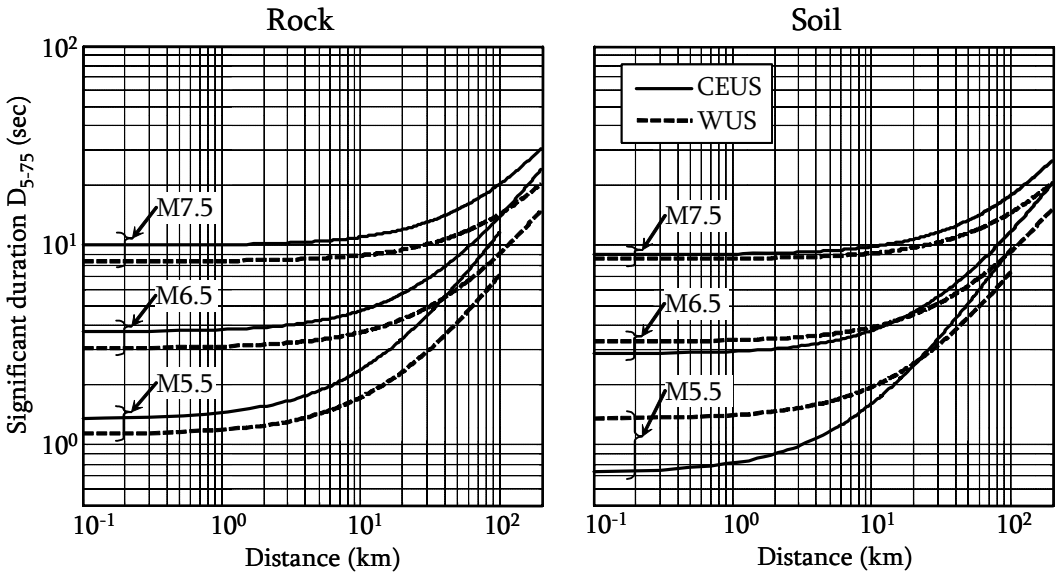

Figure 5-10. D_{5-75} comparison of CEUS and WUS for rock (left) and soil (right) sites.

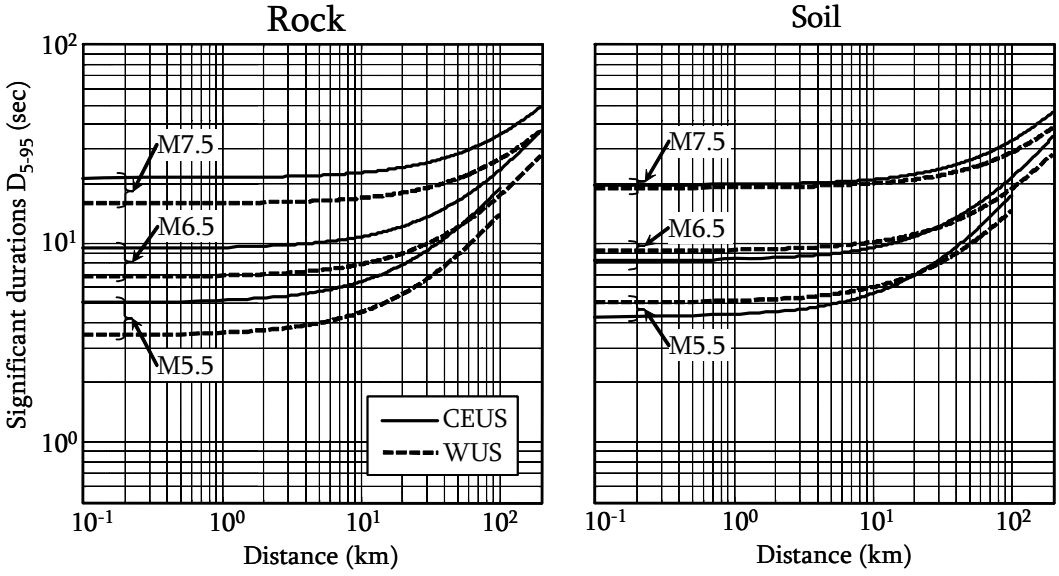

Figure 5-11. D_{5-95} comparison of CEUS and WUS for rock (left) and soil (right) sites.

5.2.4 Comparison with Existing Relationships

The proposed relationship for WUS is compared to two existing empirical relationships for active shallow crustal regions (e.g., WUS) that were developed through the NLME regression analyses by Abrahamson and Silva (1996) and Kempton and Stewart (2006). Abrahamson and Silva's model was developed using data from 655 strong ground motion recordings from 58 earthquakes in active shallow crustal regions. The model is expressed as a function of earthquake magnitude, site-to-source distance, and local site conditions. Their model was based on the same site classification system as used in this study (i.e., according to Geomatrix site codes, A and B for rock sites; C and D for soil sites). Different from this study's models and Kempton and Stewart's model, a cut-off distance of 10 km was used based on the observed trend that significant durations were independent of the site-to source distance for distances closer than 10 km. Kempton and Stewart used a similar functional form to the Abrahamson and Silva model for developing a "base" model using data from 1557 recordings from 73 shallow crustal earthquakes. Kempton and Stewart expanded the base model by adding several terms that incorporate near-fault directivity and deep basin effects. Also, local site conditions were represented via the average shear wave velocity in the upper 30 m ($V_{S\text{-}30}$) of a profile instead of using site classifications.

Figure 5-12 and Figure 5-13 show comparisons of the significant durations predicted by this study, Abrahamson and Silva (1996), and Kempton and Stewart (2006). Comparing the durations for WUS motions using the predictive relation from this study and from existing models for large magnitudes for rock and soil sites, the existing relations

consistently predict longer durations than this study's relation. This might be attributed to the duration criteria for $D_{5\text{-}75}$ used in the data selection described previously in Chapter 2.

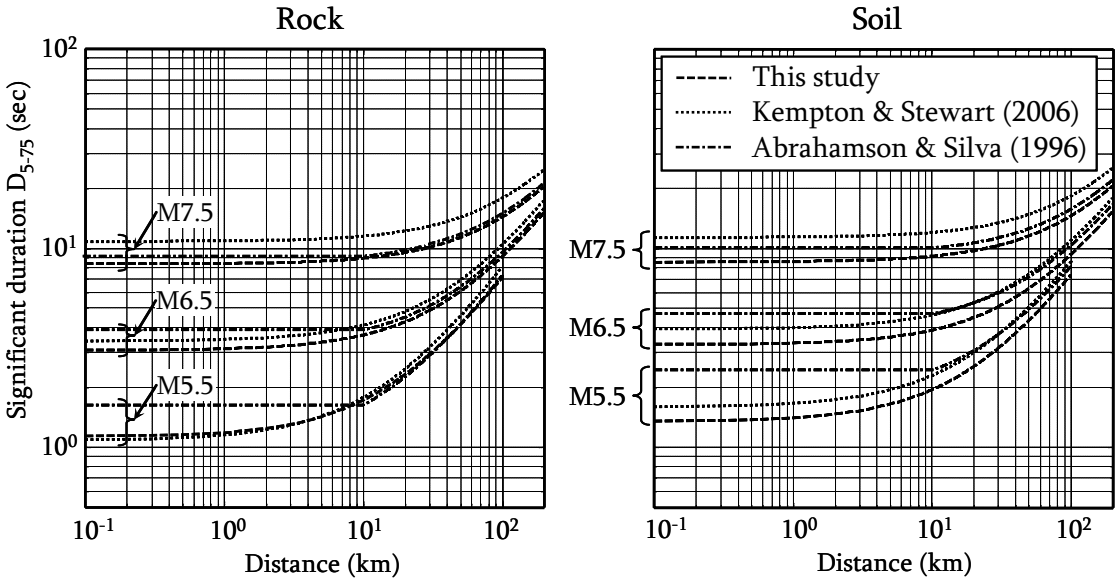

Figure 5-12. $D_{5\text{-}75}$ comparison of this study's model and existing relationships for WUS. The base model was used for Kempton & Stewart (2006).

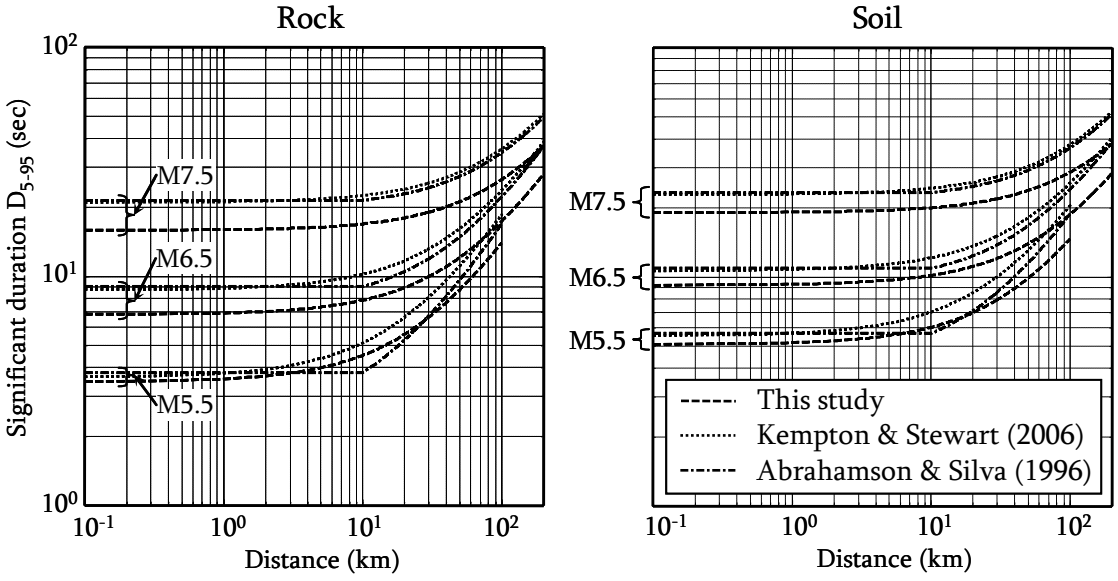

Figure 5-13. $D_{5\text{-}95}$ comparison of this study's model and existing relationships for WUS. The base model was used for Kempton & Stewart (2006).

5.3 Bracketed Duration and Effective Duration: $D_{bracket}$ and D_{eff}

5.3.1 Definitions

Different from the significant durations which are based on a relative criterion, the bracketed duration is determined using an absolute criterion based on the time interval between the first and last exceedance of ground acceleration above or below threshold acceleration. Commonly, the threshold acceleration is +/- 0.05 g (e.g., Bolt, 1973; Hays, 1975; Page et al., 1972). An example of the bracketed duration determination is shown in Figure 5-14. Consequently, it is possible for a ground motion to have zero-duration if the peak ground acceleration (*pga*) of the motion is less than the specified threshold.

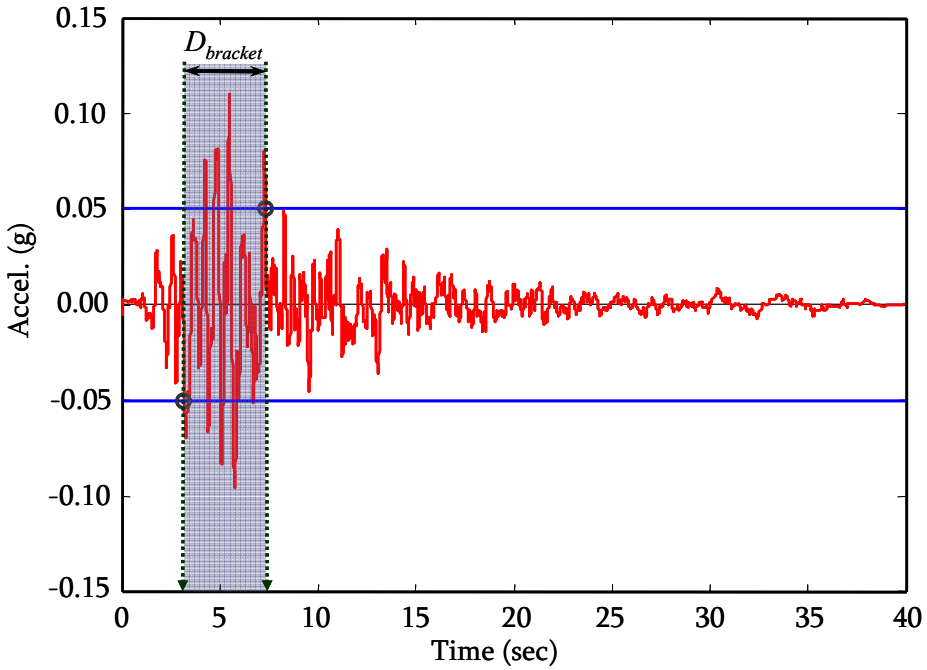

Figure 5-14. Determination of the bracketed duration for a ground acceleration time history (BES090: M6.9; R49.9km) from the 1989 Loma Prieta earthquake.

Effective duration (D_{eff}) proposed by Bommer and Martinez-Pereira (1999) is defined using both relative and absolute criteria. The effective duration is based on Arias intensity (Arias, 1970):

$$I_{xx} = \frac{\pi}{2g}\int_0^{t_d} a_x^2(t)dt \qquad \text{(Eq. 5-8)}$$

where: I_{xx} is Arias intensity for a given direction, x; g is the coefficient of acceleration due to gravity; t_d is the total duration; and $a_x(t)$ is the ground acceleration in the x-direction. The effective duration is defined as the time interval between the times corresponding to an Arias intensity of 0.01 m/sec and to an Arias intensity value 0.125 m/sec below the maximum Arias intensity. An example of the effective duration determination is shown in Figure 5-15. Therefore, earthquake motions that have Arias intensities less than 0.135 m/sec have zero effective durations.

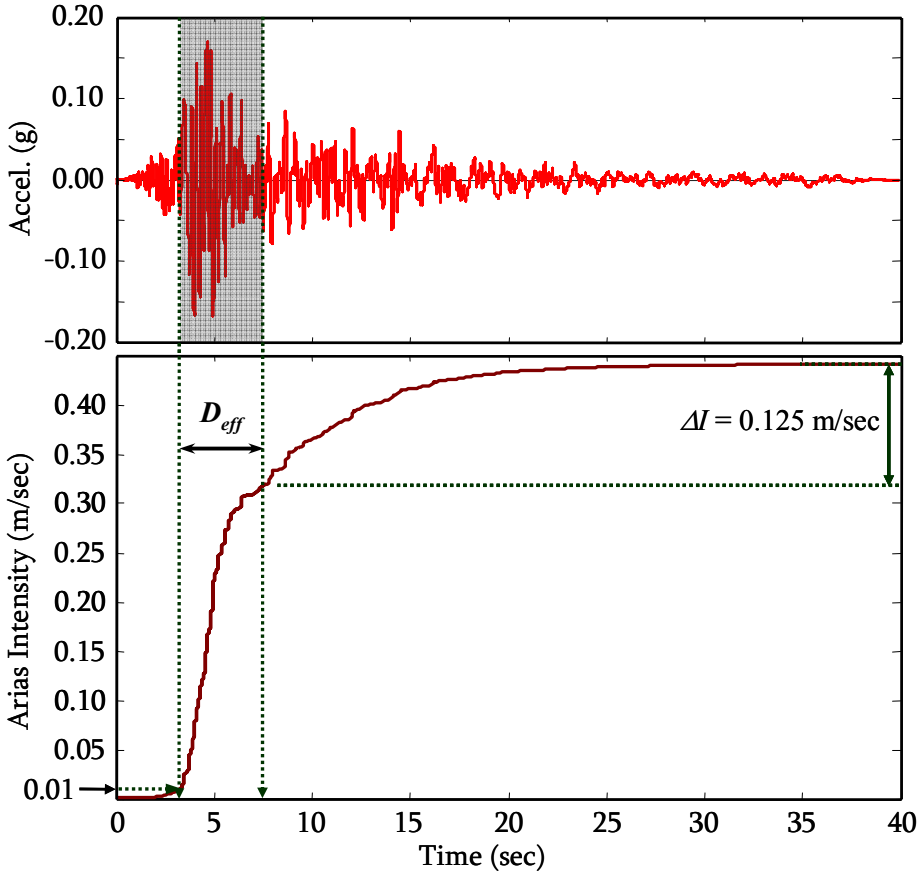

Figure 5-15. Determination of the effective duration in Arias intensity plot for a ground acceleration time history (BES090: M6.9; R49.9km) from the 1989 Loma Prieta earthquake.

5.3.2 Proposed Model

The proposed model consists of two parts: one is the non-zero duration model that is developed through the NLME regression analyses using non-zero duration data; the other is a weighting function that represents the probability of non-zero duration occurrence for a given earthquake magnitude, distance, and site condition, which is estimated through logistic regressions. The two-part model approach was used because of the considerable number of zero-duration motions, as shown in Figure 5-16. Comparing CEUS and WUS, WUS appears to have more zero-duration motions than CEUS. Also, rock motion data

include more zero-durations than soil motion data. Comparing the bracketed and effective durations, effective duration data contain almost twice as many zero-duration motions than bracketed duration data.

The entire ground motion duration data set (i.e., zero and non-zero duration data) does not follow a normal distribution, as may be observed from the normal Q-Q plots shown in Figure 5-17. Also, a log-normal distribution cannot be used to represent this data set due to the inclusion of the zero-durations (i.e., log of zero is infinity). Furthermore, the zero-durations do not correlate well to the independent variables (e.g., magnitude and site-to-source distance) in the regression analyses. Hence, only non-zero duration data were used in the NLME regression analyses. The total number of non-zero duration data used in the NLME regressions was 568 and 478 for bracketed duration for CEUS and WUS, respectively, and 507 and 318 for effective duration for CEUS and WUS, respectively.

However, the zero-duration data needs to be incorporated in the predictive models, otherwise the models would be biased toward longer durations. This is especially true for the effective duration due to the considerable number of zero-duration motions. As a result, a logistic regression method was employed to model the probability of zero-duration occurrence as a function of earthquake magnitude, distance, and site condition. Then, these probability models were applied as weighting functions to the NLME regression results.

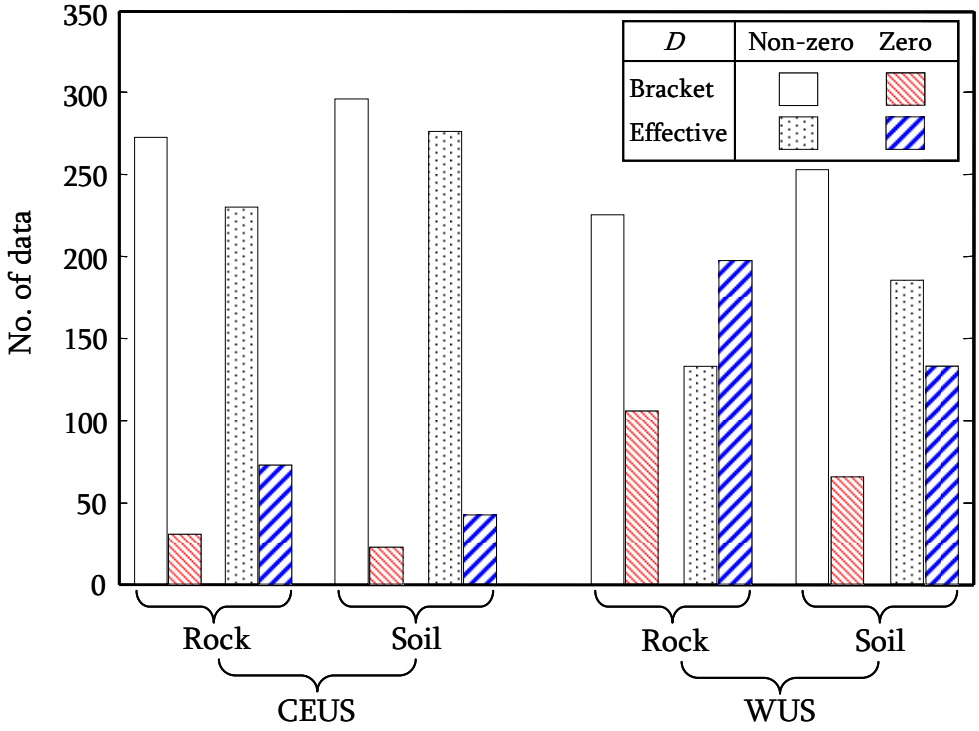

Figure 5-16. Zero bracketed and effective duration population.

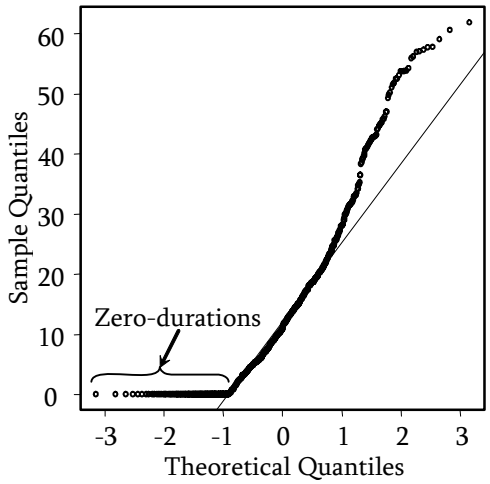

Figure 5-17. Normal Q-Q plot of bracketed duration data: WUS.

5.3.2.1 Non-zero Duration Model

In assessing the normal distribution of the non-zero duration data, it was found that adding one second to the durations contributed to optimizing the overall log-normality of intra-event errors as well as duration data. For example, Figure 5-18 shows the improvement in the log-normal distributions of the WUS bracketed duration data and the resulting intra-event errors. As may be observed from this figure, $\ln(D_{bracket}+1)$ more closely follows a normal distribution than $\ln(D_{bracket})$. Accordingly, the NLME regression analyses were performed on $\ln(D+1)$, where D is the bracketed or effective duration.

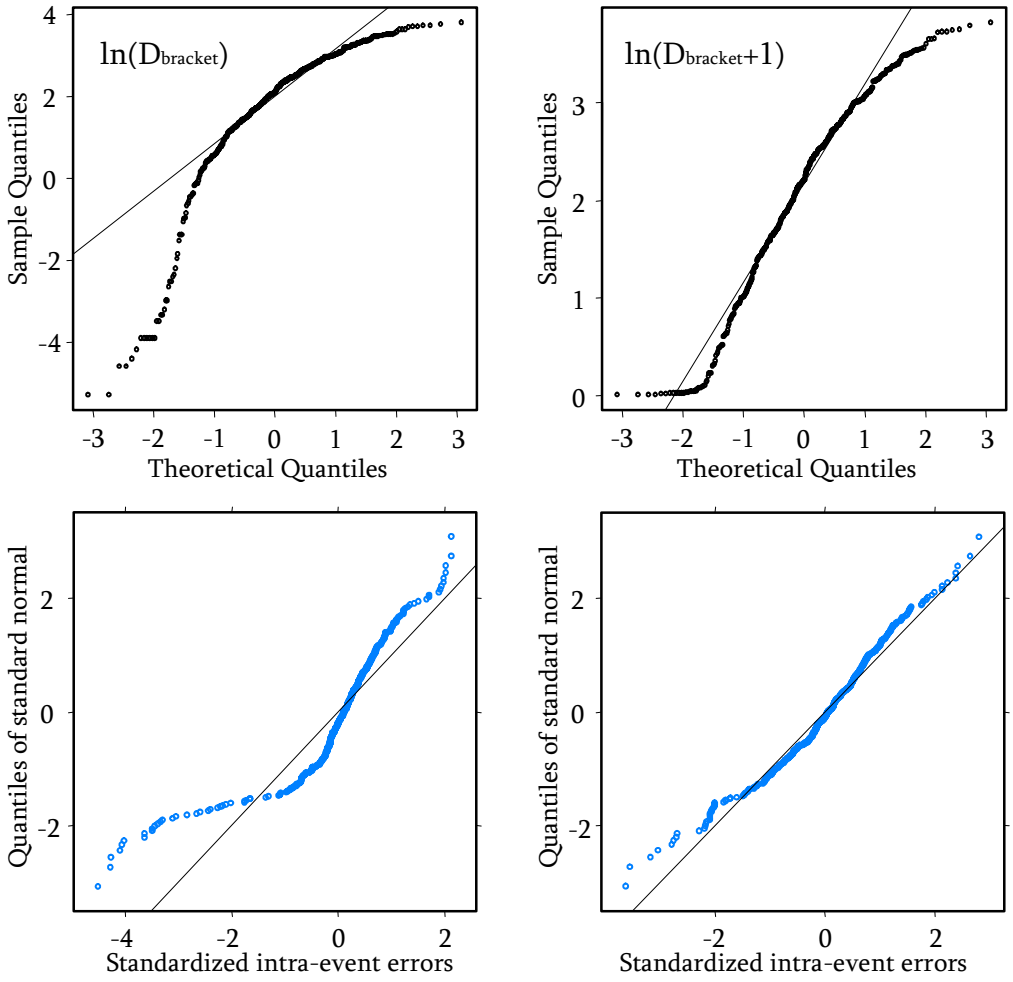

Figure 5-18. Comparisons of normal Q-Q plots for $\ln(D_{bracket})$ (left) and $\ln(D_{bracket}+1)$ (right) and their intra-event errors resulted (bottom): WUS.

After considering numerous functional forms of the predictive relationship in the NLME regressions, the proposed model for both bracketed and effective durations was found to provide the best fit of non-zero duration data, which is given by:

$$D_{bracket} \text{ or } D_{eff} = \exp\left(C_1 + C_2(M-6) + C_3 R + (S_1 + S_2 R)S_S\right) - 1 \qquad \text{(Eq. 5-9)}$$

where: C_1 through C_3, S_1, and S_2 are regression coefficients; M is moment magnitude; R is the closest distance to the fault rupture plane (km); and S_S is a binary number representing local site conditions: $S_S = 0$ for rock sites, $S_S = 1$ for soil sites. Note that the proposed model shown as Eq. 5-9 was rewritten from its original form by taking exponential and subtracting 1 from both sides of the original equation, i.e.: $D = \exp[\ln(D+1)]-1$.

5.3.2.2 Combined Model with Weighting Function

To estimate the probability of the occurrence of a zero-duration motion, logistic regressions were implemented separately for each tectonic regime and site condition, as a function of M and R. The logistic function is given by:

$$p(D=0 \mid M,R) = \frac{e^{\beta_1+\beta_2 M+\beta_3 R}}{1+e^{\beta_1+\beta_2 M+\beta_3 R}} \qquad \text{(Eq. 5-10)}$$

where: $p(D = 0|M, R)$ is the probability of zero-duration for a given M and R; β_1 through β_3 are the regression coefficients determined from separate logistic regressions for each site condition of CEUS and WUS. Then, the probability of non-zero duration occurrence is determined by subtracting the probability of zero-duration from the total probability of 1 as shown below:

$$p(D>0 \mid M,R) = 1 - p(D=0 \mid M,R) = \frac{1}{1+e^{\beta_1+\beta_2 M+\beta_3 R}} \qquad \text{(Eq. 5-11)}$$

Eq. 5-11 in conjunction with a suite of regression coefficients for a given site condition and tectonic region is used as the weighting function that is multiplied with Eq. 5-9. Finally, the combined model proposed for horizontal durations including zero-durations is given by:

$$D_{bracket} \text{ or } D_{eff} = \left\{\exp\left(C_1 + C_2\left(M-6\right) + C_3 R + \left(S_1 + S_2 R\right)S_S\right) - 1\right\} \cdot p\left(D > 0 \mid M, R, S_S\right) \quad \text{(Eq. 5-12)}$$

5.3.3 Regression Results

The results from the NLME regression analyses of non-zero duration data are shown in Table 5-2. Most of the p-values for the regression coefficients are less than 5% (i.e., 0.05), which indicates they have statistical significance. For WUS, some coefficients (i.e., S_1 for $D_{bracket}$; S_1 and S_2 for D_{eff}) appeared to be statistically insignificant (i.e., p-values > 5% or 0.05). However, it was decided to retain these coefficients in the proposed models because excluding them would result in higher total standard deviations ($\sigma_{ln\ total}$). Comparing CEUS and WUS, the standard deviations are similar to each other.

Table 5-2. NLME Regression results: regression coefficients; p-values (in parentheses); and standard deviations of inter-event, intra-event, and total errors.

CEUS								
	C_1	C_2	C_3	S_1	S_2	τ_{ln}	σ_{ln}	$\sigma_{ln\ total}$ †
$D_{bracket}$	2.67 (0.000)	0.75 (0.000)	-0.0058 (0.000)	-0.16 (0.033)	0.0021 (0.053)	0.43	0.51	0.67
D_{eff}	2.03 (0.000)	0.99 (0.000)	-0.0066 (0.000)	-0.18 (0.007)	0.0043 (0.000)	0.32	0.45	0.55
WUS								
	C_1	C_2	C_3	S_1	S_2	τ_{ln}	σ_{ln}	$\sigma_{ln\ total}$ †
$D_{bracket}$	2.04 (0.000)	0.95 (0.000)	-0.022 (0.000)	0.074 (0.391)	0.0045 (0.0113)	0.38	0.53	0.65
D_{eff}	1.49 (0.000)	1.04 (0.000)	-0.014 (0.000)	0.14 (0.077)	0.0020 (0.388)	0.36	0.42	0.55

† : the total standard deviation values are valid for ln(D+1).

The distributional assumptions of the intra-event errors and random-effects were assessed using normal Q-Q plots. Figure 5-19 and Figure 5-20 are the normal Q-Q plots for bracketed and effective durations, respectively. For both durations, there are some outliers, but in general, the overall distributions of intra-event errors and random-effects follow the normal distributions for both CEUS and WUS. Additionally, the scatter plots for intra-event errors and random-effects are provided in Figure 5-21 and Figure 5-22 for bracketed and effective durations, respectively. As with the normal Q-Q plots, there are some asymmetrical data points with respect to the zero lines of the standardized inter-event errors or random-effects. However, the number of these data points is negligibly small.

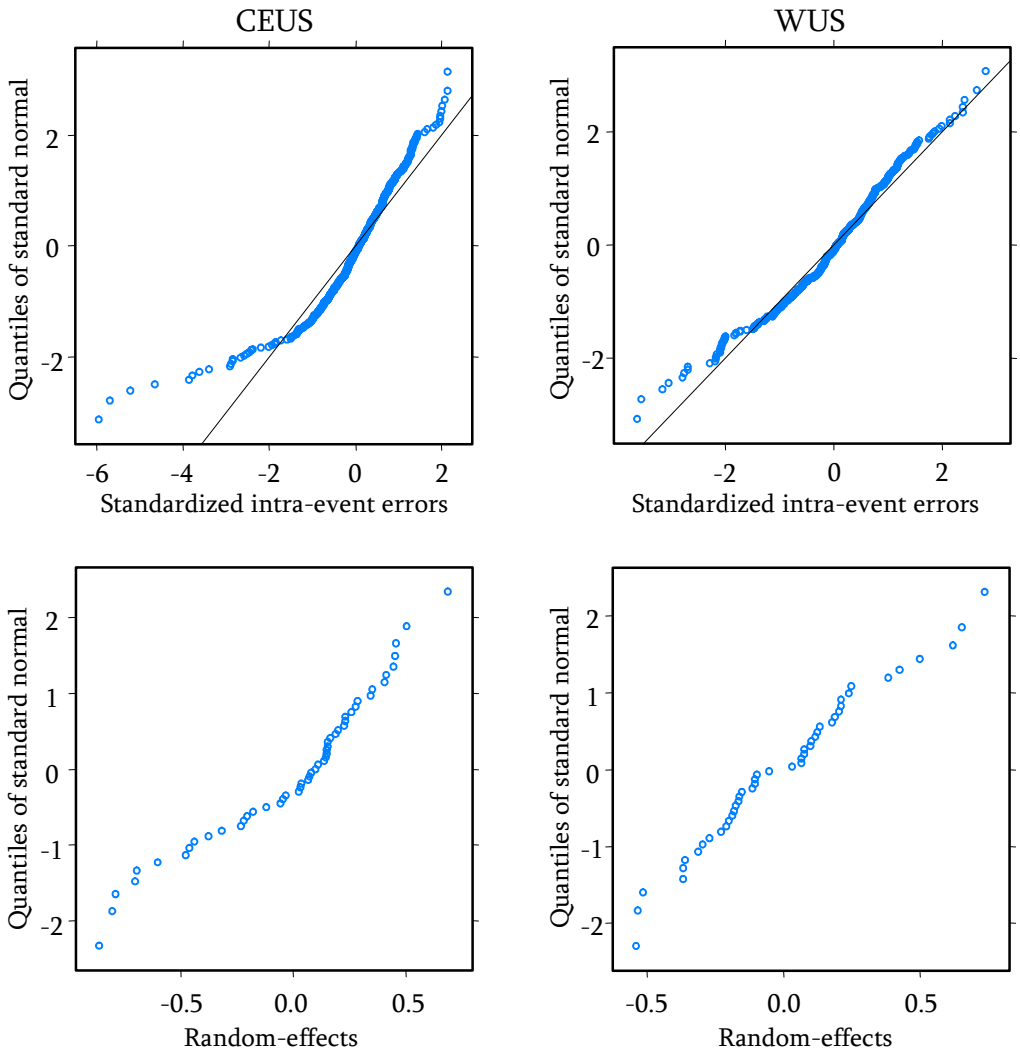

Figure 5-19. Normal Q-Q plots of intra-event errors (top) and random-effects (bottom) for CEUS (left) and WUS (right): $D_{bracket}$.

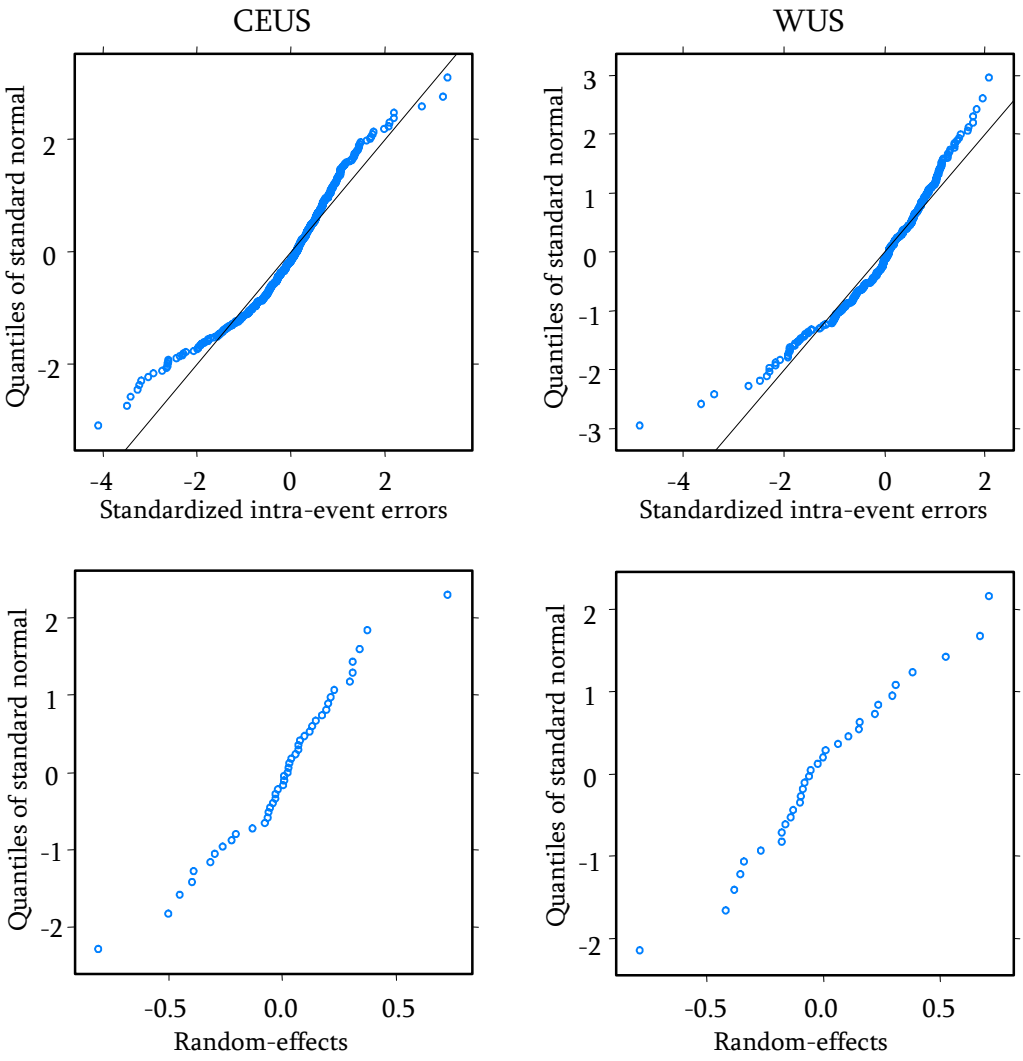

Figure 5-20. Normal Q-Q plots of intra-event errors (top) and random-effects (bottom) for CEUS (left) and WUS (right): D_{eff}.

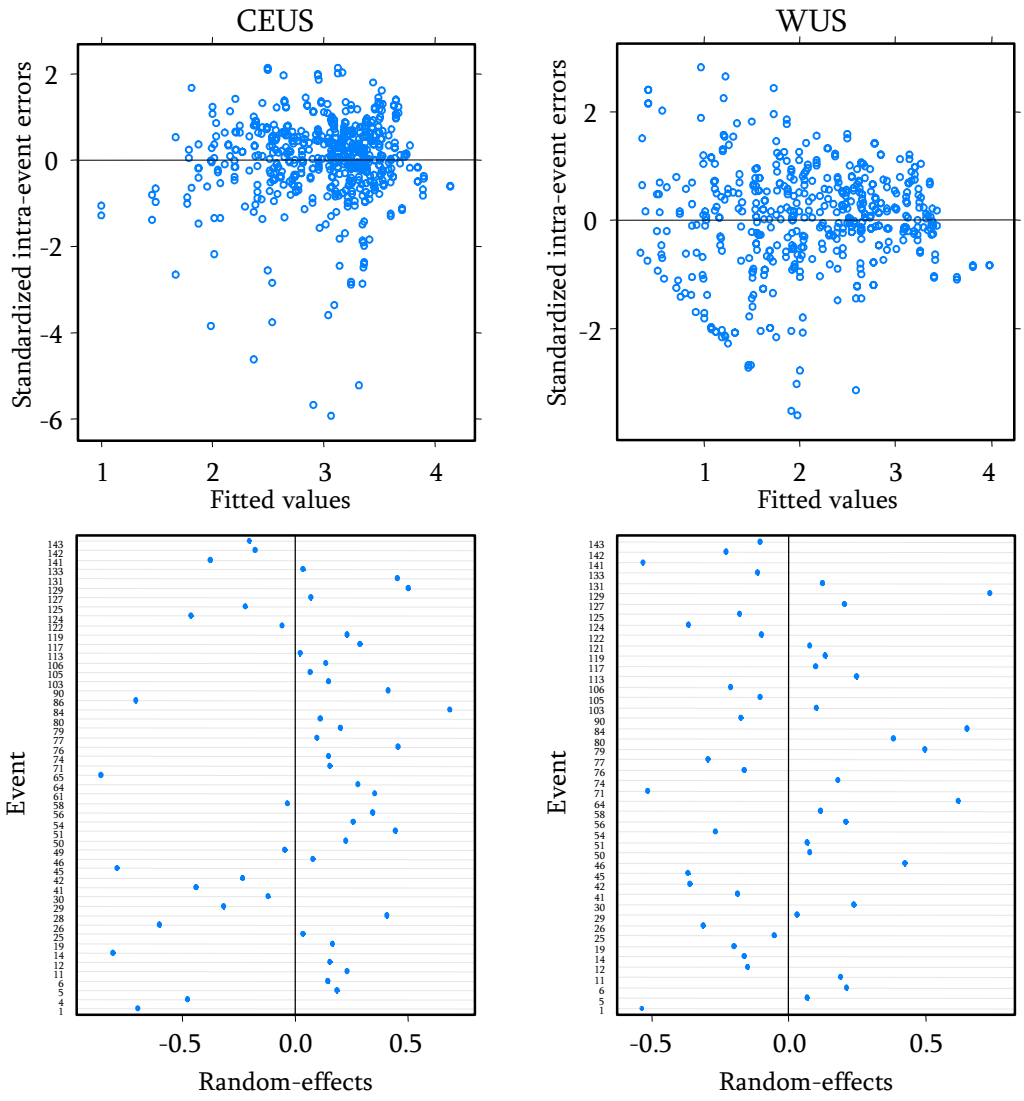

Figure 5-21. Scatter plots of intra-event errors (top) and random-effects (bottom) for CEUS (left) and WUS (right): $D_{bracket}$.

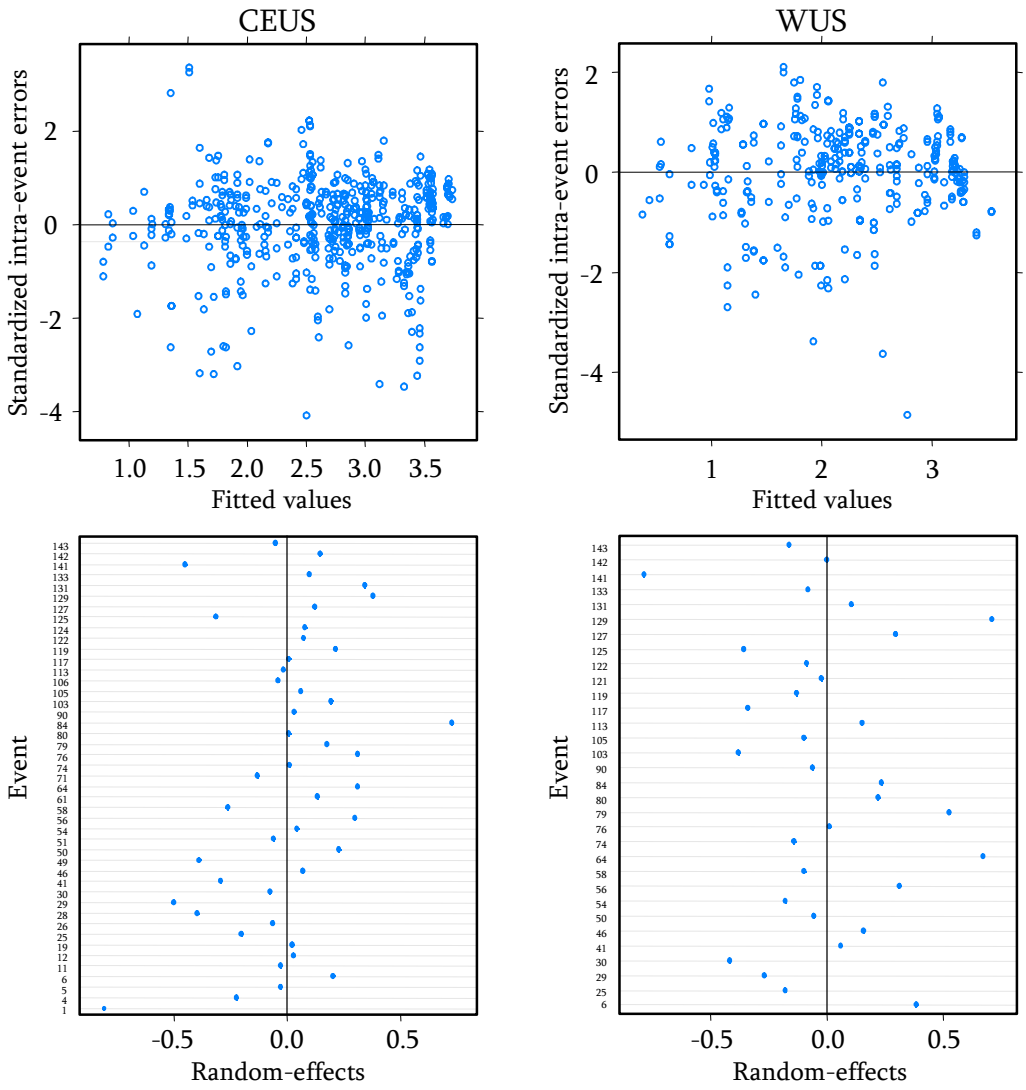

Figure 5-22. Scatter plots of intra-event errors (top) and random-effects (bottom) for CEUS (left) and WUS (right): D_{eff}.

Using Eq. 5-9 in conjunction with the regression coefficients from Table 5-2, the median and median plus/minus $\sigma_{ln\ total}$ predicted for non-zero $D_{bracket}$ and D_{eff} motions are plotted in Figure 5-23 and Figure 5-24, respectively, for M5.5, M6.5, and M7.5. Also plotted in these figures are the non-zero duration data from the respective magnitude bins. As shown in Figure 5-23 and Figure 5-24, the proposed relations represent the data well for the magnitude and distance ranges. It should be noted that the extrapolation to small

magnitudes (i.e., M 5-6) at distances less than about 8 km may not be valid due to the absence of near-fault ground motion recordings for the small magnitudes in the ground motion data set.

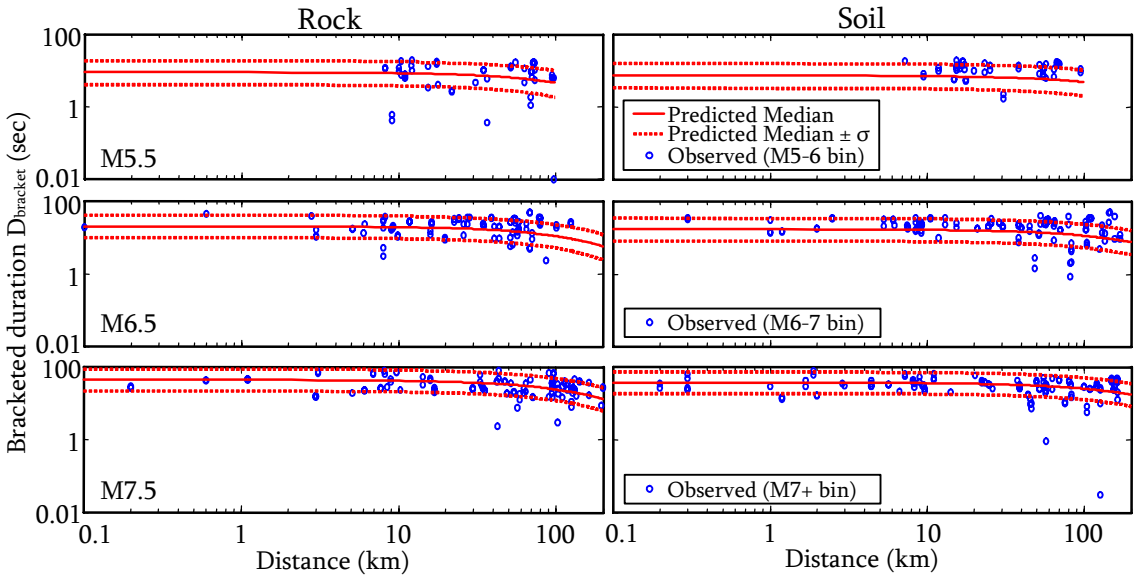

Figure 5-23. Predicted median and median +/- $\sigma_{ln\ total}$ for non-zero $D_{bracket}$ versus distance for M5.5, M6.5, and M7.5 for rock (left) and soil (right) sites for CEUS. Also plotted are the data from the respective magnitude bins.

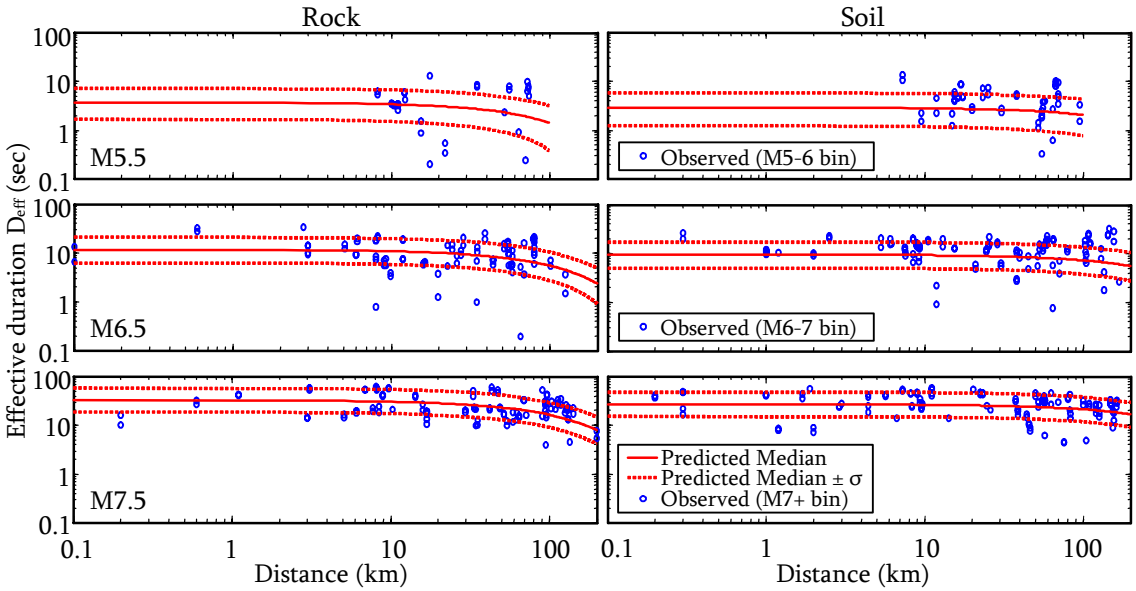

Figure 5-24. Predicted median and median +/- $\sigma_{ln\ total}$ for non-zero D_{eff} versus distance for M5.5, M6.5, and M7.5 for rock (left) and soil (right) sites for CEUS. Also plotted are the data from the respective magnitude bins.

Figure 5-25 shows the predicted medians of the non-zero duration model (i.e., Eq. 5-9) as a function of distance for different earthquake magnitudes. For both CEUS and WUS, the bracketed and effective durations decrease with increasing distance, but increase with increasing magnitude. Significant dependences of durations on magnitude are observed, especially at distances below 50 km where an increase in one magnitude unit results in at least a twofold increase in duration. For WUS, soil motions are consistently estimated to have longer durations than rock motions. However, for CEUS, soil motions appear to have shorter bracketed and effective durations than rock motions at the distances below about 75 km and 45 km, respectively. However, at greater distances, soil motions have longer durations than rock motions, which is attributed to the relatively lower rates of duration attenuation of soil motions. Figure 5-26 shows comparisons of the bracketed and effective durations for CEUS and WUS motions. For both rock and soil sites, CEUS motions consistently have longer durations than WUS motions. Also, it is clearly seen that as distance increases, WUS durations tend to decrease at a faster rate than CEUS durations. Consequently, CEUS motions have significantly longer durations than WUS motions at the farther distances.

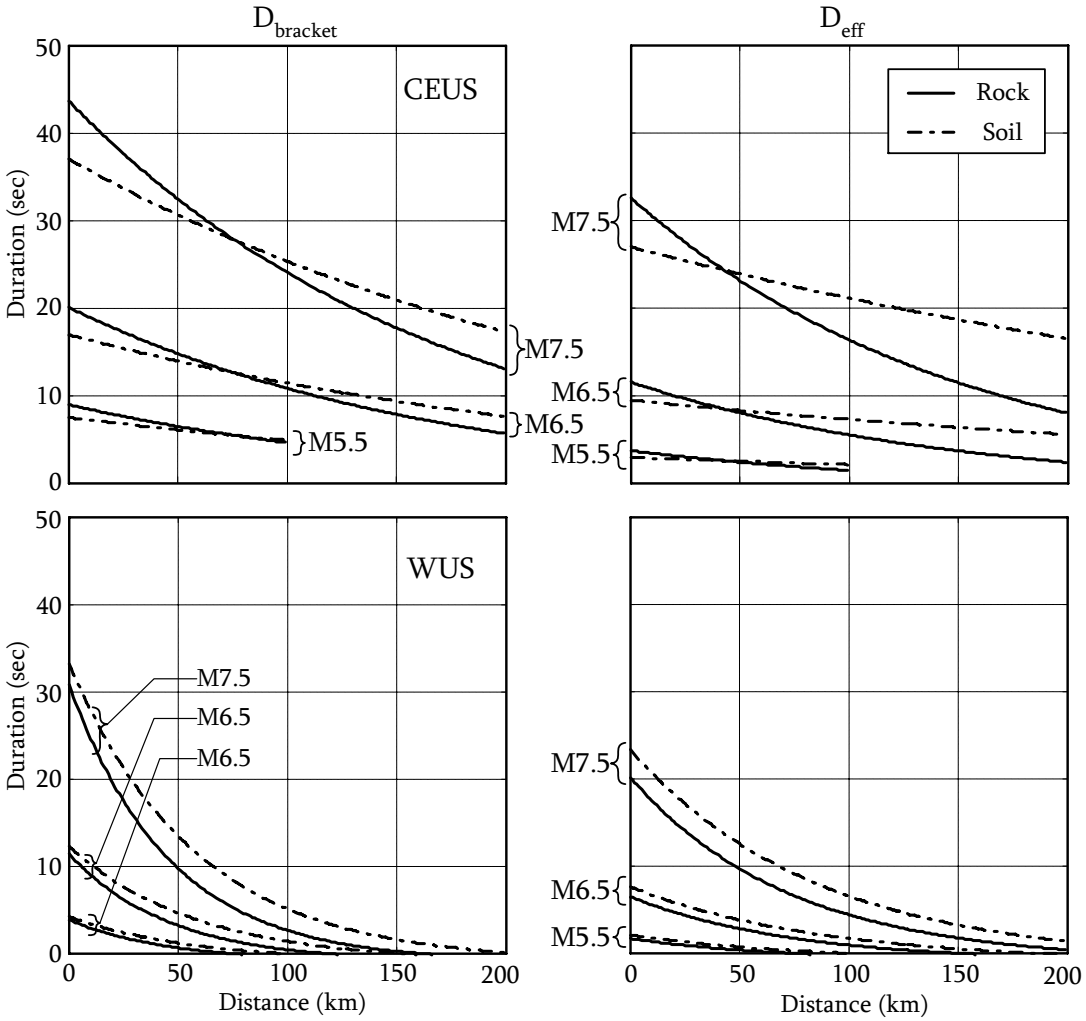

Figure 5-25. Predicted medians for non-zero $D_{bracket}$ (left) and D_{eff} (right) versus distance for the magnitudes 5.5, 6.5, and 7.5 at rock and soil sites for CEUS (top) and WUS (bottom).

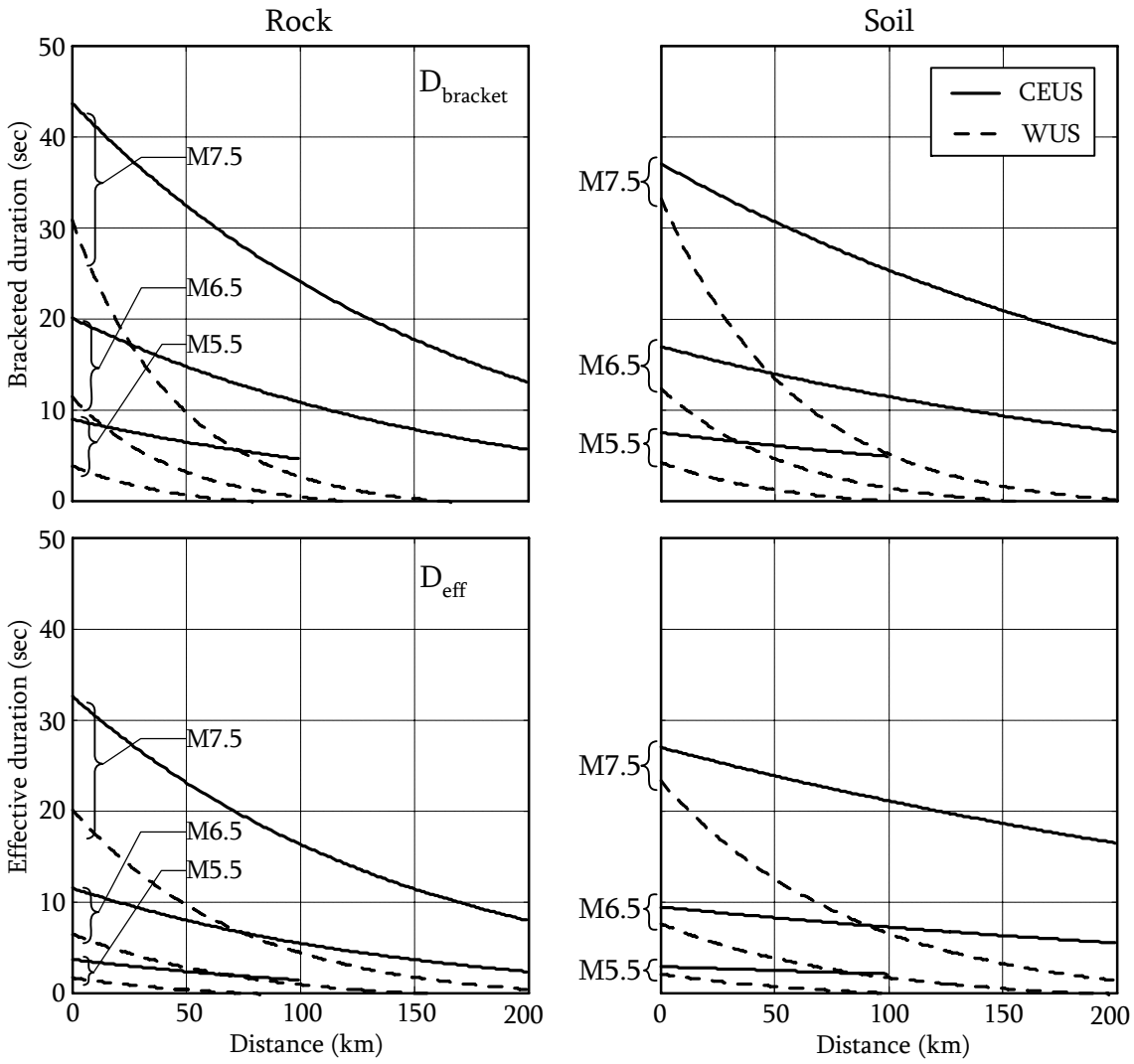

Figure 5-26. Comparisons of CEUS and WUS durations predicted by non-zero duration model: $D_{bracket}$ (top) and D_{eff} (bottom) at rock (left) and soil (right) sites.

The probability of a motion having zero-duration was considered in the proposed duration relations by Eq. 5-11, which was developed using logistic regressions. The regression results are shown in Table 5-3. Also, Figure 5-27 shows the variations in the probability of non-zero duration occurrence as a function of distance for different earthquake magnitudes. The probability of non-zero duration increases with magnitude but decreases as distance increases. Comparing the probabilities for bracketed and

effective durations, for both CEUS and WUS, effective durations are estimated to have a smaller probability of non-zero duration than bracketed durations for a given M and R at rock and soil sites, which was expected because there are more zero-duration motions for effective durations (Figure 5-16). Comparing rock and soil motions, rock motions tend to have less probability of non-zero duration than soil motions.

Table 5-3. Logistic regression coefficients for weighting functions.

CEUS				
	Site	β_1	β_2	β_3
$D_{bracket}$	Rock	9.47	-2.28	0.042
	Soil	4.19	-1.32	0.025
D_{eff}	Rock	9.12	-1.95	0.039
	Soil	4.24	-1.21	0.025
WUS				
	Site	β_1	β_2	β_3
$D_{bracket}$	Rock	4.11	-1.24	0.058
	Soil	-0.39	-0.56	0.039
D_{eff}	Rock	8.60	-1.83	0.099
	Soil	8.71	-1.76	0.052

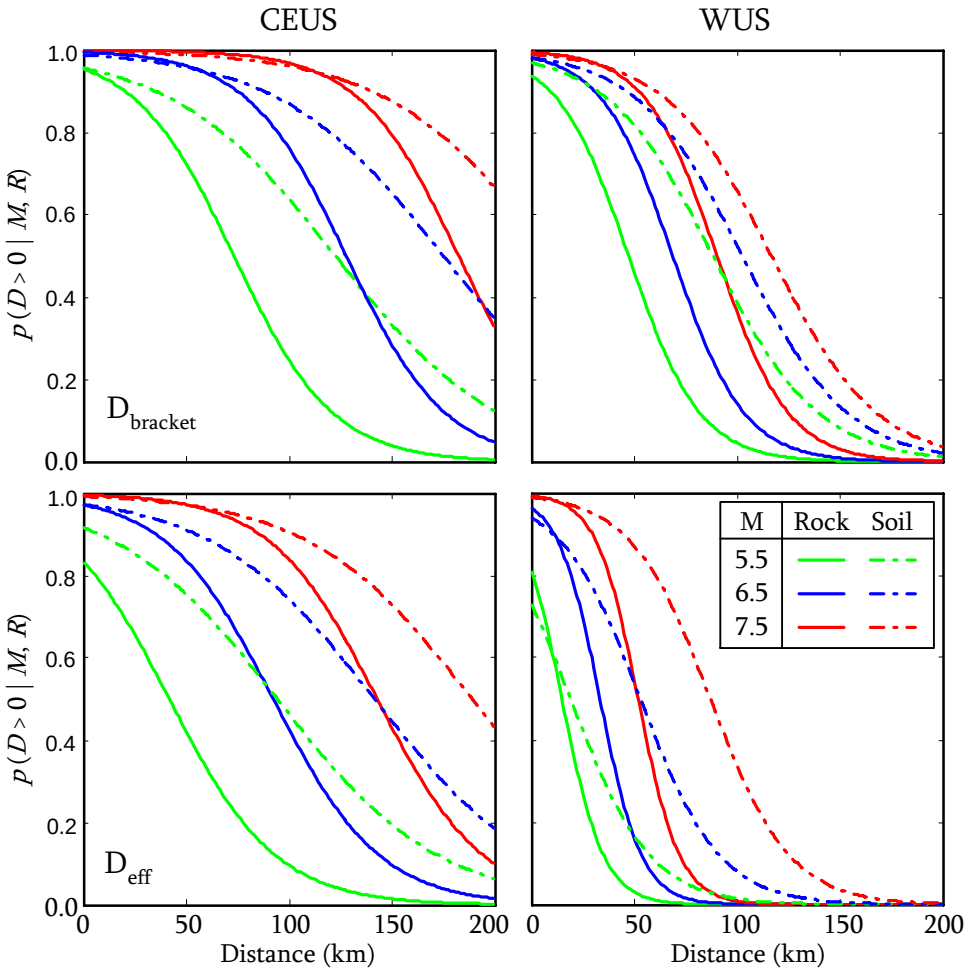

Figure 5-27. Weighting functions for $D_{bracket}$ (top) and D_{eff} (bottom) for CEUS (left) and WUS (right).

The probability of non-zero duration is used as a weighting function. The weighting function is multiplied to the non-zero durations model (i.e., Eq. 5-9), as shown in Eq. 5-12. Using Eqs. 5-11 and 5-12 in conjunction with the coefficients listed in Table 5-2 and Table 5-3, the median durations predicted for CEUS and WUS are shown in Figure 5-28. Also, the CEUS and WUS comparison plots are shown in Figure 5-29. The median durations were reduced from those predicted by the non-zero duration model, especially

at greater distances. However, the overall trends remain similar to those from the non-zero duration model.

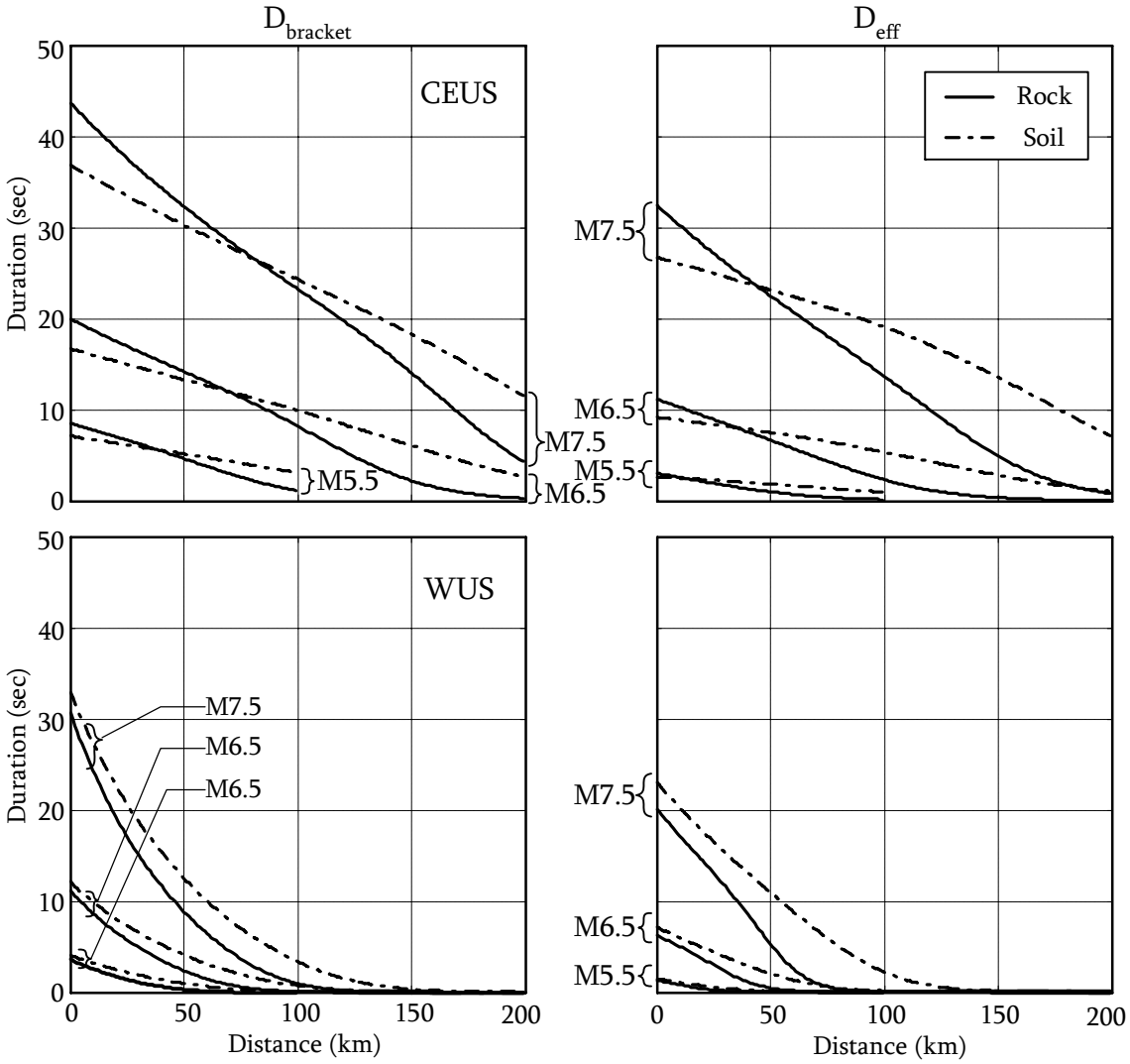

Figure 5-28. Predicted medians for $D_{bracket}$ and D_{eff} at rock and soil sites of CEUS and WUS by the combined model (Eq. 5-12).

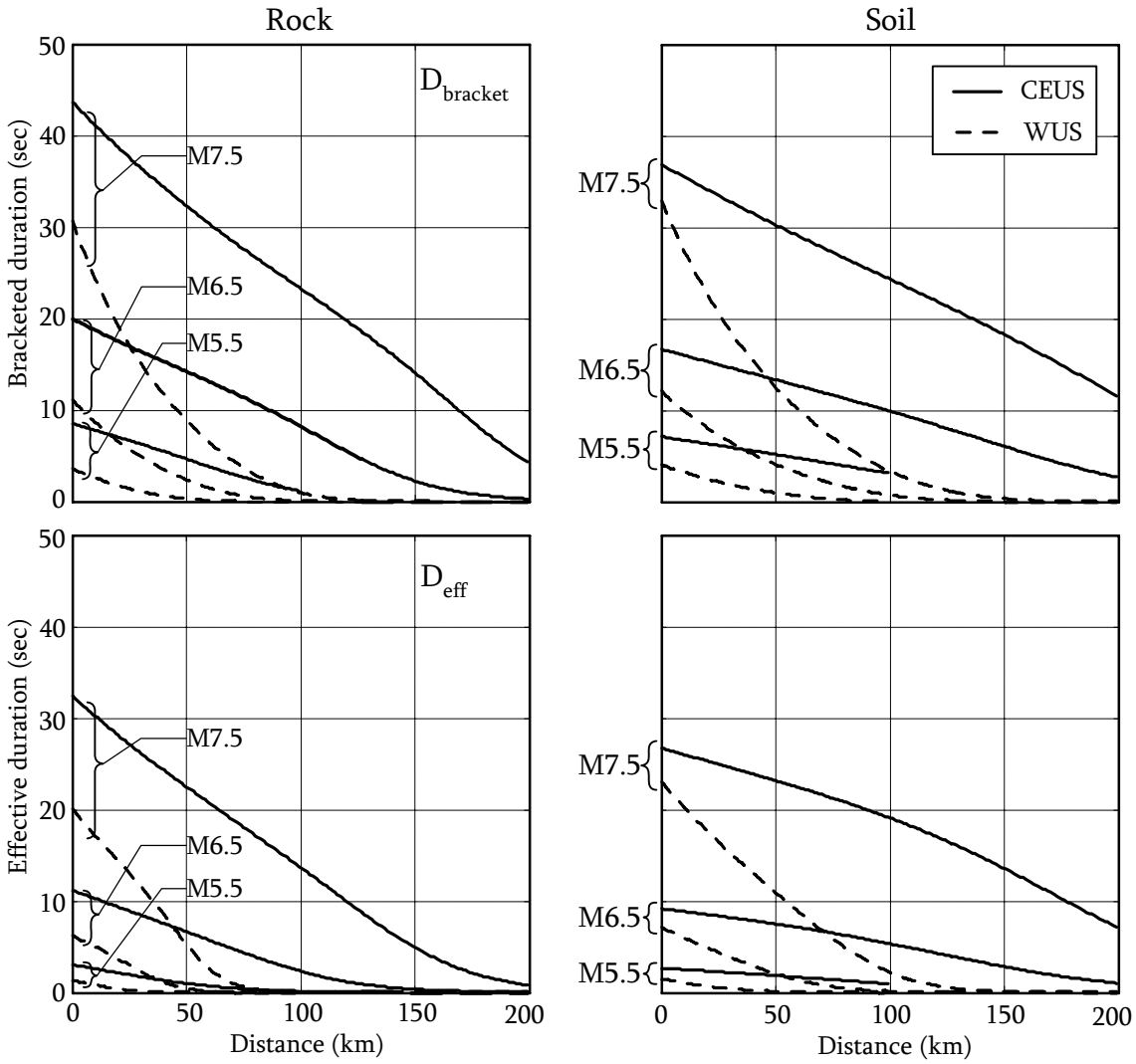

Figure 5-29. Comparisons of CEUS and WUS durations predicted by the combined model (Eq. 5-12): $D_{bracket}$ (top) and D_{eff} (bottom) at rock (left) and soil (right) sites.

5.3.4 Comparison with Existing Relationships

For effective duration, no comparison can be made with existing relationships since the model proposed herein is the first predictive relation developed for this duration. The bracketed duration relation proposed in this study is compared with the widely used model proposed by Chang and Krinitzsky (1977). Chang and Krinitzsky determined

upper bounds of the bracketed durations for rock data and soil data from a limited ground motion data set of 201 horizontal ground motions from 25 WUS earthquakes, mostly from the 1971 San Fernando earthquake (M6.6). Chang and Krinitzsky (1977) did not give specifics of how they performed their regression analyses. However, they linear-extrapolated or interpolated their relationship developed from magnitude and distance ranges where data was available to ranges for which little-to-no data was available. Also, they truncated the durations for far field soil sites, based on zero-durations observed from the duration data from the 1952 Kern county earthquake (M7.7). Figure 5-30 shows the comparison of the bracketed duration relations. Considerable differences exist between the WUS predictions from this study and from Chang and Krinitzsky (1977), except for the predictions for M7.5 for WUS rock sites. Overall, Chang and Krinitzsky model predicts significantly longer durations than this study's WUS model, especially for soil sites. This is likely due to Chang and Krinitzsky (1977) using upper-bound durations and not fully accounting for zero-duration motions.

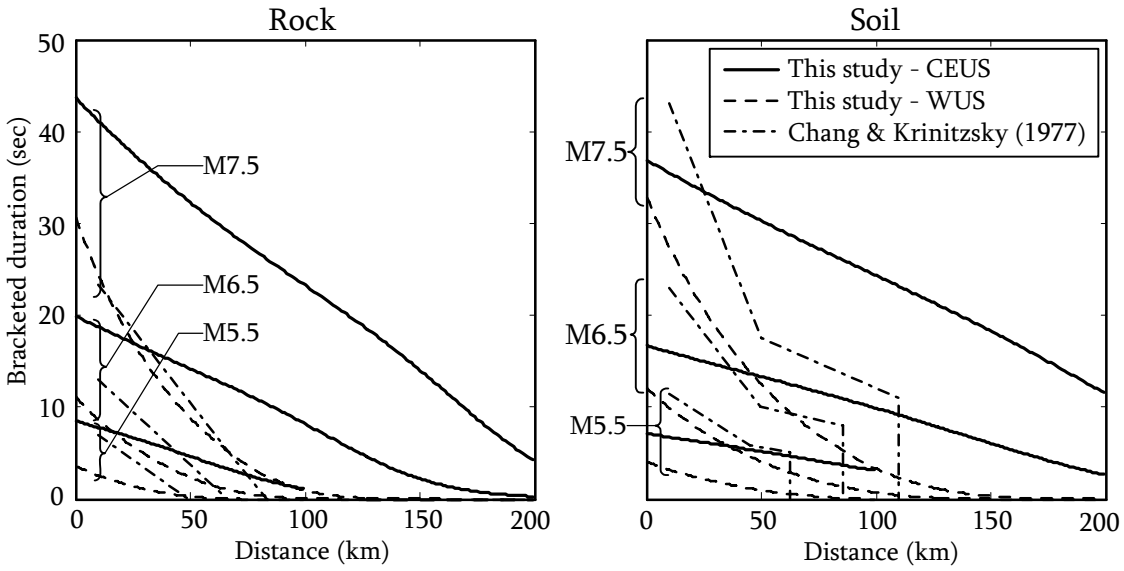

Figure 5-30. Comparison of bracketed durations by this study, and Chang and Krinitzsky (1977).

5.4 Conclusions

Empirical predictive relationships for durations of horizontal strong ground motions in CEUS have been developed in this study. The durations considered herein are the significant durations ($D_{5\text{-}75}$ and $D_{5\text{-}95}$); the bracketed duration ($D_{bracket}$); and the effective duration (D_{eff}). For the bracketed duration and effective duration, zero-durations were incorporated into the models through weighting functions representing the probability of non-zero duration.

Significant durations for CEUS motions increase with increasing magnitude and increasing distance. However, contrary to the trends commonly observed from WUS motions, significant durations of CEUS motions for rock sites tended to be slightly longer than those for soil sites. Additional analyses are needed to better understand this

contradictory trend. Comparing CEUS and WUS motion correlations from this study, significant durations for rock motions in CEUS were consistently longer than those in WUS, while for soil motions, both CEUS and WUS motions were estimated to have similar significant durations.

Both the bracketed and effective durations were predicted to decrease with increasing distance, but to increase significantly with increasing magnitude. While soil motions in WUS were consistently estimated to have longer durations than comparable rock motions, soil motions in CEUS were predicted to have longer durations than rock motions at distances farther than about 75 km and 45 km for bracketed and effective durations, respectively. This is attributed to the relatively lower rates of duration attenuation for soil motions in CEUS. Comparing CEUS and WUS motions, for both rock and soil sites CEUS motions consistently had longer durations than WUS motions. Also, WUS durations tended to attenuate at a higher rate with respect to distance than CEUS durations, which resulted in more significant duration differences between CEUS and WUS motions at longer distances. In comparison with the existing relationship (Chang and Krinitzsky, 1977) for the bracketed duration, Chang and Krinitzsky model predicted significantly longer durations than this study's WUS model, especially for soil sites. This is likely attributed to their upper-bound-based methodology and lack of consideration of zero-durations.

References

Abrahamson, N. A., and Silva, W. J. (1996). "Empirical ground motion models." *Report*, Brookhaven National Laboratory.

Arias, A. (1970). "A measure of earthquake intensity." Seismic Design for Nuclear Power Plants, R. J. Hansen, ed., The MIT press, Cambridge, MA, 438-483.

Bolt, B. A. (1973). "Duration of strong ground motions." *Fifth World Conference on Earthquake Engineering*, Vol. 1, Rome, 1304-1313.

Bommer, J. J., and Martinez-Pereira, A. (1999). "The effective duration of earthquake strong motion". *Journal of Earthquake Engineering*, 3(2), 127-172.

Boore, D. M. (1983). "Stochastic simulation of high-frequency ground motions based on seismological models of the radiated spectra". *Bulletin of the Seismological Society of America*, 73(6A), 1865-1894.

Brune, J. N. (1970). "Tectonic stress and spectra of seismic shear waves from earthquakes". *Journal of Geophysical Research*, 75(26), 611-614.

Brune, J. N. (1971). "Correction". *Journal of Geophysical Research*, 76(20), 1441-1450.

Chang, F. K., and Krinitzsky, E. L. (1977). "State-of-the-Art for Assessing Earthquake Hazards in the United States. Report 8. Duration, Spectral Content, and Predominant Period of Strong Motion Earthquake Records from Western United States." United States.

Hanks, T. C. (1979). "b-values and omega-gamma seismic source models - implications for tectonic stress variations along active crustal fault zones and the estimation of high-frequency strong ground motion". *Journal of Geophysical Research*, 84(NB5), 2235-2242.

Hanks, T. C., and Kanamori, H. (1979). "A moment magnitude scale". *Journal of Geophysical Research*, 84, 2348-50.

Hays, W. W. (1975). "A note on the duration of earthquake and nuclear-explosion ground motions". *Bulletin of the Seismological Society of America*, 65(4), 875-883.

Husid, L. R. (1969). "Características de terremotos. Análisis general." *Revista del IDIEM 8*, Santiago de Chile, 21-42.

Kempton, J. J., and Stewart, J. P. (2006). "Prediction equations for significant duration of earthquake ground motions considering site and near-source effects". *Earthquake Spectra*, 22(4), 985-1013.

McGuire, R. K., and Hanks, T. C. (1980). "RMS accelerations and spectral amplitudes of strong ground motion during the san-fernando, california earthquake". *Bulletin of the Seismological Society of America*, 70(5), 1907-1919.

Page, R. A., Boore, D. M., Joyner, W. B., and Coulter, H. W. (1972). "Ground motion values for use in seismic design of the trans-Alaska pipeline system". *US Geological Survey Circular 672*.

Somerville, P. G., Smith, N. F., Graves, R. W., and Abrahamson, N. A. (1997). "Modification of empirical strong ground motion attenuation relations to include the amplitude and duration effects of rupture directivity". *Seismological Research Letters*, 68(1), 199-222.

Trifunac, M. D., and Brady, A. G. (1975). "Study on duration of strong earthquake ground motion". *Bulletin of the Seismological Society of America*, 65(3), 581-626.

Chapter 6

Intensity Parameters

6.1 Background

Numerous attempts were made to quantify the severity of earthquake shaking that correlates to earthquake-induced damage potential to man-made structures (e.g., buildings, dams). Based on the observed effects from the past earthquakes, empirical intensity scales (e.g., modified Mercalli intensity scale) were developed based on qualitative descriptions of shaking/damage. However, the empirical scales have considerable drawbacks in that they are subjective, irreproducible, and not directly useable in engineering design. Consequently, various intensity parameters (or indices) were developed in attempts to provide a quantitative measure of earthquake intensity that is objective, reproducible, and directly useable in engineering design.

Different from other engineering characteristic parameters, most of the intensity definitions incorporate the effects of multiple ground motion characteristics, such as amplitude, frequency content, and duration. Therefore, intensity measures are frequently used in engineering analyses because they not only represent the severity of ground shakings but also correlate well to earthquake-induced damage potential to structural or geotechnical systems. For example, Borja et al. (2002) compared the results from two site

response analysis codes using Arias intensity (Arias, 1970) as one of the criteria. Additionally, Kayen and Mitchell (1997) developed an assessment approach for liquefaction potential of soil deposits subjected to earthquakes, wherein they quantified earthquake demand in terms of Arias intensity.

In this chapter, empirical relationship for Arias intensity (I_a) developed both for CEUS and WUS are presented. The intensity definition is reviewed, and the proposed model and the NLME regression results are presented. Also, the CEUS model is compared to existing empirical relationships developed by Kayen and Mitchell (1997) and Travasarou et al. (2003) as well as the WUS one developed in this study. Lastly, major findings are summarized.

6.2 Arias Intensity: I_a

6.2.1 Definition

Developed for a measure of seismic destructiveness, Arias intensity is "… the sum of total energies per unit weight stored in the oscillators of a population of undamped linear oscillators uniformly distributed as to their frequencies, at the moment the earthquake ends (or for that matter, at any instant after the end of ground motion)" (Arias, 1970). Arias intensity is computed for a given direction of motion, *x*, by:

$$I_{xx} = \frac{\pi}{2g}\int_0^{t_d} a_x^2(t)\,dt \qquad \text{(Eq. 6-1)}$$

where: g is the coefficient of acceleration due to gravity; t_d is the total duration; and $a_x(t)$ is the ground acceleration in the x-direction. Accordingly, I_{xx} has units of velocity; m/sec is typically used.

Because ground motion amplitude, frequency content, and duration all influence the damage potential of earthquake motions, as well as influence Arias intensity, Arias intensity is seemingly a reliable index for seismic design. An example ground acceleration time history (i.e., $a_x(t)$) is shown in Figure 6-1. Below the acceleration time history is a corresponding plot of the squared acceleration time history (i.e., $a_x^2(t)$). By definition, Arias intensity is proportional to the area below the $a_x^2(t)$ curve, which is shown as a function of time at the bottom of Figure 6-1. The Arias intensity for the example acceleration time history is about 0.41 m/sec, as shown in Figure 6-1.

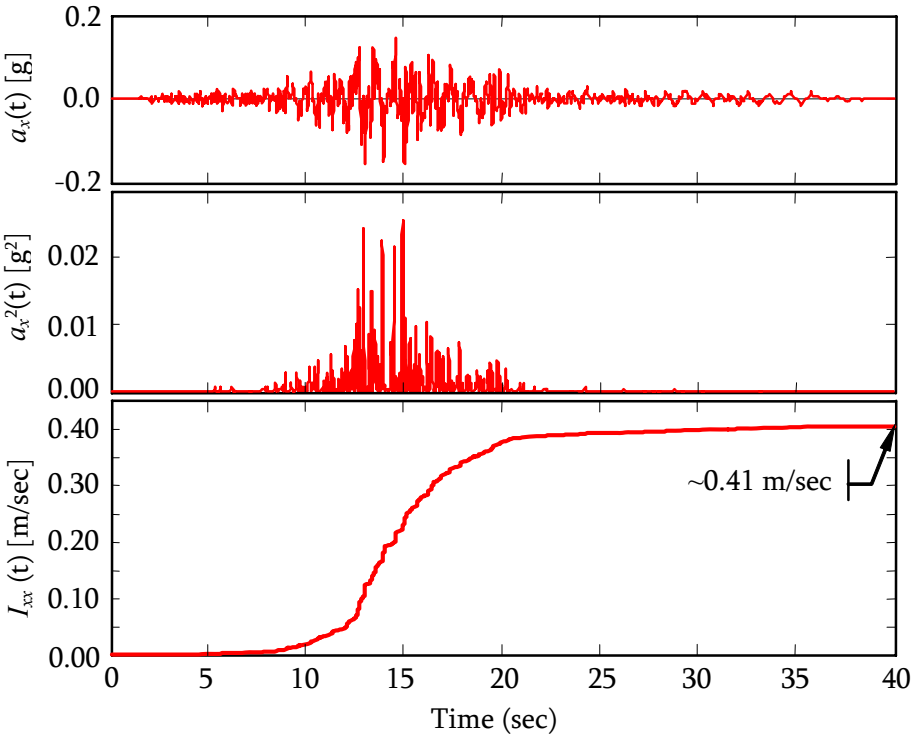

Figure 6-1. Example of Arias intensity determination for a ground acceleration time history (HWB220: M6.9; R58.9km) from the 1989 Loma Prieta earthquake.

The averaged Arias intensity of two orthogonal horizontal components, designated by I_a, is considered in developing empirical predictive relationships. This is because predicting the average of the medians of the two horizontal components is considered appropriate for engineering design (Travasarou et al., 2003).

6.2.2 Proposed Model

The functional form of the predictive relationship was obtained by modifying the model proposed by Travasarou et al. (2003). Their model was based on Brune's point source model (Brune, 1970; 1971) for the smoothed Fourier amplitude spectrum of ground motions (Chapter 2). Using Parseval's theorem (i.e., Eq. 2-8), the definition of Arias intensity (i.e., Eq. 6-1) was rewritten by substituting the integral of the squared

acceleration in Eq. 6-1 with the integral of the squared Brune's point source model (i.e., the square of Fourier amplitude spectrum). Then, the regression model was built based on observing the magnitude and site-to-source distance dependencies of Arias intensity from trend plots.

Assuming a log-normal distribution of the data, the proposed functional form of the predictive relationship is:

$$\ln I_a = C_1 + C_2(M-6) + C_3(M-6)^2 + C_4 \ln(M/6) + C_5 \ln\left(\sqrt{R^2+h^2}\right) + [S_1 + S_2(M-6)]S_S \quad \text{(Eq. 6-2)}$$

where: I_a is the average Arias intensity of two horizontal components (m/sec); C_1 through C_5, h, and S_1 and S_2 are regression coefficients; M is the moment magnitude; R is the closest distance to the fault rupture plane (km); and S_S is a binary number representing local site conditions: $S_S = 0$ for rock sites, $S_S = 1$ for soil sites. The term $(M-6)^2$ was added to the Travasarou et al. (2003) model, which considerably lowered the total standard deviation of the regression results for CEUS.

6.2.3 Regression Results

The results from the NLME regression analyses using the model shown in Eq. 6-2 are shown in Table 6-1. For CEUS, all the coefficients have significant statistical contribution (i.e., p-values < 5% or 0.05). For WUS, some coefficients appeared to be statistically insignificant (i.e., C_2 and C_4). However, excluding these coefficients from the model resulted in higher total standard deviations ($\sigma_{ln\ total}$). Furthermore, the terms including C_2 and C_4 were required to account for the magnitude dependence of the intensity measure. Accordingly, it was decided to keep these terms in the WUS model.

Also, note that the coefficient C_3 for WUS is zero. This is because the term $C_3(M-6)^2$ was actually removed from the model for the regression analyses for WUS because it caused an increase in the total standard deviation along with a high p-value. For a consistent form of the proposed predictive relation for CEUS and WUS, $C_3 = 0$ is used. Comparing the standard deviations for CEUS and WUS, they have a similar level of uncertainty.

Table 6-1. Regression coefficients; their p-values (in parentheses); and standard deviations of inter-event, intra-event, and total errors.

CEUS										
C_1	C_2	C_3	C_4	C_5	h	S_1	S_2	τ_{ln}	σ_{ln}	$\sigma_{ln\ total}$
3.22 (0.000)	-107.59 (0.000)	7.91 (0.001)	651.14 (0.000)	-1.28 (0.000)	6.06 (0.002)	0.56 (0.001)	-0.45 (0.005)	0.67	0.89	1.11
WUS										
C_1	C_2	C_3	C_4	C_5	h	S_1	S_2	τ_{ln}	σ_{ln}	$\sigma_{ln\ total}$
3.10 (0.000)	-1.11 (0.724)	0 (n/a)	15.13 (0.442)	-1.65 (0.000)	7.24 (0.000)	0.51 (0.001)	-0.095 (0.530)	0.68	0.84	1.08

The distributional assumptions of the intra-event errors and random-effects were assessed by the normal Q-Q plots shown in Figure 6-2. It seems plausible that both intra-event errors and random-effects follow the normal distribution for both CEUS and WUS. Additionally, the scatter plots for intra-event errors and random-effects are shown in Figure 6-3, in which symmetrical distributions are observed with respect to the zero lines of the standardized inter-event errors and random-effects, respectively.

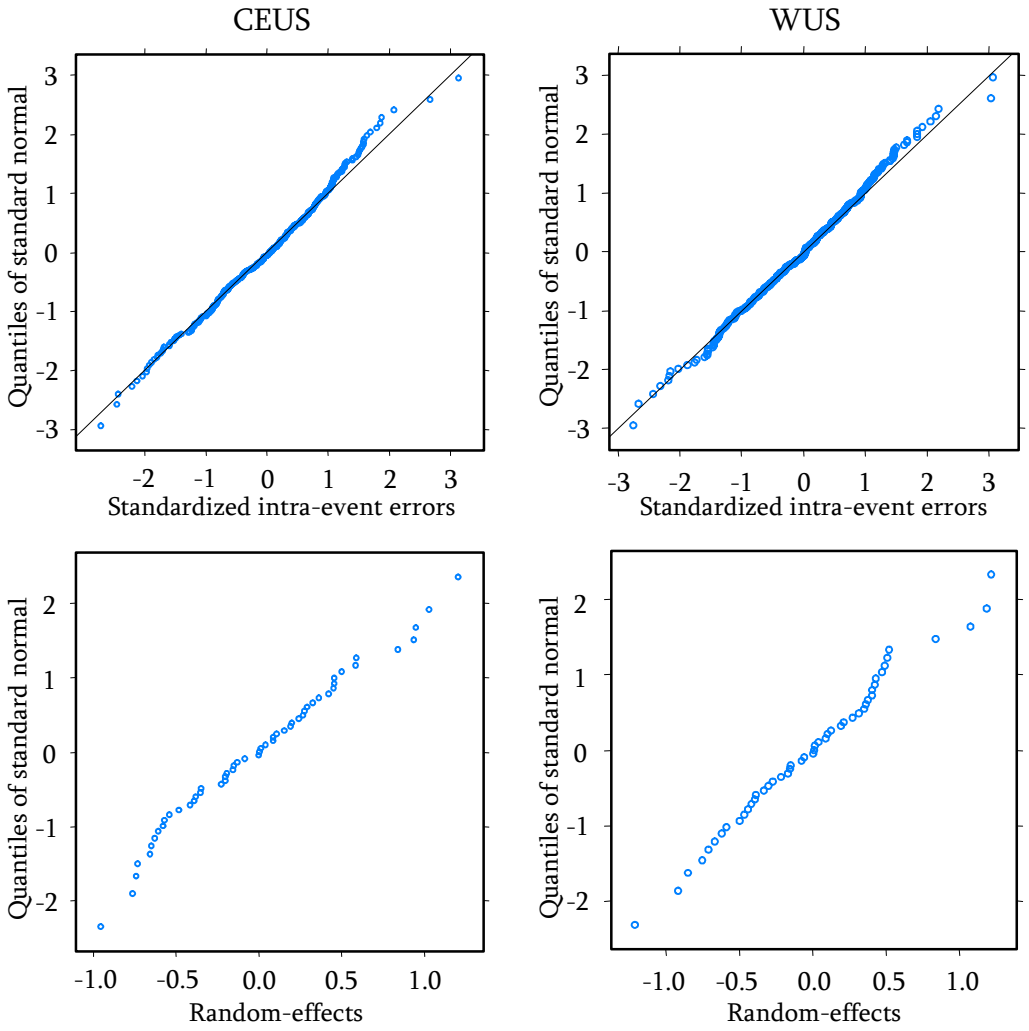

Figure 6-2. Normal Q-Q plots of intra-event errors (top) and random-effects (bottom) for CEUS (left) and WUS (right).

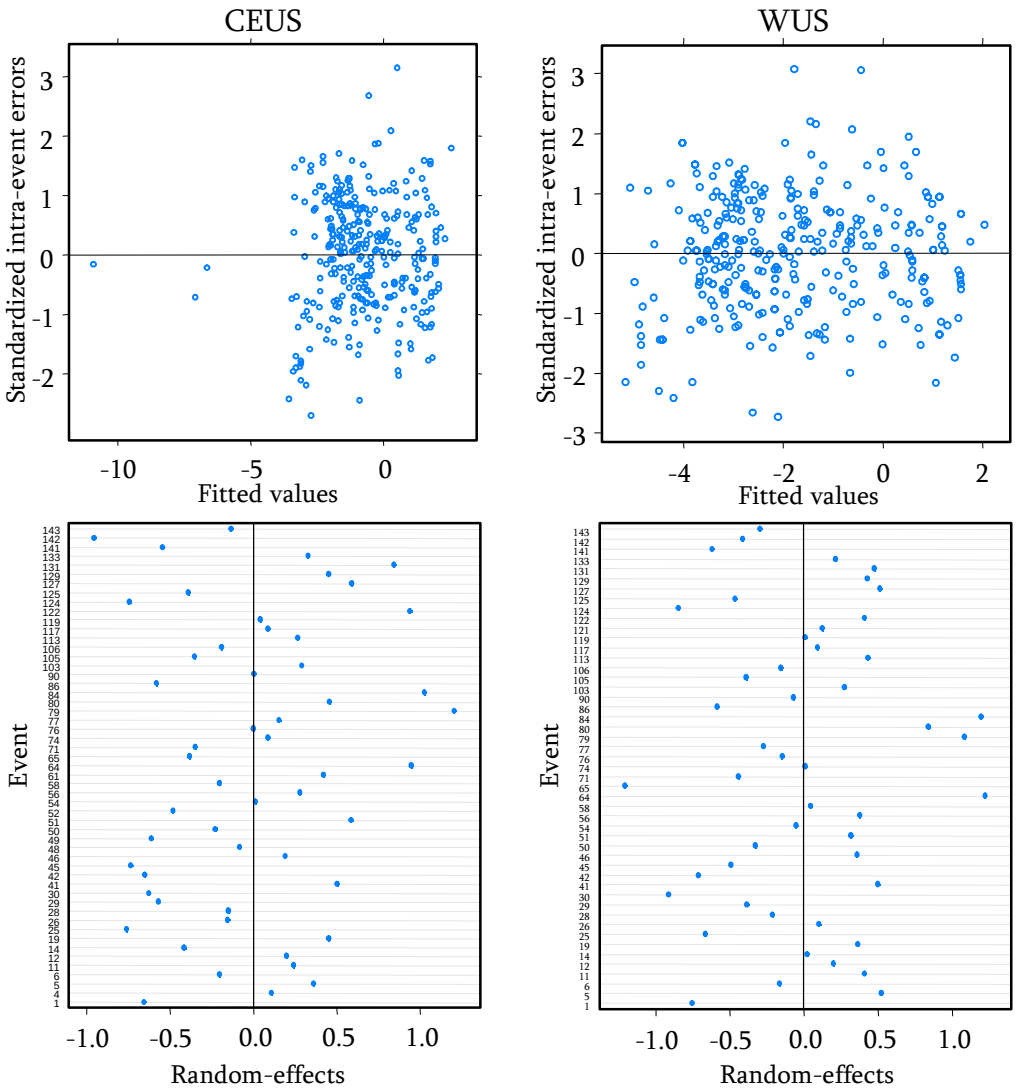

Figure 6-3. Scatter plots of intra-event errors (top) and random-effects (bottom) for CEUS (left) and WUS (right).

The predictive relationship for CEUS is plotted with the actual data values for three magnitude ranges as shown in Figure 6-4, where M5.5, M6.5, and M7.5 were used for plotting the predictive relationship. Also, shown in this figure are the predicted values for the median plus/minus one standard deviation ($\sigma_{ln\ total}$), which encompasses about 68% of the observed data. One can readily see that there are several significant outliers for M5.5 cases, especially for soil sites. However, these seeming outliers are data from the 1989

M4.7 New Madrid, MO earthquake; these data are in reasonable agreement with predicted values for M4.7. Both for rock and soil sites, the proposed model appears to well-represent the data throughout the magnitude and distance ranges.

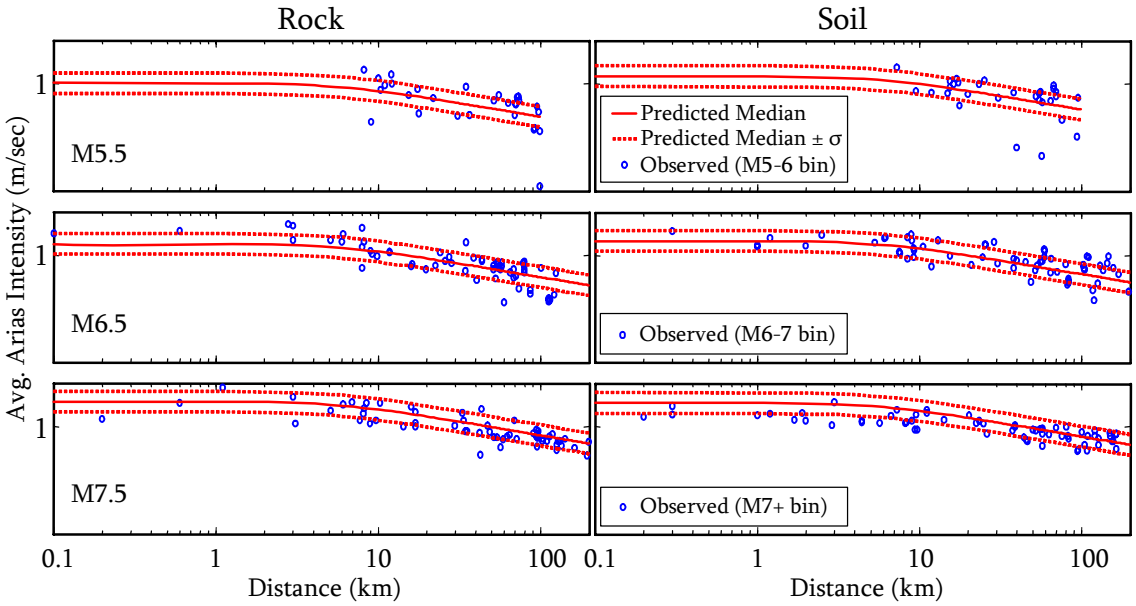

Figure 6-4. Predicted medians versus site-to-source distance for three magnitude bins for rock (left) and soil (right) sites of CEUS. The central magnitudes for each bin were used to compute the predicted curves. Also shown in the plots are the Arias intensity values from the data set.

The average Arias intensities in CEUS, predicted for rock and soil sites, are shown in Figure 6-5. The average Arias intensity decreases with increasing distance and increases with increasing magnitude. Comparing rock and soil motions, soil motions tend to have greater Arias intensity than rock motions by factors of about 2 and 1.5 for M5.5 and M6.5, respectively. Interestingly, this trend decays as magnitude increases. Consequently, soil motions for magnitude 7.5 are estimated to have even smaller Arias intensity than rock motions, which is inconsistent with the predictions for WUS motions (as will be shown

subsequently). Further investigations are needed to better understand this trend. However, this trend may be attributed to the longer significant durations predicted for rock motions than for soil motions in CEUS, as presented in Chapter 5.

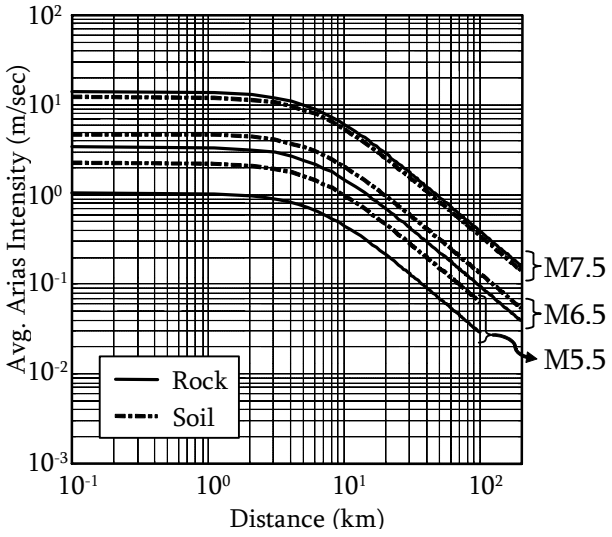

Figure 6-5. Predicted median versus distance for the magnitudes 5.5, 6.5, and 7.5; rock and soil sites for CEUS.

The comparison plots of CEUS and WUS for both rock and soil sites are shown in Figure 6-6. As may be observed from this figure, CEUS motions have larger intensities than WUS ones for both rock and soil sites. For rock sites, CEUS motions with large magnitudes (i.e., M7.5) are estimated to have significantly greater intensities than WUS motions by factors of 3 to 8 at distances of 0.1 km to 200 km, respectively. In contrast, at soil sites, the intensity values for small magnitudes (i.e., M5-6) show a pronounced difference between CEUS and WUS by factors of 3 to 7 at distances of 0.1 km to 200 km, respectively. This might stem from the larger intensities predicted for rock site than those for soil site for M7.5 in CEUS.

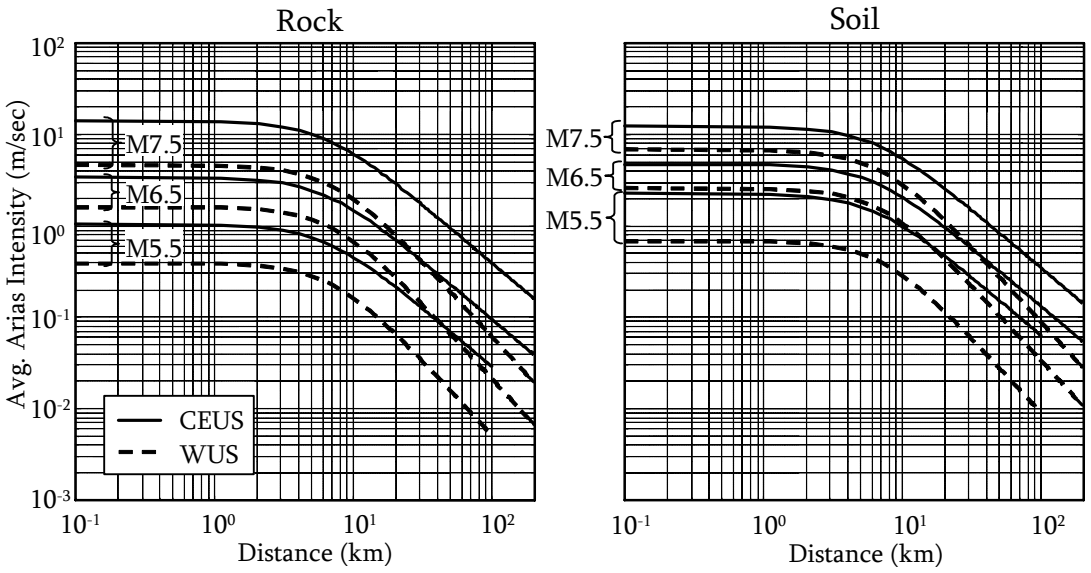

Figure 6-6. Comparison of CEUS and WUS for rock (left) and soil (right) sites.

6.2.4 Comparison with Existing Relationships

The proposed predictive relationships for CEUS and WUS are compared to the existing empirical relationships for active shallow crustal regions (e.g., WUS) that were proposed by Kayen and Mitchell (1997), and Travasarou et al. (2003). Kayen and Mitchell model predicts the sum of Arias intensities of two orthogonal horizontal components as a function of moment magnitude, surface distance to the fault rupture plane, and site conditions such as rock, alluvium, and soft soil. Kayen and Mitchell's relation was developed using data from 66 strong ground motion records, largely from California. Travasarou et al. model predicts the average Arias intensity of the two horizontal components as a function of moment magnitude; the closest distance to the fault rupture plane; fault mechanism such as strike slip, reverse, and normal faults; and local site condition such as site categories B, C, and D based on the geotechnical site classification

system by Rodriguez-Marek et al. (2001). Travasarou et al. developed their model using data from 1208 recorded motions from 75 earthquakes.

For the comparisons, site categories B and D for Travasarou et al. model and rock and alluvium sites for Kayen and Mitchell model were used. These conditions are considered comparable to the site classifications for rock and soil used in this study (i.e., Geomatrix site classification). Also, the medians predicted by Kayen and Mitchell model were divided by 2 in order to convert them to the average of the two horizontal components. Finally, a reverse fault mechanism was assumed for Travasarou et al. model in this comparison, while this study's model does not include fault mechanisms.

Figure 6-7 shows the comparisons with these existing models both for rock and soil sites. First, it is observed that CEUS motions have consistently larger Arias intensity values than WUS motions for both rock and soil sites. In fact, this is not the case for M7.5 predictions by Kayen and Mitchell model. Yet, as already pointed out by Travasarou et al. (2003), Kayen and Mitchell model tends to significantly over-predict Arias intensity for larger magnitudes and underestimate Arias intensity for smaller magnitudes. Similar trends are observed in this study too. However, Kayen and Mitchell predicts values for M6.5 of WUS that are in a good agreement with those from both Travasarou et al. (2003) and this study. The model for WUS proposed herein tends to produce similar values to those from Travasarou et al. model, which is not a surprise because this study used an analogous model to Travasarou et al. model for WUS.

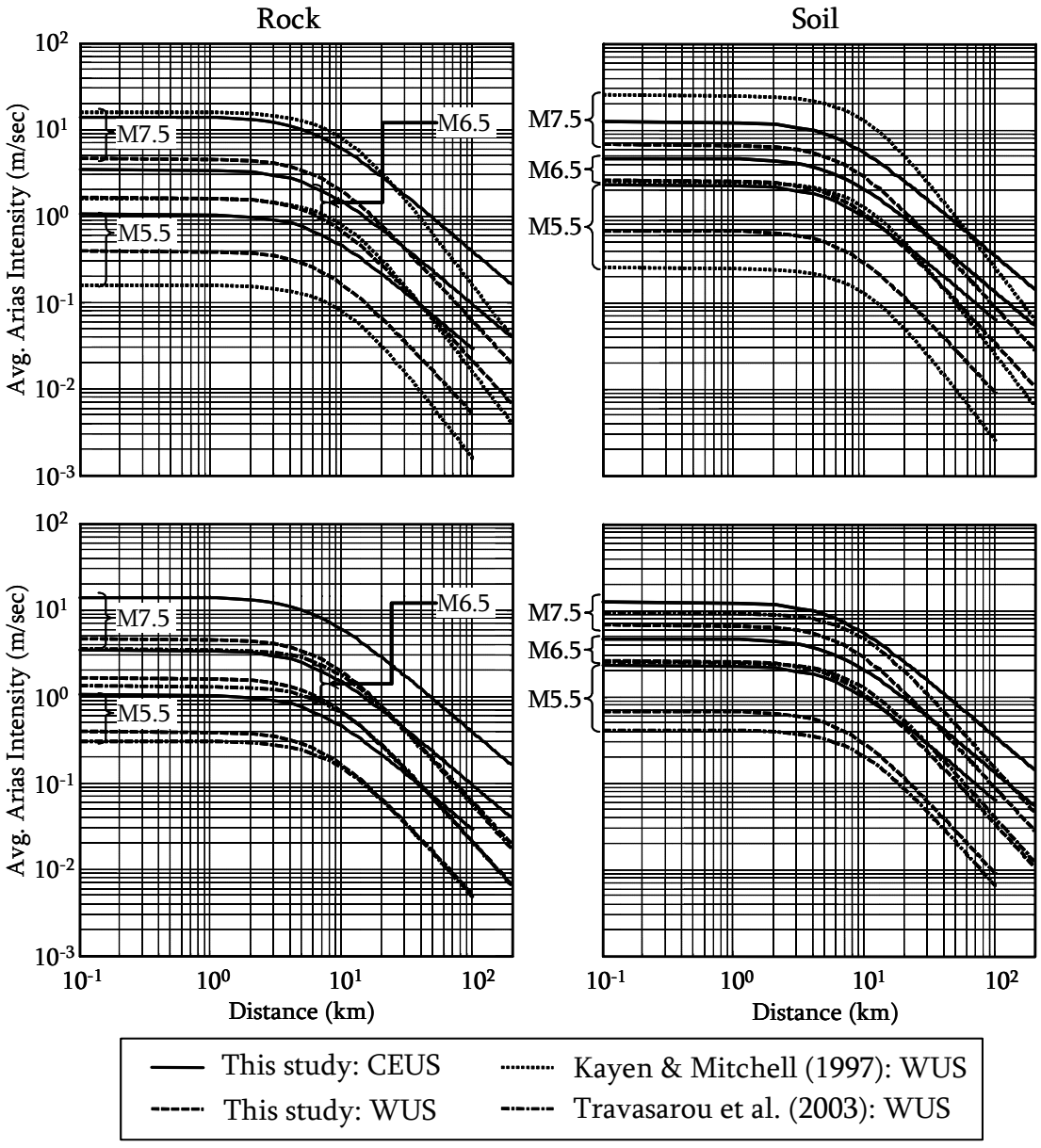

Figure 6-7. Comparison of this study's models and existing relationships: Kayen and Mitchell, 1997 (top) and Travasarou et al., 2003 (bottom). For Travasarou et al. (2003) model, a reverse fault mechanism was assumed and the site category B and D per Rodriguez-Marek et al. (2001) were considered for rock and soil sites, respectively.

6.3 Conclusions

Empirical predictive relationship for Arias intensity for horizontal CEUS motions was developed. Based on the predictions by the relationship, Arias intensity for CEUS decreases with increasing distance and increases with increasing magnitude. Comparing rock and soil motions in CEUS, for small and intermediate magnitudes, soil motions were estimated to have larger Arias intensities than rock motions. However, an opposite trend was observed for large magnitudes (i.e., M7.5). Further investigation is needed to better understand this trend, particularly since significant durations were estimated to be longer for rock motions than for soil motions in CEUS. In comparison of the CEUS and WUS models, CEUS motions were predicted to have larger intensities than WUS motions for both rock and soil sites. Also, the CEUS and WUS models by this study were compared with the existing relationships for active shallow crustal motions (Kayen and Mitchell, 1997; Travasarou et al., 2003). The WUS model proposed in this study is in a good agreement with Travasarou et al. model, while Kayen and Mitchell's model tends to significantly overestimate Arias intensity for large magnitudes and underestimate Arias intensity for small magnitudes. It was also confirmed with Travasarou et al. model that Arias intensity for CEUS motions predicted using the relation proposed herein have consistently larger Arias intensity values than WUS motions for both rock and soil sites.

References

Arias, A. (1970). "A measure of earthquake intensity." Seismic Design for Nuclear Power Plants, R. J. Hansen, ed., The MIT press, Cambridge, MA, 438-483.

Borja, R. I., Duvernay, B. G., and Lin, C.-H. (2002). "Ground Response in Lotung: Total Stress Analyses and Parametric Studies". *Journal of Geotechnical & Geoenvironmental Engineering*, 128(1), 54.

Brune, J. N. (1970). "Tectonic stress and spectra of seismic shear waves from earthquakes". *Journal of Geophysical Research*, 75(26), 611-614.

Brune, J. N. (1971). "Correction". *Journal of Geophysical Research*, 76(20), 1441-1450.

Kayen, R. E., and Mitchell, J. K. (1997). "Assessment of liquefaction potential during earthquakes by Arias intensity". *Journal of Geotechnical and Geoenvironmental Engineering*, 123(12), 1162-1174.

Rodriguez-Marek, A., Bray, J. D., and Abrahamson, N. A. (2001). "An Empirical Geotechnical Seismic Site Response Procedure". *Earthquake Spectra*, 17(1), 65-87.

Travasarou, T., Bray, J. D., and Abrahamson, N. A. (2003). "Empirical attenuation relationship for Arias Intensity". *Earthquake Engineering & Structural Dynamics*, 32(7), 1133-1155.

Chapter 7

Equivalent Number of Stress and Strain Cycles

7.1 Background

The concept of "equivalent uniform cycles" was originally developed for evaluating metal fatigue and has its roots in the macro cumulative damage fatigue hypothesis. The premise of the concept is that a random load can be represented by an equivalently damaging number of uniform cycles. The equivalent number of uniform cycles concept is very useful in geotechnical earthquake engineering. For example, the number of equivalent stress cycles ($n_{eq\tau}$) underlies the magnitude scaling factors (MSF) used in liquefaction evaluation procedure based on in-situ tests and provides a convenient metric for comparing the duration of earthquake motions (Green and Terri, 2005). Also, the number of equivalent strain cycles ($n_{eq\gamma}$) is used to evaluate the compression of unsaturated fills subjected to earthquake shaking (Green and Lee, 2006; Tokimatsu and Seed, 1987).

One of the earliest approaches for computing equivalent uniform cycles was proposed independently by Palmgren (1924) and Miner (1945), with the approach commonly referred to as the Palmgren-Miner (P-M) cumulative damage hypothesis. Due to its simplicity and relatively good agreement with experimental data for various metals, the

P-M hypothesis is widely used to this day. The implementation procedure of the P-M hypothesis outlined in Miner (1945) applies to high cycle fatigue conditions (low amplitude, large number of cycles), wherein the amplitude of the loading is such that the material response is constrained to the elastic range.

In the late 1960's to early 1970's, Professors H.B. Seed, K.L. Lee, I.M. Idriss, and colleagues adopted Miner's implementation procedure of the P-M hypothesis, with slight modifications, to compute the number of equivalent stress cycles for evaluating the cyclic liquefaction potential of soil (e.g., Annaki and Lee, 1977; Seed et al., 1975). This is despite a significant amount of plastic strain induced in the soil during each load cycle, which is more characteristic of low cycle fatigue (large amplitude, small number of cycles). Accordingly, the method of implementation of the P-M hypothesis needs to be such that the non-linear stress-strain response of the material is properly taken into account (e.g., Collins, 1981). In this regard, Green (2001) proposed an alternative approach for implementing the P-M hypothesis for computing the number of equivalent stress cycles, in which the dissipated energy of the random and uniform motions are equated. Consequently, the non-linear stress-strain behavior of the soil is taken directly into account.

Martin et al. (1975) showed that the cumulative volumetric strain is influenced by the amplitude of the load and the sequencing of the peaks (i.e., load-dependent). However, the sequencing of the pulses in a random motion is not considered in the equivalent number of uniform cycles based on the P-M hypothesis since a linear accumulation of

damage is assumed in the hypothesis. Therefore, implementing the P-M hypothesis for the number of equivalent strain cycles might be inappropriate. In this vein, Green and Lee (2006) developed the theoretical framework for a method for computing the number of equivalent strain cycles based on the Richart and Newmark (1948) (R-N) cumulative damage fatigue hypothesis, which is load-dependent. The simplified Martin, Finn, and Seed (1975) model by Byrne (1991) producing compatible cumulative damage curves to those of the R-N hypothesis was used in this study to compute cumulative volumetric strains.

In this study, the energy-based alternative approach by Green (2001) was used to compute the number of equivalent stress cycles, and the load-dependent procedure outlined in Green and Lee (2006) was used to compute the number of equivalent strain cycles. All the horizontal rock motions in the CEUS and WUS bins were treated as rock outcrop motions, irrespective of the actual site conditions at which they were recorded, and used as the input motions and propagated up through soil profiles. The site response analyses were performed using the equivalent linear site response code SHAKEVT (Green, 2001), a modified version of SHAKE91 (Idriss and Sun, 1992). As one option, SHAKEVT outputs the shear stress and strain time histories on top of each layer subjected to seismic loading. Due to the limit on the number of data points of input acceleration time history (16384 pts.) in SHAKEVT, the rock motions in the data set was reduced from total 302 and 330 to 270 and 296 for CEUS and WUS, respectively. All of the rock motions removed from the data set were from the 1999 Chi-Chi earthquake (M7.6). For both the number of equivalent stress and strain cycles, the empirical

predictive relationships were developed as functions of moment magnitude, site-to-source distance, and depth in the soil profile. In this study, the two orthogonal horizontal components of motion from a given station/event were treated as individual data points in the regression analyses.

The chapter is organized into two parts: 1) the number of equivalent stress cycles; and 2) the number of equivalent strain cycles. In each part, the computation of the equivalent number of cycles is presented, wherein the definition of the $n_{eq\tau}$ or $n_{eq\gamma}$ and the site response analyses are described. Then, the proposed functional form of the predictive relationship is introduced and the NLME regression results are presented. Using the proposed relationships, comparisons in trends are made regarding the effects of magnitude, site-to-source distance, and depth. Also, the difference in the equivalent number of cycles between CEUS and WUS motions is identified. In addition, for the number of equivalent stress cycles, both the CEUS and WUS relations are compared with existing relationships (Liu et al., 2001; Seed et al., 1975), and the findings are described and discussed. However, no comparisons are made for the strain-based cycles due to absence of existing relationships. Lastly, the major findings from this study and desired future studies are summarized.

7.2 Equivalent Number of Stress Cycles: $n_{eq\tau}$

7.2.1 Definition

Based on the P-M cumulative damage hypothesis, the number of equivalent stress cycles expressed in terms of dissipated energy is given by:

$$n_{eq} = \frac{\sum_i \omega_i}{\omega_{ref\,(1\,cycle)}} \qquad \text{(Green, 2001)} \qquad \text{(Eq. 7-1)}$$

where, the numerator in this expression is the energy dissipated in a unit volume of soil at a specified depth due to the passage of the ground motions, which is equal to the cumulative area bounded by the shear stress-shear strain hysteretic loops obtained from site response analyses; the denominator of this expression (i.e., $\omega_{ref\,(1\,cycle)}$) is the energy that would be dissipated in the same unit volume of soil if it were subjected to one cycle of sinusoidal loading having an amplitude equal to 0.65× the maximum absolute shear stress (τ_{max}) as a reference amplitude. These two quantities are illustrated in Figure 7-1. The numerator of Eq. 7-1 can be computed using the trapezoidal rule:

$$\sum_i \omega_i = \frac{1}{2}\sum_{j=1}^{i}(\tau_{j+1} + \tau_j)(\gamma_{j+1} - \gamma_j) \qquad \text{(Eq. 7-2)}$$

where: τ_j and γ_j are the shear stress and shear strain at time $j{\cdot}\Delta t$, and Δt is the time step at which the time histories are discretized. The shear stress and strain time histories at soil layers used to compute $n_{eq\tau}$ at depth in the profile were obtained from the site response analyses described in the following section.

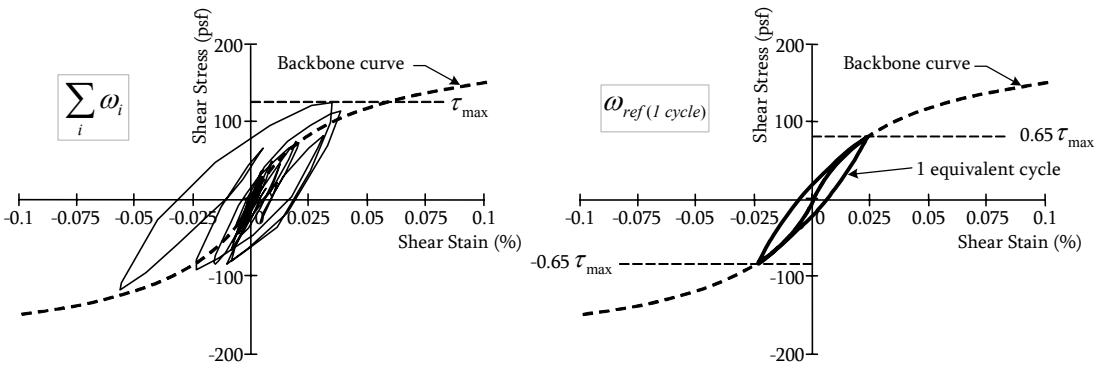

Figure 7-1. Graphical illustration of the numerator and denominator of Eq. 7-1 (Green et al., 2008).

7.2.2 Site Response Analyses

The equivalent linear site response code SHAKEVT (Green, 2001), a modified version of SHAKE91 (Idriss and Sun, 1992), was used to propagate the CEUS and WUS rock motions up through soil profiles. In these analyses, the shear stress and strain time histories on the top of each layer were computed, which were used to compute $n_{eq\tau}$ at the depths corresponding to the top of each layer. A 30 m-deep soil profile was used in this study and the total unit weight of soil was assumed to be 19.6 kN/m^3 (≈ 125 pcf). The soil profile was subdivided into 12 layers overlying bedrock, wherein the ground water table was assumed to be at a depth of 1.52 m. The profile is listed in Table 7-1.

To account for the difference in the geological characteristics between the two different tectonic regimes (i.e., CEUS and WUS), shear wave velocities of 2439 m/sec and 640 m/sec were used for the bedrocks of CEUS and WUS, respectively. Also, to consider the variation in dynamic property of the soil layers with respect to depth, the small strain secant shear moduli G_{max} of each layer are modeled by:

$$\left(G_{\max}\right)_{\text{model}} = G_0 \cdot z^n \qquad \text{(Eq. 7-3)}$$

where: $(G_{\max})_{\text{model}}$ is the small strain secant shear modulus modeled; z is depth; G_0 is defined as:

$$G_0 = \frac{\left(G_{\max}\right)_{z_{ref}}}{z_{ref}^{\ n}} \qquad \text{(Eq. 7-4)}$$

where, $\left(G_{\max}\right)_{z_{ref}}$ is $G_{\max}$ at a reference depth z_{ref}; z_{ref} of 3.96 m was used since it is the depth at which liquefaction has been observed to occur most frequently. Also, the $N_{1,60}$ value of 12 is used in estimating the $G_{\max}$ at z_{ref} (termed as reference $G_{\max}$ subsequently). Consequently, the soil at the depth is representative of sandy soil having a loose-to-medium density. As may be surmised from Eq. 7-3 and Eq. 7-4, the modeled $G_{\max}$ will increase with increasing depth and have a common value at the z_{ref} (i.e., the reference $G_{\max}$) for an n values greater than zero. If n is equal to zero, $G_{\max}$ will be constant with depth and equal to the reference $G_{\max}$. Shear wave velocity (V_S) is related to the modeled shear moduli ($(G_{\max})_{\text{model}}$) by:

$$V_S(z) = \sqrt{\frac{\left(G_{\max}\right)_{\text{model}} \cdot g}{\gamma_t}} \qquad \text{(Eq. 7-5)}$$

where: g is the acceleration due to gravity; γ_t is the total unit weight of soil. A total of six different shear wave velocity profiles corresponding to the model parameter n = 0.0, 0.1, 0.2, 0.3, 0.4, and 0.5 were considered in this study. The shear wave velocity for each soil layer was computed using Eqs. 7-3 through 7-5 for depths corresponding to the center of the layer. The shear wave velocity profiles used in this study are tabulated in Table 7-2 and illustrated in Figure 7-2.

Table 7-1. Depth profile and total unit weight of soil used in this study.

Layer No.	Top (m)	Bottom (m)	Thickness (m)	γ_t (kN/m^3)
1	0.00	0.46	0.46	19.6
2	0.46	0.91	0.46	19.6
3	0.91	1.52	0.61	19.6
4	1.52	2.38	0.85	19.6
5	2.38	3.54	1.16	19.6
6	3.54	5.12	1.58	19.6
7	5.12	7.28	2.16	19.6
8	7.28	10.15	2.87	19.6
9	10.15	13.87	3.72	19.6
10	13.87	18.50	4.63	19.6
11	18.50	24.38	5.88	19.6
12	24.38	30.48	6.10	19.6
Bedrock	30.48			22.0

Table 7-2. Shear wave velocity profiles used in this study.

Layer No.	V_S (m/s)					
	n = 0.0	n = 0.1	n = 0.2	n = 0.3	n = 0.4	n = 0.5
1	139.1	122.7	108.3	95.6	84.4	74.6
2	139.1	127.0	116.1	106.1	97.0	88.7
3	139.1	130.9	123.2	116.0	109.3	102.9
4	139.1	134.1	129.3	124.6	120.2	115.9
5	139.1	136.9	134.8	132.7	130.7	128.8
6	139.1	139.6	140.1	140.6	141.1	141.7
7	139.1	142.1	145.2	148.4	151.7	155.1
8	139.1	144.5	150.3	156.2	162.4	168.9
9	139.1	146.9	155.2	164.0	173.2	183.1
10	139.1	149.1	159.9	171.5	183.9	197.3
11	139.1	151.2	164.5	178.9	194.6	211.7
12	139.1	153.1	168.6	185.7	204.5	225.3
Bedrock	CEUS: 2439 WUS: 640					

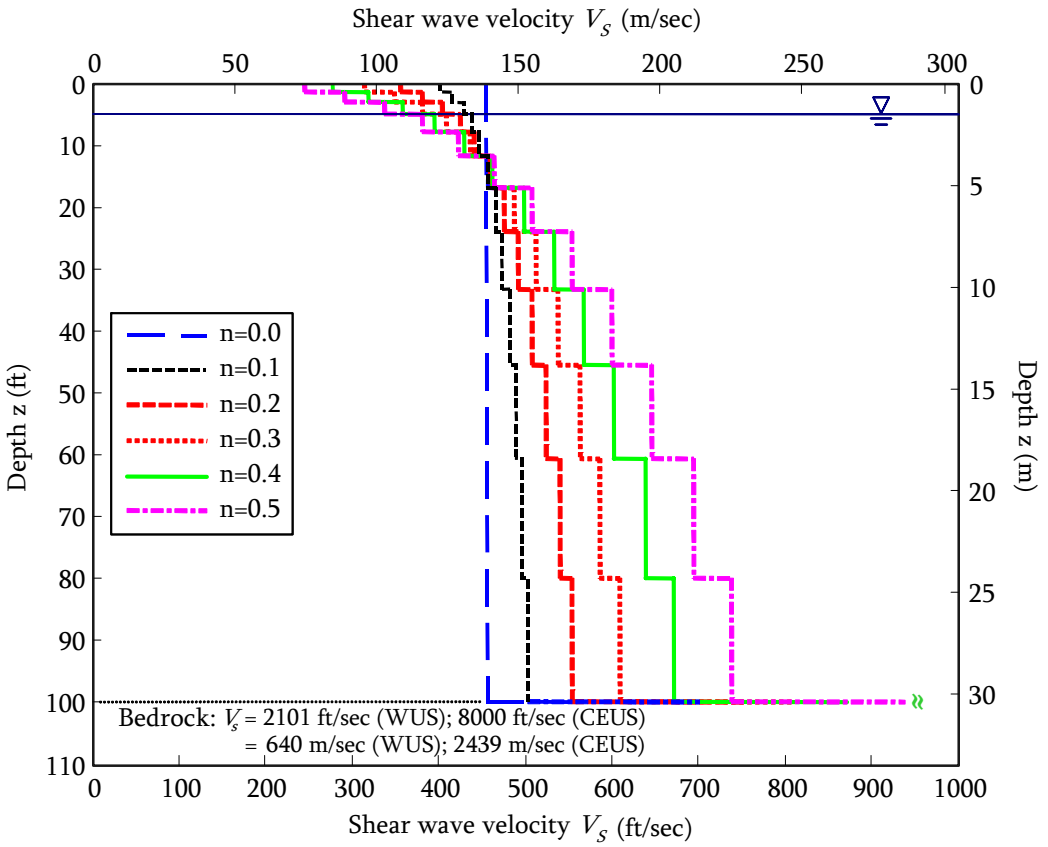

Figure 7-2. Shear wave velocity profiles used for $n_{eq\tau}$.

The shear modulus and damping degradation curves account for non-linear behavior under seismic loading. The G/G_{max} and damping degradation curves developed by Ishibashi and Zhang (1993) were used. The G/G_{max} degradation is given by:

$$\frac{G}{G_{\max}} = K(\gamma, I_p) \cdot (\sigma'_{m0})^{m'(\gamma, I_p)} \qquad \text{(Eq. 7-6)}$$

$$K(\gamma, I_p) = 0.5 \cdot \left\{ 1 + \tanh\left[\ln\left(\frac{0.000102 + n(I_p)}{\gamma} \right)^{0.492} \right] \right\} \qquad \text{(Eq. 7-7)}$$

$$n(I_p) = \begin{Bmatrix} 0.0 & for & I_p = 0 & (sandy\ soils) \\ 3.37\times10^{-6} I_p^{1.404} & for & 0 < I_p \le 15 & (low\ plastic\ soils) \\ 7.0\times10^{-7} I_p^{1.976} & for & 15 < I_p \le 70 & (medium\ plastic\ soils) \\ 2.7\times10^{-5} I_p^{1.115} & for & I_p > 70 & (high\ plastic\ soils) \end{Bmatrix} \quad \text{(Eq. 7-8)}$$

$$m'(\gamma, I_p) = 0.272 \cdot \left\{1 - \tanh\left[\ln\left(\frac{0.000556}{\gamma}\right)^{0.4}\right]\right\} \cdot e^{-0.0145 I_P^{1.3}} \quad \text{(Eq. 7-9)}$$

where: γ is shear strain; I_p is the plasticity index; σ'_{m0} is the initial mean effective confining stress in kPa determined by:

$$\sigma'_{mo} = \left(\frac{1+2K_0}{3}\right)\sigma'_{vo} \quad \text{(Eq. 7-10)}$$

where: σ'_{v0} is the initial effective vertical stress in kPa; K_0 is the coefficient of lateral earth pressure at rest determined by:

$$K_0 = 1 - \sin(\phi') \qquad \text{(Jaky, 1944)} \quad \text{(Eq. 7-11)}$$

where, ϕ' is the effective internal friction angle estimated by:

$$\phi' = (20 \cdot N_{1,60})^{0.5} + 20 \qquad \text{(Hatanaka and Uchida, 1996)} \quad \text{(Eq. 7-12)}$$

The damping degradation curve is given by:

$$D(\gamma, I_p) = \frac{0.333 \cdot (1 + e^{-0.0145 I_P^{1.3}})}{2} \left\{0.586 \cdot \left(\frac{G}{G_{\max}}\right)^2_{(\gamma, I_P)} - 1.547 \cdot \left(\frac{G}{G_{\max}}\right)_{(\gamma, I_P)} + 1\right\}$$

(Eq. 7-13)

where, $G/G_{\max}$ was determined by Eq. 7-6. Figure 7-3 shows examples of shear modulus and corresponding damping degradation curves for various initial effective vertical stresses in sandy soils (i.e., $I_p = 0$). The shear modulus ratios and damping curves for each

layer were computed using the soil state/properties at the center of the layer. The curves were compute at discretized shear strains approximately evenly-spaced in the log scale: 0.0001, 0.0003, 0.001, 0.003, 0.01, 0.03, 0.1, 0.3, and 1.0 % strains, with values at intermediate strains determined by log-linear interpolation.

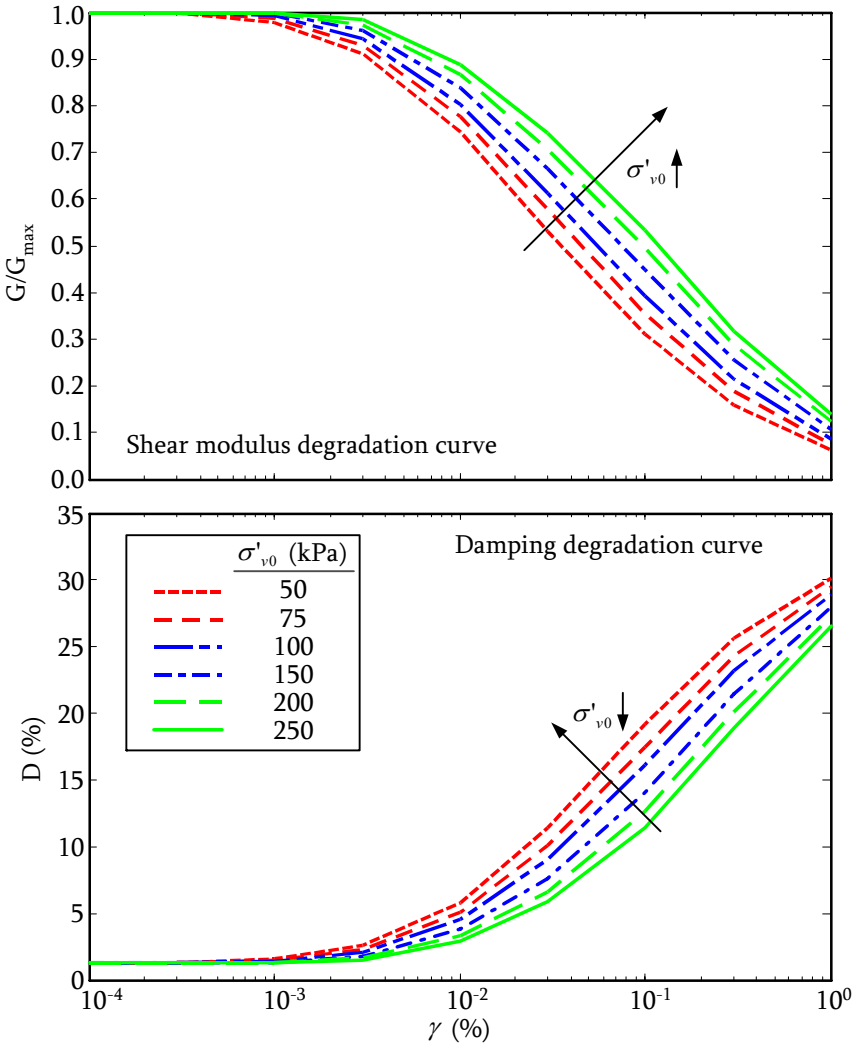

Figure 7-3. Examples of shear modulus and damping degradation curves per Ishibashi and Zhang (1993).

7.2.3 Proposed Model

After observing trends in $n_{eq\tau}$ data and considering numerous functional forms, the regression model best representing the data as a function of earthquake magnitude, distance, and depth is:

$$\ln\left(n_{eq\tau}\right) = \exp\left(C_1 z\right) + C_2 R^{C_3} + C_4 M + C_5 \qquad \text{(Eq. 7-14)}$$

where: C_1 through C_5 are regression coefficients; z is depth (m); M is moment magnitude; R is the closest distance to the fault rupture plane (km). This model is used in the NLME regression analyses for each soil.

7.2.4 Regression Results

The results from the NLME regression analyses (i.e., regression coefficients, p-values, and standard deviations) for each shear wave velocity profile are listed in Table 7-3 for both CEUS and WUS. Although the coefficient C_4 was estimated to be statistically insignificant (i.e., p-value > 5 % or 0.05), it was decided to keep the term with C_4 in the proposed predictive relationship in order to reduce the total standard deviations and to ensure a magnitude dependence. Based on the total standard deviations of CEUS and WUS, the $n_{eq\tau}$ predictions for CEUS are likely to have more uncertainties than those for WUS. Also, in comparisons of the total standard deviations among the different shear wave velocity profiles, although they are comparable to each other, the regressions for the n = 0.5 profile resulted in the lowest total standard deviation both for CEUS and WUS.

Table 7-3. Regression coefficients; their p-values (in parentheses); and standard deviations of inter-event, intra-event, and total errors.

CEUS								
n	C_1	C_2	C_3	C_4	C_5	τ_{ln}	σ_{ln}	$\sigma_{ln\ total}$
0.0	-0.0211 (0.000)	2.111 (0.001)	0.120 (0.000)	0.005 (0.954)	-1.80 (0.044)	0.36	0.51	0.62
0.1	-0.0214 (0.000)	2.266 (0.002)	0.113 (0.000)	0.018 (0.835)	-2.03 (0.032)	0.36	0.50	0.62
0.2	-0.0219 (0.000)	2.415 (0.002)	0.107 (0.000)	0.042 (0.630)	-2.29 (0.021)	0.36	0.49	0.61
0.3	-0.0209 (0.000)	2.150 (0.000)	0.120 (0.000)	0.040 (0.646)	-1.99 (0.022)	0.36	0.48	0.60
0.4	-0.0190 (0.000)	1.857 (0.000)	0.136 (0.000)	0.050 (0.554)	-1.77 (0.019)	0.34	0.48	0.59
0.5	-0.0171 (0.000)	1.760 (0.000)	0.141 (0.000)	0.055 (0.502)	-1.69 (0.020)	0.34	0.48	0.59
WUS								
n	C_1	C_2	C_3	C_4	C_5	τ_{ln}	σ_{ln}	$\sigma_{ln\ total}$
0.0	-0.0123 (0.000)	1.820 (0.002)	0.120 (0.000)	0.074 (0.363)	-2.02 (0.015)	0.30	0.45	0.54
0.1	-0.0116 (0.000)	2.042 (0.003)	0.108 (0.000)	0.116 (0.177)	-2.47 (0.007)	0.31	0.42	0.52
0.2	-0.0112 (0.000)	2.083 (0.002)	0.107 (0.000)	0.104 (0.232)	-2.43 (0.008)	0.32	0.41	0.52
0.3	-0.0104 (0.000)	1.904 (0.001)	0.117 (0.000)	0.107 (0.199)	-2.27 (0.006)	0.30	0.41	0.51
0.4	-0.0101 (0.000)	1.664 (0.000)	0.131 (0.000)	0.122 (0.140)	-2.11 (0.004)	0.30	0.40	0.50
0.5	-0.0107 (0.000)	1.370 (0.000)	0.150 (0.000)	0.154 (0.062)	-1.98 (0.003)	0.30	0.40	0.50

The distributional assumptions of the intra-event errors and random-effects were assessed using normal Q-Q plots. Figure 7-4 shows the normal Q-Q plots of intra-event errors and random-effects for the profile $n = 0.3$ for both CEUS and WUS. As may be seen from these plots, the overall distributions of both intra-event errors and random-effects follow normal distributions. Additionally, the scatter plots for intra-event errors and random-effects for $n = 0.3$ are shown in Figure 7-5. In general, the overall distributions are

symmetrical with respect to the zero lines of the standardized inter-event errors and random-effects. Similar distributions were observed from the normal Q-Q plots for the other profiles.

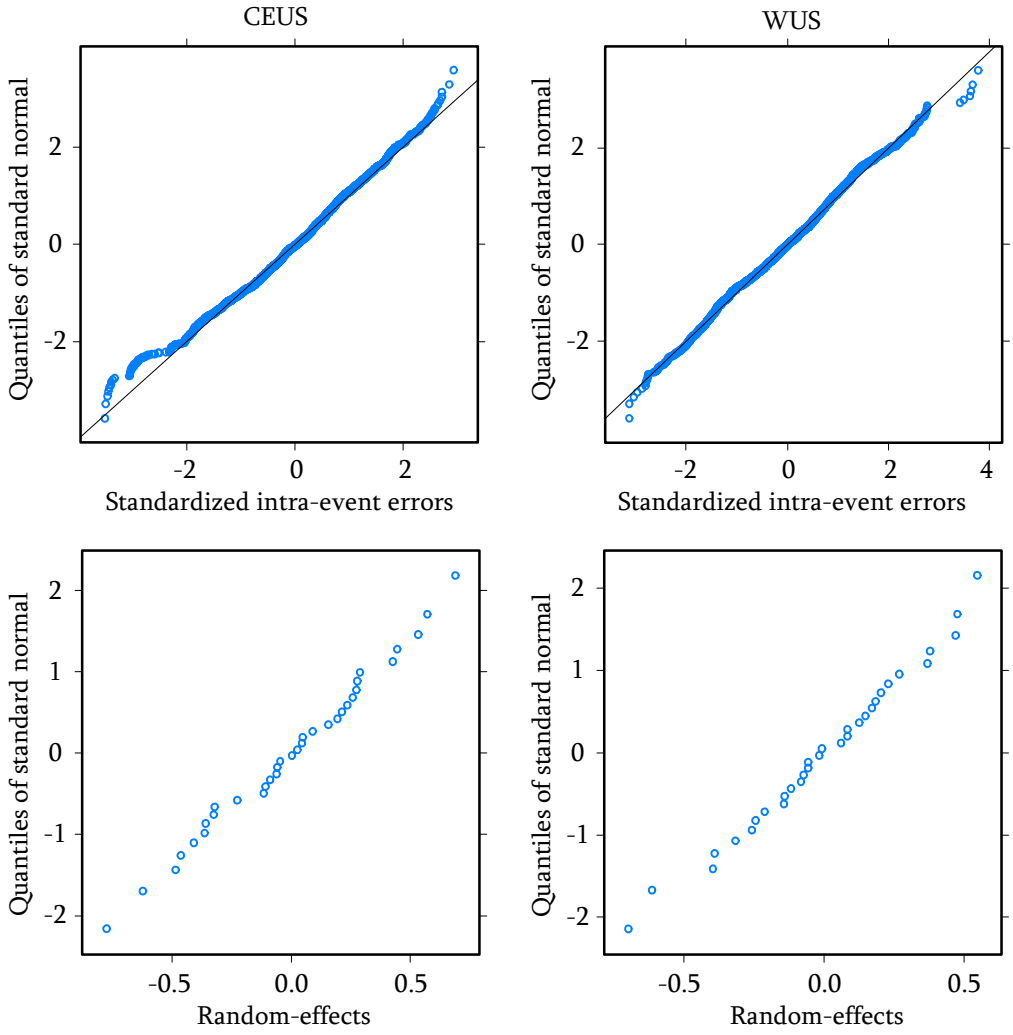

Figure 7-4. Normal Q-Q plots of intra-event errors (top) and random-effects (bottom) for CEUS (left) and WUS (right): $n = 0.3$.

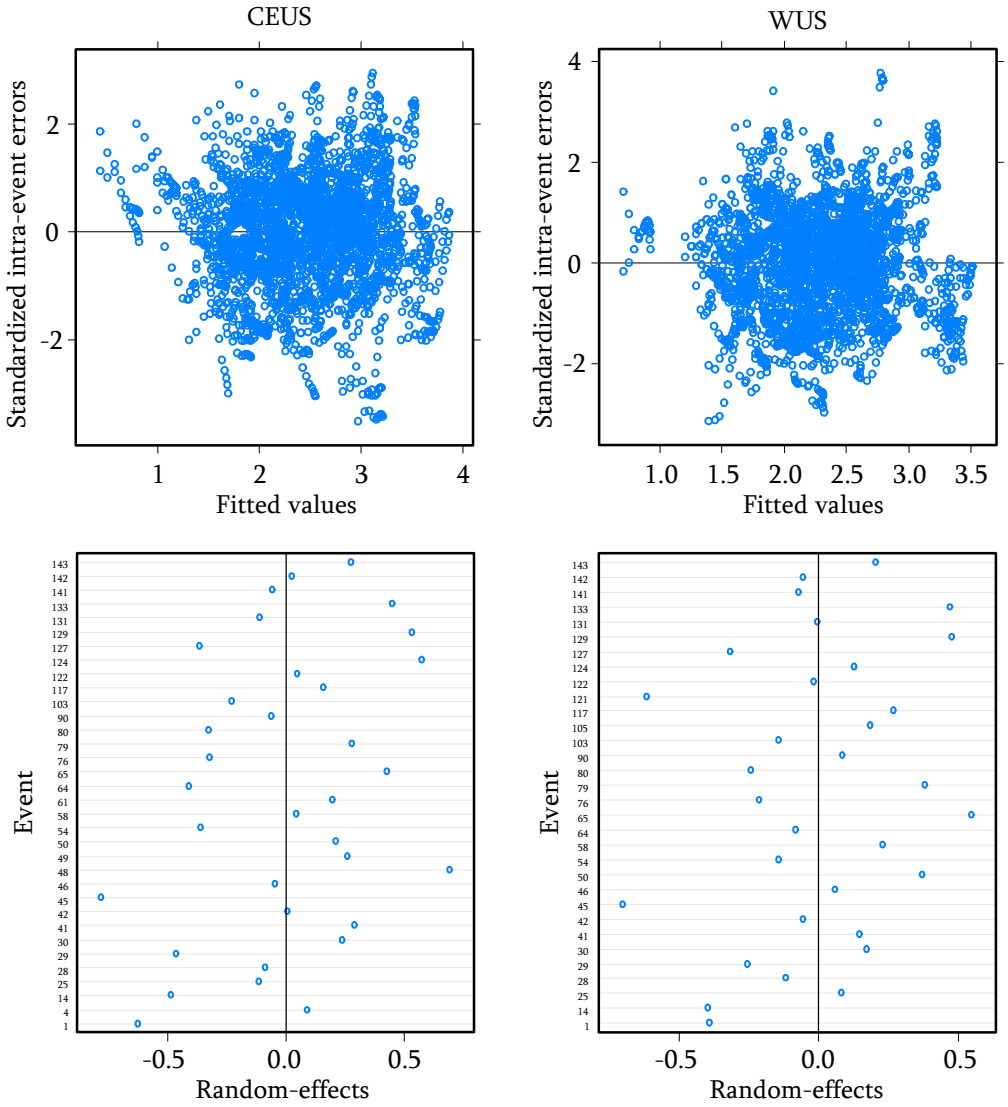

Figure 7-5. Scatter plots of intra-event errors (top) and random-effects (bottom) for CEUS (left) and WUS (right): $n = 0.3$.

Using the proposed predictive relationship (Eq. 7-14) in conjunction with the regression coefficients listed in Table 7-3, the predicted medians for the number of equivalent stress cycles are plotted in Figure 7-6 and Figure 7-7 for both CEUS and WUS. These figures allow the magnitude and distance dependencies to be discerned for the various soil profiles. Note that View A and B are different views of the same plot. One can readily observe that the $n_{eq\tau}$ increases as distance increases, for all of the soil profiles. The magnitude dependence is shown to be less significant than the distance dependence, especially for near-fault regions (i.e., R < ~ 25 km). However, the $n_{eq\tau}$ for far-field motions are clearly shown to increase with increasing earthquake magnitude, although for the n = 0.0 profile (i.e., uniform profile), the predicted $n_{eq\tau}$ is relatively independent of magnitude. Additionally, comparing the two different tectonic regions, CEUS motions are consistently estimated to have larger $n_{eq\tau}$ than WUS motions for all the profiles.

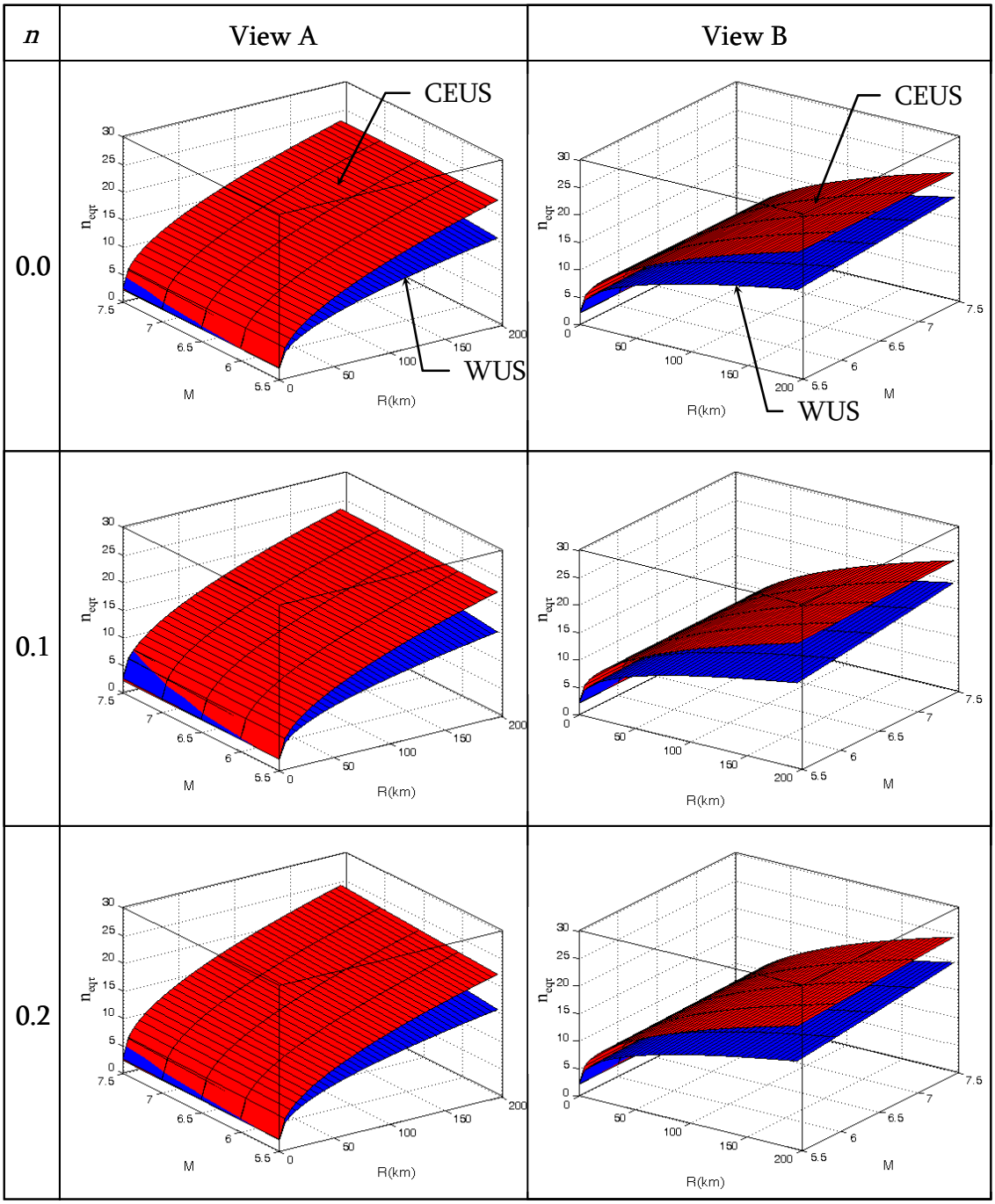

Figure 7-6. Magnitude and distance dependencies of the predicted $n_{eq\tau}$ at a depth of 3.54 m (i.e., top of layer 6) for CEUS and WUS: n = 0.0, 0.1, 0.2.

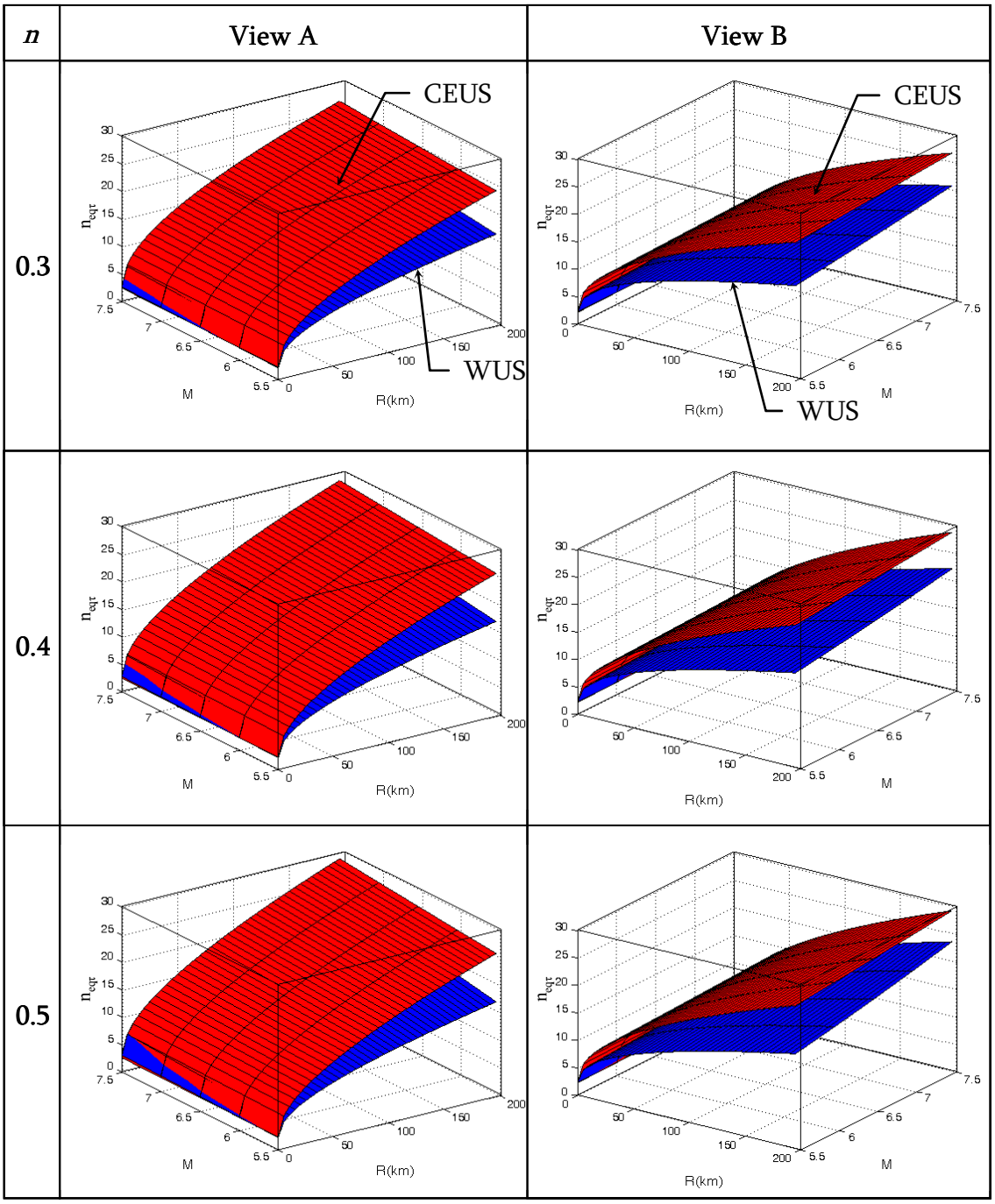

Figure 7-7. Magnitude and distance dependencies of the predicted $n_{eq\tau}$ at a depth of 3.54 m (i.e., top of layer 6) for CEUS and WUS: n = 0.3, 0.4, 0.5.

To examine depth dependence, the $n_{eq\tau}$ values were normalized by $n_{eq\tau}$ at a depth of 3.54 m (i.e., top of layer 6). Figure 7-8 shows the normalized $n_{eq\tau}$ as a function of depth for the various soil profiles for both CEUS and WUS motions. Overall, the $n_{eq\tau}$ values are predicted to decrease as depth increases. For CEUS motions, the $n_{eq\tau}$ at the profile n = 0.5 are shown to have a slightly smaller variation with depth than those at the other profiles, while for WUS motions depth dependence is comparable among the different profiles. It should be noted that the normalized $n_{eq\tau}$ values are independent of magnitude and distance since the magnitude and distance terms of the proposed model cancel in the normalization. That is, Figure 7-8 is valid for all magnitudes and distances.

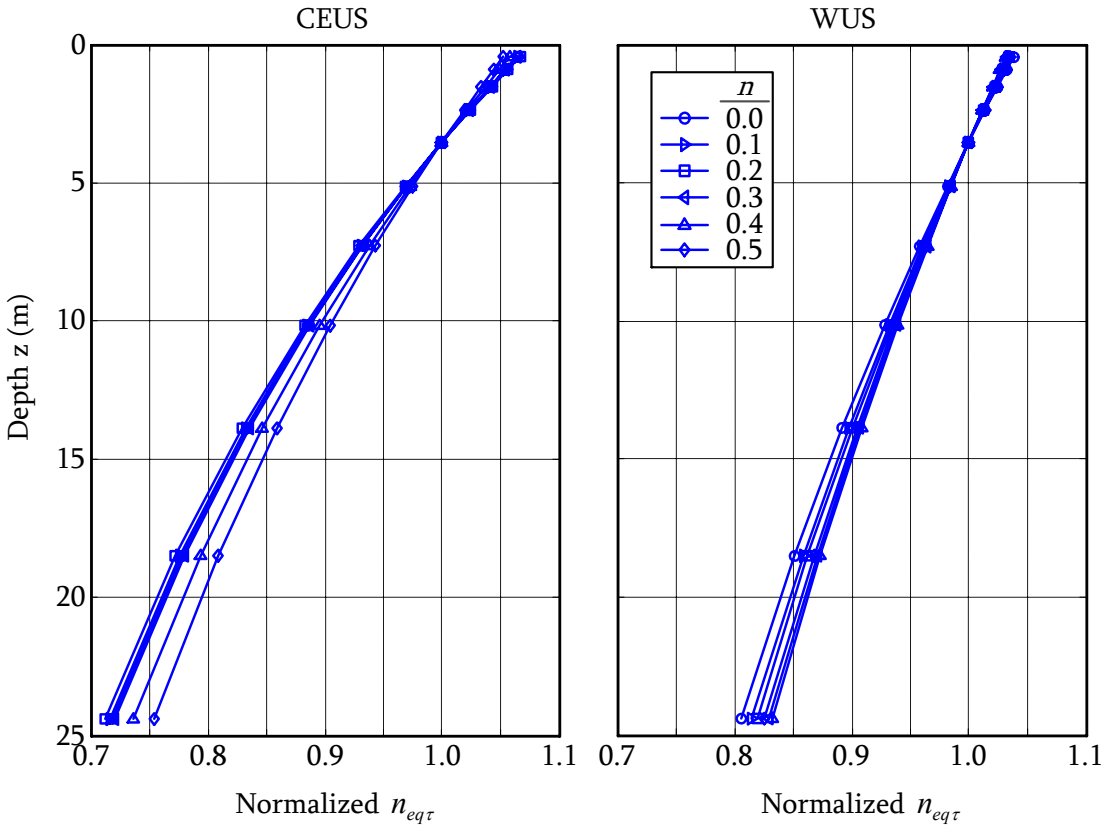

Figure 7-8. Depth dependence of the $n_{eq\tau}$ predicted for different soil profiles for CEUS (left) and WUS (right). $n_{eq\tau}$ is normalized by $n_{eq\tau}$ at z = 3.54 m (i.e., top of layer 6).

The depth dependences of the $n_{eq\tau}$ for n = 0.3 for CEUS and WUS are compared in Figure 7-9. The $n_{eq\tau}$ predicted for CEUS vary as a function of depth more than those for WUS. This trend is consistent among all the profiles.

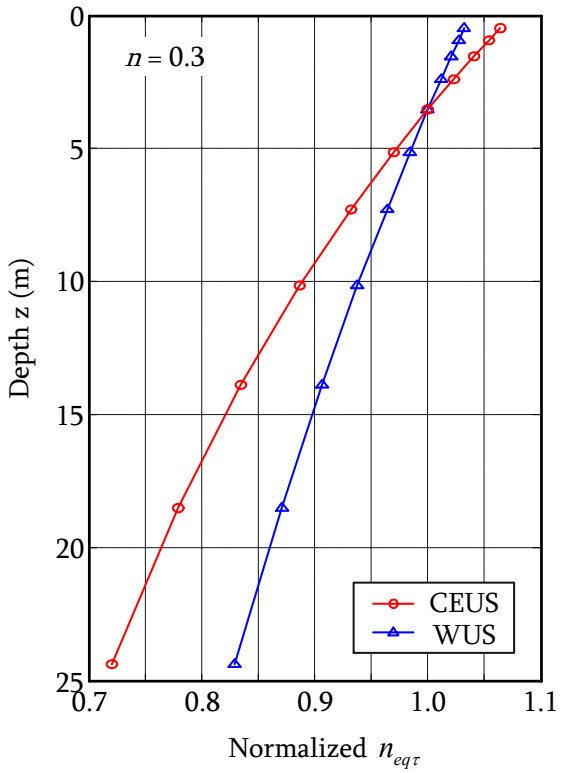

Figure 7-9. Comparison of depth dependencies for CEUS and WUS: n = 0.3.

7.2.5 Comparison with Existing Relationships

The proposed predictive relationships for CEUS and WUS are compared to the existing relationships developed for active shallow crustal regions. Comparisons with Seed et al. (1975) and Liu et al. (2001) models are made herein. Liu et al. (2001) adopted the approach proposed by Seed et al. (1975) for computing $n_{eq\tau}$, which is based on the P-M hypothesis but does not explicitly consider non-linear soil behavior. However, Liu et al. (2001) used a much larger ground motion database than Seed et al. (1975) used. As

shown in Figure 7-10, there are significant differences in the $n_{eq\tau}$ predictions among the relationships. The Liu et al. model predicts significantly larger $n_{eq\tau}$ than the others for all magnitudes and distances. Also, the Seed et al. (1975) and the Liu et al. (2001) relations show a much higher variation of $n_{eq\tau}$ as a function of magnitude than the relationship proposed herein. The Seed et al. relationship is independent of site-to-source distance, while the Liu et al. relationship and the relationship proposed herein have similar distance dependencies in the far-field. In the near-field, the relationship proposed herein has a higher distance dependency than the Liu et al. relationship.

The considerable difference in the $n_{eq\tau}$ predictions likely stems from the different approaches used to implement P-M fatigue hypothesis (i.e., the dissipated energy-based approach (Green, 2001) vs. the approach by peak counting in conjunction with the weighting factor curves (Seed et al., 1975; Liu et al., 2001).

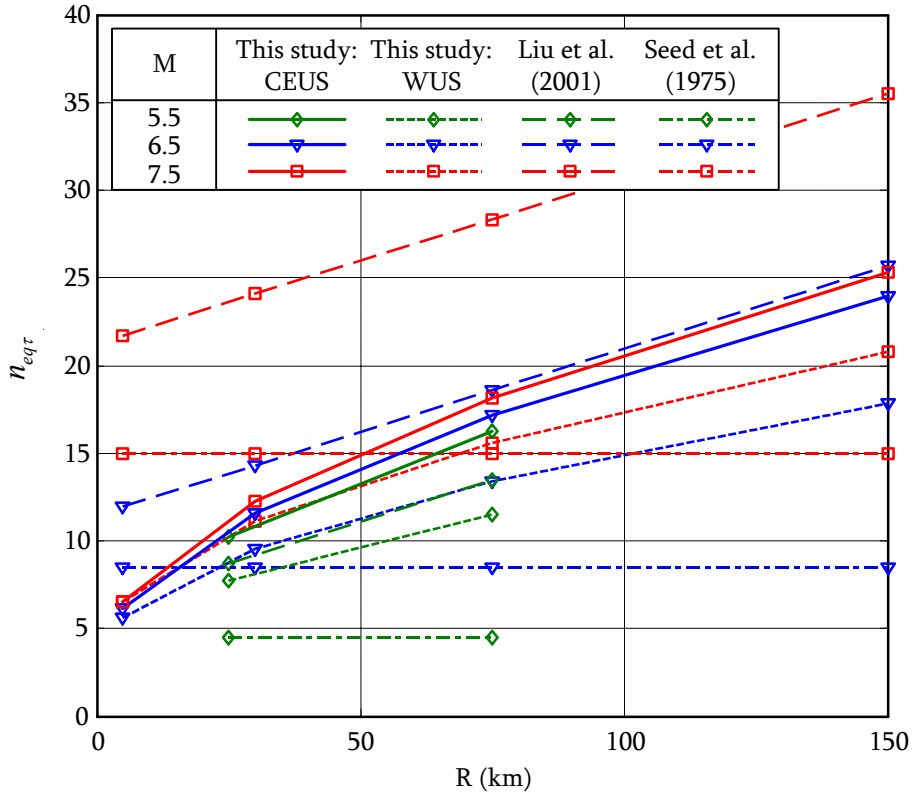

Figure 7-10. Comparison of the $n_{eq\tau}$ predictions from existing relations. The $n_{eq\tau}$ at a depth of 3.54 m (i.e., top of layer 6) for the n = 0.5 profile is used in the comparison.

7.3 Equivalent Number of Strain Cycles: $n_{eq\gamma}$

7.3.1 Definition

Martin, Finn, and Seed (1975) developed a model for computing incremental volumetric strain ($\Delta\varepsilon_v$) in dry sands subjected to cyclic shearing. Based on experimental data, Byrne (1991) simplified the model as:

$$(\Delta\varepsilon_v)_{1/2cycle} = 0.5\,\gamma\,C_1 \exp(-C_2\,\frac{\varepsilon_v}{\gamma}) \qquad \text{(Eq. 7-15)}$$

where, $(\Delta\varepsilon_v)_{1/2cycle}$ is the incremental volumetric strain per half cycle of shear strain; and γ is the peak shear strain for the half cycle. C_1 and C_2 are empirical model parameters accounting for the strength of sand:

$$C_1 = \begin{cases} 8.7 N_{1,60}^{-1.25} \\ \text{or} \\ 7600\, D_r^{-2.5} \end{cases} \qquad \text{(Eq. 7-16)}$$

$$C_2 = \frac{0.4}{C_1} \qquad \text{(Eq. 7-17)}$$

where, D_r is the relative density of soil in percent.

To compute the cumulative volumetric strains using the shear strain history obtained from the SHAKEVT, the simplified Martin, Finn, and Seed model can be rewritten as:

$$(\Delta\varepsilon_v)_i = 0.5 \left| \gamma_i \right| C_1 \exp(-C_2 \frac{(\varepsilon_v)_i}{\left| \gamma_i \right|}) \qquad \text{(Eq. 7-18)}$$

where, $(\Delta\varepsilon_v)_i$ is the i^{th} incremental volumetric strain induced by the i^{th} half strain cycle; and γ_i is the peak shear strain for the i^{th} half strain cycle. The cumulative volumetric strain after the i^{th} half strain cycle can be computed by the following equation:

$$(\varepsilon_v)_{i+1} = (\varepsilon_v)_i + (\Delta\varepsilon_v)_i \qquad \text{(Eq. 7-19)}$$

Using Eqs. 7-18 and 7-19, the cumulative volumetric strain at the end of shaking can be computed. The number of equivalent strain cycles is computed by subjecting the soil to $n_{eq\gamma}$ cycles of a uniform load such that the cumulative volumetric strain is equal to that induced by the earthquake shear strain time history.

By convention, the amplitude of the uniform cyclic load (i.e., effective shear strain: γ_{eff}) is:

$$\gamma_{eff} = 0.65|\gamma_{\max}| \quad \text{(Eq. 7-20)}$$

where, $\gamma_{\max}$ is the maximum shear strain (positive or negative) in the earthquake shear strain time history. The ith incremental volumetric strain induced by a half cycle of the uniform load is:

$$(\Delta\varepsilon_v)_i = 0.5\ \gamma_{eff}\ C_1 \exp\left(-C_2 \frac{(\varepsilon_v)_i}{\gamma_{eff}}\right) \quad \text{(Eq. 7-21)}$$

The cumulative volumetric strain after the ith half strain cycle is computed using Eq 7-19. The computations of Eqs. 7-19 and 7-21 are repeated until the cumulative volumetric strain from the uniform cyclic strain history equals that induced by the earthquake strain time history obtained from SHAKEVT. The number of equivalent strain cycles ($n_{eq\gamma}$) is equal to half the number of half cycles required to equate the cumulative volumetric strains.

7.3.2 Site Response Analyses

Similarly as in the number of equivalent stress cycles, the CEUS and WUS rock motions were propagated up through a soil profile by utilizing the equivalent linear site response code SHAKEVT (Green, 2001). The shear strain time histories on top of each layer were computed, which in turn were used to compute $n_{eq\gamma}$ at the depths corresponding to the top of each layer. A 30 m-deep soil profile was used in this study, with the total unit weight of soil assumed to be 19.6 kN/m^3 (≈ 125 pcf). The soil profile was subdivided into 12 layers overlying bedrock. Since this study developed the $n_{eq\gamma}$ predictive relation for use in

the Tokimatsu and Seed (1987) seismic compression evaluation procedure for dry sands, no ground water table was considered in the soil profile. To account for the difference in the geological characteristics between the two different tectonic regions (i.e., CEUS and WUS), shear wave velocities of 1524 m/sec and 762 m/sec were used for the bedrocks of CEUS and WUS, respectively. Only one shear wave velocity profile was used in the analyses, which was modeled in a similar manner to the profiles used for the equivalent stress cycle analyses. $n = 0.4$ was used to compute the shear wave velocity of the soil profile as a function of depth. However, this $n = 0.4$ differs from the $n = 0.4$ used for stress cycles computations because the effective stresses are different. The properties of the soil profile used in this study are tabulated in Table 7-4, and the shear wave velocity profile is illustrated in Figure 7-11.

Table 7-4. Soil profile used for $n_{eq\gamma}$ computations ($n = 0.4$).

Layer No.	Top (m)	Bottom (m)	Thickness (m)	V_S (m/s)	γ_t (kN/m^3)
1	0.00	0.46	0.46	89.5	19.6
2	0.46	0.91	0.46	117.8	19.6
3	0.91	1.52	0.61	136.0	19.6
4	1.52	2.38	0.85	153.0	19.6
5	2.38	3.54	1.16	169.8	19.6
6	3.54	5.12	1.58	186.7	19.6
7	5.12	7.28	2.16	204.3	19.6
8	7.28	10.15	2.87	222.5	19.6
9	10.15	13.87	3.72	241.0	19.6
10	13.87	18.50	4.63	259.7	19.6
11	18.50	24.38	5.88	278.6	19.6
12	24.38	30.48	6.10	296.3	19.6
Bedrock	30.48		WUS: CEUS:	762 1524	22.0 22.0

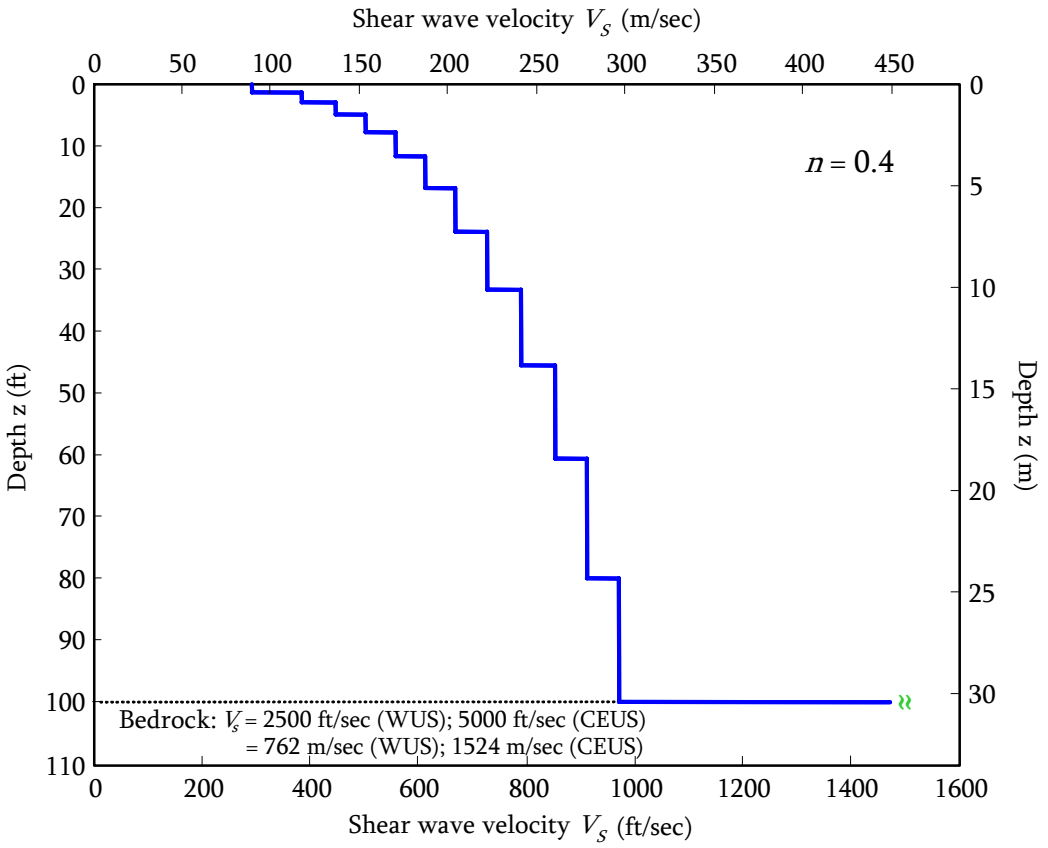

Figure 7-11. Shear wave velocity profile used for $n_{eq\gamma}$ computations.

Similar to the site response analyses for the equivalent stress cycles, shear modulus and damping degradation curves are used to account for non-linear behavior of the soil. The G/G_{max} and damping degradation curves by Ishibashi and Zhang (1993) were used.

7.3.3 Proposed Model

After identifying initial trends in the $n_{eq\gamma}$ data and considering numerous functional forms for relating the $n_{eq\gamma}$ to earthquake magnitude, distance, and depth, the same regression model as that used for the number of equivalent stress cycles represented the data best, i.e.:

$$\ln\left(n_{eq\gamma}\right) = \exp\left(C_1 z\right) + C_2 R^{C_3} + C_4 M + C_5 \qquad \text{(Eq. 7-22)}$$

where: C_1 through C_5 are regression coefficients; z is depth (m); M is moment magnitude; R is the closest distance to the fault rupture plane (km).

7.3.4 Regression Results

The results of the NLME regression analyses (i.e., regression coefficients, p-values, and standard deviations) are listed in Table 7-5 for both CEUS and WUS. All the coefficients were estimated to have significant statistical contributions (i.e., the p-value < 5 % or 0.05). Similar to the equivalent stress cycles relation, the total standard deviation for CEUS was greater than that of WUS.

Table 7-5. Regression coefficients, p-values (in parentheses), and standard deviations of inter-event, intra-event, and total errors.

CEUS							
C_1	C_2	C_3	C_4	C_5	τ_{ln}	σ_{ln}	$\sigma_{ln\ total}$
-0.020 (0.000)	0.80 (0.001)	0.22 (0.000)	0.19 (0.004)	-1.30 (0.007)	0.26	0.47	0.54
WUS							
C_1	C_2	C_3	C_4	C_5	τ_{ln}	σ_{ln}	$\sigma_{ln\ total}$
-0.0099 (0.000)	0.67 (0.002)	0.21 (0.000)	0.28 (0.000)	-1.79 (0.000)	0.24	0.41	0.48

The distributional assumptions of the intra-event errors and random-effects were assessed by the normal Q-Q plots shown in Figure 7-12. For CEUS and WUS, the overall distributions of both intra-event errors and random-effects are normal. Additionally, the scatter plots for intra-event errors and random-effects are shown in Figure 7-13. As may be observed from these figures, the overall distributions appear to be symmetrical with respect to the zero lines of the standardized inter-event errors and random-effects, representing normal distributions.

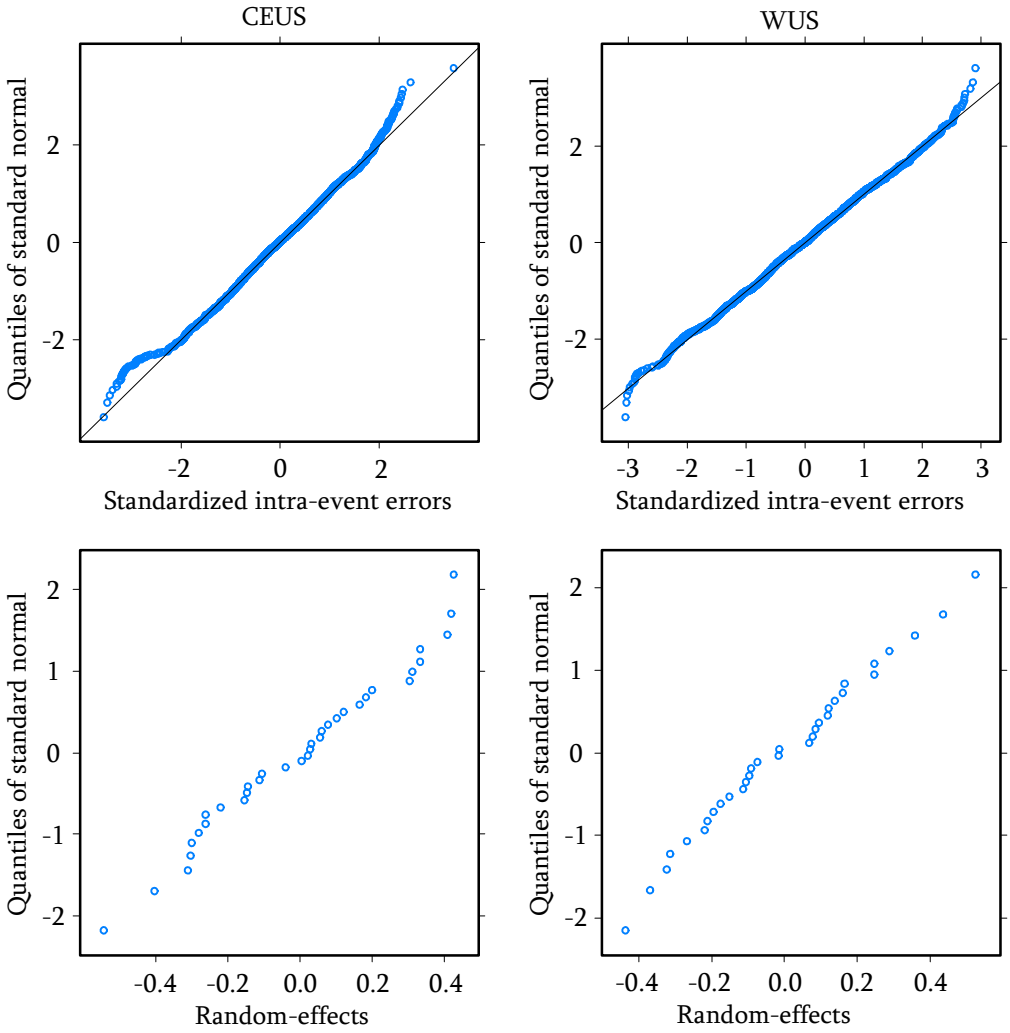

Figure 7-12. Normal Q-Q plots of intra-event errors (top) and random-effects (bottom) for CEUS (left) and WUS (right).

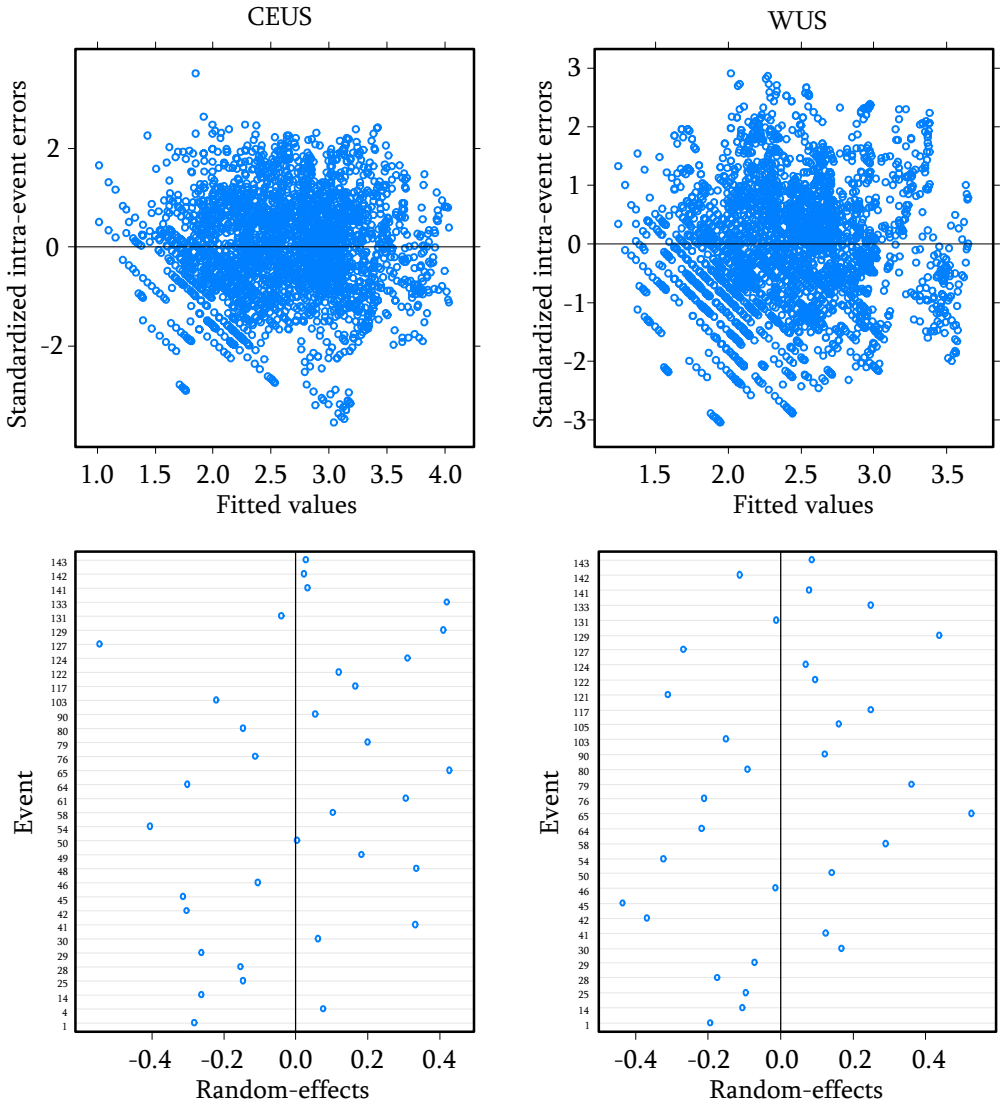

Figure 7-13. Scatter plots of intra-event errors (top) and random-effects (bottom) for CEUS (left) and WUS (right).

The predicted medians for the $n_{eq\gamma}$ at z = 3.54 m for CEUS and WUS motions are plotted in Figure 7-14. This figure allows the magnitude and distance dependencies of $n_{eq\gamma}$ to be discerned. Similar to the equivalent stress cycles, $n_{eq\gamma}$ increases as distance increases. This trend becomes more pronounced as earthquake magnitude increases. In near-fault regions (i.e., R < ~ 25 km), the magnitude dependence seems to be insignificant. However, the $n_{eq\gamma}$ for far-field motions show moderate increases with increasing earthquake magnitude. Additionally, comparing the two different tectonic regions, CEUS motions are consistently estimated to have larger $n_{eq\gamma}$ than WUS motions.

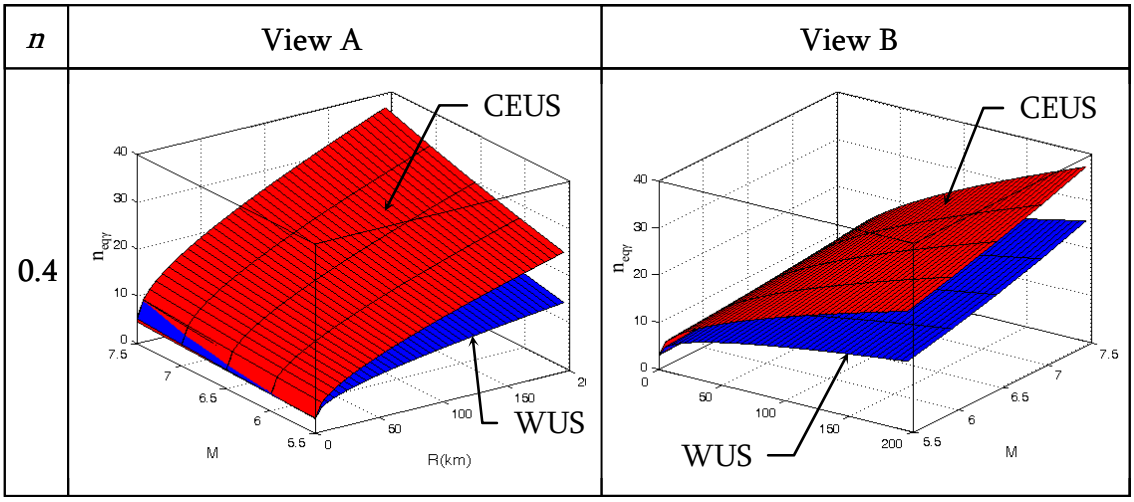

Figure 7-14. Magnitude and distance dependencies of the predicted $n_{eq\gamma}$ at a depth of 3.54 m (i.e., top of layer 6) for CEUS and WUS.

To examine depth dependence, the $n_{eq\gamma}$ are normalized by $n_{eq\gamma}$ at a depth of 3.54 m (i.e., top of layer 6). Figure 7-15 shows the normalized $n_{eq\gamma}$ as a function of depth for both CEUS and WUS motions. As may be observed from this figure, $n_{eq\gamma}$ decreases as depth increases. Comparing the two different tectonic regimes, the $n_{eq\gamma}$ predicted for CEUS vary as a function of depth more than those for WUS.

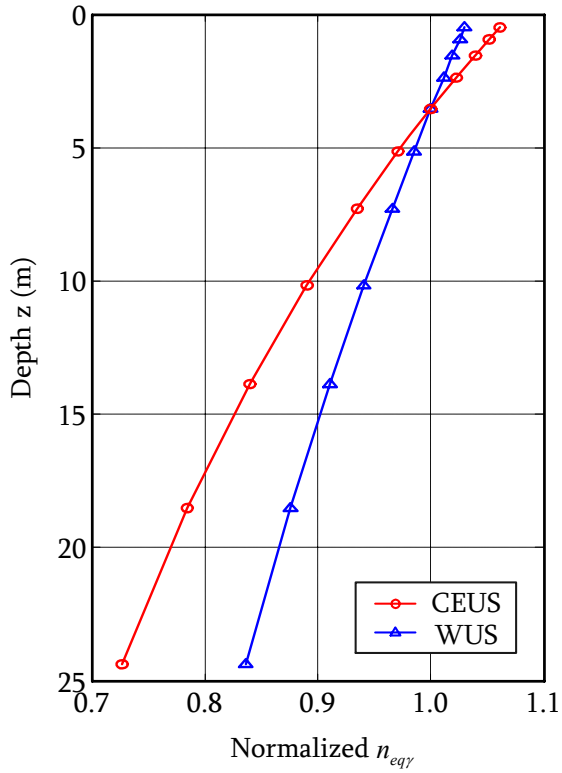

Figure 7-15. Depth dependence of the $n_{eq\gamma}$ for CEUS (left) and WUS (right). $n_{eq\gamma}$ was normalized by the $n_{eq\gamma}$ at z = 3.54 m (i.e., top of layer 6).

Figure 7-16 compares the $n_{eq\gamma}$ predictions at a depth of 3.54 m (i.e., top of layer 6) for CEUS and WUS motions. Although the $n_{eq\gamma}$ predictions for CEUS and WUS are comparable within near-fault regions, the $n_{eq\gamma}$ for CEUS become larger than those for WUS as distance increases.

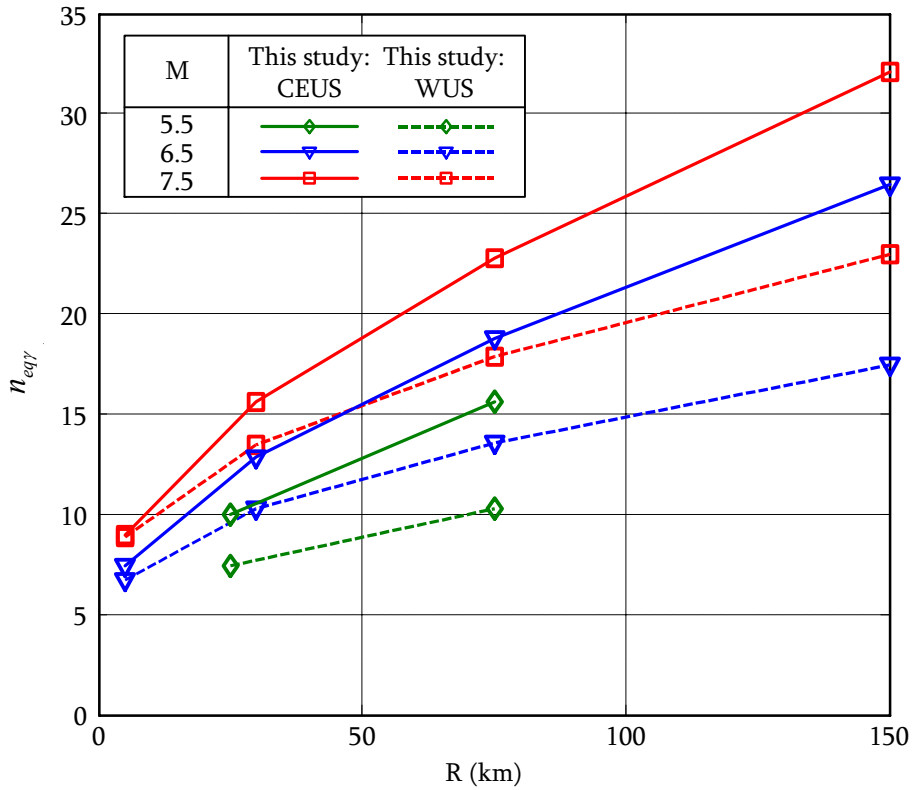

Figure 7-16. Comparison of the $n_{eq\gamma}$ predictions for CEUS and WUS at a depth of 3.54 m (i.e., top of layer 6).

7.4 Conclusions

Empirical predictive relationships for the number of equivalent stress and strain cycles for horizontal CEUS and WUS motions are proposed. The relationships account for the earthquake magnitude, site-to-source distance, and depth dependences. The proposed model for the number of equivalent stress cycles $n_{eq\tau}$ was developed using $n_{eq\tau}$ data computed by Green's (2001) energy-based approach. Based on the predictions from the proposed model, $n_{eq\tau}$ increases as distance increases but decreases as depth increases. Also, $n_{eq\tau}$ increases as earthquake magnitude increases although the magnitude

dependence is not significant within near-fault regions (i.e., R < 25 km). In comparing CEUS and WUS relations, it was found that the $n_{eq\tau}$ for CEUS tended to be larger and more depth-dependent than that for WUS. Also, there were significant differences among the $n_{eq\tau}$ predictions by this study's model and those from existing relationships. This difference is attributed to the different ways in which the P-M hypothesis was implemented for computing $n_{eq\tau}$.

The proposed predictive relationship for the number of equivalent strain cycles ($n_{eq\gamma}$) was based on data computed using the Green and Lee (2006) procedure. Similar to the findings from the equivalent stress cycles, $n_{eq\gamma}$ increases with increasing distance and increasing earthquake magnitude but decreases as depth increases. In comparing CEUS and WUS relations, CEUS relations predicted larger $n_{eq\gamma}$ and show greater depth dependence than WUS relations.

References

Annaki, M., and Lee, K. L. (1977). "Equivalent uniform cycle concept for soil dynamics". *American Society of Civil Engineers, Journal of the Geotechnical Engineering Division*, 103(6), 549-564.

Byrne, P. M. (1991). "A cyclic shear-volume coupling and pore pressure model for sand." *Proc., 2nd International Conference on Recent Advances in Geotechnical Earthquake Engineering and Soil Dynamics*, Paper No. 1.24, St. Louis, Missouri.

Collins, J. A. (1981). *Failure of materials in mechanical design: analysis, prediction, prevention*, Wiley, New York.

Green, R. A. (2001). "Energy-based evaluation and remediation of liquefiable soils," Ph.D. dissertation, Virginia Polytechnic Institute and State University, Blacksburg, Virginia.

Green, R. A., and Lee, J. (2006). "Computation of number of equivalent strain cycles: a theoretical framework". *Geomechanics II: Testing, Modeling, and Simulation*, ASCE Geotechnical Special Publication 156, 471-487.

Green, R. A., Lee, J., White, T. M., and Baker, J. W. (2008). "The significance of near-fault effects on liquefaction." *14th World Conference on Earthquake Engineering*, Beijing, China.

Green, R. A., and Terri, G. A. (2005). "Number of equivalent cycles concept for liquefaction evaluations - Revisited". *Journal of Geotechnical and Geoenvironmental Engineering*, 131(4), 477-488.

Hatanaka, M., and Uchida, A. (1996). "Empirical correlation between penetration resistance and internal friction angle of sandy soils". *Soils and Foundations*, 36(4), 1-9.

Idriss, I. M., and Sun, J. I. (1992). "SHAKE91: a computer program for conducting equivalent linear seismic response analyses of horizontally layered soil deposits." University of California, Davis.

Ishibashi, I., and Zhang, X. (1993). "Unified dynamic shear moduli and damping ratios of sand and clay". *Soils and Foundations*, 33(1), 182-191.

Jaky, J. (1944). "The coefficient of earth pressure at rest". *Journal of Society Hungarian Arch. Eng.*

Liu, A. H., Stewart, J. P., Abrahamson, N. A., and Moriwaki, Y. (2001). "Equivalent number of uniform stress cycles for soil liquefaction analysis". *Journal of Geotechnical and Geoenvironmental Engineering*, 127(12), 1017-1026.

Martin, G. R., Finn, W. D. L., and Seed, H. B. (1975). "Fundamentals of liquefaction under cyclic loading". *American Society of Civil Engineers, Journal of the Geotechnical Engineering Division*, 101(5), 423-438.

Miner, M. A. (1945). "Cumulative damage in fatigue". *Transactions, ASME*, 67, A159-A164.

Palmgren, A. (1924). "Die lebensdauer von kugella geru". *ZVDI*, 68(14), 339-341.

Richart, F. E., and Newmark, N. M. (1948). "An hypothesis for determination of cumulative damage in fatigue." *ASTM Proceedings*, 48: 767-800.

Seed, H. B., and Idriss, I. M. (1971). "Simplified procedure for evaluating soil liquefaction potential". *ASCE J. Soil Mech. Found. Div.*, 97(SM9), 1249-73.

Seed, H. B., Idriss, I. M., Makdisi, F., and Banerjee, N. (1975). "Representation of Irregular Stress Time Histories by Equivalent Uniform Stress Series in Liquefaction Analysis." Report No. EERC 75-29, Earthquake Engineering Research Center, College of Engineering, Univ. of California, Berkeley, California, United States.

Tokimatsu, K., and Seed, B. H. (1987). "Evaluation of settlement in sands due to earthquake shaking". *Journal of Geotechnical Engineering*, 113(8), 861-878.

Chapter 8

Pore Pressure Generation Calibration Parameters

8.1 Background

The generation of pore water pressures in soils during cyclic loadings such as earthquakes or pile driving has been studied for many years (e.g., Booker et al., 1976; Lee and Albaisa, 1974; Martin et al., 1975) and is still an area of active research (e.g., Peng et al., 2004; Sun and Yuan, 2006). In particular, the cyclic behavior of fine-grained soils has received considerable attention after the 1999 Kocaeli earthquake in Turkey, in which these soils exhibited behavior previously considered by some to be limited to coarser grained soils (e.g., Boulanger and Idriss, 2004; Boulanger and Idriss, 2006; Bray et al., 2004; Martin II et al., 2004; Sanin and Wijewickreme, 2006; Wijewickreme et al., 2005).

The pore pressure generation is often quantified in terms of excess pore pressure ratio r_u (or pore pressure ratio), defined as the ratio of the excess pore pressure u_{xs} (i.e., the pore pressure above static water pressure) to the initial effective confining stress σ'_0 acting on the soil (i.e., $r_u = u_{xs}/\sigma'_0$). This ratio varies from zero (i.e., no excess pore pressures) to unity (i.e., complete transfer of the load to the pore water or "liquefaction") and, therefore, provides more insight than the magnitude of the excess pore pressure alone.

In an attempt to better understand, quantify, and model the pore pressure generation in sands and non-plastic silty soils, Polito et al. (2008) confirmed the validity of two existing models (Green et al., 2000; Seed et al., 1975a) for predicting the pore pressure ratios in silty sands, based on the results of approximately 150 cyclic triaxial tests performed on soils ranging from clean sands to pure silt, with the specimens having a wide range of densities and subjected to a range of loading amplitudes. Also, Polito et al. (2008) evaluated the applicability of the two models, and proposed empirical correlations for the pore pressure calibration parameters required by the two models, wherein the author of this thesis developed the empirical relationships by implementing the non-linear mixed-effects (NLME) regression method.

In this chapter, the details on developing the empirical correlations proposed by Polito et al. (2008) are presented. Accordingly, the chapter briefly reviews the two pore pressure generation models and the properties of the cyclic triaxial soil specimens used by Polito et al. (2008). Next, the proposed correlations for the pore pressure calibration parameters of the two models are introduced, and the regression results are presented along with the assessment of the distributional assumptions inherent to the NLME method. Based on the correlations developed herein, the calibration parameters' dependencies on each variable are described. Lastly, major findings are summarized.

8.2 Pore Pressure Generation Models

8.2.1 Seed et al. Model

In the 1970's, Seed et al. (1975a) developed an empirical model for predicting r_u using data from tests performed on clean sands. In their model, r_u is a function of the cycle ratio, which is the ratio of the number of applied uniform cycles of loading N to the number of cycles required to cause liquefaction in the soil N_ℓ, and an empirically determined parameter α, which is given by:

$$r_u = \frac{1}{2} + \frac{1}{\pi}\arcsin\left(2\left(\frac{N}{N_l}\right)^{1/\alpha} - 1\right) \qquad \text{(Eq. 8-1)}$$

Later, Booker et al. (1976) proposed an alternative, somewhat simplified version of this equation:

$$r_u = \frac{2}{\pi}\arcsin\left(\frac{N}{N_l}\right)^{\frac{1}{2\alpha}} \qquad \text{(Eq. 8-2)}$$

Each of the above equations makes use of two calibration parameters (i.e., N_ℓ and α) that can be determined from stress-controlled cyclic triaxial tests, as well as other types of constant volume, cyclic tests. For a given soil, N_ℓ increases as relative density increases and decreases as the magnitude of loading increases, with the magnitude of loading typically expressed in terms of cyclic stress ratio *CSR*. The use of N_ℓ has its drawbacks as it can only be applied to liquefiable soils. However, "non-liquefiable" soils, such as dense sands and soils with plastic fines, can still undergo significant pore pressure increases and deformations as a result of cyclic softening (Boulanger and Idriss, 2006).

The second parameter α is an empirical constant. Both Eq. 8-1 and Eq. 8-2 have been found to produce results that are in good agreement with the results from cyclic triaxial tests (Lee and Albaisa, 1974) and cyclic simple shear tests (DeAlba et al., 1975) on clean sands. Lee and Albaisa's recommended upper and lower bounds of residual pore pressure ratio for Monterey #0 sand are shown in Figure 8-1. Also shown in this figure is the predicted excess pore pressure ratio curve generated using Eq. 8-2 with $\alpha = 0.7$ (i.e., the recommended value for clean sands per Booker et al., 1976).

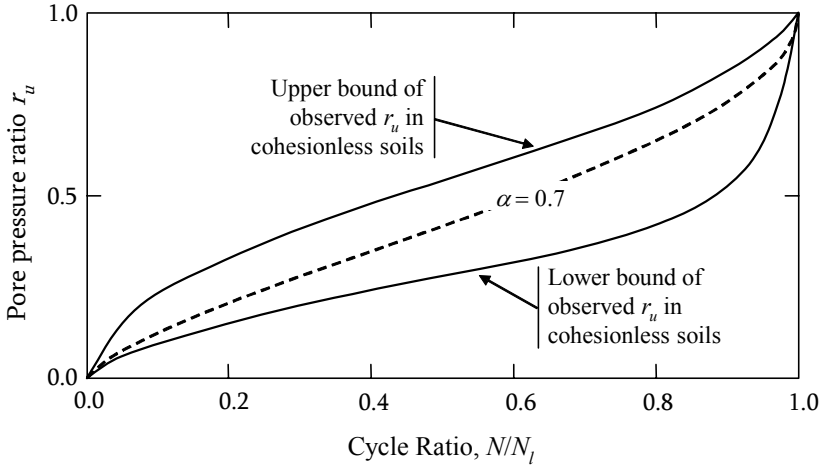

Figure 8-1. Observed bounds of excess pore pressure generation as a function of cycle ratio and approximate average of bounds given by Eq. 8-2 with $\alpha = 0.7$ (adapted from Seed et al., 1975a).

In addition to the two calibration parameters, implementation of either Eq. 8-1 or 2 for use in earthquake site response analyses requires that the earthquake motion be converted to an equivalent number of uniform cycles (Seed et al., 1983). Such load conversion procedures are outlined in Seed et al. (1975b), Liu et al. (2001), Green and Terri (2005), and Hancock and Bommer (2005). This required conversion is the greatest disadvantage in using either Eq. 8-1 or 2 for predicting pore pressure generation in soils subjected to

earthquake-type loadings. The pore pressure generation model by Green et al. (2000) described below alleviates the need for converting earthquake motions to an equivalent uniform load.

8.2.2 GMP Model

Green, Mitchell, and Polito (2000) developed the GMP model, which is an empirical expression that relates r_u to the energy dissipated per unit volume of soil (i.e., unit energy). The GMP model was developed using data from tests performed on non-plastic silt-sand mixtures that ranged in fines contents from clean sands to pure silts. The GMP model is given by:

$$r_u = \sqrt{\frac{W_S}{PEC}} \leq 1 \qquad \text{(Eq. 8-3)}$$

where: W_S is the energy dissipated per unit volume of soil divided by the initial effective confining pressure (i.e., normalized unit energy); and *PEC* is the "pseudo energy capacity", a calibration parameter.

For undrained cyclic triaxial test loadings, W_S can be computed numerically by:

$$W_S = \frac{1}{2\sigma'_0} \sum_{i=1}^{n-1} \left(\sigma_{d,i+1} + \sigma_{d,i}\right)\left(\varepsilon_{a,i+1} - \varepsilon_{a,i}\right) \qquad \text{(Eq. 8-4)}$$

where: n is the number of load increments to liquefaction; $\sigma_{d,\mathrm{i}}$ and $\sigma_{d,\mathrm{i+1}}$ are the applied deviator stress at load increment i and i+1, respectively; and $\varepsilon_{a,\mathrm{i}}$ and $\varepsilon_{a,\mathrm{i+1}}$ are the axial strain at load increment i and i+1, respectively. Figure 8-2 graphically shows the application of Eq. 8-4. As may be observed from this figure, Eq. 8-4 is simply the

trapezoidal rule used to compute the area bounded the stress-strain hysteresis loops divided by the initial effective confining stress, which is the normalized unit energy.

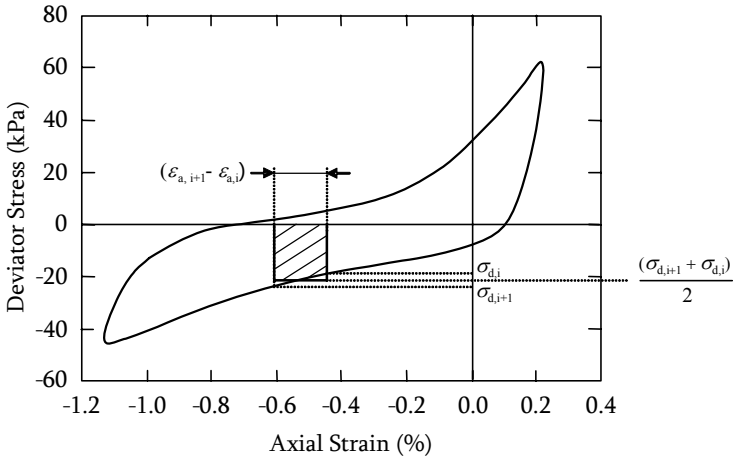

Figure 8-2. The dissipated energy per unit volume for a soil sample in cyclic triaxial loading is defined as the area bound by the stress-strain hysteresis loops (adapted from Green et al., 2000).

The pseudo energy capacity *PEC* is determined from cyclic test data by plotting r_u versus the square root of W_S. The square root of *PEC* is the value on the horizontal axis corresponding to the intersection of a straight line drawn through the origin and the point of $r_u = 0.65$ and a horizontal line drawn at $r_u = 1.0$. This process of determining *PEC* is illustrated graphically in Figure 8-3. Numerically this procedure simplifies to:

$$PEC = \frac{W_{S,\, r_u=0.65}}{0.4225} \qquad \text{(Eq. 8-5)}$$

where, $W_{S,r_u=0.65}$ is the value of W_S corresponding to $r_u = 0.65$. The term "pseudo energy capacity" is used to indicate that the calibration parameter has a physical significance, rather than just being a general curve fit parameter. Specifically, *PEC* is approximately equal to, but generally less than, the normalized unit energy dissipated in a sample at the point of initial liquefaction (i.e., when $r_u = 1.0$). The definition of *PEC* and the

procedures for determining it were developed empirically from analyzing numerous cyclic tests (Green, 2001; Green et al., 2000).

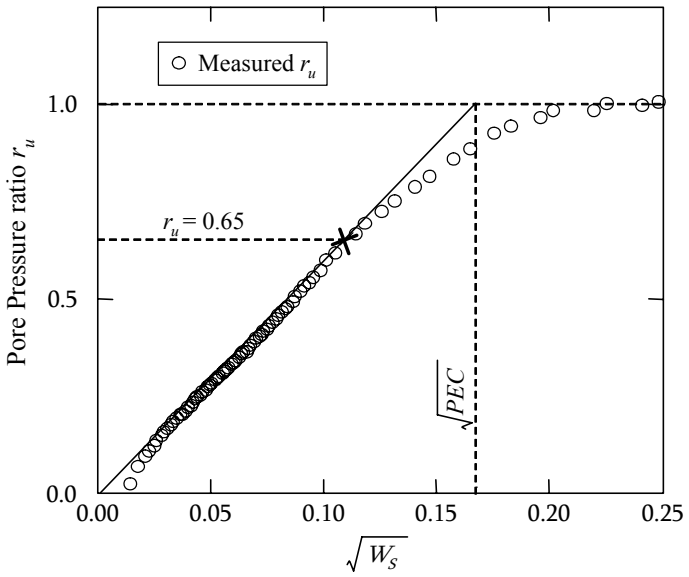

Figure 8-3. Graphic illustration of how *PEC* is determined from cyclic test data. The data shown in this figure is from a cyclic triaxial test conducted on Yatesville clean sand (adapted from Green et al., 2000).

8.3 Physical Properties of the Soils and Specimens

The data from the 145 cyclic triaxial tests were culled from nearly 300 cyclic triaxial tests (Polito, 1999; Polito and Martin, 2001). The specimens tested by Polito et al. (2008) were comprised of one of two base sands, mixed with varying amounts of non-plastic silt. Eight combinations of sand and silt were created using each of the two sands, with silt contents varying from 4 to 75 percent by weight. Additionally, tests were performed on clean sand and pure silt specimens. The distribution of the number of specimens tested at each silt content is given in Figure 8-4.

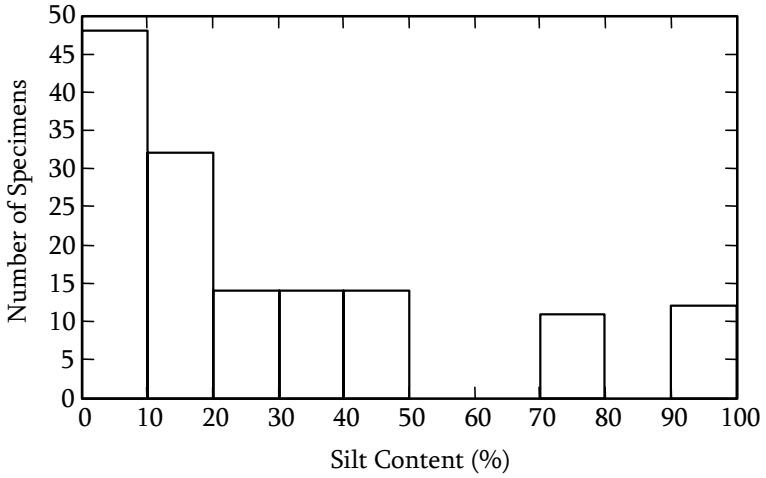

Figure 8-4. Distribution of silt contents for specimens (Polito et al., 2008).

The first sand used in the testing program was Monterey No. 0/30, a commercially available sand from California. It has the same mineralogy and a similar gradation to Monterey No. 0 sand, which has been used in numerous liquefaction studies in the past (e.g., Silver, 1977). Monterey No. 0/30 is a medium to fine sand, having over 98 percent retained between the No. 20 (0.84 mm) and No. 100 (0.15 mm) sieves. It has a median grain size, D_{50}, of 0.43 mm and its grains are sub-angular to sub-rounded in shape.

The second sand used by Polito et al. (2008) was Yatesville sand. It consists of the coarse fraction of Yatesville silty sand, which was obtained from a dam site in Louisa County, Kentucky. It is a medium to fine sand, having approximately 99 percent passing the No. 20 (0.84 mm), 45 percent passing the No. 100 (0.15 mm) sieves, and a median grain size, D_{50}, of 0.18 mm. Its grains are sub-angular to sub-rounded in shape.

The silt used by Polito et al. (2008) was derived from the fine-grained portion of the Yatesville silty sand. It has a maximum grain size of 0.074 mm, a minimum grain size of

0.004 mm, and a median grain size, D_{50}, of 0.03 mm. The silt is non-plastic, with no discernible liquid or plastic limit. Grain size distributions for both of the sands and the silt are shown in Figure 8-5.

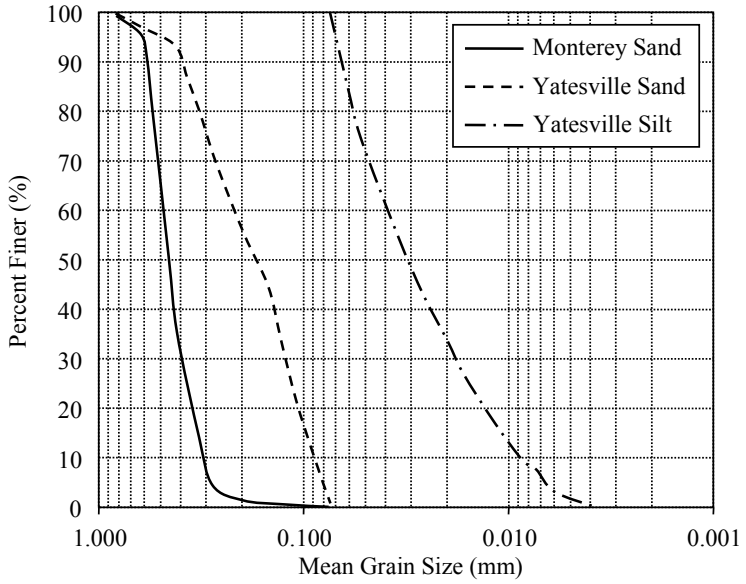

Figure 8-5. Grain size distributions for the soils (Polito et al., 2008).

The test specimens used by Polito et al. (2008) were selected from approximately 300 tests based upon two criteria:

- Possessing a relative density between 0 and 110 percent.
- Reaching initial liquefaction (i.e., $r_u = 1.0$) in more than 2, but less than 60 cycles.

These criteria were used because they represent a probable range of densities and cyclic loadings for soils under natural conditions. As previously noted, 145 of the 300 available tests met both criteria. The distributions of the specimens based upon their relative density and the number of cycles required to liquefy them, N_ℓ, are shown in Figure 8-6 and Figure 8-7, respectively.

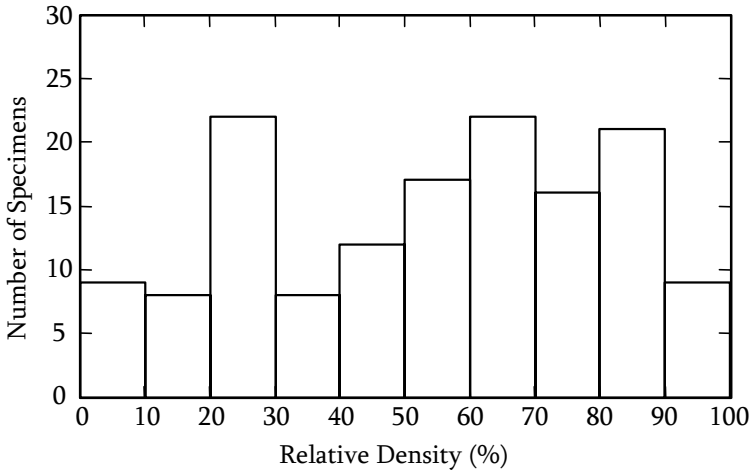

Figure 8-6. Distribution of relative densities for specimens (Polito et al., 2008).

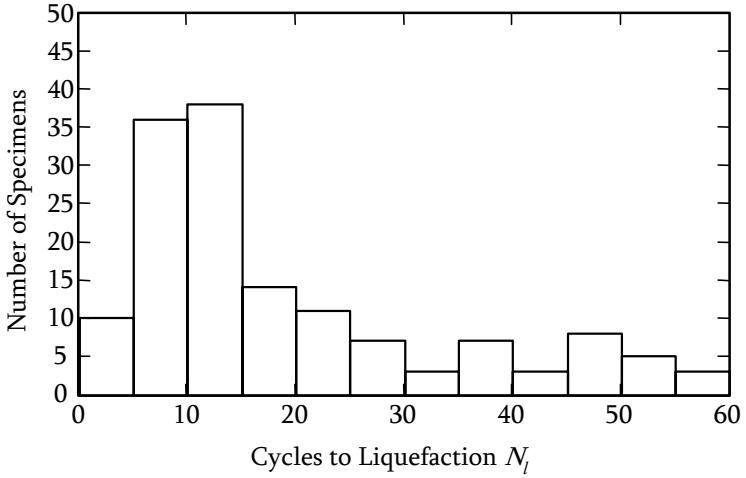

Figure 8-7. Distribution of number of the cycles to initial liquefaction N_ℓ for specimens (Polito et al., 2008).

The specimens were 71 mm (2.8 in.) in diameter and 154 mm (6.1 in.) in height and were formed by moist tamping at a water content that produced 50 % saturation in the specimen. In order to obtain a uniform density throughout the specimen, the undercompaction method of specimen preparation proposed by Ladd (1978) was used. Testing was performed using an electro-pneumatic cyclic triaxial testing apparatus designed by Professor Clarence Chan (Chan, 1985). The tests were performed in accordance with the procedures set forth by Silver (1977).

8.4 Proposed Models and Regression Results

Correlations relating α and *PEC* to relative density D_r, cyclic stress ratio *CSR* (only for α), and fines content *FC* were developed by implementing the NLME modeling with the data grouped by *FC* as random-effects. During the data observations, it was found that both α and *PEC* with the *FC* greater than or equal to about 35% show distinct trends from those with the *FC* less than 35%. This is clearly shown in Figure 8-8. Therefore, separate regressions for these two *FC* ranges are appropriate.

8.4.1 Correlation for α

After considering various forms of equations in the regression analyses, the following model produced the lowest total standard deviation σ_{total} for both *FC* ranges:

$$\alpha = C_1 \cdot FC + C_2 \cdot D_r + C_3 \cdot CSR + C_4 \qquad \text{(Eq. 8-6)}$$

where: D_r is relative density in percent; *CSR* is cyclic stress ratio; *FC* is fines content in percent; and C_1 through C_4 are regression coefficients. Herein, C_4 was set as both fixed- and random-effects coefficient. Table 8-1 shows the regression coefficients, their p-values, the standard deviations determined from the two separate regressions for each range of *FC* (i.e., $FC < 35\%$ and $FC \geq 35\%$). It is noted that the random-effects were estimated as zero for $FC \geq 35\%$, which indicates no variation in the estimated C_4 values among the groups of $FC \geq 35\%$. Consequently, the inter-group errors were zero. Based on the resulting p-values, the coefficients C_3 and C_2 for $FC < 35\%$ and $FC \geq 35\%$, respectively, appear to have no significant statistical contributions. However, it was

decided to keep them in the correlations to account for *CSR* and D_r dependencies of the α, even though the levels of the dependencies are very low.

The distributional assumptions on the intra-event errors and random-effects were assessed by the normal Q-Q plots. Figure 8-9 shows the normal Q-Q plots of intra-group errors and random-effects; the normal Q-Q plot of random-effects is for the FC < 35%. No significant violation of the normality assumptions is observed in either of the plots. Also, scatter plots of intra-group errors and random-effects are shown in Figure 8-10, wherein one can observe symmetrical distributions with respect to the zero lines of the standardized inter-event errors and random-effects.

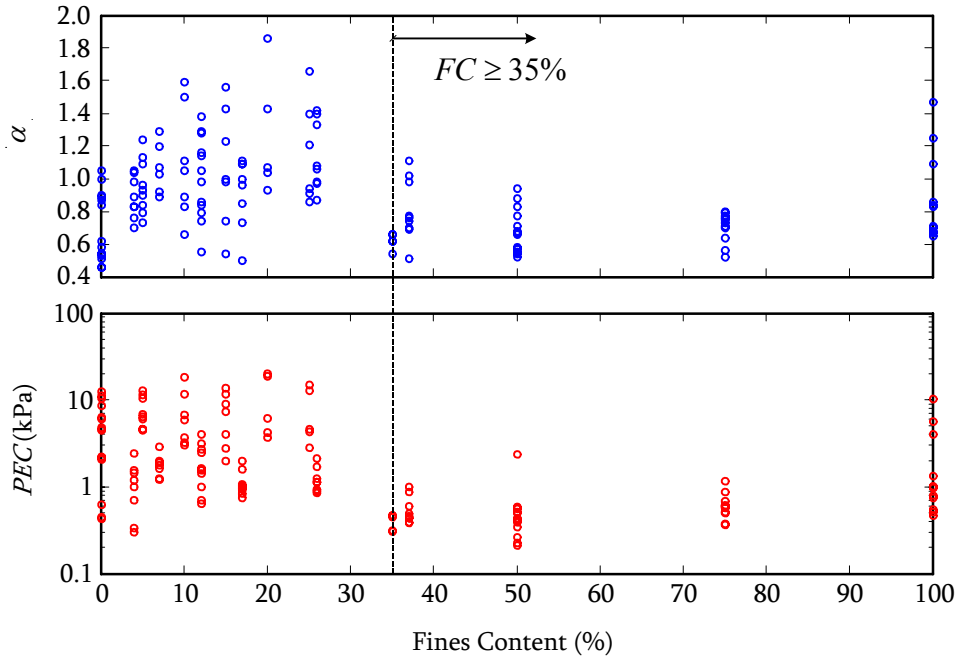

Figure 8-8. α and *PEC* data distributions with respect to fines content.

Table 8-1. Regression results for α: the p-values in parentheses.

FC	C_1	C_2	C_3	C_4	τ	σ	σ_{total}
<35%	0.0117 (0.020)	0.00740 (0.000)	0.0103 (0.970)	0.51 (0.000)	0.11	0.19	0.22
≥35%	0.00215 (0.075)	-0.00094 (0.358)	1.67 (0.000)	0.43 (0.000)	0.00†	0.14	0.14

†: random-effects were estimated as zero.

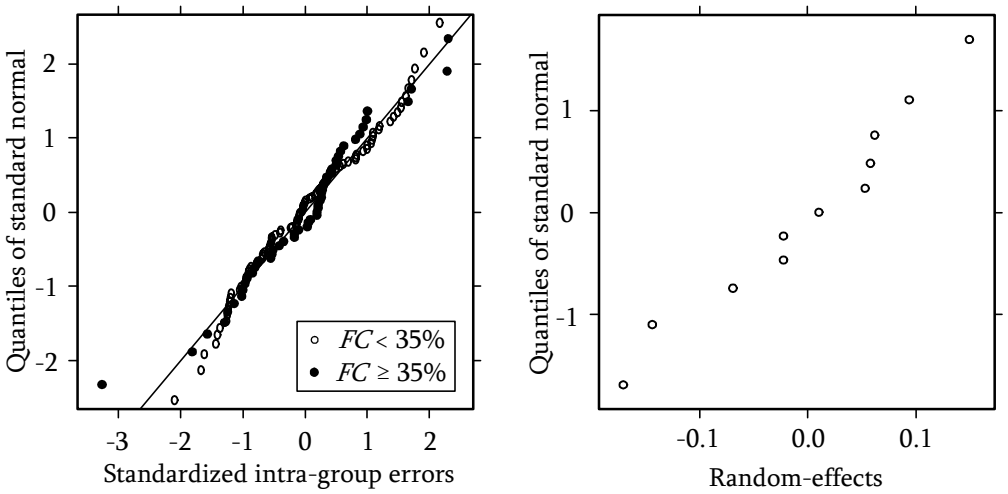

Figure 8-9. Normal Q-Q plots of intra-group errors and random-effects.

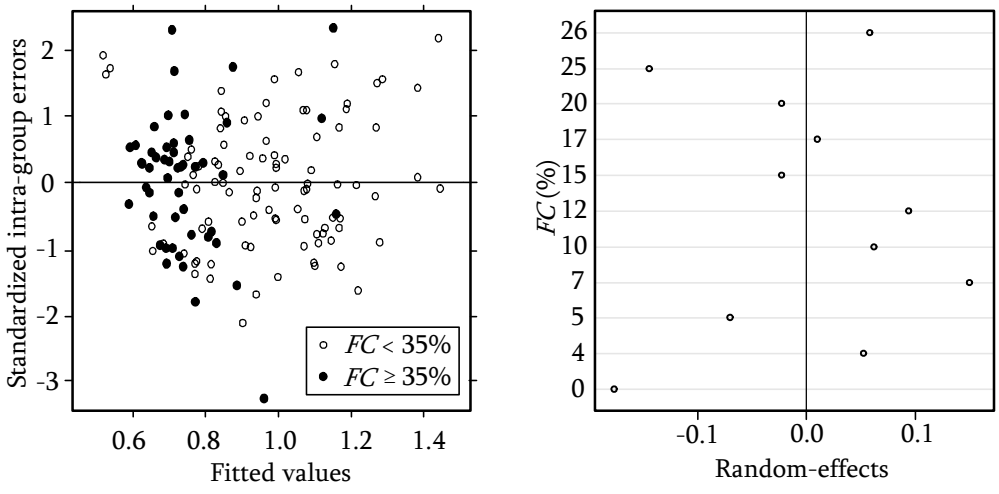

Figure 8-10. Scatter plots of intra-group errors and random-effects.

Eq. 8-6 in conjunction with the coefficients listed in Table 8-1 is plotted in Figure 8-11 (a) and (b) in terms of *CSR* and D_r, respectively, for various *FC*. As may be observed from these figures and Eq. 8-6, for *FC* < 35% α is relatively independent of *CSR*, but increases with increasing *FC* and D_r. In contrast, for *FC* ≥ 35% α increases significantly as *CSR* increases, but is relatively independent of D_r, decreasing slightly as D_r increases. Also plotted in these figures are lines corresponding to $\alpha = 0.7$, which is the value recommended by Booker et al. (1976) for clean sands. Contrary to Booker et al.'s recommendation, Figure 8-11 shows that $\alpha = 0.7$ is too low, except for silty sands subjected to small *CSR*s.

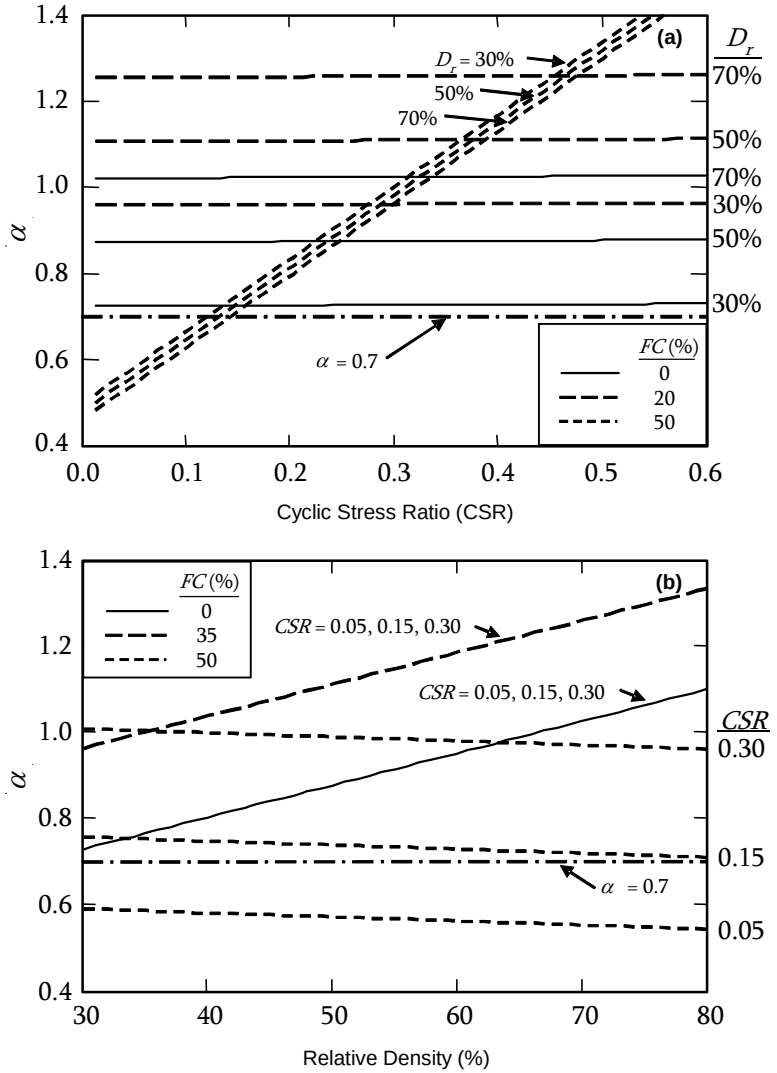

Figure 8-11. Correlation for α: (a) α as a function of *CSR* for three different *FC* and D_r; and (b) α as a function of D_r for three different *CSR* and *FC* (Polito et al., 2008).

Finally, the fact that the correlation for α (i.e., Eq. 8-6) changes trends for sands having *FC* less than and greater than 35% is not altogether surprising, as it is consistent with the limiting silt content concept (Green et al., 2006; Polito, 1999; Polito and Martin, 2001). The limiting silt content is the maximum amount of silt that can be contained in the void space while maintaining a contiguous sand skeleton. The limiting silt content is the transition point below which the soil structure is primarily one of silt grains contained

within a sand matrix and above which it is predominately sand grains suspended in a silt matrix with little, if any, sand grain to sand grain contact. Figure 8-12 provides a visual description of these differing conditions. The Monterey No. 0/30 and Yatesville sands used in the study have limiting silt contents between 25% and 36%.

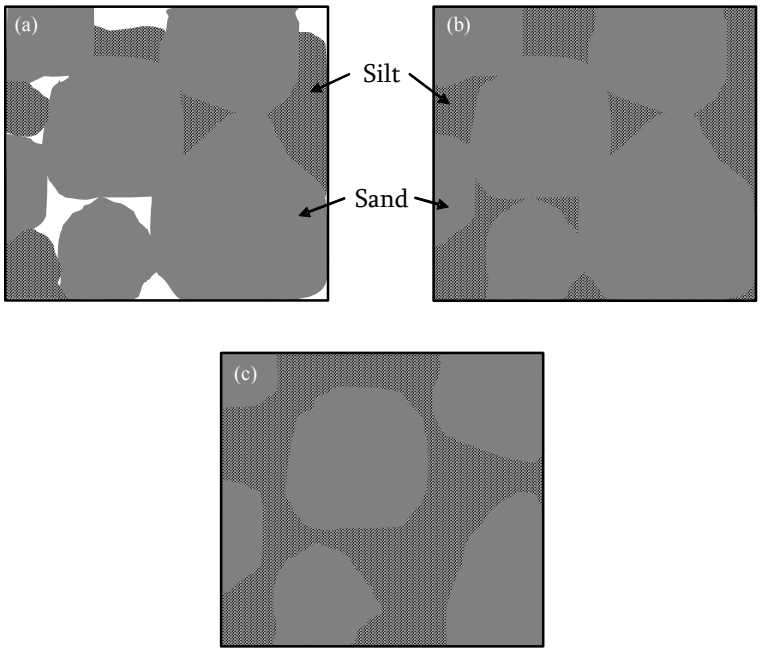

Figure 8-12. Visual description of the limiting silt content: (a) Below the limiting silt content; (b) At the limiting silt content; and (c) Above the limiting silt content (Polito et al., 2008).

8.4.2 Correlation for *PEC*

Based on various forms of equations considered in the regression analyses for *PEC* and the log-normal distribution of the *PEC* data, the regression model best representing the data was found to be:

$$\ln(PEC) = \begin{cases} \exp(C_3 \cdot D_r) + C_4 & \text{for } FC < 35\% \\ C_1 \cdot FC^{C_2} + \exp(C_3 \cdot D_r) + C_4 & \text{for } FC \geq 35\% \end{cases} \quad \text{(Eq. 8-7)}$$

where: D_r is relative density in percent; FC is fines content in percent; and C_1 through C_4 are regression coefficients. Similar to the correlation for α, C_4 was set as both fixed-and

random-effects coefficient. However, for *PEC*, two different models for each range of *FC* were fitted with one NLME regression analysis. The resulting regression coefficients, their p-values, and standard deviations are listed in Table 8-2. The coefficients with high p-values were kept in the proposed correlation for the same reason as they were in the α correlation. The distributional assumptions are valid based on the normal Q-Q plots of intra-group errors and random-effects shown in Figure 8-13. Also, their scatter plots are shown in Figure 8-14, where the distributions are symmetrical to the zero lines of intra-group errors and random-effects.

Table 8-2. Regression results for *PEC*: the p-values in parentheses.

C_1	C_2	C_3	C_4	τ	σ	$\sigma_{ln\ total}$
-0.60 (0.358)	0.31 (0.239)	0.014 (0.000)	-1.02 (0.000)	0.44	0.49	0.66

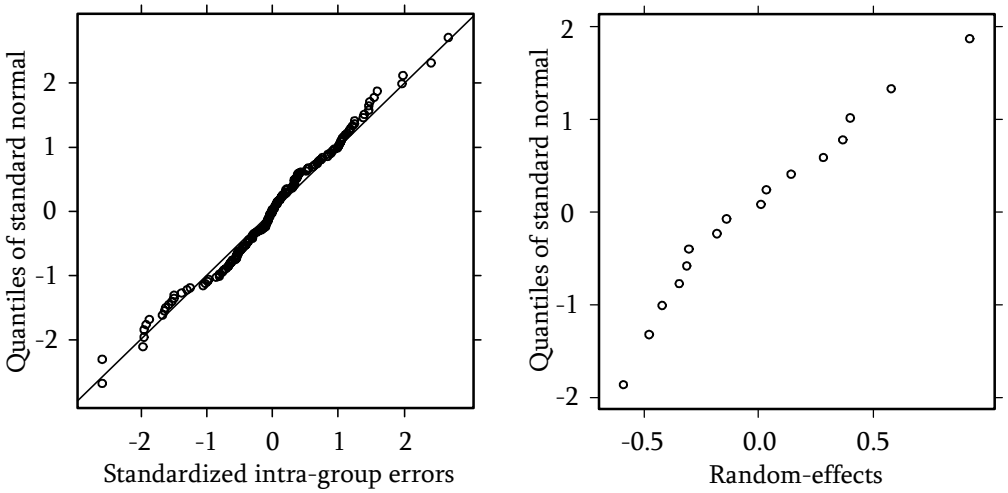

Figure 8-13. Normal Q-Q plots of intra-group errors and random-effects.

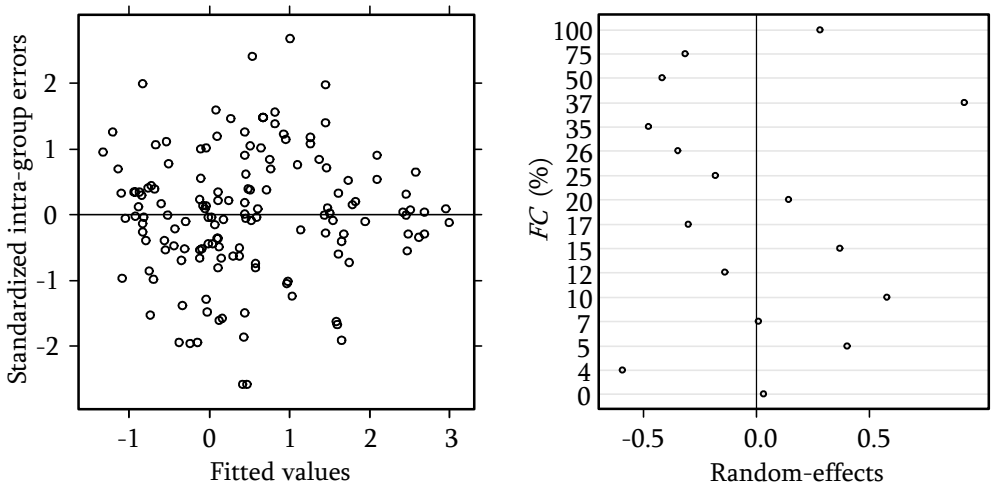

Figure 8-14. Scatter plots of intra-group errors and random-effects.

Eq. 8-7 in conjunction with the coefficients listed in Table 8-2 is plotted in Figure 8-15 for various *FC* as a function D_r. As may be observed from this figure and Eq. 8-7, for *FC* < 35% *PEC* increases as D_r increases, and decreases as *FC* increases. In contrast, for *FC* ≥ 35% *PEC* is relatively independent of D_r and *FC*, increasing slightly as D_r increases and decreasing slightly as *FC* increases. As with the trends identified for α (Eq. 8-6 and Figure 8-11), the trends observed from Figure 8-15 are consistent with the limiting silt content concept.

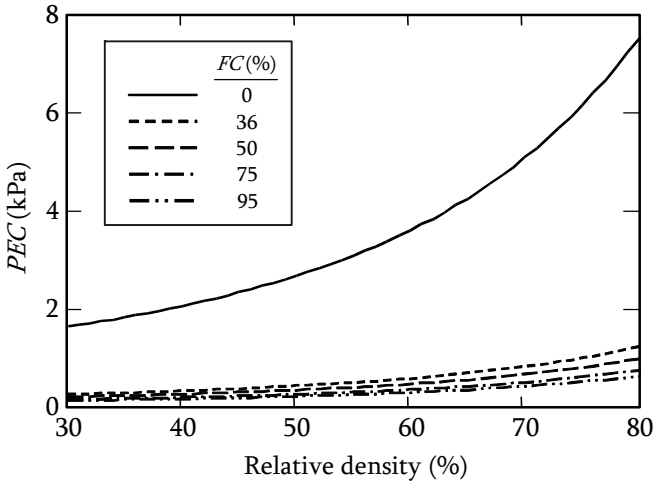

Figure 8-15. Plot of the correlation for *PEC* as a function of D_r for various *FC* (Polito et al., 2008).

8.5 Conclusions

Using data from approximately 150 cyclic triaxial tests covering a wide range of non-plastic silt contents and densities, the correlations for estimating the calibration parameters required by the pore pressure generation models (i.e., Green et al., 2000; Seed et al., 1975a) were developed by implementing the NLME modeling.

There were drastic changes in both calibration parameters between the fines content ranges: $FC < 35\%$ and $FC \geq 35\%$, which is consistent with the limiting fines content concept. Also, the correlation developed for α showed that the value suggested by Booker et al. (1976) for clean sands (i.e., $\alpha = 0.7$) is too low, except for silty sands subjected to small *CSR*s.

References

Booker, J. R., Rahman, M. S., and Seed, B. H. (1976). "GADFLEA - A Computer Program for the Analysis of Pore Pressure Generation and Dissipation during Cyclic or Earthquake Loading." *Report No. EERC 76-24*, Earthquake Engineering Research Center, University of California at Berkeley, Berkeley, CA.

Boulanger, R. W., and Idriss, I. M. (2004). "Evaluating the potential for liquefaction or cyclic failure of silts and clays." *Report No. UCD/CGM-04/01*, Center for Geotech. Modeling, Univ. of California at Davis, Davis, California.

Boulanger, R. W., and Idriss, I. M. (2006). "Liquefaction susceptibility criteria for silts and clays". *Journal of Geotechnical and Geoenvironmental Engineering*, 132(11), 1413-1426.

Bray, J. D., Sancio, R. B., Durgunoglu, T., Onalp, A., Youd, T. L., Stewart, J. P., Seed, R. B., Cetin, O. K., Bol, E., Baturay, M. B., Christensen, C., and Karadayilar, T. (2004). "Subsurface characterization at ground failure sites in Adapazari, Turkey". *Journal of Geotechnical and Geoenvironmental Engineering*, 130(7), 673-685.

Chan, C. K. (1985). *Instruction manual, CKC E/P cyclic loading triaxial system users' manual*, Soil Engineering Equipment Company, San Francisco.

DeAlba, P., Chan, C. K., and Seed, B. H. (1975). "Determination of soil liquefaction characteristics by large-scale laboratory tests." *Report No. EERC 75-14*, Earthquake Engineering Research Center, Univ. of California at Berkeley, Berkeley, California.

Green, R. A. (2001). "Energy-based evaluation and remediation of liquefiable soils," Ph.D. dissertation, Virginia Polytechnic Institute and State University, Blacksburg, Virginia.

Green, R. A., Mitchell, J. K., and Polito, C. P. (2000). "An Energy-Based Pore Pressure Generation Model for Cohesionless Soils." *Proc. John Booker Memorial Symposium*, Melbourne, Australia.

Green, R. A., Olson, S. M., and Polito, C. P. (2006). "A comparative study of the influence of fines on the liquefaction susceptibility of sands: Field versus laboratory." *Proc. 8th National Conference on Earthquake Engineering*, Earthquake Engineering Research Institute, Paper No. 8NCEE-001251, Oakland, California.

Green, R. A., and Terri, G. A. (2005). "Number of equivalent cycles concept for liquefaction evaluations - Revisited". *Journal of Geotechnical and Geoenvironmental Engineering*, 131(4), 477-488.

Hancock, J., and Bommer, J. J. (2005). "The effective number of cycles of earthquake ground motion". *Earthquake Engineering and Structural Dynamics*, 34(6), 637-664.

Ladd, R. S. (1978). "Preparing test specimens using undercompaction". *Geotech. Test. J.*, 1(1), 16-23.

Lee, K. L., and Albaisa, A. (1974). "Earthquake induced settlements in saturated sands". *American Society of Civil Engineers, Journal of the Geotechnical Engineering Division*, 100(GT4), 387-406.

Liu, A. H., Stewart, J. P., Abrahamson, N. A., and Moriwaki, Y. (2001). "Equivalent number of uniform stress cycles for soil liquefaction analysis". *Journal of Geotechnical and Geoenvironmental Engineering*, 127(12), 1017-1026.

Martin, G. R., Finn, W. D. L., and Seed, H. B. (1975). "Fundamentals of liquefaction under cyclic loading". *American Society of Civil Engineers, Journal of the Geotechnical Engineering Division*, 101(5), 423-438.

Martin II, J. R., Guney Olgun, C., Mitchell, J. K., and Turan Durgunoglu, H. (2004). "High-modulus columns for liquefaction mitigation". *Journal of Geotechnical and Geoenvironmental Engineering*, 130(6), 561-571.

Peng, J., Lu, J., Law, K. H., and Elgamal, A. (2004). "PARCYCLIC: Finite-element modeling of earthquake liquefaction response on parallel computers." *Proc. 13th World Conference on Earthquake Engineering*, International Association for Earthquake Engineering, Paper No. 361, Tokyo, Japan.

Polito, C. P. (1999). "The effects of non-plastic and plastic fines on the liquefaction of sandy soils," Ph.D. dissertation, Virginia Polytechnic Institute and State University, Blacksburg, Virginia.

Polito, C. P., Green, R. A., and Lee, J. (2008). "Pore pressure generation models for sands and silty soils subjected to cyclic loading". *Journal of Geotechnical and Geoenvironmental Engineering*, 134(10), 1490-1500.

Polito, C. P., and Martin, J. R. (2001). "The effects of non-plastic fines on the liquefaction resistance of sands". *Journal of Geotechnical & Geoenvironmental Engineering*, 127(5), 408-415.

Sanin, M. V., and Wijewickreme, D. (2006). "Cyclic shear response of channel-fill Fraser River Delta silt". *Soil Dynamics and Earthquake Engineering*, 26(9), 854-869.

Seed, B. H., Martin, P. P., and Lysmer, J. (1975a). "The generation and dissipation of pore water pressures during soil liquefaction." *Report No. EERC 75-26*,

Earthquake Engineering Research Center, University of California at Berkeley, Berkeley, California.

Seed, H. B., Idriss, I. M., and Arango, I. (1983). "Evaluation of liquefaction potential using field performance data". *Journal of Geotechnical Engineering*, 109(3), 458-482.

Seed, H. B., Idriss, I. M., Makdisi, F., and Banerjee, N. (1975b). "Representation of Irregular Stress Time Histories by Equivalent Uniform Stress Series in Liquefaction Analysis." Report No. EERC 75-29, Earthquake Engineering Research Center, College of Engineering, Univ. of California, Berkeley, California, United States.

Silver, M. L. (1977). "Laboratory triaxial testing procedures to determine the cyclic strength of soils." *NUREG-0031*, National Technical Information Service, Springfield, Virginia.

Sun, R., and Yuan, X. (2006). "A simplified formula for estimating real-time pore water pressure of anisotropically-consolidated saturated sands under random earthquake loads." Reston, VA 20191-4400, United States, 444-451.

Wijewickreme, D., Sanin, M. V., and Greenaway, G. R. (2005). "Cyclic shear response of fine-grained mine tailings". *Canadian Geotechnical Journal*, 42(5), 1408-1421.

Chapter 9

Conclusions

9.1 Restatement of Objective of Study

The objectives of this study are:

3. To develop empirical correlations (i.e., predictive equations or relationships) for stable continental regions (e.g., central/eastern US: CEUS) relating various engineering characteristic parameters of the horizontal components of earthquake ground motions to design earthquake parameters, such as earthquake magnitude, site-to-source distance, and local site conditions (i.e., rock vs. soil).
4. To identify the differences in engineering characteristics of earthquake ground motions from stable continental regions and active seismic regions (e.g., western US: WUS).

9.2 Summary of Findings

• Characteristic Periods

Characteristic periods considered in this study are:

- predominant spectral period (T_p)
- smoothed spectral predominant period (T_0)
- average spectral period (T_{avg})

- mean period (T_m)
- spectral velocity-acceleration ratio periods ($T_{V/A50}$ and $T_{V/A84}$).

For all the definitions of characteristic period, rock motions had shorter periods (i.e., higher frequencies) than soil motions for both CEUS and WUS. Also, the characteristic periods of rock motions increased more as a function of distance than soil motions. In comparing CEUS and WUS predictive relationships developed in this study, CEUS motions had shorter periods than WUS motions. This was also observed in comparison with previously developed relationships (i.e., Rathje et al., 1998; Rathje et al., 2004) for active shallow crustal motions (e.g., WUS motions). Additionally, the empirical CEUS model for T_m for rock sites developed in this study was compared with a theoretical CEUS model derived from the Brune point source model (Brune, 1970; 1971) by Rathje et al. (1998). No significant differences between predictions using the two models were observed.

• Strong Ground Motion Durations

Strong ground motion durations considered in this study are:

- significant durations ($D_{5\text{-}75}$ and $D_{5\text{-}95}$)
- bracketed duration ($D_{bracket}$)
- effective duration (D_{eff}).

Significant durations for CEUS increased as earthquake magnitude and distance increased. Interestingly, rock motions in CEUS were consistently estimated to have longer significant durations than soil motions, which is opposite to the trend observed from WUS motions. Additional analyses are required to better understand this

unexpected trend. In comparing CEUS and WUS motions, significant durations for rock motions in CEUS were consistently longer than those in WUS. However, significant durations of soil motions in CEUS and WUS were similar.

Both bracketed and effective durations decrease with increasing distance, but increased significantly with increasing magnitude. Soil motions in WUS were estimated to have longer durations than comparable rock motions. However, soil motions in CEUS had longer durations than rock motions at distances farther than about 75 km and 45 km for bracketed and effective durations, respectively. From comparing CEUS and WUS motions, it was found that CEUS motions had systematically longer durations than WUS motions. This trend became more pronounced as distance increased due to more rapid duration decreases with distance in WUS than in CEUS. In comparison with the previously developed relationship by Chang and Krinitzsky (1977) for bracketed duration, Chang and Krinitzsky's model predicted significantly longer durations than this study's WUS model, especially for soil sites. This is not surprising because the Chang and Krinitzsky model was developed based on upper-bounds of durations and motions having zero-duration were not considered. Accordingly, Chang and Krinitzsky model is not recommended due to its overly conservative predictions, particularly for soil sites.

• Intensity Measures

Average Arias intensities of the two orthogonal horizontal ground motions from a station/earthquake were considered in this study. For CEUS, Arias intensity decreased as distance increased, but increased as earthquake magnitude increased. In comparing rock

and soil motions in CEUS, soil motions for small and intermediate earthquake magnitudes had greater Arias intensities than comparable rock motions. Strangely, soil motions for large magnitudes (i.e., M7.5) had smaller intensities than comparable rock motions. Further investigation is needed to better understand this unexpected trend. In comparing CEUS and WUS motions, CEUS motions had larger intensities than WUS ones for both rock and soil sites. Meanwhile, as pointed out by Travasarou et al. (2003), the Kayen and Mitchell (1997) produced overly conservative estimations of Arias intensity for large magnitudes and underestimations for small magnitudes. Accordingly, Kayen and Mitchell's model is not recommended for estimating Arias intensity.

• Number of Equivalent Stress and Strain Cycles

The proposed model for the number of equivalent stress cycles ($n_{eq\tau}$) was developed using $n_{eq\tau}$ data computed using Green (2001) energy-based approach. The proposed predictive relationship shows that $n_{eq\tau}$ increases as distance increases, but decreases as depth increases. Also, $n_{eq\tau}$ increases as earthquake magnitude increases, although magnitude dependence was not significant in near-fault regions (i.e., R < 25 km). From comparing CEUS and WUS motions, it was found that $n_{eq\tau}$ for CEUS were larger and more depth dependent than for WUS. In comparison with previously developed relationships, there were significant differences between the $n_{eq\tau}$ predictions by this study's model and those predicted by Liu et al. (2001) and Seed et al. (1975b) models. The discrepancy likely stem from the different approaches used to implement the P-M hypothesis.

The proposed predictive relationship for the number of equivalent strain cycles ($n_{eq\gamma}$) was developed using $n_{eq\gamma}$ data generated by implementing Green and Lee (2006) procedure. Similarly to the findings for $n_{eq\tau}$, $n_{eq\gamma}$ increases with increasing distance and earthquake magnitude but decreases as depth increases. In comparing CEUS and WUS motions, CEUS motions were predicted to have larger $n_{eq\gamma}$ and more depth dependence than WUS motions.

• Pore Pressure Generation Calibration Parameters

The relationships developed for the calibration parameters (i.e., *PEC* and α) for the Green et al. (2000) and Seed et al. (1975a) pore pressure generation models showed that the calibration parameters drastically changed values for soils having fines contents (*FC*) above and below 35%. This finding is in line with the limiting fines content concept (Polito, 1999). Also, the correlation developed for α showed that the α value recommended by Booker et al. (1976) for clean sands (i.e., $\alpha = 0.7$) is too low, except for silty sands subjected to small *CSR*s.

9.3 Uncertainties in Proposed Models

Characteristics of earthquake ground motions are affected by various factors:

- earthquake magnitude
- site-to-source distance
- local site conditions
- tectonic environment

- fault mechanism (e.g., normal fault) including rupture propagation type (e.g., unilateral rupture propagation)
- near-fault effects (e.g., forward-directivity)
- topographical effects (e.g., basin effects)
- other unknown factors.

Incorporating these effects in predictive relationship for earthquake ground motion characteristics largely depends on analyzing ground motion recordings. The empirical relations for WUS developed before the 1990's generally only accounted for the influence of earthquake magnitude, distance, and site conditions. This was due to limitations in the ground motion databases. In recent years, however, other effects (e.g., basin effects, forward-directivity effects, and fault mechanism) have been incorporated into predictive relations (e.g., Kempton and Stewart, 2006; Rathje et al., 2004; Travasarou et al., 2003). This was possible because of the availability of more robust ground motion databases (e.g., the Pacific Earthquake Engineering Research strong motion database), as compared to the databases used to develop pre-1990 models. Consequently, predictive relations for WUS have become more sophisticated with reduced uncertainties (i.e., epistemic uncertainties) as a result of including the influence of various effects that were not included in previous predictive models.

In contrast to the WUS, the scarcity of strong motion recordings for CEUS makes it difficult to reduce uncertainties in ground motion characteristic predictions. In this study, most of the strong motion data used were scaled motions, not recorded motions. Consequently, it was not feasible in this study to consider effects other than earthquake

magnitude, distance, and local site conditions. Furthermore, as discussed in Chapter 2, the uncertainty inherent to the approach used to scale the motions adds an unquantified uncertainty to the CEUS predictive relationships. Additional earthquake recordings for stable continental regions, particularly for magnitudes greater than 6.0, are required to reduce this uncertainty.

9.4 Future Studies/Analyses

1. As a way to examine the validity of the ground motion scaling procedure, predictive relations should be developed using only recorded CEUS motions; these relations will be limited to small magnitude events. Additionally, relations should be developed using only CEUS motions that were scaled from WUS motions. The magnitudes and site-to-source distances of the scaled motions should be comparable to those of the recorded CEUS motions. The sets of predictive relationships should be compared. If the relationships compare well, then the ground motion scaling procedure is validated to the extent possible.
2. It is desirable to validate the CEUS scaled motions having forward-directivity effects. If recorded forward-directivity ground motions are available for CEUS, they should be compared with the CEUS motions scaled from forward-directivity WUS motions.
3. For engineering parameters having multiple definitions (e.g., characteristic periods), parametric studies are needed to identify which definition is best for specific engineering designs or analyses.
4. Mean period (T_m) predictive relation developed in this study was compared to a theoretically-derived model proposed by Rathje et al. (1998). However, there are

inconsistencies in the assumed parameters for the Brune point source model (Brune, 1970; 1971) used in the two studies. It would be interesting to compare the relation developed in this study to a theoretical relation that used the same point source parameters as were used in the scaling of the ground motions used in this study.

5. An empirical relationship for another intensity measures, such as the response spectral intensity (SI) can be developed using a theory-based regression model. Since the definition of SI is based on response spectra, a regression model can be formulated using Brune point source model (Brune, 1970; 1971) in conjunction with random vibration theory (RVT).
6. The sequencing of load pulses can be a significant factor in estimating the equivalent number of uniform cycles based on macro cumulative damage fatigue hypothesis. Accordingly, it is important for future studies to determine whether stress cycles are load-independent or load-dependent.
7. More soil profiles should be used in developing the relationship for the number of equivalent strain cycles so that the influence of dynamic soil properties can be identified.

References

Booker, J. R., Rahman, M. S., and Seed, B. H. (1976). "GADFLEA - A Computer Program for the Analysis of Pore Pressure Generation and Dissipation during Cyclic or Earthquake Loading." *Report No. EERC 76-24*, Earthquake Engineering Research Center, University of California at Berkeley, Berkeley, CA.

Boore, D. M. (1983). "Stochastic simulation of high-frequency ground motions based on seismological models of the radiated spectra". *Bulletin of the Seismological Society of America*, 73(6A), 1865-1894.

Brune, J. N. (1970). "Tectonic stress and spectra of seismic shear waves from earthquakes". *Journal of Geophysical Research*, 75(26), 611-614.

Brune, J. N. (1971). "Correction". *Journal of Geophysical Research*, 76(20), 1441-1450.

Chang, F. K., and Krinitzsky, E. L. (1977). "State-of-the-Art for Assessing Earthquake Hazards in the United States. Report 8. Duration, Spectral Content, and Predominant Period of Strong Motion Earthquake Records from Western United States." United States.

Green, R. A. (2001). "Energy-based evaluation and remediation of liquefiable soils," Ph.D. dissertation, Virginia Polytechnic Institute and State University, Blacksburg, Virginia.

Green, R. A., and Lee, J. (2006). "Computation of number of equivalent strain cycles: a theoretical framework". *Geomechanics II: Testing, Modeling, and Simulation*, ASCE Geotechnical Special Publication 156, 471-487.

Green, R. A., Mitchell, J. K., and Polito, C. P. (2000). "An Energy-Based Pore Pressure Generation Model for Cohesionless Soils." *Proc. John Booker Memorial Symposium*, Melbourne, Australia.

Kayen, R. E., and Mitchell, J. K. (1997). "Assessment of liquefaction potential during earthquakes by Arias intensity". *Journal of Geotechnical and Geoenvironmental Engineering*, 123(12), 1162-1174.

Kempton, J. J., and Stewart, J. P. (2006). "Prediction equations for significant duration of earthquake ground motions considering site and near-source effects". *Earthquake Spectra*, 22(4), 985-1013.

Liu, A. H., Stewart, J. P., Abrahamson, N. A., and Moriwaki, Y. (2001). "Equivalent number of uniform stress cycles for soil liquefaction analysis". *Journal of Geotechnical and Geoenvironmental Engineering*, 127(12), 1017-1026.

Polito, C. P. (1999). "The effects of non-plastic and plastic fines on the liquefaction of sandy soils," Ph.D. dissertation, Virginia Polytechnic Institute and State University, Blacksburg, Virginia.

Rathje, E. M., Abrahamson, N. A., and Bray, J. D. (1998). "Simplified frequency content estimates of earthquake ground motions". *Journal of Geotechnical and Geoenvironmental Engineering*, 124(2), 150-159.

Rathje, E. M., Faraj, F., Russell, S., and Bray, J. D. (2004). "Empirical relationships for frequency content parameters of earthquake ground motions". *Earthquake Spectra*, 20(1), 119-144.

Seed, B. H., Martin, P. P., and Lysmer, J. (1975a). "The generation and dissipation of pore water pressures during soil liquefaction." *Report No. EERC 75-26*, Earthquake Engineering Research Center, University of California at Berkeley, Berkeley, California.

Seed, H. B., Idriss, I. M., Makdisi, F., and Banerjee, N. (1975b). "Representation of Irregular Stress Time Histories by Equivalent Uniform Stress Series in Liquefaction Analysis." Report No. EERC 75-29, Earthquake Engineering Research Center, College of Engineering, Univ. of California, Berkeley, California, United States.

Travasarou, T., Bray, J. D., and Abrahamson, N. A. (2003). "Empirical attenuation relationship for Arias Intensity". *Earthquake Engineering & Structural Dynamics*, 32(7), 1133-1155.